

Wissenschaftlich-Technische Berichte
FZR-465
2007

Annual Report 2006

Institute of Safety Research

Editors:
Prof. Dr. Frank-Peter Weiss
Prof. Dr. Udo Rindelhardt



**Forschungszentrum
Dresden** Rossendorf

Cover Picture:

Scheme of the PROMISE experiment at Forschungszentrum Dresden-Rossendorf. The room-temperature metallic melt GaInSn between two rotating copper cylinders is exposed to an axial (yellow coil) as well as an azimuthal (central rod with 6000 A current) magnetic field. Velocities in the melt are measured by ultrasonic sensors (see contribution page 58ff).

Forschungszentrum Dresden - Rossendorf e.V.
Institute of Safety Research

P.O. Box 51 01 19
D-01314 Dresden
Germany

Director	Prof. Frank-Peter Weiss
phone	+ 49 (3 51) 2 60 34 80
fax	+ 49 (3 51) 2 60 34 40
e-mail	f.p.weiss@fzd.de
internet	http://www.fzd.de/FWS

CONTENTS

Preface

Selected reports

C. Beckert, U. Grundmann

Development and verification of a multigroup SP3 method for reactor core calculations 2

S. Kliem, U. Rohde

Boron dilution analyses at reactor shutdown conditions using the coupled code DYN3D/ATHLET 8

E. Altstadt, C. Beckert, H. Freiesleben, V. Galindo, E. Grosse, A.R. Junghans, C. Klug, B. Naumann, S. Schneider, R. Schlenk, A. Wagner, F.-P. Weiss

A photon neutron source for time-of-flight measurements at the radiation source ELBE 14

E. Krepper

Capability of actual CFD codes to support fuel rod bundle design 21

E. Bodele, D. Lucas

Simulation of bubble entrainment caused by liquid jet impinging on a free liquid surface 28

Ch. Vallee, Th. Höhne

CFD validation of stratified two-phase flows in a horizontal channel 33

E. Krepper, D. Lucas, H.-M. Prasser, M. Beyer, Th. Frank

CFD simulation of the two phase flow around an obstacle applying an inhomogeneous multiple bubble size class approach 39

F. Moretti, D. Melideo, F. D'Auria, Th. Höhne, S. Kliem

CFX simulations of ROCOM slug mixing experiments 46

Ch. Zhang, S. Eckert, G. Gerbeth

Bubble-driven liquid metal flows under the influence of a DC magnetic field 53

F. Stefani, Th. Gundrum, G. Gerbeth, R. Hollerbach, G. Rüdiger

Observation of magnetorotational instability in a liquid metal Taylor-Couette experiment 58

U. Hampel, A. Bieberle, E. Schleicher, G. Hessel, C. Zippe

High resolution gamma ray tomography and its application to the measurement of phase fractions in chemical reactions 64

H. Kryk, G. Hessel, W. Schmitt Online monitoring of Grignard reactions	70
H.-W. Viehrig, U. Rindelhardt, W. Keller Trepaning procedure applied at the RPV of the former Greifswald Nuclear Power Plant	76
A. Ulbricht, F. Bergner SANS response of VVER-440 type weld material after neutron irradiation, post irradiation annealing and reirradiation	81
E. Altstadt, H.-G. Willschütz Simulation of the corium-wall-interaction for an in-vessel-retention scenario	87
Summaries of research activities	93
Accident analysis of nuclear reactors	94
Materials and components safety	97
Particle and radiation transport	99
Safety and efficiency of chemical processes	102
Liquid metal magnetohydrodynamics	104
Thermal fluid dynamics of multiphase systems	106
TOPFLOW thermal hydraulic test facility	110
Publications	112
Publications in journals	113
Conference contributions and other oral presentations	119
Contributions to proceedings and other collected editions	133
FZR reports and other reports	145
Granted Patents	148
PhD and diploma theses	149
Awards	150
Guests	151
Meetings and workshops	154
Seminars of the Institute	155
Lecture courses	157
Departments of the Institute	158
Personnel	159

Preface

The Institute of Safety Research (ISR) is one of the six Research Institutes of Forschungszentrum Dresden-Rossendorf e.V. (FZD e.V.) which is a member institution of the Wissenschaftsgemeinschaft Gottfried Wilhelm Leibniz (Leibniz Association).

Together with the Institute of Radiochemistry, ISR constitutes the research programme „Safety and Environment“, which is one of the three scientific programmes of FZD. In the framework of this research programme, the institute is responsible for the two programme areas “Plant and Reactor Safety” and “Thermal Fluid Dynamics”, respectively (see Table 1). By participating in the development of a pulsed photo-neutron source at the radiation source ELBE (E**l**ectron linear accelerator for **b**eams of high brilliance and low **e**mittance), we also contribute to the projects, “neutron induced processes” and “irradiation induced transmutation”, which are constituents of the FZD programme dedicated to the structure of matter.

The research of ISR aims at assessing and enhancing the safety of industrial plants and at improving the environmental sustainability of the processes involved. The applications are related to nuclear plants of present and future designs as well as to installations of process industries.

To achieve the goals that were previously mentioned, the institute performs research in thermal fluid dynamics including magneto-hydrodynamics (MHD) and in materials sciences as related to material and component ageing. The thermal fluid dynamics research work is essentially based on the experiments performed at the **T**ransient **T**wo-**P**hase **F**low Test Facility, TOPFLOW. TOPFLOW is one of the large research and user facilities of FZD and represents the reference thermal hydraulic experiment of the so called “German CFD (Computational Fluid Dynamics) Initiative”. The development and validation of our reactor dynamics code DYN3D, coupled to thermal hydraulic computation models, for the safety analyses of current and future nuclear reactors is a further asset of ISRs portfolio. In 2006, DYN3D became an integral part of the European software platform NURESIM for the numerical simulation of light water reactors. There are about 12 organisations using DYN3D in 7 European countries and in Russia.

Programme / Programme area	Project / User facility
Safety and environment / Plant and reactor safety	Accident analysis of nuclear reactors
	Safety of materials and components
	Particle and radiation transport
	Safety and efficiency of chemical processes
Safety and environment / Thermal fluid dynamics	Magneto-hydrodynamics
	Thermal fluid dynamics of multi-phase flows
Safety and environment / User facility TOPFLOW	Transient two-phase flow test facility
Structure of matter / Sub-atomic physics	Design and construction of a pulsed photo-neutron source at ELBE

Table 1. Research projects and user facility of the Institute of Safety Research, 2006

Our work is financed through the basic funding of FZD as well as by external funds from public and private research grants, and from contracts with the industry. 39 % (2.888 k€) of our total expenditure were covered by such external funds in 2006 with 12 % from research grants

of the Federal Government, 13 % originated from Deutsche Forschungsgemeinschaft, 5 % from the EU, and 9 % from research contracts mainly with the industry (see Fig.1). The deployment of the total budget on the different projects and the user facility TOPFLOW (see Table 1) is illustrated in Fig. 2.

Together with the Dresden Technical University and with the Zittau University of Applied Sciences, the ISR represents the East German Centre of Competence in Nuclear Technology (Kompetenzzentrum Ost für Kerntechnik) which in turn is a member of the German Alliance for Competence in Nuclear Technology (Kompetenzverbund Kerntechnik). As such, the ISR also takes care to keep and promote the expertise in nuclear engineering. For that end, a strategic partnership was established between Kompetenzzentrum Ost and Vattenfall Europe Nuclear Energy (VENE).

Beyond this, ISR in general cares for the next generation of young scientists by supervising PhD, Master, and Diploma students for example. The quality of the education at ISR is underlined by the prizes awarded to our PhD students. Jiří Krepel received one of the 2006 doctoral students awards of FZD and the 2006 award of the Czech electric power company ČEZ for his dissertation on the simulation of Molten Salt Reactors. André Bieberle was awarded the “Siempelkamp Kompetenzpreis“ for his work on the measurement of the void distribution in BWR fuel elements by gamma ray tomography which was performed in close collaboration with AREVA.

Amongst the many excellent results obtained in 2006, two deserve particular reference.

It is well known that the steel of nuclear reactor pressure vessels (RPV) ages due to fast neutron irradiation during operation. This problem is of special importance to the Soviet type VVER reactors and to all those Western Pressurized Water Reactors which have attained permission for life time extension. In case of impermissible RPV embrittlement, thermal annealing is the only method to reconstitute ductile materials behaviour.

In this context, the properties of VVER-440 weld material were studied by means of Small Angle Neutron Scattering (SANS) after annealing (475°C/100h) and succeeding re-irradiation. It could be shown that annealing almost completely resolves the irradiation induced defect clusters with a mean radius of about 1nm. The thermal treatment leads to the creation of larger and stable Cu rich segregations. Then, re-irradiation again forms such 1nm defect clusters. However, the number of such clusters is saturated more quickly than during the first exposure. Moreover, the SANS analyses prove that the composition of the defect clusters generated by re-irradiation differs from the composition of the initial clusters. Re-irradiation defects contain fewer vacancies, but are richer in Cu, Si, and Ni (A. Ulbricht, F. Bergner, J. Böhmert, M. Valo, M.-H. Mathon, A. Heinemann: SANS response of VVER440-type weld material after neutron irradiation, post-irradiation annealing and re-irradiation; Philosophical Magazine, Volume 87, Issue 12, 1855 – 1870, April 2007). The accompanying mechanical investigations indicate that the embrittlement of weld material progresses more slowly during re-irradiation than when it is first exposed to neutrons.

In MHD, the ISR develops magnetic field technologies to improve industrial processes involving electrically conducting fluids such as semiconductor melts in crystal growth or metallic melts in the casting industry. Beyond this, we deal with MHD problems of basic scientific nature. The phenomenon, e.g., of the so called magneto-rotational instability (MRI) is of decisive meaning for the explanation of the creation of stars and black holes in the centre

of cosmic accretion disks. These central objects are growing by swallowing the matter in their vicinity. Since the total angular momentum must be conserved during this process, the “sucked in” gas must lose its angular momentum. If the flow in the accretion disk would be laminar, the outward transport of angular momentum is known to be much too small to explain the observed accretion rates. Only a turbulent flow would be able to accomplish this. Thus, the question arose, which phenomenon makes the hydrodynamically stable Kepler’s flow switch over to a turbulent flow regime. In 1991, Balbus and Hawley theoretically proved that this can happen by effect of the named MRI in the presence of an axial magnetic field. Now, in the framework of a common project of the ISR and the Astrophysical Institute Potsdam (AIP), based on the theory of G. Rüdiger (AIP) and R. Hollerbach (University of Leeds) MRI could for the first time be shown to occur in a Taylor-Couette flow. According to the theory, the experiment could be scaled down to laboratory size by combining the axial magnetic field with an azimuthal one. The experiment performed at ISR, in fact showed that MRI could be observed as travelling waves of the axial flow velocities in a certain band of magnetic field strengths. The axial and azimuthal magnetic field bands leading to instability as well as the measured wave frequency are in surprisingly good agreement with the theoretical predictions (F. Stefani, Th. Gundrum, G. Gerbeth, G. Rüdiger, M. Schultz, J. Szklarski, R. Hollerbach: Experimental evidence for magneto-rotational instability in a Taylor-Couette flow under the influence of a helical magnetic field; Phys. Rev. Letters, Vol. 97, 184502, 2006). F. Stefani, G. Gerbeth, and Th. Gundrum were awarded the FZD Research Prize 2006 for this outstanding result.

During the reporting period, the ISR organised important meetings and workshops with international participation. In particular, it is worth mentioning the international workshop on “Multi-Phase Flow: Simulation, Experiment and Application”, which was jointly hosted by ISR and ANSYS/CFX[®] and which continues the series of meetings on that topic in Rossendorf. I further mention the two Topical Days of the German Kerntechnische Gesellschaft held in Rossendorf on “State of the art in LWR fuel element development and design methods” and “Topical issues of German reactor safety research”. Meetings such as these underline the national and international scientific reputation of the Institute of Safety Research.

I would like to thank all staff members of the institute for their excellent work and for making the year 2006 another successful one for ISR.

F.-P. Weiß

F.-P. Weiß

Rossendorf, 7 April 2007

Fig. 1: Funding sources 2006

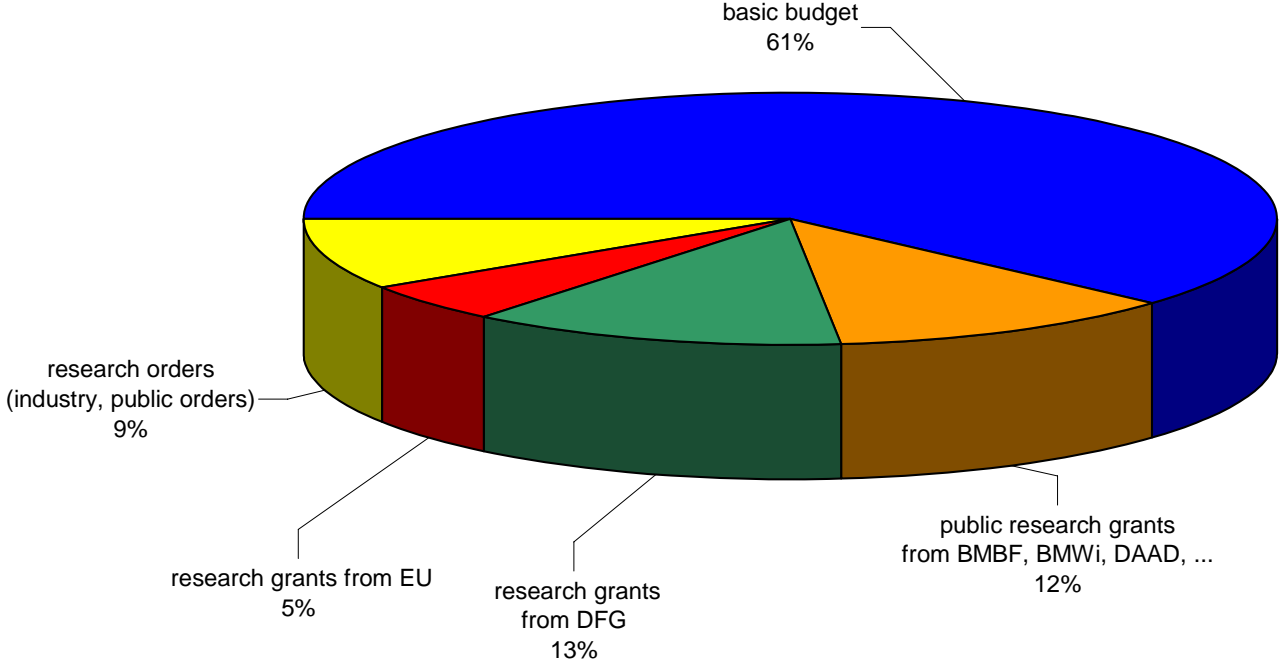
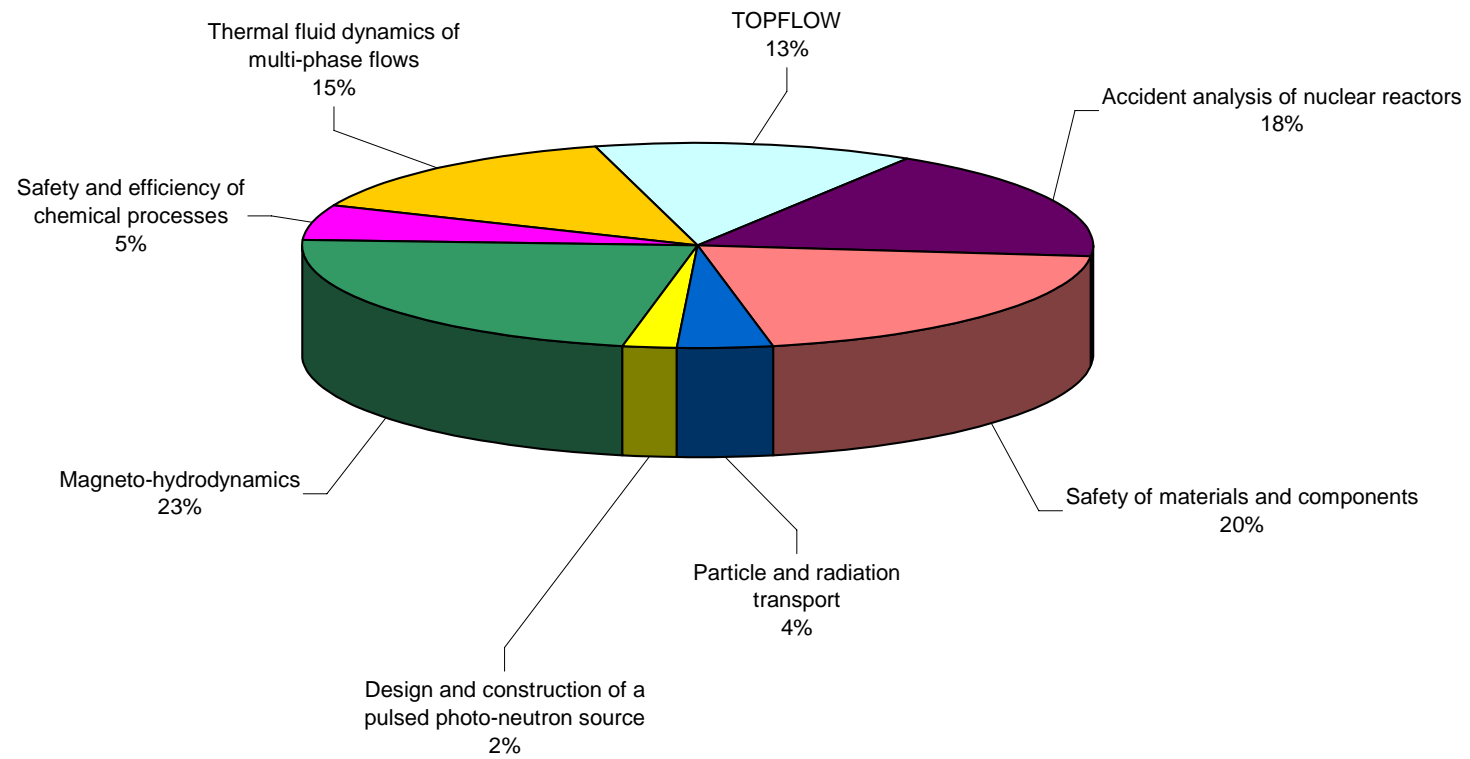


Fig. 2: Deployment of funding on the projects and user facilities 2006



Selected reports

DEVELOPMENT AND VERIFICATION OF A MULTIGROUP SP₃ METHOD FOR REACTOR CORE CALCULATIONS

Carsten Beckert and Ulrich Grundmann

1. Introduction

Considering the standard methods for calculations of light water reactor cores, assembly homogenized cross sections for two neutron energy groups are generated from multigroup transport calculations for the single assemblies. These so-called cell calculations are performed versus the exposure and for different state parameters as fuel temperature, moderator density, moderator temperature and boron concentration. Three-dimensional core calculations are based on the two group neutron diffusion equation and nodal methods with the libraries of group constants generated from the cell calculations. Improvements of these standard techniques are required because the reactors are loaded with UO₂ and MOX fuel assemblies, the unload burnup of the assemblies is increased, and new types of reactors are investigated. Therefore, the DYN3D core model [1] which is based on a standard method was extended to more neutron energy groups [2]. Moreover, a transport approximation based on the simplified P₃ (SP₃) method was implemented in the code. The SP₃ equations are solved by a nodal method which is shortly described in chapter 2. This method allows to calculate the assemblies in radial direction not only as whole but also by a number of nodes. Different approximations of the diffusion coefficient which occurs in the SP₃ method are discussed in chapter 3. The method was verified by comparisons with transport solutions for a steady state of the OECD/NEA and U.S. NRC PWR MOX/UO₂ Core Transient Benchmark. Pinwise calculations were performed with the new method and with the diffusion approximation. In chapter 4, the achieved accuracy is shown by comparisons with a reference solution of the transport code DeCART.

2. Nodal solution of the multigroup SP₃ equations

Brantley and Larsen [3] consider the P₃ group equations, eliminate the odd flux moments $\phi_{1,g}^i(\mathbf{r})$ and $\phi_{3,g}^i(\mathbf{r})$, and obtain the equations of the SP₃ approximation for $\Phi_{0,g}^i(\mathbf{r}) = \phi_{0,g}^i(\mathbf{r}) + 2\phi_{2,g}^i(\mathbf{r})$ and $\Phi_{2,g}^i(\mathbf{r}) = \phi_{2,g}^i(\mathbf{r})$ with the zeroth and second flux moment by variational analysis in three-dimensional geometry:

$$\begin{aligned} -D_{0,g}^i \Delta \Phi_{0,g}^i(\mathbf{r}) + \sigma_{r,0,g}^i \Phi_{0,g}^i(\mathbf{r}) - 2\sigma_{r,0,g}^i \Phi_{2,g}^i(\mathbf{r}) &= S_{0,g}^i(\mathbf{r}), \\ -D_{2,g}^i \Delta \Phi_{2,g}^i(\mathbf{r}) + \left[\sigma_{r,2,g}^i + \frac{4}{5} \sigma_{r,0,g}^i \right] \Phi_{2,g}^i(\mathbf{r}) - \frac{2}{5} \sigma_{r,0,g}^i \Phi_{0,g}^i(\mathbf{r}) &= -\frac{2}{5} S_{0,g}^i(\mathbf{r}), \end{aligned} \quad (1)$$

with

$$S_{0,g}^i(\mathbf{r}) = \sum_{\substack{g'=1, \\ g' \neq g}}^G \sigma_{0,gg'}^i \left[\Phi_{0,g'}^i(\mathbf{r}) - 2\Phi_{2,g'}^i(\mathbf{r}) \right] + \frac{1}{k_{eff}} \chi_g^i \sum_{g'=1}^G \nu \sigma_{fg'}^i \left[\Phi_{0,g'}^i(\mathbf{r}) - 2\Phi_{2,g'}^i(\mathbf{r}) \right] + Q_{0,g}^i(\mathbf{r}) \quad (2)$$

for each volume i of the system and for each energy group g , ($g = 1, \dots, G$). k_{eff} is the effective multiplication eigenvalue, χ_g^i the fission spectrum integrated over group g , $\nu \sigma_{fg'}^i$ the macroscopic production cross section of group g' and $Q_{0,g}^i$ an external source for group g . It is assumed in the SP₃ equations that the higher moments $\sigma_{n,gg'}$ of the macroscopic scattering cross sections from energy group g' to g can be neglected for different groups

$$\sigma_{n,gg'}^i = 0 \quad \text{for } g' \neq g, \quad n = 1, 2, 3, \quad (3)$$

Defining the group ‘‘removal’’ cross sections by

$$\sigma_{r,n,g}^i = \sigma_{t,g}^i - \sigma_{n,gg}^i \quad \text{for } n = 0, 1, 2, 3, \quad (4)$$

where $\sigma_{t,g}$ is the macroscopic total cross section of group g , the diffusion coefficients are given by

$$D_{0,g}^i = \frac{1}{3\sigma_{r,1,g}^i} \quad \text{and} \quad D_{2,g}^i = \frac{9}{35\sigma_{r,3,g}^i}. \quad (5)$$

In the volumes (nodes) i the group constants are assumed spatially constant. Transverse integrations are carried out to reduce the equation systems (1) to one-dimensional equations in axial direction z and two-dimensional equations in the x, y – plane.

Henceforth, the node and the group index are omitted in this chapter. Considering a node of the radial plane the moments Φ_0, Φ_2 of the group fluxes are described by a spatial expansion with polynomials $h_k(x, y)$ up to second order and exponential functions:

$$\Phi_n(x, y) = \sum_{k=0}^4 c_{n,k} h_k(x, y) + \sum_{j=1}^2 \varepsilon_n^j \left(d_1^j e^{B_j x} + d_2^j e^{B_j y} + d_3^j e^{-B_j x} + d_4^j e^{-B_j y} \right) \quad n = 0, 2. \quad (6)$$

The exponential functions are the solutions of the homogeneous equation system. A quadratic equation system is obtained for the B_j^2 which results in two positive roots B_1^2, B_2^2 . With $\varepsilon_0^{1,2} = 1$, the other components of the eigenvector $\varepsilon_2^{1,2}$ are given by

$$\varepsilon_2^{1,2} = \frac{\sigma_{r,0} - D_0 B_{1,2}^2}{2\sigma_{r,0}} \quad (7)$$

The one-dimensional equation system of the axial direction z is treated in a similar way. The fission and scattering sources and the leakage terms are approximated by the polynomials only.

An inner and outer iteration scheme is applied to solve the equation system for all nodes of the core. In the inner iteration process, it is assumed that the polynomial coefficients of the leakage, the fission and scattering sources are given from the last outer iteration. Based on these coefficients the polynomial coefficients of the flux expansions are determined from the reduced equation systems. Using these coefficients the outgoing partial currents are calculated for each node from the given incoming currents. The incoming currents are determined from the outgoing currents of the neighboring nodes using the interface conditions between the nodes or the conditions at the core boundary. After few (3 - 5) inner iterations the polynomial coefficients of the source terms are updated from the flux expansions by weighting with the polynomials. The new coefficients of the source and leakage terms are used for the next outer iteration step. A Chebychev extrapolation scheme is applied to accelerate the outer iteration.

3. Application of the transport cross section in the SP₃ equations

In contrast to equation (3), the first order anisotropic group to group scattering will now be considered by using the so-called transport cross section, which is commonly used when the diffusion approximation is applied instead of the P₁ equations. Bell and Glasstone [4] consider the two P₁ equations for continuous energy and one-dimensional geometry. They ask, how to choose the diffusion coefficient $D(x, E)$ in order to describe the P₁ equations adequately with the diffusion equation. They use the approximation

$$\int \sigma_1(x, E' \rightarrow E) \Phi_1(x, E') dE' \approx \int \sigma_1(x, E \rightarrow E') \Phi_1(x, E) dE', \quad (8)$$

where $\sigma_1(x, E \rightarrow E')$ is the first moment of the macroscopic cross section for neutrons scattering from energy E to energy E' and $\Phi_1(x, E)$ the first flux moment at energy E . This approximation is based on the argument that in the slowing down region the contribution of the left hand side comes from energies $E' > E$. If there is no absorption, it is nearly the same as the slowing down from energy E to lower energies. The right hand side can be described as

$$\int \sigma_1(x, E \rightarrow E') \Phi_1(x, E) dE' = \sigma_0(x, E) \bar{\mu}(x, E) \Phi_1(x, E), \quad (9)$$

where $\sigma_0(x, E)$ is the macroscopic scattering cross section and $\bar{\mu}(x, E)$ the average scattering angle. With the transport cross section defined by

$$\sigma_{tr}(x, E) \equiv \sigma_t(x, E) - \int \sigma_1(x, E \rightarrow E') dE' = \sigma_t(x, E) - \bar{\mu}(x, E) \sigma_0(x, E), \quad (10)$$

the diffusion coefficient

$$D(x, E) = \frac{1}{3\sigma_{tr}(x, E)} \quad (11)$$

is obtained. So the diffusion theory represents a form of the P_1 approximation in which the contribution of the anisotropic scattering to the energy transfer has been approximated by equation (8). For situations involving large energy transfer and anisotropic scattering the approximation leading to diffusion theory would not be expected to be satisfactory. Stamm'ler and Abbate [5] state that equation (8) is a good approximation, if there is weak absorption.

Considering again the multigroup equation system (1) with spatially constant cross sections in the nodes i it follows from approximation (8) for the first order group cross sections and flux moments

$$\sum_{g'=1}^G \sigma_{1,gg'}^i \Phi_{1,g'}^i(\mathbf{r}) \approx \sum_{g'=1}^G \sigma_{1,g'g}^i \Phi_{1,g}^i(\mathbf{r}). \quad (12)$$

The corresponding transport cross section for node i and group g is given by

$$\sigma_{tr,g}^i = \sigma_{t,g}^i - \sum_{g'=1}^G \sigma_{1,g'g}^i. \quad (13)$$

Using approximation (12) and the transport cross section from (13) the diffusion coefficient

$$\tilde{D}_{0,g}^i = \frac{1}{3\sigma_{tr,g}^i} \quad (14)$$

occurs in the SP_3 equations (1) instead of $D_{0,g}^i$ from the first equation of (5). The effect of the different approximations $D_{0,g}^i$ and $\tilde{D}_{0,g}^i$ of the diffusion coefficient in the SP_3 equations on the results is investigated in the next chapter.

4. Numerical results and comparisons

The SP_3 method was tested by calculations of the steady state of the OECD/NEA and U.S. NRC PWR MOX/UO₂ Core Transient Benchmark [6]. The core has uniform fuel composition in axial direction and a 45 degree reflectional (90 degree rotational) symmetry (see Fig. 1). The core height corresponds to the active fuel length of 367.76 cm. The burnup is constant in axial direction. The core of the benchmark consists of 30 % MOX fuel with average 4.0 and 4.3 % Pu-fissile. The UO₂ assemblies have enrichments of 4.2 and 4.5 %. The core is surrounded by assemblies which consist of the baffle layer and the water reflector. The different colors refer to fresh, once and twice burnt fuel. Fig. 2 shows the configurations

	1	2	3	4	5	6	7	8
A	U 4.2% (CR-D) 35.0	U 4.2%	U 4.2% (CR-A) 22.5	U 4.5%	U 4.5% (CR-SD) 37.5	M 4.3% 17.5	U 4.5% (CR-C) 0.15	U 4.2%
B	U 4.2%	U 4.2%	U 4.5%	M 4.0%	U 4.2%	U 4.2% (CR-SB) 32.5	M 4.0%	U 4.5%
C	U 4.2% (CR-A) 22.5	U 4.5%	U 4.2% (CR-C) 22.5	U 4.2%	U 4.2%	M 4.3%	U 4.5% (CR-B) 0.15	M 4.3%
D	U 4.5%	M 4.0%	U 4.2%	M 4.0%	U 4.2%	U 4.5% (CR-SC) 20.0	M 4.3%	U 4.5%
E	U 4.5% (CR-SD) 37.5	U 4.2%	U 4.2%	U 4.2%	U 4.2% (CR-D) 37.5	U 4.5%	U 4.2% (CR-SA) 17.5	
F	M 4.3%	U 4.2% (CR-SB) 32.5	M 4.3%	U 4.5% (CR-SC) 20.0	U 4.5%	M 4.3%	U 4.5%	32.5
G	U 4.5% (CR-C) 0.15	M 4.0%	U 4.5% (CR-B) 0.15	M 4.3%	U 4.2% (CR-SA) 17.5	U 4.5%	Assembly Type CR Position Burnup [GWd/t]	
H	U 4.2%	U 4.5%	M 4.3%	U 4.5%				
	32.5	17.5	35.0	20.0				

Fig. 1: Core configuration of the PWR MOX/ UO_2 benchmark.

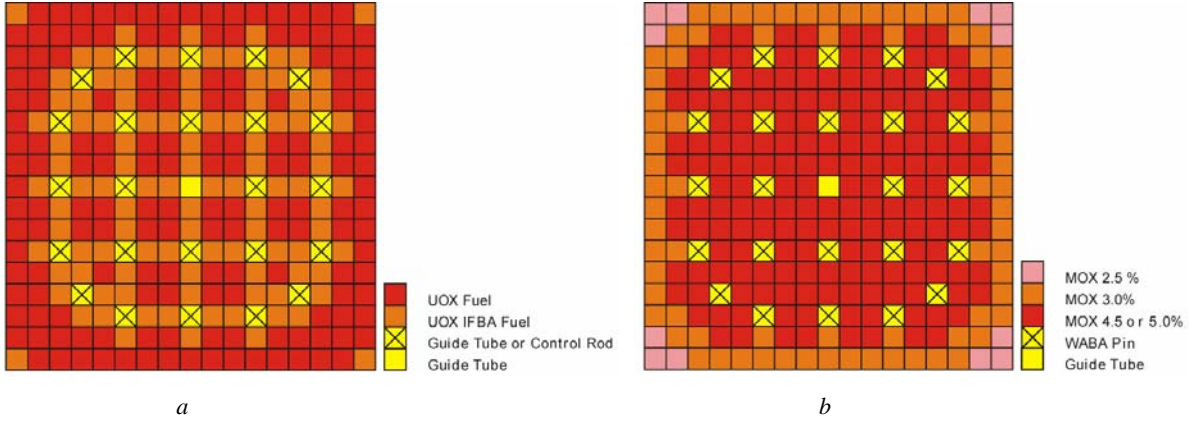


Fig. 2: Structure of the UO_2 assembly (a) and the MOX assembly (b).

the P_1 scattering moments were used from the code RESMOD, because there are no P_1 data for Iron within HELIOS 1.8 [8].

A solution generated with the code DeCART [9] is used as reference. The method of characteristics is applied for the solution of the neutron transport equation in DeCART. The heterogeneous structure of the pin cells was modeled. A 47 group library based on HELIOS version 1.8 with transport corrected P_0 scattering and subgroup methods for the resonance region was used.

Three different DYN3D calculations were carried out with 1 node per pin. Firstly, a diffusion calculation DYN3D-DIFF was performed with the diffusion coefficient defined by (14). The SP_3 calculation DYN3D- SP_3 -REM with the approximation (4) for the removal cross sections shows an accuracy which is not sufficient. The DYN3D- SP_3 -TR calculation is performed with the SP_3 method and the diffusion coefficient of approximation (14). The eigenvalues k_{eff} are compared with the DeCART result in Table 1. The DYN3D-DIFF and the DYN3D- SP_3 -TR results show a good agreement in the order of 60 pcm compared to the deviation of DYN3D- SP_3 -REM result of 344 pcm. The maximum deviations of the DYN3D- SP_3 -REM assembly powers are about 10 % compared to the DeCART solution (Fig. 3). The SP_3 calcu-

of the UO_2 and the MOX assemblies. The considered state is a hot zero power (HZP) state with all control rods out of core. Reflective boundary conditions in the axial direction are considered. Due to these assumptions, the problem is two-dimensional. A 16-group cross section library with pinwise homogenized cross sections generated by the Gesellschaft fuer Anlagen- und Reaktorsicherheit (GRS) mbH with the cell code HELIOS 1.8 [7] for calculations with DORT [8] is used for pinwise calculations with DYN3D using SP_3 and diffusion methods. HELIOS 1.8 yields only P_N data up to the first order. Therefore, it is assumed $\sigma_{n,gg}^i = 0$ for $n = 2, 3$. The transport cross sections (13) and the P_1 scattering moments are available in the library. For the baffle

Table 1: Eigenvalues k_{eff} and the RMS of the relative deviations (in %) of the assembly powers compared to the DeCART results.

Code	k_{eff}	RMS ass. powers
DeCART (Ref.)	1.05852	-
DYN3D-DIFF	1.05910	2.00
DYN3D-SP3-REM	1.06216	5.72
DYN3D-SP3-TR	1.05916	0.87

lation DYN3D-SP3-TR shows a maximum deviation of assembly powers lower than 2 %, which is more accurate than the DYN3D-DIFF results with a maximum deviation of about 4 %. The RMS values of the comparisons of the assembly powers can be seen in Table 1. The results of DYN3D-SP3-TR with the RMS value of 0.87 % are much better than the DYN3D-SP3-REM results and better than the diffusion calculation. The application of the removal cross sections (4) with the approximations (3) in the SP₃ equations gives smaller values of the diffusion coefficients $D_{0,g}^i$ of

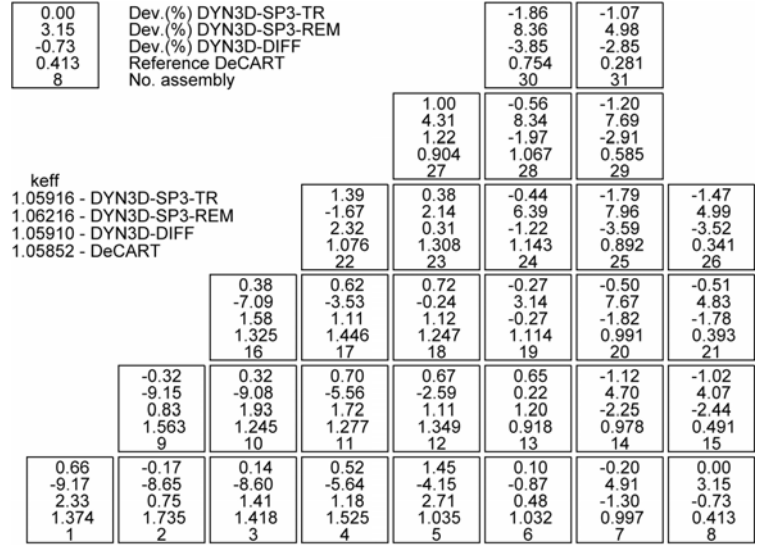


Fig. 3: Comparisons of the assembly powers of the three DYN3D calculations with the DeCART reference solution.

equation (5) than the diffusion theory. Therefore less neutrons stream out of the core boundary, the distribution of the assembly powers is too flat, and the eigenvalue is too large. The SP₃ theory with the usual diffusion coefficients $\tilde{D}_{0,g}^i$ from equation (14) instead of the coefficients $D_{0,g}^i$ provides a good agreement with the reference solution of DeCART and shows also an improvement compared to the diffusion calculation.

The pin powers of the DeCART solution are available for the diagonal row (assemblies 1, 9, 16, 22, 27, and 30 of Fig. 3). Table 2 shows the maximum and the averaged (RMS) relative

Table 2: Maximum and RMS of the relative deviations (in %) of the normalized pin powers compared to the DeCART results for the assemblies in the diagonal row.

Ass.	DYN3D- SP3-TR		DYN3D- SP3-REM		DYN3D-DIFF	
	Max.	RMS	Max.	RMS	Max.	RMS
1	-2.18	1.58	-2.94	1.67	-2.55	1.60
9	-1.12	0.66	-1.91	0.84	-1.00	0.64
16	-1.69	0.96	-4.19	1.84	-1.53	0.93
22	-0.76	0.33	3.17	1.26	1.02	0.43
27	-2.79	1.71	-4.83	2.35	-4.28	1.79
30	-1.30	0.58	-4.94	1.13	2.36	0.80

deviations between the three DYN3D and the DeCART results of the assembly-normalized pin powers. For the DYN3D-SP3-TR results the maximum deviation of 2.79 % is given in the UO₂-assembly no. 27. The results DYN3D-SP3-REM and DYN3D-DIFF show slightly higher deviations of the normalized pin powers. Concerning the whole core normalized pin powers the deviations of the assembly powers have to be considered too. Altogether the DYN3D-SP3-TR results show the lowest deviations compared to the DeCART solution. The accuracy is in the order of the DORT solution with homogenized pin cells [8].

5. Conclusion and outlook

A nodal method for solving the multigroup SP₃ equations was presented and implemented in the DYN3D code. The results of pinwise calculations for the steady state of the OECD/NEA and U.S. NRC PWR MOX/UO₂ Core Transient Benchmark were compared with results of the transport code DeCART. Using the approximation of the transport cross section of the diffusion theory in the SP₃ method, the deviations of the DYN3D results compared to DeCART are in the order of the differences between other transport solutions. The SP₃ method shows also an obvious improvement compared to the diffusion solution. It is encouraging to develop the method for standard application in core calculations including the simulation of transients. Further verifications are necessary, especially for cores with MOX loadings.

References

- [1] U. Grundmann, U. Rohde, S. Mittag, S. Kliem (2005), DYN3D version 3.2 - code for calculation of transients in light water reactors (LWR) with hexagonal or quadratic fuel elements - description of models and methods -, Rossendorf, Report FZR-434.
- [2] U. Grundmann (2006), Calculations of a steady state of the OECD/NRC PWR MOX/UO₂ transient benchmark with DYN3D, Annual Meeting on Nuclear Technology, Aachen.
- [3] P.S. Brantley, E. W. Larsen (2000), The Simplified P₃ Approximation, Nucl. Sci. Eng. 134, 1-21.
- [4] G. I. Bell, S. Glasstone, (1970), Nuclear Reactor Theory, Van Nostrand Reinhold Company, New York.
- [5] R. J. J. Stamm'ler, M. J. Abbate (1983), Methods of Steady-State Reactor Physics in Nuclear Design, Academic Press Inc., London.
- [6] T. Kozłowski, T.J. Downar (2003), OECD/NEA and U.S. NRC PWR MOX/UO₂ Core Transient Benchmark, NEA/NSC/DOC(2003) 20, Working Party of the Physics of Plutonium Fuels and Innovative Fuel Cycles, OECD/NEA Nuclear Science Committee.
- [7] Studsvik® Scandpower (2003), HELIOS Methods, Version 1.8, Studsvik Scandpower.
- [8] A. Seubert, S. Langenbuch, W. Zwermann (2006), Solution of the Stationary State of the PWR MOX/UO₂ Core Transient Benchmark, Proc. of PHYSOR-2006, ANS Topical Meeting on Reactor Physics, Vancouver, BC, Canada.
- [9] H. G. Joo, J. Y. Cho, Y. Kim (2002), Dynamic Implementation of the Equivalence Theory in the Heterogeneous Whole Core Transport Calculation, Proceedings of PHYSOR 2002, Seoul, Korea.

Acknowledgement

This work is funded by the German Federal Ministry of Economics and Technology. The authors thank A. Seubert of the Gesellschaft fuer Anlagen- und Reaktorsicherheit (GRS) mbH for providing the library of group constants.

BORON DILUTION ANALYSES AT REACTOR SHUTDOWN CONDITIONS USING THE COUPLED CODE DYN3D/ATHLET

Sören Kliem and Ulrich Rohde

1. Introduction

Slugs of under-borated, or even boron-free, coolant can be formed in the primary circuit during different accident scenarios, e. g. due to a malfunction of the chemical and volume control system, or due to an SBLOCA with partial failure of the safety injection system. An unintentional, or even unavoidable, decrease of boron concentration in the reactor core leads to a reactivity increase and may result in a power excursion, a so-called boron dilution transient. Whether re-criticality of the scrammed reactor occurs, and how high the power peak is, depends among other factors, in a sensitive manner, on the mixing of the too weakly borated water with the ambient coolant in the downcomer and the lower plenum on its way to the core.

For an adequate simulation of such boron dilution transients, 3D neutron kinetic core models coupled with advanced thermal hydraulic system codes are necessary. Such analyses also require the simulation of the above mentioned coolant mixing processes inside the reactor pressure vessel (RPV).

For providing the time dependent boron concentration distribution at the core inlet, a fast running model for the coolant mixing has been developed and successfully validated for German KONVOI-type reactors [1]. This model (SAPR (Semi-Analytical Perturbation Reconstruction)) is based on the linear superposition of precalculated transfer functions. The obtained transfer functions are valid for a given hydraulic process. The SAPR-model was implemented into the 3D neutron kinetic core model DYN3D and the coupled DYN3D/ATHLET code system.

In the past, the SAPR-model in combination with the code DYN3D and the coupled code complex DYN3D/ATHLET was applied to the analysis of boron dilution transients after the start-up of the first main coolant pump [2, 3]. In the frame of the current work, the SAPR-model has been extended to transients with natural circulation conditions. Information on the validation of the new functions can be found in [4].

In the following, the application of the code system DYN3D/ATHLET to a hypothetical boron dilution event during the operation of the residual heat removal system (RHRS) after the completion of the core reloading and the closure of the vessel head is described.

2. Boundary conditions and scenario

As the initial condition of the scenario, it is assumed that the reactor is completely filled with coolant with a boron concentration of 2200 ppm after the reloading. The decay heat is removed by the RHRS. This system is operated at a level of 10 % of the nominal flow rate of one loop at atmospheric pressure with a water temperature of 25 °C.

For the analysis presented here, it is postulated that the piping of the RHRS is partially filled with a certain amount of deborated water. This deborated water is injected into the RPV during start-up of the RHRS. The deborated water enters the RPV, mixes with the highly

borated water on the way to the reactor core and finally leads to an inhomogeneous decrease of the boron concentration in the reactor core. Depending on the injected volume of deborated water and the degree of mixing, the perturbation can cause a re-criticality of the shut-down reactor.

This special scenario can be investigated in the following four step parameter study:

1. Calculation of the transient boron concentration at the inlet into each fuel assembly for different initial slug volumes (step width: 2 m^3). This step is performed using the stand-alone SAPR-model.
2. Extraction of the core inlet boron concentration distribution at the moment of its minimum.
3. Stationary core calculations using DYN3D and the extracted core inlet boron concentration distribution.
4. Transient calculations using the coupled code DYN3D/ATHLET for the slug volumes, for which super-criticality was predicted in the stationary calculations.

For the calculations, a generic PWR reactor core was presumed at the beginning of an equilibrium cycle with fully inserted control rods [2]. The corresponding few group cross section data were created using the code HELIOS [5].

3. Stationary core calculations

Fig. 1 shows the core inlet boron distribution at the moment of the minimum for each considered slug volume. These distributions serve as the basis for the stationary calculations.

Fig. 2 shows the static core reactivity in dependence on the initial slug volume. For each slug volume, two calculations were performed, one using the minimum boron concentration uniformly distributed over the whole core (“Uniform distribution”) and the second using the calculated core inlet distribution (Fig. 1) but extended over the entire core height (“2D-Distribution”). The use of the minimum value over the whole core obviously leads to higher reactivity values; re-criticality would be reached already for a slug volume between 2 and 4 m^3 while for the second case the calculated critical slug volume is near to 8 m^3 . The assumption of “uniform distribution” is highly conservative. The assumption of “2D distribution” is conservative too, if the slug is smaller than the water volume in the core, so that the core can never be filled completely by the slug.

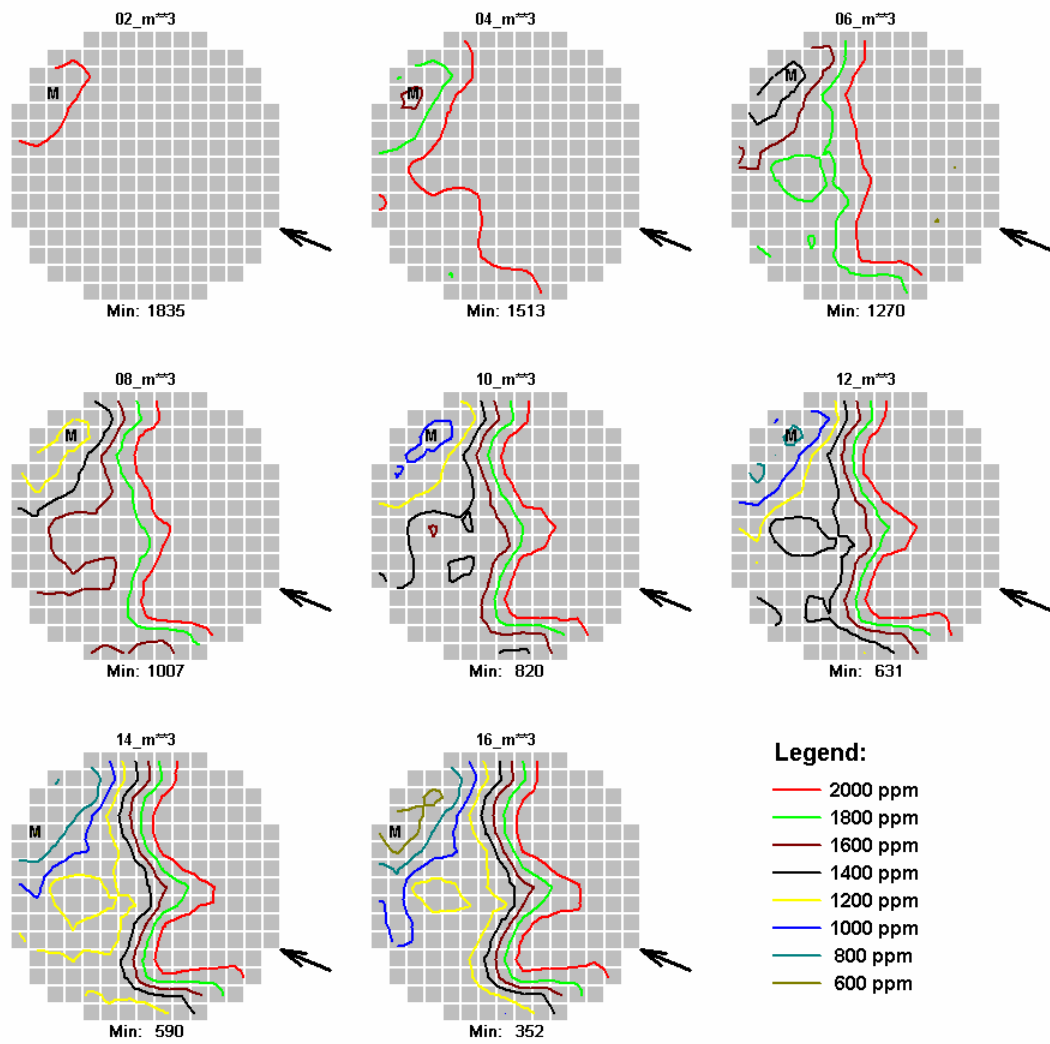


Fig. 1: 2D Boron concentration distribution in the reactor core inlet plane in dependence on the slug volume

“M” in the core inlet plane: fuel element position with the minimum boron concentration; Minimum in ppm; Arrow: position of the loop with the slug

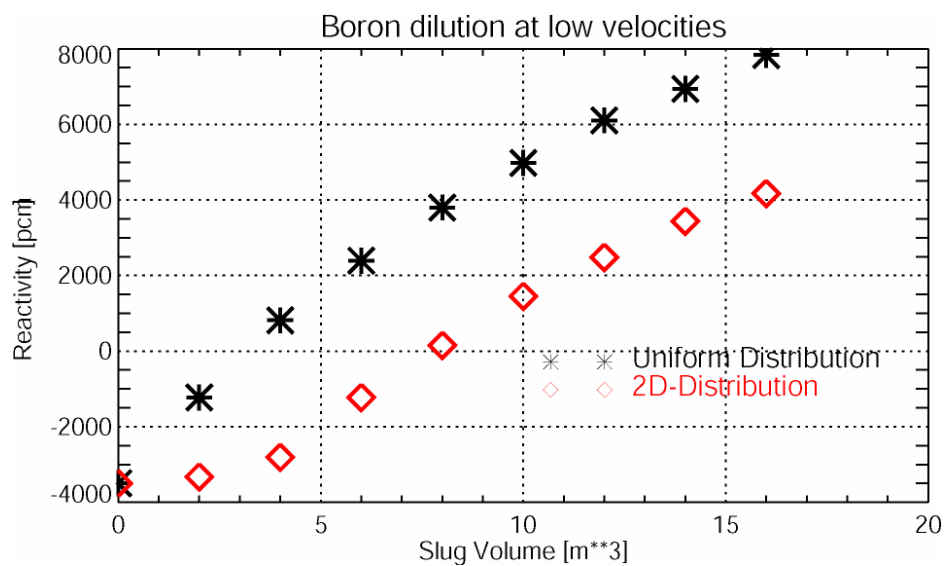


Fig. 2: Dependence of the static core reactivity on the initial slug volume

4. Transient core calculations

For the transient calculations, a DYN3D/ATHLET-model consisting of the lower plenum, reactor core and upper plenum was created. The reactor core consists of parallel channels without cross connections. The time dependent boron concentration calculated under step 1 serves as inlet boundary conditions for the transient calculations. The thermal hydraulic part of the reactor core was modeled in two options: In order to reduce the computation time, the first option consists of 41 superchannels, each of them containing about five neighboring coolant channels. In the second option each of the 193 fuel elements of the reactor was modeled as a single channel. The modeling of the neutron kinetic part is identical between both options (1:1), as the influence of this variation on the total computation time is negligible.

The first transient calculation was performed for the slug volume of 8 m^3 using the model with the reduced number of coolant channels.

The average boron concentration in the reactor core reaches a minimum value of about 1750 ppm 70 s after the injection of the deborated water into the cold leg (Fig. 3).

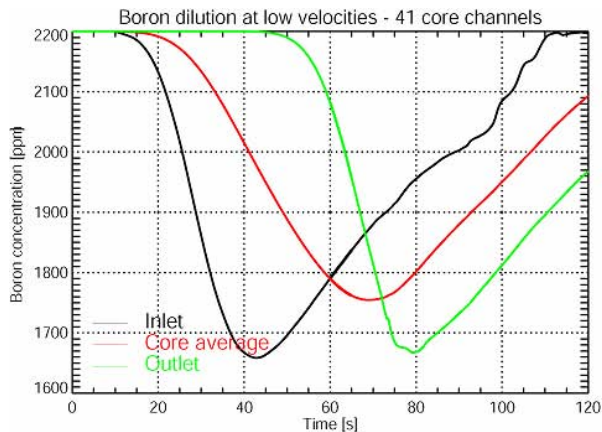


Fig. 3: Boron concentration in the reactor core

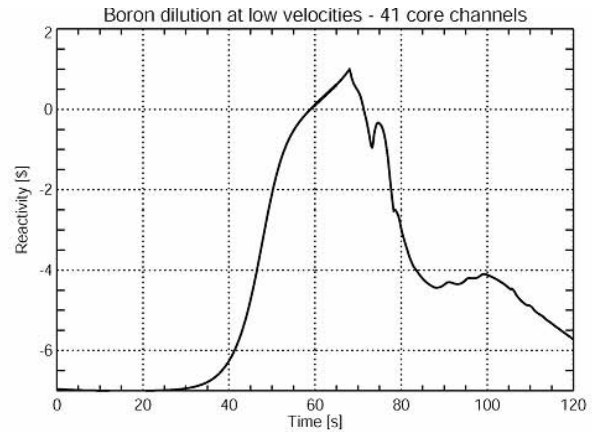


Fig. 4: Time history of the reactivity

The decreasing boron concentration leads to a positive reactivity insertion. At $t = 60 \text{ s}$, the scram reactivity is compensated and re-criticality is reached (Fig. 4). Due to the further decrease of the boron concentration the reactor becomes super-critical with a power peak of 935 MW and a maximum fuel center line temperature of $302 \text{ }^\circ\text{C}$. With the increasing boron concentration after the minimum the reactor returns to the sub-critical state.

Table 1: Key parameters of the transient calculations

N°	Channels modelled	Volume [m^3]	$C_{b_{\min}}$ [ppm] ^a	P_{\max} [MW] ^b	$T_{\text{Fuel}_{\max}}$ [$^\circ\text{C}$]	$T_{\text{Cladding}_{\max}}$ [$^\circ\text{C}$]
1	41	8	1021	935	302	151
2	41	10	846	686	298	168
3	41	12	654	2736	365	168
4	41	15	436	3414	379	174
5	193	15	382	2143 ^c /4563	436	177

^a overall minimum reached in the calculation

^b maximum calculated core power

^c maximum value during the first power peak

Further calculations were performed for slug volumes of 10, 12 and the maximum value of 15 m^3 . With the increasing slug volume the re-criticality is reached earlier and the time span of super-criticality increases. The maximum values of the reached core power and the fuel temperature are increasing with growing slug volume. Table 1 gives an overview about key parameters of the calculations. The power increase in all calculations is accompanied by significant coolant boiling in single channels. It should be pointed out, that the thermal hydraulics simulations at low pressure are quite challenging because of the high density difference between water and steam and therefore, high sensitivity of void fraction to coolant enthalpy.

For the maximum slug volume of 15 m^3 a calculation with the detailed modeling of the reactor core was performed. The results are compared with the calculation using 41 channels.

Due to the non-averaging of the boron concentrations curves over some channels, the concentration distribution is got with finer resolution in the core. The absolute local minimum of the concentration becomes lower, the reactivity insertion is faster and the re-criticality is reached earlier in the calculation with 193 channels (Fig. 5). The power increase is stopped in this calculation at the lower level of 2143 MW versus 3414 MW in the reference calculation with 41 channels. This has two reasons: Firstly, the positive reactivity insertion at that earlier time is lower and secondly, the feedback is more effective in the calculation with detailed resolution, because the thermal hydraulic parameters are not averaged over some channels.

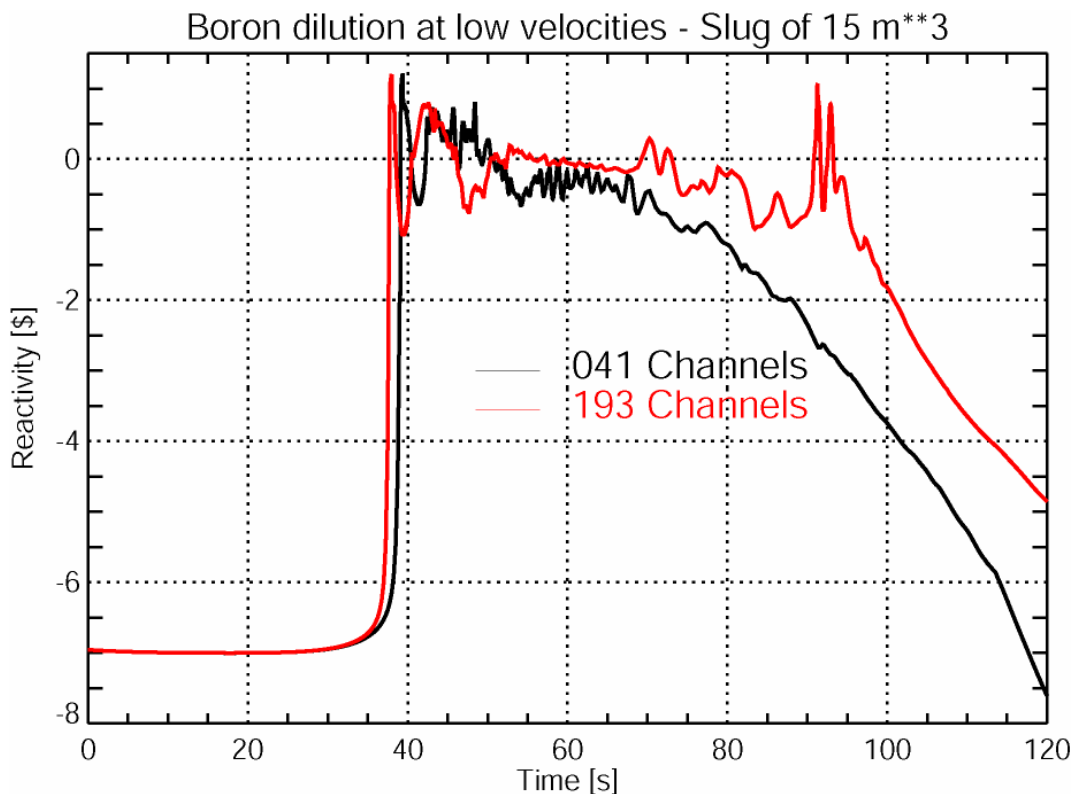


Fig. 5: Time history of the reactivity (variation of the channel number)

At $t = 92 \text{ s}$, the detailed calculation provides another prompt super-critical state with the power increasing again, which is fully missing in the calculation with 41 channels. The maximum power of 4563 MW reached at this time is higher than during the first power peak. This effect is also connected with the different resolution in the modeling: The total energy, produced in the detailed calculation until this power peak occurs at 92 s, was smaller. This

lower energy production resulted in a smaller decrease of the coolant density. The corresponding reactivity effect is also smaller; i.e. the sub-criticality during this phase is not as deep as in the calculation using 41 coolant channels. When the vapor produced during the first phase of the transient is transported into the upper plenum, the reactivity increase connected with this effect starts from a higher level and reaches again positive values.

5. Conclusions

A parameter study of a hypothetical boron dilution event during the work of the RHRS was performed. Based on a validated coolant mixing model for the lower plenum of the RPV, realistic boron concentration distributions at the inlet into each fuel assembly were obtained and used for a number of stationary and transient core calculations. For the generic core loading pattern used in the calculations, re-criticality is reached in the stationary calculations with realistic core inlet boron distribution for slug volumes of about 8 m³. Transient core calculations from 8 to the maximum initial slug volume of 15 m³ showed, that the maximum calculated fuel and cladding temperatures are below critical values. Although, local coolant boiling occurs in all calculations over several tenths of seconds, the integrity of the fuel is always ensured.

References

- [1] S. Kliem, H.-M. Prasser (2001), A semi-analytical model for the description of coolant mixing inside the KONVOI reactor pressure vessel during pump start-up, in: Proceedings of the Annual Meeting on Nuclear Technology '01 (pp. 107-112), INFORUM GmbH, Bonn
- [2] S. Kliem, U. Rohde, F.-P. Weiss (2004), Core response of a PWR to a slug of under-borated water, Nucl. Eng. Design, 230, 121
- [3] S. Kliem, U. Grundmann, U. Rohde (2005), Methodenentwicklung zur Analyse von Störfallszenarien mit Frischdampfleck und Borverdünnung mit Hilfe des Codesystems ATHLET-DYN3D - Abschlussbericht Teil 2, Rossendorf, Report FZR-438, ISSN 1437-322X
- [4] S. Kliem (2005), Realistische Simulation von Reaktivitätsstörfällen mit gekoppelten neutronenkinetisch-thermohydraulischen Systemcodes, Rossendorf, Zwischenbericht zum VGB-Projekt: SA“AT“ 51/04
- [5] S. Mittag, U. Grundmann, R. Koch, J. Semmrich (2002), Creation and use of 2-group diffusion parameters libraries for the calculation of a KWU-KONVOI reactor by means of the reactor dynamics code DYN3D, Rossendorf, Report FZR-346, ISSN 1437-322X

Acknowledgements

This work was funded by the Nuclear Special Committee “Plant engineering” of VGB PowerTech.

A PHOTO-NEUTRON SOURCE FOR TIME-OF-FLIGHT MEASUREMENTS AT THE RADIATION SOURCE ELBE

Eberhard Altstadt, Carsten Beckert, Hartwig Freiesleben¹, Vladimir Galindo, Eckart Grosse², Arnd R. Junghans², Joakim Klug², Bärbel Naumann¹, Steffen Schneider, Rainer Schlenk, Andreas Wagner² and Frank-Peter Weiss

1. Introduction

The radiation source ELBE (Electron Linear accelerator with high Brilliance and low Emit-tance) at Forschungszentrum Dresden-Rossendorf produces an electron beam that allows to generate sub-ns neutron pulses by stopping the electrons in a heavy radiator and producing neutrons by bremsstrahlung photons through (γ,n) -reactions. In order to enable measurements of energy resolved neutron cross sections like (n,γ) , $(n,n'\gamma)$, (n,p) , (n,α) , and (n,f) at a time-of-flight arrangement with a short flight path of only a few meters it is necessary to keep the volume of the radiator for neutron production as small as possible to avoid multiple scattering of the emerging neutrons, which would broaden the neutron pulses. The power deposition of the electron beam in the small radiator volume of 1 cm^3 reaches up to 25 kW. This is such a high power density that any solid high Z number material would melt. Therefore, the neutron radiator consists of liquid lead circulated by an electromagnetic pump. From the thermal and mechanical point of view, molybdenum turned out to be the most suited target wall material in the region where the electrons impinge on the radiator.

The measurement of neutron induced reaction cross sections for fusion and fission reactors, and for accelerator driven systems aiming at the transmutation of nuclear waste is the main task to be pursued at the photo-neutron source. The transmutation of long-lived radioactive nuclides is currently discussed [1] to reduce the necessary safe isolation time of radioactive waste in geological disposals and is among others subject of the Integrated EU-project EU-ROTRANS [2]. A topical overview on the state of the art in nuclear cross sections and on the relevant deficits is given in [3]. Requests are also made for neutron cross sections which are placed in the relevant energy range at ELBE between 50 keV and 10 MeV. Furthermore, experiments can be performed at ELBE which address problems of nuclear astrophysics.

A sketch of the whole time-of-flight facility (ELBE n-TOF) is shown in Fig. 1. After passing through two thin (200 μm) beryllium windows, the electron beam of ELBE is directed onto the

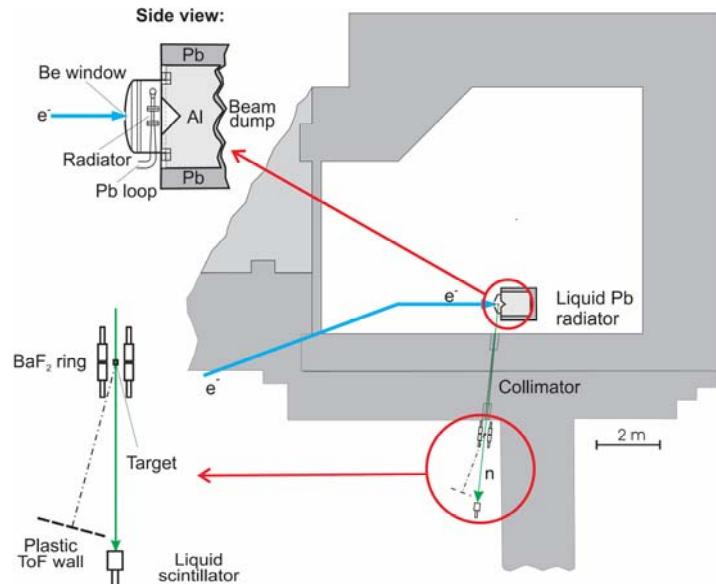


Fig. 1: Floor plan of the n-ToF set-up in the neutron cave. Inserts show a side view of the liquid lead neutron radiator and the detector arrangement in the measuring hall

¹ Technische Universität Dresden, Institute for Nuclear and Particle Physics

² Forschungszentrum Dresden-Rossendorf, Institute of Radiation Physics

neutron radiator inside a vacuum chamber where bremsstrahlung photons are produced, generating photo-neutrons by (γ, n) -reactions. In this way, the electron pulse structure is transformed into a similar pulse structure of the neutrons needed for time-of-flight experiments. The neutrons, which are emitted at an angle of about 90° , are decoupled to the measuring position through a collimator in the shielding concrete wall of 2.4 m thickness. A flight path of about 3.9 m is sufficient to separate the neutron pulses from the bremsstrahlung flashes and secondary electrons. A beam dump is located in the primary beam direction behind the neutron radiator and forms part of the vacuum housing. Particle transport calculations predict a neutron source strength in the range of $7.9 \cdot 10^{12}$ n/s to $2.7 \cdot 10^{13}$ n/s for electron energies between $E_e = 20$ and 40 MeV. At the measuring place 3.9 m away from the radiator, an average neutron flux of about $1.5 \cdot 10^7$ n/(cm² s) will be obtained. The short beam pulses allow for a neutron energy resolution of better than 1 % for neutron energies between $E_n = 50$ keV and 5 MeV. The usable energies range up to about 10 MeV.

2. Beam parameters of the radiation source ELBE

The ELBE radiation source is centered around a superconducting electron LINAC which produces quasi-continuous electron beams, whose energy can be varied up to $E_e = 40$ MeV. Beam intensities of up to $I_e = 1$ mA can be delivered with a wide variability in the electron pulse structure. The maximum frequency is $f_e = 260$ MHz. This frequency can be lowered by factors of 2^n . The pulse length is less than 10 ps. Picosecond electron pulses will also be used to generate sub-ns neutron pulses. The small emittance of the electron beam at the radiator ($\epsilon_{RMS} \approx 10\pi$ mm·mrad) permits the irradiation of very small radiator volumes. A new superconducting radio frequency photo electron injector (SRF gun) is being developed, allowing for an unreduced beam current of $I_e = 1$ mA at a repetition rate of $f_e = 0.5$ MHz [4]. With this new photo gun, the measurable neutron energy ranges from $E_n = 50$ keV to 10 MeV.

As can be seen in Table 1, the ELBE n-TOF set-up has a very competitive luminosity in the accessible energy range compared with all existing high-resolution neutron beams. The proton-accelerator based sources at Los Alamos and the planned Oak Ridge Neutron Spallation Source lose a significant part of their intensity advantage over ELBE when they increase their flight path in order to reach an energy resolution better than 1 %, as expected for ELBE.

Table 1: Parameters of operational and planned neutron time-of-flight facilities

Facility	CERN n_TOF		LANL NSC	ORNL SNS	FZK VdG	ORNL ORELA	IRMM GELINA	ELBE	ELBE with SRF
Pulse charge [nC]	$\approx 10^3$		$4 \cdot 10^3$	$3 \cdot 10^4$	0.01	≈ 100	≈ 100	0.08	2
Power [kW]	10		60	1000	0.4	8	7	5	40
Pulse rate [s ⁻¹]	0.4		20	60	$2.5 \cdot 10^5$	500	800	$1.6 \cdot 10^6$	$5 \cdot 10^5$
Flight path [m]	183	≈ 20 in Phase-2	60	84	0.8	40	20	3.9	3.9
n pulse length [ns]	> 7		125	100-700	≈ 1	> 4	> 1	< 0.4	< 0.4
E_{min} [eV]	0.1		1	0.1	10^3	10	10	$2 \cdot 10^5$	$5 \cdot 10^4$
E_{max} [eV]	$3 \cdot 10^8$		$\approx 10^8$	$\approx 10^8$	$2 \cdot 10^5$	$5 \cdot 10^6$	$4 \cdot 10^6$	10^7	10^7
Resol. at 1 MeV [%]	0.5	5 in Phase-2	≈ 10	> 10	≈ 10	< 1	< 2	≈ 1	≈ 1
n flux density [s ⁻¹ cm ⁻² E-decade ⁻¹]	10^5	$\approx 10^7$ in Phase-2	$\approx 10^6$	$10^6 - 10^7$	$\approx 10^4$	10^4	$4 \cdot 10^4$	$4 \cdot 10^5$	$3 \cdot 10^6$

3. Design of the main components

The construction of the pulsed photo-neutron source was preceded by detailed simulations, which did not only include the generation of neutrons in the radiator, their transport through the collimator, the background radiation, activation, and shielding but also the thermal stress

and strain in the components hit by the electron beam. A detailed description of these calculations can be found in [5, 6]. A technical concept for the liquid Pb loop was elaborated. A prototype of this loop was constructed and operated in order to study the materials compatibility of the liquid Pb with different wall materials and to test the control regime of the heat exchanger.

The final design of the photo-neutron source essentially consisting of the liquid lead loop including the e-target section, the beam dump, and the vacuum chamber housing the radiator is shown in Fig. 2. Due to the necessity for a movable radiator the electron beam has to be guided through two beryllium windows confining the high vacuum of the electron beam and the vacuum around the radiator. The latter Be window can also be seen in Fig. 2. The liquid Pb is circulated by an electromagnetic (EM) pump in a circuit made mainly from low activation stainless steel. The radiator section (where the e- beam hits the Pb) is made from Mo (see Fig. 3). The whole circuit is equipped with electric heaters to reach the operating point at 400 °C. The heat exchanger cools down the Pb from ≈ 470 °C to 400 °C.

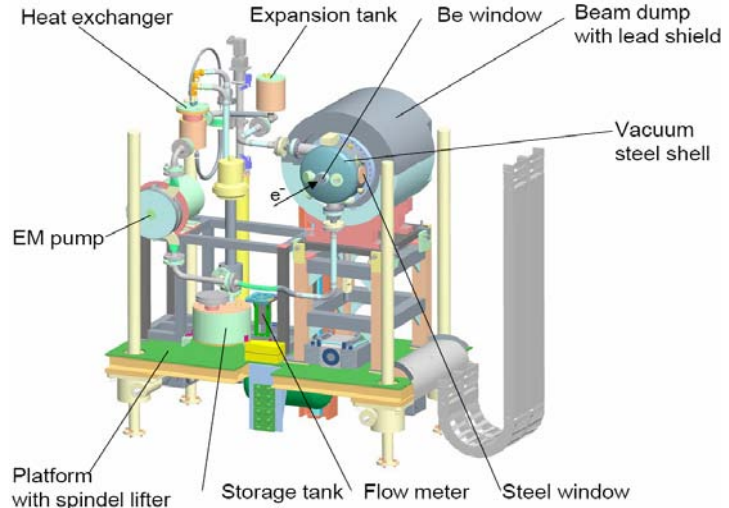


Fig. 2: 3D sketch of the pulsed neutron radiator

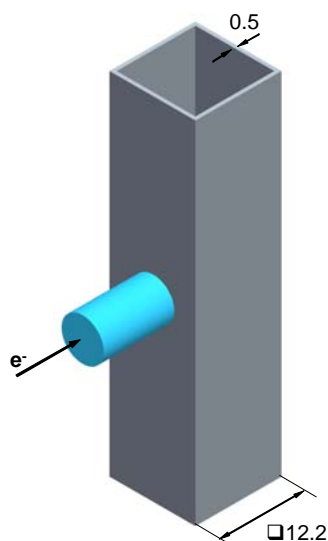


Fig. 3: Sketch of the Mo channel of the radiator with the electron beam of ELBE indicated

The electrons that are not stopped in the Pb radiator and the bremsstrahlung both concentrated in a forward peaked cone are dumped in an aluminum cylinder behind the target. About 50 % of the initial power of the electron beam will be deposited in the dump (e.g., for $E_e = 40$ MeV and $I_e = 1$ mA the initial power is 40 kW with 20 kW deposited). The dump is directly cooled by water and housed in a Pb shell in order to minimize heat radiation from the dump to other components of the photo-neutron source and to comply with radiation protection prescriptions.

The photo-neutrons that are radiated isotropically from the target are decoupled to the collimator under an angle of about 90° relative to the electron beam line through a thin steel window of the vacuum chamber to lower the background of photons, electrons and scattered neutrons at the measuring position. The whole construction follows the basic principle to have as little material in the range of view of the collimator as possible. For the same reason, the wall thickness of the vacuum chamber is also reduced at the side opposite to the neutron window to avoid backscattering of neutrons to the collimator that would decrease the achievable time resolution.

3.1. Radiator

The material selection of the radiator has to satisfy neutronic and thermo-mechanical criteria. Soon it became clear that liquid lead is the best material. So, it was the main task of the neu-

tronic and thermo-mechanic calculations to find the right wall material and best target size.

A material depth and width in the order of two radiation lengths (11.2 mm) was found to be optimum considering the finite size of the electron beam spot on the radiator. Further increasing the cross section of the lead radiator does not result in significant gain in neutron intensity but leads to broader neutron pulses due to multiple scattering in the radiator. Anticipating the result of the thermo-mechanical design, the lead flows through a Mo channel with a wall thickness of 0.5 mm (Fig. 3). For this target configuration, the MCNP [7] calculations predict a maximum source strength of $2.7 \cdot 10^{13}$ n/s and a maximum average neutron flux of about $1.5 \cdot 10^7$ n/(cm² s) at the measuring position 3.9 m away from the radiator for $E_{e^-} = 40$ MeV electrons and an electron current of $I_{e^-} = 1$ mA (Table 2). It can also be concluded from Table 2 that the source strength as well as the neutron flux at the measuring position sensitively depend on the electron energy.

Table 2: Neutron source strength and neutron flux at the measuring position after a flight path of $L = 3.9$ m with an electron current of $I_{e^-} = 1$ mA.

Electron energy in MeV	Neutron source strength at the radiator in n/s	Neutron flux at the measuring position in n/(cm ² s)
20	$7.9 \cdot 10^{12}$	$4.3 \cdot 10^6$
30	$1.9 \cdot 10^{13}$	$1.0 \cdot 10^7$
40	$2.7 \cdot 10^{13}$	$1.5 \cdot 10^7$

The MCNP calculation yields a width of the neutron pulse at the radiator of 280 ps (FWHM) for an electron beam with an incident energy of $E_{e^-} = 40$ MeV and a diameter of $d_b = 3$ mm. With the assumed absolute detector time resolution of 600 ps, the energy resolution at the measuring position is better than 1 % for neutron energies $E_n < 4.5$ MeV. The particle energy spectra at the radiator show that the usable neutron energies range up to 10 MeV.

Different materials were considered as candidates for the wall of the radiator channel [4]. Mo turned out to be a feasible wall material with very high fracture strain even at room temperature (RT) and high thermal conductivity. The material tests proved its chemical resistance to the liquid lead. Due to the static pressure in the lead circuit a wall thickness of 0.5 mm (see Fig. 3) had to be chosen.

The local heat generation rates were calculated for all components of the photo-neutron source using the Monte-Carlo Code FLUKA [8, 9]. Assuming $E_{e^-} = 50$ MeV and beam diameters of $d_b = 3$ mm and 8 mm at the surface of the Mo channel, the maximum heat generation rate in the liquid lead is approximately 249 kW/cm³ and 46 kW/cm³ respectively. The numerical flow and heat transfer simulations for the radiator were performed using the multi-purpose finite elements code FIDAP [10]. The calculations of the temperature distribution in the radiator section were performed assuming mean flow velocities of $\langle v_{Pb} \rangle = 1$ m/s, 2 m/s, and 5 m/s and a lead temperature of 400 °C at the inlet to the neutron radiator channel. The maximum temperatures change only slightly for different beam energies. In contrast to that, the beam diameter has a significant influence to the maximum temperatures. For the beam diameter of $d_b = 8$ mm, all considered lead velocities yield temperatures uncritical with respect to the mechanical strength. For the beam diameter of $d_b = 3$ mm this holds only for the velocity of $\langle v_{Pb} \rangle = 5$ m/s. In all calculations, the maximum temperatures in the wall are by far lower than the melting temperature of Mo and the maximum temperatures in the liquid Pb are lower than the boiling temperature of Pb. Notwithstanding that, the cooling loop for the lead was designed for a mean velocity of at least $\langle v_{Pb} \rangle = 2$ m/s in the radiator channel to have a sufficient safety margin.

The mechanical analyses of the radiator channel were done with the finite element code ANSYS® [11]. Deflections, stresses, and strains were calculated. The construction of the Pb loop has to ensure that no significant thermal stresses occur. As a consequence of the strong temperature gradients a local plastification of the channel wall is unavoidable. In this context, the high ductility and the relatively low thermal expansion coefficient are significant advantages of Mo. The results show that from the mechanical point of view there is no risk of destruction of the radiator channel. Mo fulfills the thermal and mechanical requirements of the radiator channel. Fig. 4 shows the results of the two calculations.

3.2. Beam dump

Pure Al was selected as dump material since it is a low activation material and because of its good thermal conductivity. Additionally, the cylindrical Al core has a cone-shaped notch (diameter and depth 100 mm) in the centre of the front side. The major part of the scattered electron beam hits the beam dump at this cone surface. A stainless steel tube coil is placed in the Al body. It guides the cooling water flow to prevent corrosion effects due to direct contact of the Al with the cooling water. To ensure that the deposited heat can safely be removed from the beam dump, a thermal analysis was performed [12]. The local heat generation densities were taken from the FLUKA calculations, which predict a maximum volumetric heat source of about $P_{\text{heat, max}} = 0.05 \text{ kW/cm}^3$ that is obviously much lower than in the liquid lead target.

For $E_e = 50 \text{ MeV}$ and $d_b = 8 \text{ mm}$, corresponding to a total heat input of 24 kW into the dump, the maximum temperature in the Al body is $\approx 197 \text{ }^\circ\text{C}$, which offers a sufficient distance from the melting point ($T_{\text{Al, melt}} = 660 \text{ }^\circ\text{C}$). The maximum temperature in the Pb shielding is $\approx 101 \text{ }^\circ\text{C}$, which is also sufficiently far from the melting point ($T_{\text{Pb, melt}} = 327 \text{ }^\circ\text{C}$). If the electron beam would not fully hit the radiator due to misalignment (leading to a roughly doubled deposited energy) the dump would partly melt. Therefore, it is mandatory to monitor the beam position or the Al temperatures and to immediately switch off the beam in case of misalignment.

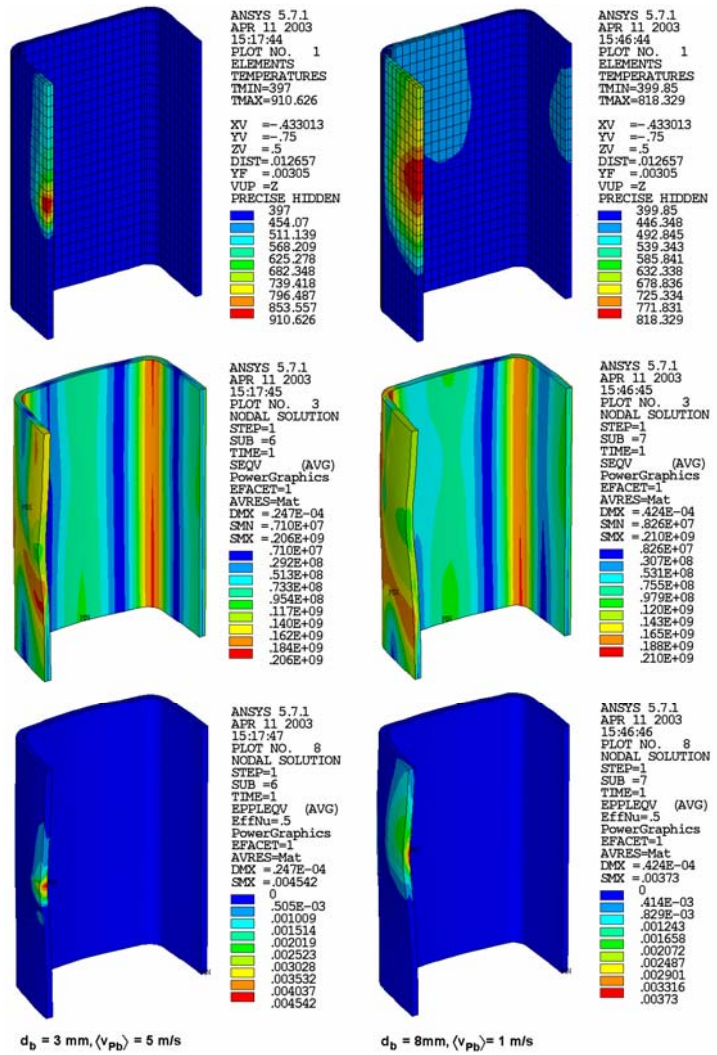


Fig. 4: Mechanical analysis results; top: temperature load T_{Mo} [$^\circ\text{C}$]; middle: equivalent stress [Pa]; bottom: plastic equivalent strain; left side: $d_b = 3 \text{ mm}$ and $\langle v_{Pb} \rangle = 5 \text{ m/s}$; right side: $d_b = 8 \text{ mm}$ and $\langle v_{Pb} \rangle = 1 \text{ m/s}$

4. Radiation background and neutron pulse structure at the measuring position

MCNP calculations of the background and flux at the measuring position 3.9 m away from the radiator were carried out taking into account the construction of the whole radiator set-up and a simplified neutron collimator. For reduction of background and increase of flux at the measuring position two concepts were pursued, 1st: remove material, especially near the radiator, out of sight of the collimator, 2nd: reduce the background of thermal neutrons from the collimator by boric polyethylene as cladding material of the collimator. Almost 92 % of the neutrons stem from the lead in the radiator, ≈ 8 % are scattered or generated in the Mo channel. A small fraction (< 0.1 %) is scattered in the steel housing accommodating the radiator. This background is due to materials close to the radiator which are in sight of the collimator.

The calculations also showed that a flight path of about $L = 3.9$ m allows separating neutrons from bremsstrahlung and electrons simply by their time of arrival at the measuring position. Neglecting all constructional components except the Pb-Mo radiator, MCNP yields a total average neutron flux of about $1.5 \cdot 10^7$ n/(cm² s) at the measuring position presuming an electron energy of $E_e = 40$ MeV and an electron current of $I_e = 1$ mA (Table 2). In Fig. 5, the neutron flux at the measuring position due to a single electron pulse is shown as function of time of arrival for $E_e = 20, 30$ and 40 MeV and for an electron bunch charge of $Q_e = 2$ nC, which will only be possible with the new superconducting SRF gun (Table 1). In the MCNP calculation, the e-pulse is δ -shaped and hits the radiator at $t = 0$ ns. Fig. 5 shows that the neutron flux increases with increasing neutron energy. The neutron pulse at the measuring position reaches the maximum flux at $t \approx 170$ ns. This corresponds to a neutron energy of about 2.7 MeV. The neutron flux is too small for cross section measurements before $t = 90$ ns. Hence, there is a maximum usable neutron energy of about 10 MeV, which corresponds to a time-of-flight of 89.2 ns. The electron beam repetition rate determines the lowest usable neutron energy as faster neutrons from the next pulse start to overlap at the target position with slower neutrons from the preceding pulse. At $t = 13$ ns the prompt photons reach the measuring position. Using a repetition rate of $f_e = 0.5$ MHz the next bunch of photons arrives at $t = 1/(0.5 \text{ MHz}) + 13 \text{ ns} = 2013 \text{ ns}$. This determines the lowest usable neutron energy at $E_n = 19.6 \text{ keV}$. Slower neutrons will be absorbed or scattered out of the neutron beam by a removable absorber in the beam line. Using the SRF gun with the repetition rate of $f_e = 0.5$ MHz the measurable neutron energy range is roughly between $E_n \approx 50 \text{ keV}$ and 10 MeV.

5. Conclusion and outlook

The ELBE radiation source offers suitable parameters for neutron time-of-flight experiments for energy dispersive studies of the interaction of fast neutrons with matter. The calculations predict a maximum source strength of $2.7 \cdot 10^{13}$ n/s and a maximum average neutron flux at the measuring position of about $1.5 \cdot 10^7$ n/(cm² s). The neutron pulse at the measuring position reaches the maximum flux at a neutron energy of about $E_n = 2.7$ MeV. Using the new SRF photo electron injector with the repetition rate of $f_e = 0.5$ MHz the measurable neutron energy range is between $E_n = 50 \text{ keV}$ and 10 MeV. The expected energy resolution at the measuring

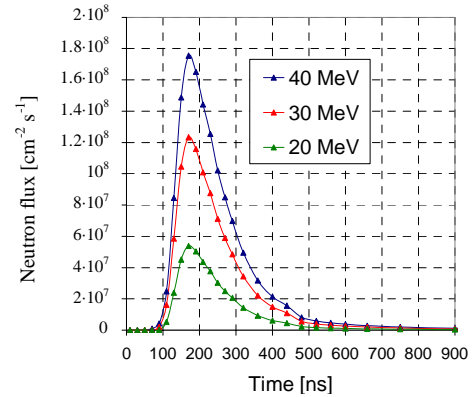


Fig. 5: Time dependent neutron flux at the measuring position due to a δ -shaped electron pulse, ($Q_e = 2$ nC, $L = 3.9$ m, $E_e = 20, 30, 40$ MeV, $d_b = 3$ mm)

position is better than 1 % for energies up to 5 MeV. The estimated background at the measuring position is low. Further particle transport calculations are just being carried out to optimize the design of the collimator. Moreover, detectors are being developed for the detection of neutrons, photons and light charged particles and are tested at the ELBE bremsstrahl.

Concerning the thermal mechanical analyses, liquid lead proved to be a feasible material for the neutron radiator. This concept enables the safe removal of the extremely high power densities of up to $P_{\text{heat}} = 50 \text{ kW/cm}^3$ which are generated by the interaction of the electron beam with the radiator material. It could be shown that the temperatures in the liquid lead and in the channel wall are low enough for safe operation. Molybdenum turned out to be the most suited material for the radiator channel due to its high melting point, high ductility, good heat conductivity, and low thermal expansion. The plastic strain induced by the thermal load does not endanger the mechanical integrity of the channel. The energy deposited in the beam dump caused by electrons not stopped in the radiator and by secondary radiation can be safely removed by water cooling of the aluminum body.

The commissioning of the pulsed photo-neutron source and first neutron measurements are scheduled for 2007.

References

- [1] M. Cometto, P. Wydler and R. Chawla (2004), A comparative physics study of alternative long-term strategies for closure of the nuclear fuel cycle, *Annals of Nuclear Energy*, 31, 413-429.
- [2] J. Knebel et al. (2006), European Research Programme for the transmutation of high level nuclear waste in an accelerator driven system, *Proceedings of the Conference on EU Research and Training in Reactor Systems (FISA 2006)* (p. 322), Luxembourg
- [3] G. Aliberti et al. (2006), Nuclear data sensitivity, uncertainty and target accuracy assessment for future nuclear systems, *Annals of Nuclear Energy*, 33, 700-733.
- [4] J. Teichert et al. (2005), Progress of the Rossendorf SRF gun project, *Proceedings of the 27th International Free Electron Laser Conference*, Stanford, California, USA
- [5] E. Altstadt et al. (2005), Energiedispersive Untersuchung der Wechselwirkung schneller Neutronen mit Materie, Rossendorf, Report FZR-426
- [6] E. Altstadt et al. (2007), A photo-neutron source for time-of-flight measurements at the radiation source ELBE, *Annals of Nuclear Energy*, 34, 36-50
- [7] J. F. Briesmeister (1993), MCNP a general MONTE CARLO N-Particle Transport Code, Version 4A, LA 12625 M
- [8] A. Fasso et al. (2003), The physics models of FLUKA: status and recent developments, *Conference on Computing in High Energy and Nuclear Physics 2003 (CHEP2003)*, eConf C0303241 (2003), arXiv:hep-ph/0306267, La Jolla, CA, USA
- [9] A. Fasso, A. Ferrari, J. Ranft, P. R. Sala (2005), FLUKA: a multi-particle transport code, CERN, INFN/TC_05/11, SLAC-R-773.
- [10] Fluent, Inc. (1998), FIDAP 8 Theory Manual, Lebanon, NH, USA
- [11] ANSYS (1999), User's Manual for Rev. 5.6, Swansons Analysis Systems, Inc.
- [12] H. Bergander (2003), FEM-Thermalberechnung des Beam Dump eines Neutronenproduktionstargets, Dresden, Germany, Technical Report HTS GmbH

Acknowledgement

This work was supported by Deutsche Forschungsgemeinschaft under contract FR 575/5 and GR 1674/2.

CAPABILITY OF CURRENT CFD CODES TO SUPPORT FUEL ROD BUNDLE DESIGN

Eckhard Krepper

1. Introduction

The integrity of the fuel rods of a fuel assembly of a water cooled nuclear reactor core can be endangered by exceeding the critical heat flux. The critical heat flux depends on the flow parameters and can be influenced by the geometrical design. Especially the spacer grids equipped with mixing vanes play an important role to increase the permissible heat flux. Verification of design improvements and their influence on the critical heat flux requires very expensive experiments. Therefore, the supplementation or even the replacement of expensive experiments by numerical analysis is of interest to fuel assembly design.

In the past many fitted to experiments empirical correlations for critical heat flux were developed and applied in purpose-developed 1D codes. However, these correlations are valid only in a limited range of fluid conditions and fluid properties and hold for the defined geometry for which they were derived. Using lookup tables based on experiments, the fluid parameter validity range can be extended. But also this method is limited to the defined geometry. Independence of the models on the geometry can be achieved by the application of CFD methods only. In Krepper et al. (2007), the models for the description of subcooled boiling are summarized. For a unique set of model parameters, the wall boiling model, which is implemented in a prototype version of CFX (see Egorov, Menter 2004), was applied to the simulation of lots of published subcooled boiling experiments (see Bartolomej et al. 1967, 1982). The model was shown to yield satisfying agreement to measured vapour volume fractions at pressures from 3 to 11 MPa, at heat fluxes up to 1.2 MW/m^2 and at mass flow rates at about $1000 \text{ kg/(m}^2\text{s)}$. This paper describes the application of CFD to model a hot channel of a fuel assembly and investigates the capability of CFD to contribute to fuel assembly design.

2. Simulation of a fuel assembly hot channel

2.1. Model options and boundary conditions

In the calculations only subcooled boiling is simulated, which is here considered as a transient phenomenon towards departure from nucleate boiling (DNB). DNB might e.g. occur at the thermal hydraulic conditions of a PWR when at full power and full pressure the inlet temperature rise causes undesired boiling in the channel.

A section between two spacer grids was simulated having a length of $z=0.5 \text{ m}$. The grid represents a subchannel between 4 rods of 9 mm diameter and a rod distance of 12.6 mm. The thermal hydraulic water properties were set for a pressure of 15.7 MPa, typical for PWR conditions. The heat flux at the rod surface was assumed to be $1.0 \cdot 10^6 \text{ W/m}^2$ and the subcooling at the inlet was set to 12 K expecting the generation of vapour in the simulated section. The axial water velocity was set to $V_z = 5 \text{ m/s}$. The faces at the maximum and minimum x-coordinate respective at the maximum and minimum y-coordinate were simulated as periodic boundary conditions, assuming that the channel is infinitely extended in these four directions (see Fig. 1).

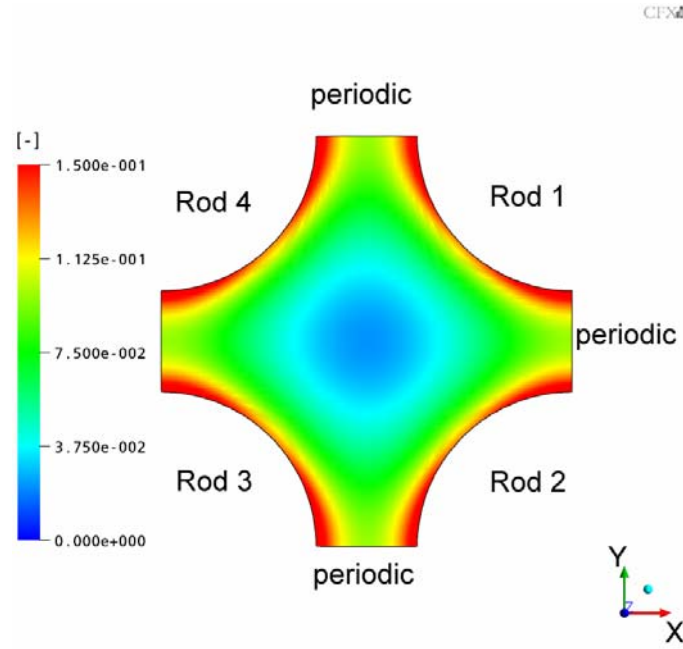


Fig. 1: Vapour volume fraction distribution in the cross section at $z = 0.475$ m without consideration of an inlet swirl

Figure 1 shows the vapour volume fraction distribution in the channel cross section at $z = 0.475$ m. Maximum vapour generation is found at the smallest distance between the rods.

2.2. Simulating a complex flow structure by suited inlet conditions

To investigate the effect of a swirl caused by mixing vanes, additional horizontal velocity components V_X and V_Y were given at the inlet according to

$$\begin{aligned} V_X &= V_R \cos\left(\alpha + \frac{\pi}{2}\right) = -V_R \frac{y}{r} \\ V_Y &= V_R \sin\left(\alpha + \frac{\pi}{2}\right) = V_R \frac{x}{r} \end{aligned} \quad \text{for } R_{min} = 1 \text{ mm} < r < R_{max} = 3.8 \text{ mm} \quad (1)$$

It could be shown that the resulting flow field very well corresponds to a flow caused by real mixing vanes (Reinders, 2004). Besides the reference case a) with zero transversal velocity ($V_R = 0$ m/s), the following cases with different transversal velocities at the circumference of the circular swirl V_R were simulated: b) $V_R = 1$ m/s, c) $V_R = 2$ m/s and d) $V_R = 3$ m/s to investigate examples of different geometrical mixing vane design. Fig. 2 shows the resulting inlet velocity field for case d) with $V_R = 3$ m/s. Fig. 3 presents the relation of the horizontal velocity components to the overall value of the velocity along the vertical axis z .

$$swirl = \frac{\sqrt{v_x^2 + v_y^2}}{\sqrt{v_x^2 + v_y^2 + v_z^2}} \quad (2)$$

Due to the centrifugal force, the heavier fluid component - the water - is pushed outwards, whereas a large amount of the lighter component - the vapour - is accumulated in the centre of the channel. The streamline presentations of Fig. 4a) for water and 4b) for vapour clearly show this phenomenon.

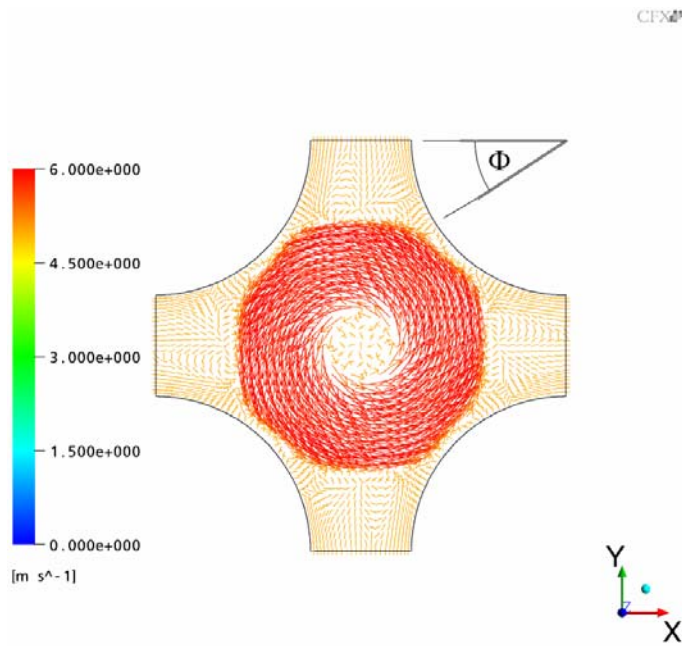


Fig. 2: Velocity field at the inlet: axial velocity $V_Z=5\text{m/s}$, velocity at the circumference of the swirl $V_R=3\text{ m/s}$ (case d)

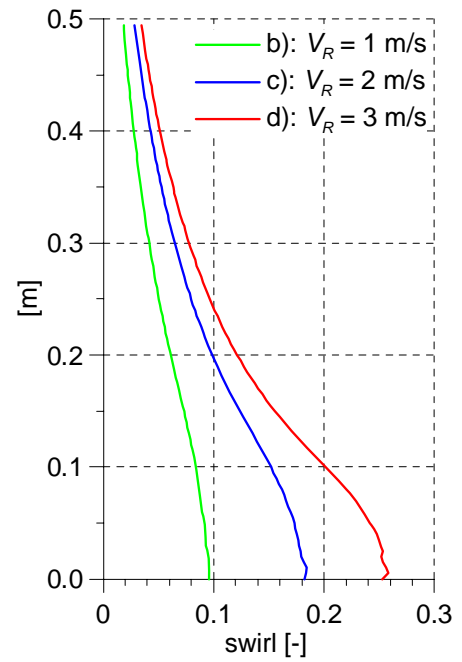
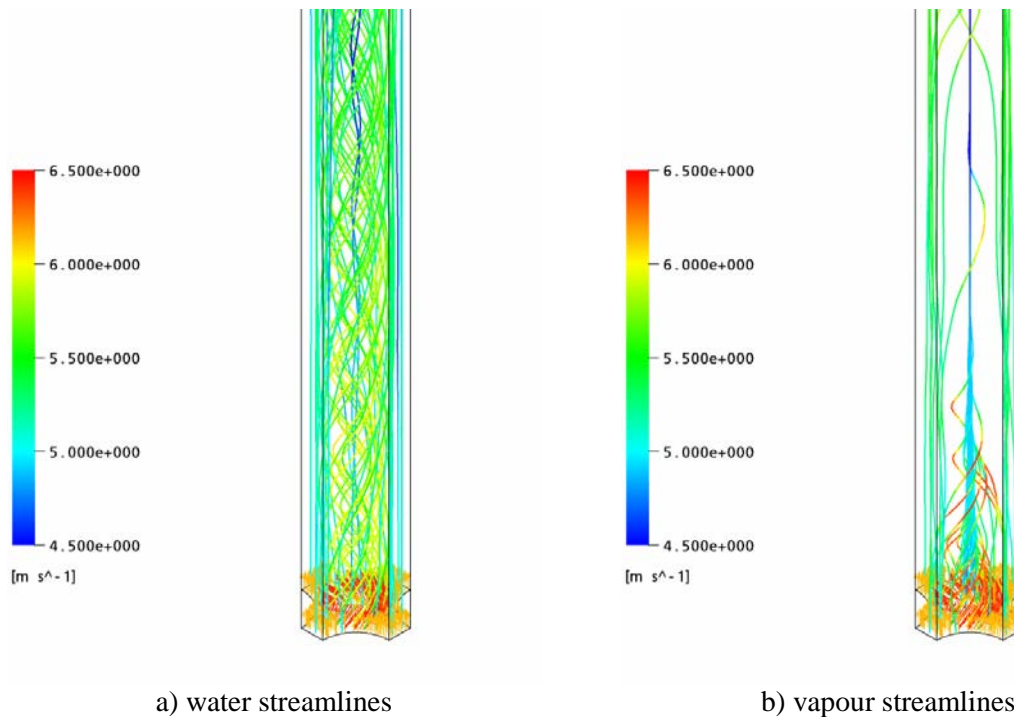


Fig. 3: Axial profiles of the swirl for the investigated cases ($V_Z=5\text{m/s}$)



a) water streamlines

b) vapour streamlines

Fig. 4: Stream line presentation of the simulated water and steam flow

Fig. 5 shows the calculated vapour volume fraction distribution at $z = 0.475\text{ m}$ considering the swirl, which is counter clockwise oriented in this example. In the shadow of the rods, accumulation of vapour bubbles is calculated.

For case d), Fig. 6 presents the influence of the swirl on the axial profile of the vapour volume fraction averaged over the whole cross section. Indeed the cross sectional averaged vapour

volume fraction is reduced by the swirl as desired - in this example from about 8 % to about 6.7 %, whereas the averaged water temperature in the channel is almost not influenced. The tangential velocity near the wall is increased by the swirl. As a consequence, higher portions of the wall heat flux are transferred by single phase convection whereas the share of evaporation is decreased (see Fig. 7a). Heat transfer by quenching plays only a limited role compared to the other two components. Furthermore the wall superheating temperature averaged over the circumference is reduced (see Fig. 7b). In the presented example the reduction at $z = 0.1$ m amounts to about 1.5 K.

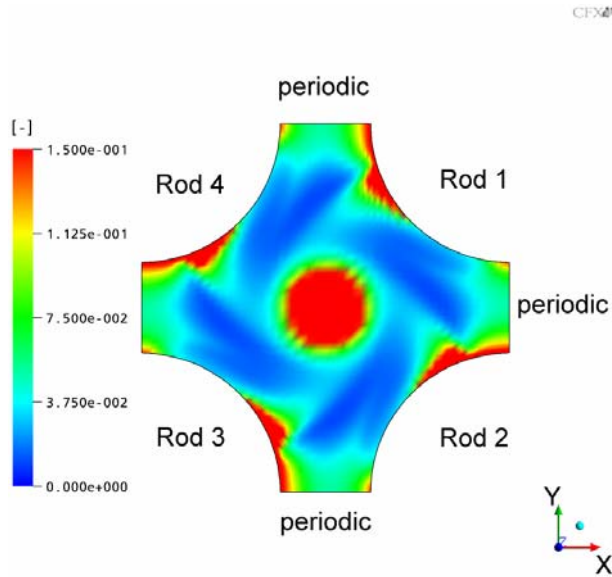


Fig. 5: Vapour volume fraction distribution in the cross section at $z=0.475$ m considering a swirl (case d)

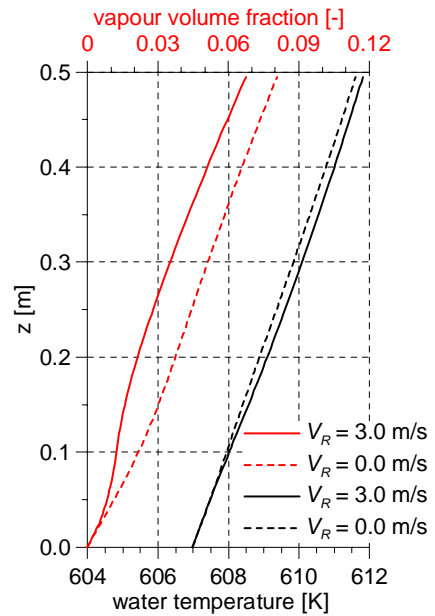


Fig. 6: Influence of the swirl on the cross sectional averaged vapour volume fraction and water temperature for case d)

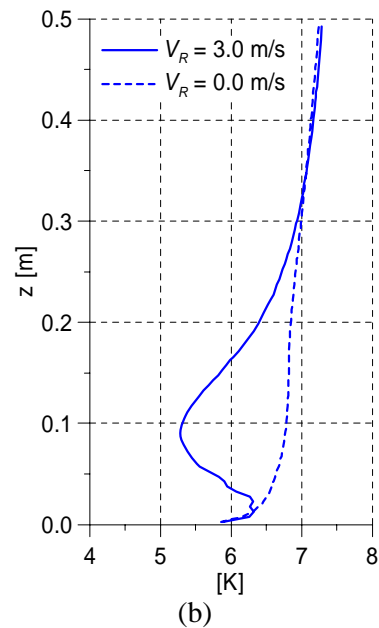
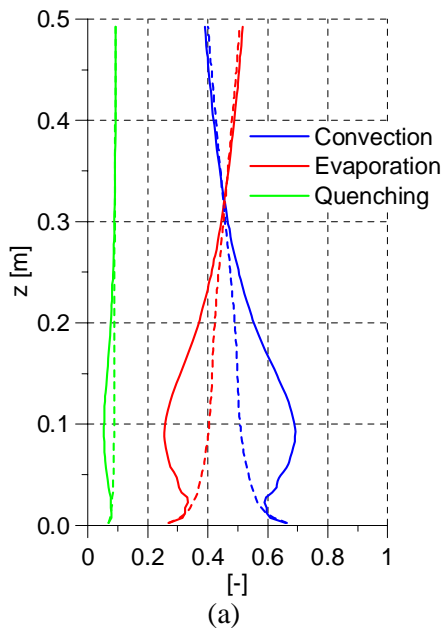


Fig. 7: Cross sectional averaged heat flux components (a) and superheating temperature at the rod surface (b) for the case d) (solid lines) and the reference case a) without swirl (dotted lines)

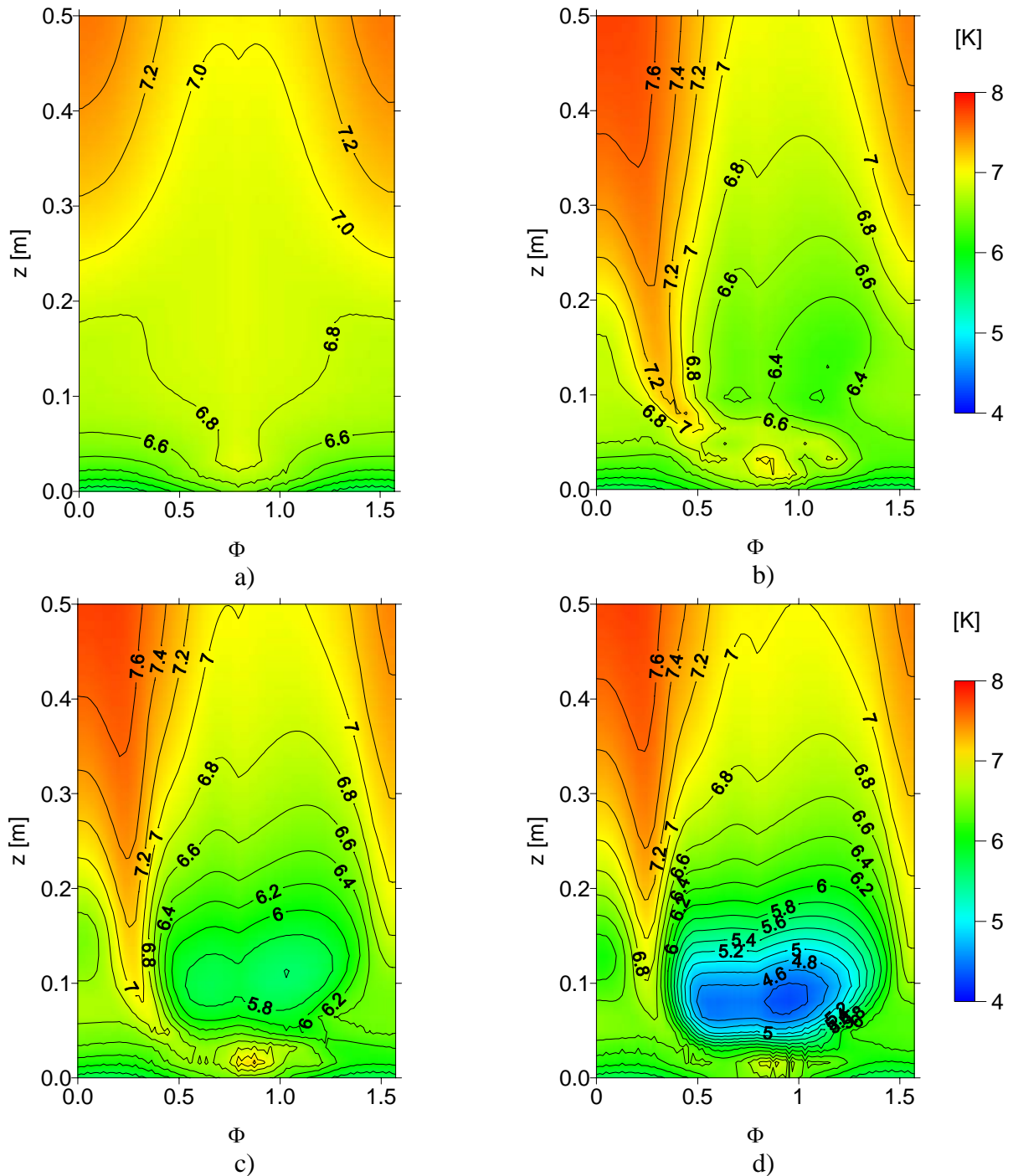


Fig. 8: Distribution of the wall superheating temperature at the surface of rod 1 without swirl (a) and considering a swirl (case b to d) (for the definition of the angle Φ , here in radians, see Fig. 2)

The application of CFD allows visualizing the distribution of the superheating T_{sup} at the rod surface of rod 1 shown in Fig. 8 for two cases a) to d). Without swirl, a symmetric distribution is found showing maximum values at locations with the smallest distance to the adjacent rods. In contrast, the assumed swirl generates a more irregularly distributed wall superheating. Hot spots (e.g. at $z = 0.15$, $\Phi = 0.3$) might be the locations, where later on the critical heat flux could occur first.

In the calculations, the wall heat conduction has not yet been considered. In reality, the heterogeneous temperature distributions calculated here might be smoothed somewhat by thermal conduction in the wall material. Corresponding model improvements are under way.

In all calculations, a monodispersed bubble size distribution was modelled in the bulk dependent on the liquid temperature. However, for this high vapour volume fraction in the centre bubble coalescence and the occurrence of larger bubbles might be expected. Hence the interfacial area and consequently the condensation in the bulk are overestimated, in the presented calculation. Therefore, higher vapour volume fractions might be found in reality.

3. Summary

Current CFD methods are not yet able to simulate critical heat flux conditions. In the present paper subcooled boiling as an intermediate state towards the development of a state of critical heat flux is modelled. Nevertheless, essential phenomena can be identified. Fig. 5 shows that concentration regions of bubbles can be calculated. By predicting the temperature at the rod surface, critical regions can be identified, which might later on lead to departure from nucleate boiling and possible damage of the fuel pin. The avoiding of uneven temperature distributions at the rod surface can be considered as a design criterion for the spacer grids.

The application of state of the art CFD with a subcooled boiling model for the simulation of a hot channel enables at least the comparison and the evaluation of different geometrical designs of the spacer grid. For quantitative assessments, however further model developments are necessary. The vapour bubble size at departure from the wall and the vapour bubble size in the bulk could be shown as parameters having a very sensitive influence on the vapour volume fraction and on the temperatures (Krepper et al. 2007). Improved models have to be validated using experiments. Unfortunately the measurement of these bubble sizes by actual experimental techniques is very challenging because of the narrow geometry of channels of about 10 mm, the vapour bubble size expected in the range of 0.5 to 2 mm and the pressure and the temperature of the fluid, which should be comparable to the values found in a typical nuclear reactor. Recent attempts applying X-ray and Gamma-tomography are very promising giving at least more exact information about the gas fraction distribution.

References

- [1] Bartolomej, G.G., Chanturiya, V.M., 1967, Experimental study of true void fraction when boiling subcooled water in vertical tubes, *Thermal Engineering* Vol. 14, pp. 123-128, translated from *Teploenergetika* Vol. 14, 1967, 2, pp. 80-83
- [2] Bartolomej, G.G. et. al, 1982, An experimental investigation of true volumetric vapour content with subcooled boiling in tubes, *Thermal Engineering* Vol. 29, pp. 132-135, translated from *Teploenergetika* Vol. 29, 1982, 3, pp. 20-23
- [3] Burns, A.D., Frank, T., Hamill, I. and Shi, J.-M. 2004. The favre averaged drag model for turbulence dispersion in Eulerian multi-phase flows. 5th Int. Conf. on Multiphase Flow, ICMF'2004, Yokohama, Japan
- [4] Egorov, Y., Menter, F., 2004. Experimental Implementation of the RPI Wall Boiling Model in CFX-5.6, Technical Report ANSYS / TR-04-10, ANSYS Germany GmbH.
- [5] Krepper, E., Koncar, B., Egorov, Y., 2006, Modelling of subcooled boiling – concept, validation and application to fuel assembly design, *Nuclear Engineering and Design* 237 (2007) 716-731
- [6] Reinders, R., 2004. personal communication.

- [7] Tomiyama, A., 1998. Struggle with computational bubble dynamics, 3rd International Conference on Multiphase Flow, ICMF'98, Lyon, France, June 8-12, 1998

Acknowledgements

Fruitful discussions and valuable hints given by F. Burtak, R. Reinders, M. Glück and T. Salnikowa, AREVA NP GmbH are gratefully acknowledged.

SIMULATION OF BUBBLE ENTRAINMENT CAUSED BY A LIQUID JET IMPINGING ON A FREE LIQUID SURFACE

Emmanuel Bodèle and Dirk Lucas

1. Context

This work is done in the framework of the European Integrated Project NURESIM (NUclear REactor SIMulations) which focuses on the development of a European code platform for nuclear reactor safety analyses [1]. In the subproject on thermohydraulics, one topic is related to two-phase Pressurized Thermal Shock (PTS) modelling for Pressurized Water Reactors (PWR). During a LOCA, the Emergency Core Cooling (ECC) injection into a partially filled cooling circuit may result in high thermal loads to the Reactor Pressure Vessel (RPV) wall. The main objectives of the numerical work consist in the development of new models for the prediction of the interactions between the phases, which influence the mixing of hot and cold water and finally the thermal loads to the structures. These interactions are very complex as depicted in Fig. 1. One special topic is the bubble entrainment in the plunging jet region. Several studies have shown that the mixing between the hot fluids (liquid and steam present in the cold leg pipe) and the cold injected liquid are strongly influenced by the behaviour of the steam entrained below the liquid surface.

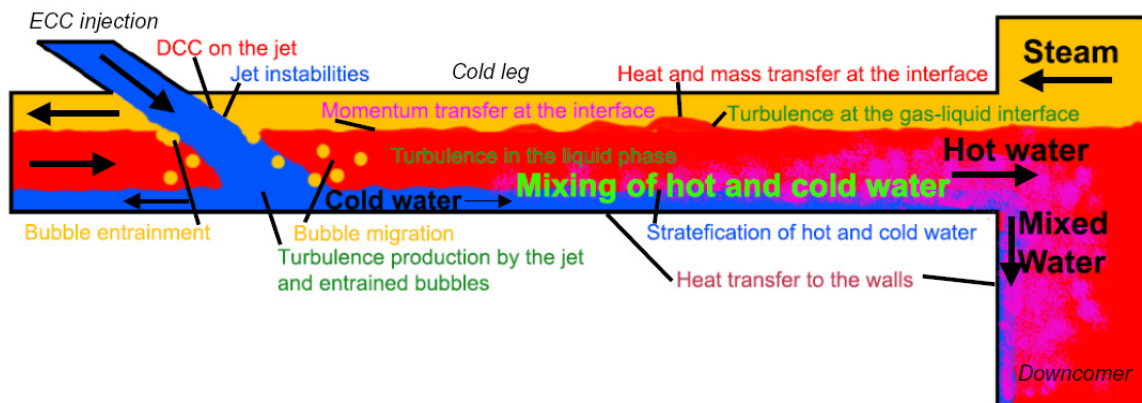


Fig. 1: Two-phase flow situation during an ECC injection into a partially filled cold leg

The characteristics of this special flow situation are reflected by the so called plunging jet configuration: i.e. a liquid jet impinges on the free liquid/steam surface within a reservoir. If the jet velocity is large enough bubbles are entrained below the surface. The numerical representation of such a configuration is connected with several difficulties. One of them is related to the scales, which have to be considered. On the one hand there is a relative large scale of the whole system considered (technical system scale \sim m). On the other hand the scales responsible for the bubble entrainment are much smaller than the generated bubbles ($\ll 1$ mm). Thus for a direct simulation of the bubble entrainment the region of the impinging jet would have to be represented in the numerical grid with a very fine resolution, which is not feasible for practical applications. Another problem arises from the simultaneous occurrence of separated and dispersed gas phases in the numerical domain. According to the different local flow structures different closure models have to be applied, e.g. for the drag between separated phases, drag between liquid and gas bubbles and possibly also the drag in the region of the impinging jet. Solving these problems is of crucial importance for the qualification of Computational Fluid Dynamics (CFD) codes for two-phase flows in general – not only for the

plunging jet configuration. The work presented here is a first step to identify possible solutions for these problems.

2. Numerical work

The numerical work is done both with the CFX-10 [2] software and the NURESIM NEPTUNE code [3] jointly developed by CEA and EDF. The numerical configuration leans against the Bonetto & Lahey experiment [4] in which a freely falling water jet introduced through a circular injector impacts a water surface in a quasi-cubic (0.9 m×0.9 m×1.4 m) partially filled acrylic tank. This experiment has been considered for the numerical study because the associated database is one of the most complete and since it provides qualitative and quantitative information on the air behaviour below the water surface (gas volume fraction, bubble size distributions, gas dispersion in the liquid phase, velocities for both the liquid and gas phases...).

In the numerical domain (Fig. 2) the same inner diameter of the injection nozzle (5.1 mm) was chosen like in the experimental facility. In order to obtain a fully developed jet before it enters into the tank, a 5 cm long part of the inlet pipe has been included in the numerical domain. For reducing the size of the mesh (Fig. 3), the dimensions of the tank have been reduced compared to the experimental setup. Thus the tank has a maximum height equal to 600 mm and a diameter of 400 mm), and a 2D-axisymmetric domain has been defined. The resulting mesh is finally composed from 49300 cells (260 prisms close to the domain axis and 49060 hexahedrons for the rest of the domain). This mesh has been used with both the CFX-10 and the NEPTUNE codes.

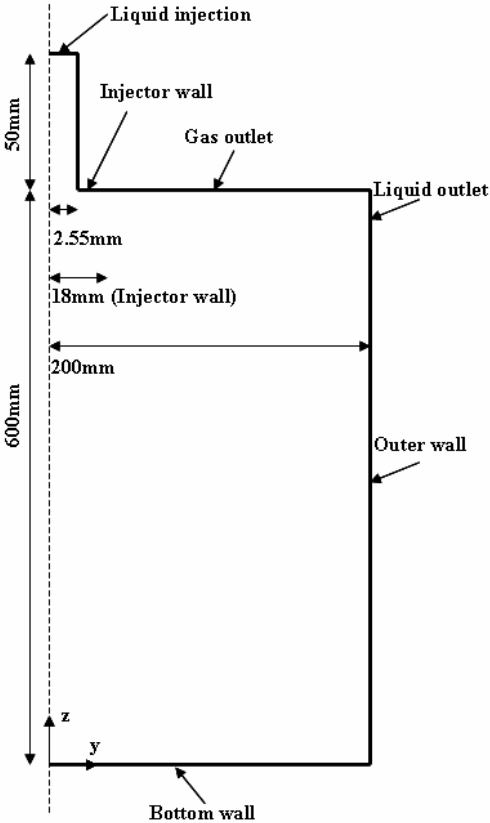


Fig. 2: Numerical configuration

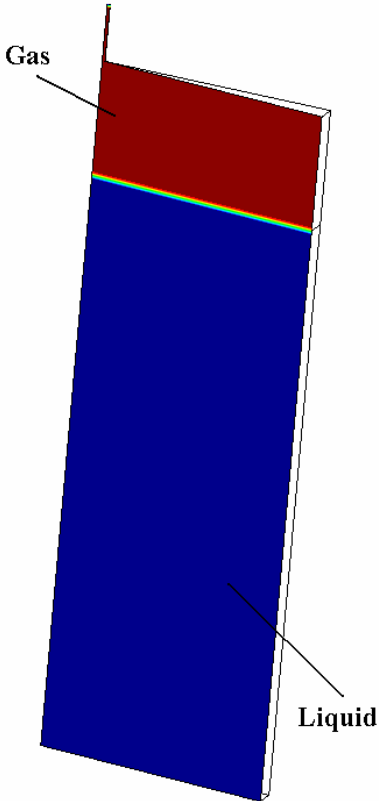


Fig. 3: Numerical domain. Initial state

The distance between the injector pipe nozzle and the unperturbed water surface is initially equal to 10 cm (Fig. 3) and the liquid injection velocity is equal to 5 m/s (representative of those used by Bonetto & Lahey during their experiments which vary from 5.2 m/s to 7 m/s). For the forces acting on the gas phase, several models have been evaluated such as the formulation of Lopez de Bertodano for the turbulent dispersion force [5] and the Tomiyama formulation for the lift force [6]. Lucas *et al.* have shown that this relation for the lift force gives good agreement with experimental data in the case of vertical pipe flows [7, 8]. For the drag between the bubbles and the liquid phase several constant values have been considered. For the turbulence, the shear stress model is used and the turbulence transfer between the phases is treated according to the model of Sato [9]. The turbulence intensity was set to 5 %. All the calculations have been performed using a transient assumption with a time step equal to 0.5 ms in order to assume a maximum Courant number of 1 in the whole domain. The total physical time simulated is equal to 20 s.

For the NEPTUNE calculations, changes in the models have been considered because of the specific model integration. The turbulence for the both phases is treated with a k- ϵ model. The turbulence transfers between the phases are treated with the specific “reverse coupling” option of the NEPTUNE CFD code.

3. Numerical results

Numerical results concern mainly the characteristics of the 2-phase flow below the free water surface (gas volume fraction, gas and liquid velocities) for which experimental data are available. The contour of the gas volume fraction obtained from averaging over the last 10 seconds of the calculations is shown on figures 4 and 5 for CFX-10 and NEPTUNE, respectively. Since flow is quite stable during this time (only a limited number of small waves are observable at the surface of the “pool”, and only very localized oscillations of the “trumpet” close to the impact), these averaged contours are representative for the steady state solution. One of the most important results is the numerical reproduction of the characteristic “trumpet” with both codes, even if deviations between the predictions can be observed. Moreover, the gas dispersion in the domain, below the liquid surface is very limited and the most important part of the entrained gas is located close to the centreline of the injector at limited depth. This qualitatively agrees with the experimental observations. It is a first result of the investigations, that in principle both codes are able to reflect the bubble entrainment in the simulation. Comparisons between simulations with and without consideration of the above mentioned non-drag bubble forces show, that the gas fraction distribution below the surface can be quantitatively reflected only if these non-drag forces are taken into account. The importance of the non-drag force for the appropriate simulation of the plunging jet configuration is another result of the investigations. Also the bubble de-entrainment is well reflected in the simulations.

The profiles of the gas volume fraction below the liquid surface (Figs. 6 and 7) show an overestimation of the amount of entrained gas. Experimentally, Bonetto & Lahey have measured a maximum gas volume fraction of 0.13 for the radial profiles and 0.14 for maximum value at the centreline, while in the simulations up to 0.6 (CFX) and 0.28 (both codes) are observed respectively. This overestimation may result from numerical effects or the inability of state of the art CFD tools to consider several regions with different models or coefficients for a similar phenomenon. In our particular case, the interfacial drag coefficient is related to the dispersed gas phase (bubbles). This coefficient is not suitable for the reproduction of the interactions at the continuous liquid/gas interfaces (horizontal “pool”

surface and jet surface). Specific improvements of the numerical tools are required, in order to permit the reproduction of various flow conditions in the same numerical domain. This is an important point for the following steps in modelling the plunging jet configuration.

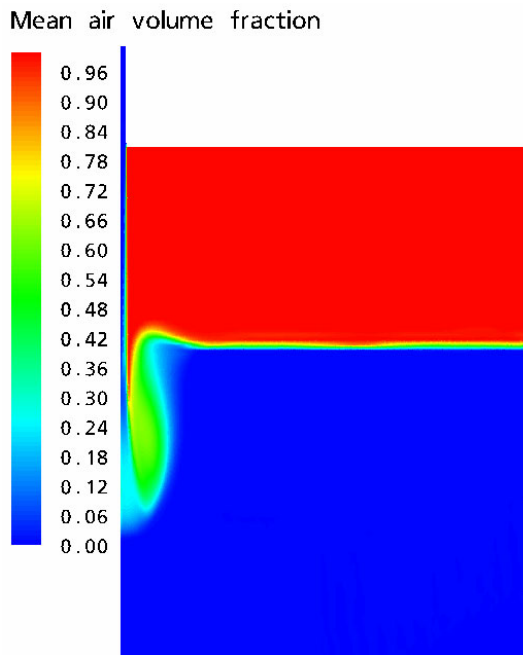


Fig. 4: Time averaged values of the gas volume fraction in case of the CFX-10 calculation

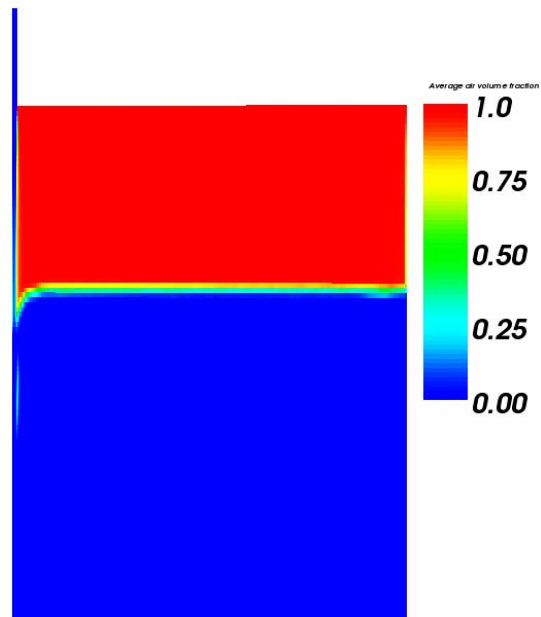


Fig. 5: Time averaged values of the gas volume fraction in case of the NEPTUNE calculation

Finally, both codes have provided similar gas penetration depths (see Fig. 6: 80 mm for NEPTUNE and close to 95 mm for CFX-10). The calculated penetration depths are higher than in the experiments, and the locations of the maximum gas concentration are also overestimated. Unfortunately the experimental data published are shown only until a maximum depth of 50 mm.

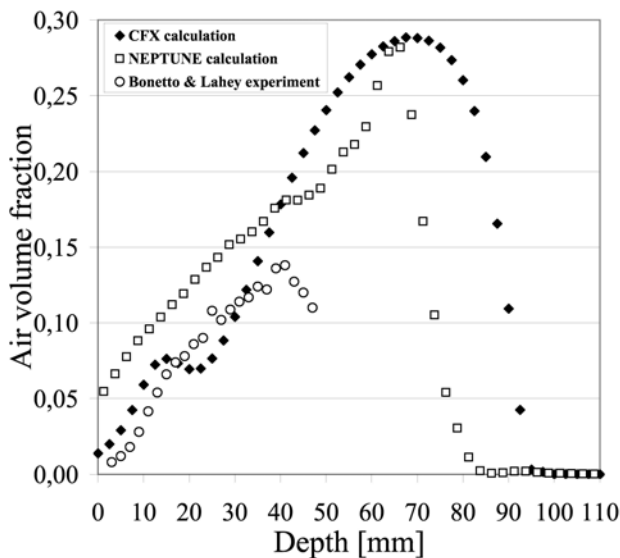


Fig. 6: Axial profiles of averaged air volume fraction at the centreline of the injector.

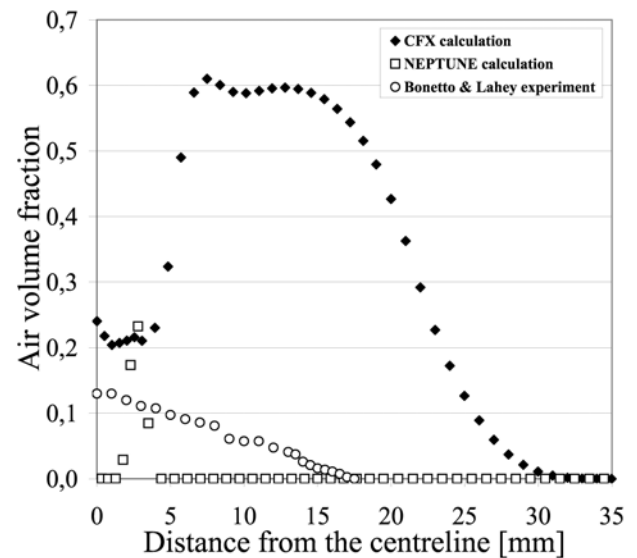


Fig. 7: Radial profiles of averaged air volume fraction 50 mm below the level of the unperturbed water surface.

4. CFD codes improvement for the prediction of the plunging jet configuration

One of the most important improvements of the numerical tools for the prediction of the plunging jet configuration consists in the development of a method which permits to distinguish the various flow regimes existing in the domain. Presently several methods are tested. The method which gives the most encouraging results consists in evaluating the gradient of the gas volume fraction. Indeed, depending on the flow regime, this gradient strongly differs and should permit to distinguish between the flow structures. Thus, in the case of gas inclusions in liquid, the gas volume fraction is almost constant whereas in the case of the continuous interface (“pool” and jet surfaces) this gradient is strongly increased because of the high variation of the gas volume fraction (from 0 to 1 in 2 or 3 cells when passing from the liquid to the gas environment). Once this identification of specific flow zones can be done, suitable models have to be implemented to reflect the local physical processes.

5. Conclusions

The numerical prediction of the plunging jet configuration is a very complex problem. Nevertheless the presently available CFD codes are able qualitatively to simulate bubble entrainment by the jet, bubble dispersion and bubble de-entrainment through the free surface. Because of the various flow regimes appearing in the same numerical domain (separated phases close to the continuous interfaces, discrete gas inclusions in the liquid below the liquid surface) the available numerical tools fail in a quantitatively satisfying prediction of the local gas volume fraction. A new method based on the gradient of the gas volume fraction allowing to switch between several models or coefficients for different flow phenomena has provided encouraging results. Nevertheless further improvement is necessary. This work, which is of general importance for the qualification of CFD codes for two-phase flows, will be continued.

References

- [1] D. G. Cacuci, J. M. Aragonés, D. Bestion, P. Coddington, L. Dada, & C. Chauliac, (2006), NURESIM: A European Platform for Nuclear Reactor simulation. FISA: conference on EU research and training in reactor systems, Luxembourg.
- [2] ANSYS-CFX-Solver, “Release 10.0: Modelling”, “Release 10.0: Theory”.
- [3] J. Laviéville, E. Quémérais, S. Mimouni, M. Boucker and N. Méchitoua (2005), NEPTUNE CFD V1.0 Theory manual.
- [4] F. Bonetto and R. T. Lahey Jr (1992), An experimental study on air carryunder due to a plunging liquid jet, *International Journal of Multiphase Flow*, 19, 281.
- [5] Lopez de Bertodano B. (1991), Turbulent bubbly flow in a triangular duct, Ph. D. Thesis, Rensselaer Polytechnic Institute, Troy New York.
- [6] Tomiyama A., Tamai H., Shimomura H., Hosokawa S. (1999), Spatial evolution of developing air-water bubble flow in a vertical pipe, in: *Proceedings of the 2nd International Symposium on two-phase flow modelling and experimentation*, Vol. II, Pisa, 1027.
- [7] D. Lucas, E. Krepper and H. M. Prasser (2001), Prediction of radial gas profiles in vertical pipe flow on the basis of bubble size distribution, *International Journal of Thermal Science*, 40, 217.
- [8] D. Lucas, J.-M. Shi, E. Krepper and H.-M. Prasser (2004), Models for the forces acting on bubble in comparison with experimental data for vertical pipe flow, *3rd International Symposium on Two-Phase Flow Modelling and Experimentation*, Pisa.
- [9] Y. Sato and K. Sekoguchi (1975), Liquid velocity distribution in two-phase bubbly flow, *International Journal of Multiphase Flow*, 2, 79.

CFD VALIDATION OF STRATIFIED TWO-PHASE FLOWS IN A HORIZONTAL CHANNEL

Christophe Vallée and Thomas Höhne

1. Introduction

In different scenarios of small break Loss of Coolant Accident (SB-LOCA), stratified two-phase flow regimes can occur in the main cooling lines of pressurized water reactors. Because these flow patterns cannot be predicted with the required accuracy and spatial resolution by the one-dimensional system codes, the stratified flows are increasingly modelled with computational fluid dynamics (CFD) codes. In CFD, closure models are required that must be validated, especially if they are to be applied to reactor safety issues.

Slug flow is a challenging flow regime for CFD, because of the acceleration of the gaseous phase and of the transition of the fast liquid slugs, which carry a significant amount of liquid with high kinetic energy. Further, it is potentially hazardous to the structure of the system due to the strong oscillating pressure levels formed behind the liquid slugs as well as the mechanical momentum of the slugs. CFD calculations of slug flow were performed and were compared with optical observations captured at the **Horizontal Air/Water Channel (HAWAC)** of the *Forschungszentrum Dresden-Rossendorf (FZD)*. It is the aim of the conducted simulations to validate the prediction of slug flow with the existing multiphase flow models available in the commercial code *ANSYS CFX* [1]. Further, it is of interest to prove the understanding of the general fluid dynamic mechanism leading to slug flow and to identify the critical parameters affecting the main slug flow parameters (like e.g. slug frequency and propagation velocity).

2. The Horizontal Air/Water Channel (HAWAC)

Experiments were carried out at the **Horizontal Air/Water Channel (Fig. 1)**, which is devoted to co-current flow experiments [2]. The 8 m long test-section has a rectangular cross-section of 100 x 30 mm² (height x width), leading to a length-to-height $L/h = 80$.

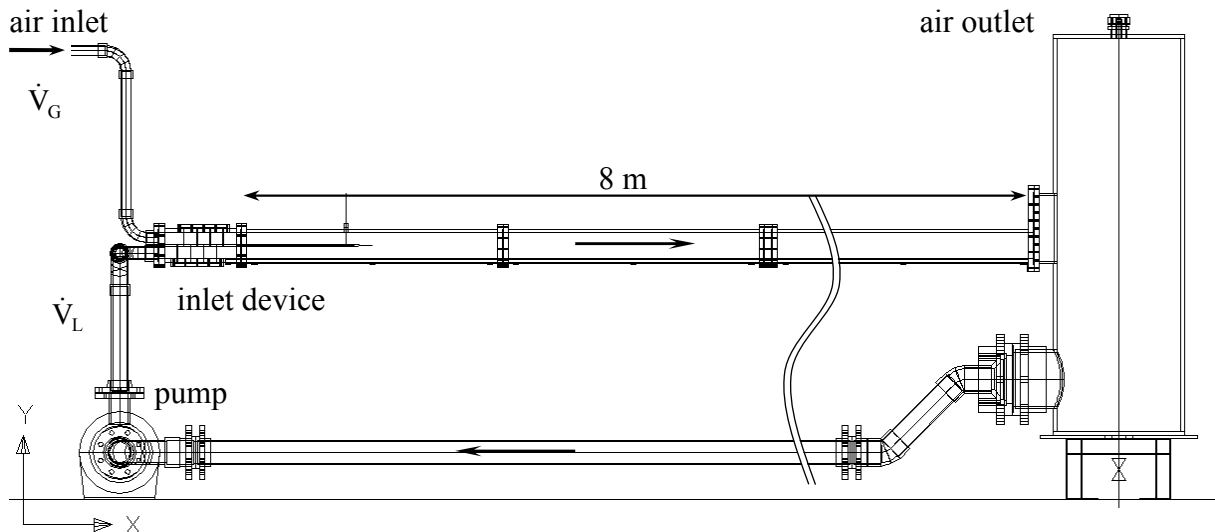


Fig. 1: Schematic view of the horizontal air/water channel (HAWAC)

A special inlet device (Fig. 2) was designed to provide defined boundary conditions at the channel inlet. Therefore, air and water have to be injected separately into the test-section: the air flows through the upper part and the water through the lower part of the inlet device. In order to provide homogenous velocity profiles at the test-section inlet, 4 wire cloth filters are mounted in each part of the inlet device. Air and water come in contact at the edge of a 500 mm long blade that divides both phases downstream of the filter segment. The free inlet cross-section for each phase can be controlled by inclining this blade up and down. In this way, the perturbation caused by the first contact between gas and liquid can be either minimised or, if required, a perturbation can be introduced (e.g. hydraulic jump). Both, filters and the inclinable blade, provide well-defined inlet boundary conditions for the CFD model and therefore offer very good validation possibilities.

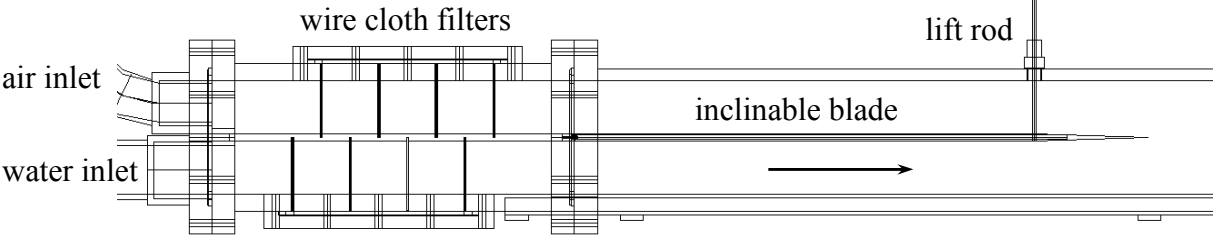


Fig. 2: The inlet device

The maximum superficial velocities achieved in the test-section are 2 m/s for the water and 8 m/s for the air. A flow pattern map (Fig. 3) was established on the basis of visual observations of the flow structure at different combinations of the gas and liquid superficial velocities. The observed flow patterns are: stratified flow, wavy flow, elongated bubble flow and slug flow.

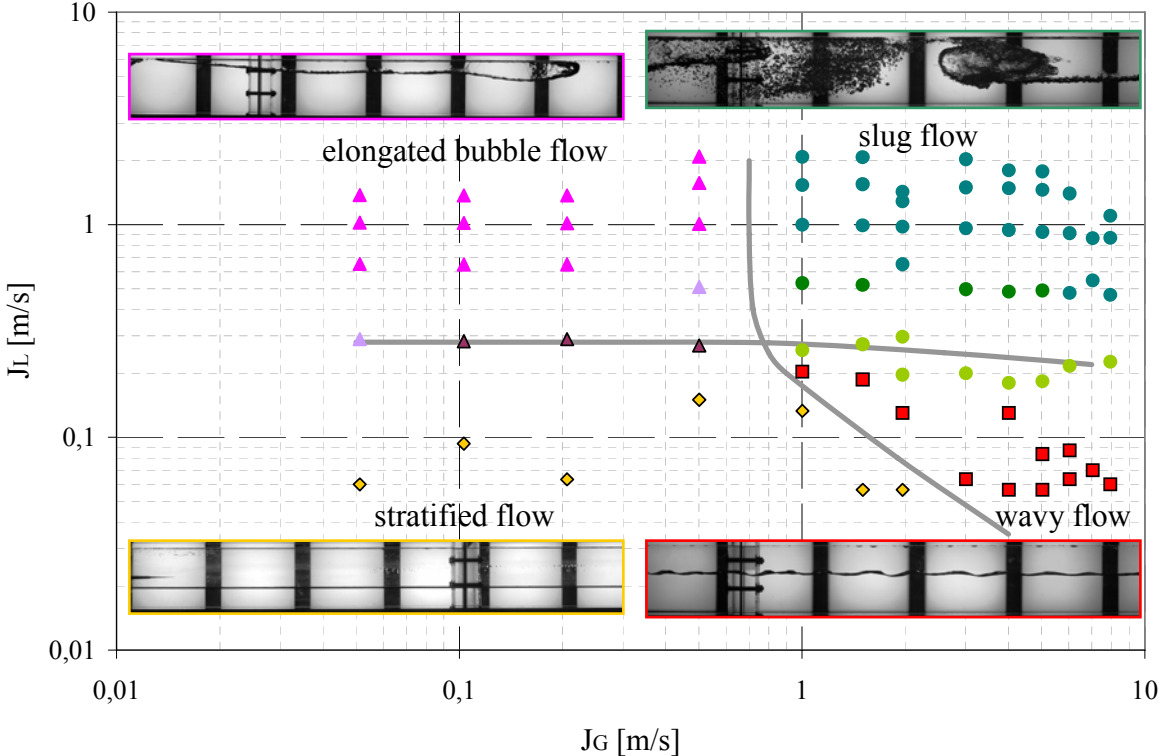


Fig. 3: Flow pattern map for the rectangular channel (inlet blade in horizontal position)

3. CFD model of the channel

The channel with rectangular cross-section was modelled using *ANSYS CFX* [1]. The model dimensions are 4000 x 100 x 30 mm³ (length x height x width), which corresponds to the first half of the test-section. The grid consists of 6 x 10⁵ hexahedral elements.

A slug flow experiment at a superficial water velocity of 1.0 m/s and a superficial air velocity of 5.0 m/s was chosen for the CFD calculations. In the experiment, the inlet blade was in horizontal position. Accordingly, the model inlet was divided into two parts: in the lower 50% of the inlet cross-section, water was injected and in the upper 50% air. An initial water level of $y_0 = 50$ mm was assumed for the entire model length.

In the simulation, both phases have been treated as isothermal and incompressible, at 25°C and at a reference pressure of 1 bar. A hydrostatic pressure was assumed for the liquid phase. Buoyancy effects between the two phases are taken into account by the directed gravity term. At the inlet, the turbulence properties were set using the “Medium intensity and Eddy viscosity ratio” option of the flow solver. This is equivalent to a turbulence intensity of 5% in both phases. The inner surface of the channel walls has been defined as hydraulically smooth with a non-slip boundary condition applied to both gaseous and liquid phases. The channel outlet was modelled with a pressure controlled outlet boundary condition.

As it was the goal of the CFD calculation to induce surface instabilities, which are later generating waves and slugs, the interfacial momentum exchange and also the turbulence parameters had to be modelled correctly. Without any special treatment of the free surface, the high velocity gradients at the free surface, especially in the gaseous phase, generate too high turbulence throughout the two-phase flow when using the differential eddy viscosity models like the k - ϵ or the k - ω model [1]. Therefore, certain damping of turbulence is necessary in the interfacial area because the mesh is too coarse to resolve the velocity gradient in the gas at the interface. On the gas side of the smooth free surface, this damping should be similar to that used near a solid wall. Moreover, on the liquid side the advanced model should take the anisotropy between the normal and the tangential Reynolds stresses into account. Yegorov [2] proposed a simple grid dependent symmetric damping procedure. This procedure provides for the solid wall-like damping of turbulence in both gas and liquid phases. It is based on the standard ω -equation, formulated by Wilcox [1] as follows:

$$\frac{\partial}{\partial t}(\rho \cdot \omega) + \nabla \cdot (\rho \cdot \mathbf{U} \cdot \omega) = \alpha \cdot \frac{\rho \cdot \omega}{k} \cdot \tau_t \cdot \dot{S} - \beta \cdot \rho \cdot \omega^2 + \nabla \cdot [(\mu + \sigma_\omega \cdot \mu_t) \cdot \nabla \omega] \quad (1)$$

where $\alpha = 0.52$ and $\beta = 0.075$ are the k - ω model closure coefficients of the generation and the destruction terms in the ω -equation, $\sigma_\omega = 0.5$ is the inverse of the turbulent Prandtl number for ω , τ_t is the Reynolds stress tensor, and \dot{S} is the strain-rate tensor.

In order to mimic the turbulence damping near the free surface, Yegorov [2] introduced the following source term in the right hand side of the gas and liquid phase ω -equations (1):

$$A \cdot \Delta y \cdot \beta \cdot \rho_i \left(B \cdot \frac{6 \cdot \mu_i}{\beta \cdot \rho_i \cdot \Delta n^2} \right)^2 \quad (2)$$

Here A is the interface area density, Δn is the typical grid cell size across the interface, ρ_i and μ_i are the density and viscosity of the phase i . The factor A activates this source term only at the free surface, where it cancels the standard ω -destruction term of the ω -equation ($-r_i \cdot \beta \cdot \rho_i \cdot \omega_i^2$) and enforces the required high value of ω_i and thus the turbulence damping.

The parallel transient calculation of 5.0 s of simulation time on 4 processors lasts 4 days. A high-resolution discretization scheme was used. For time integration, the fully implicit second order backward Euler method was applied with a constant time step of $dt = 0.001$ s and a maximum of 15 coefficient loops. A convergence in terms of the RMS values of the residuals to be less than 10^{-4} could be assured most of the time.

4. Results

Optical measurements were performed with a high-speed video camera. In the following picture sequences (Fig. 5 and 6), a comparison is presented between CFD calculation and experiment: the calculated phase distribution is visualized and comparable camera frames are shown.

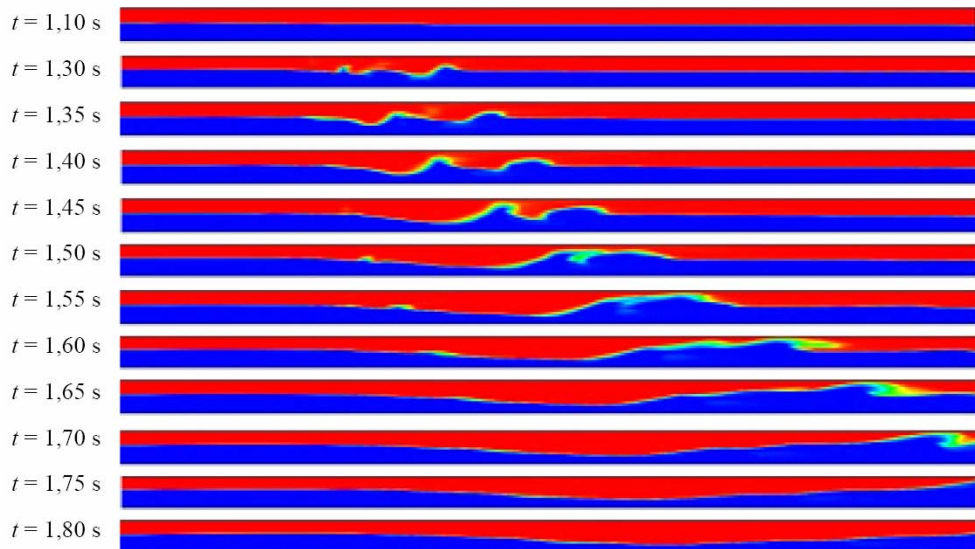


Fig. 5: Calculated sequence of void fraction at $J_L = 1.0$ m/s and $J_G = 5.0$ m/s (depicted part of the channel: 1.4 to 4 m after the inlet)

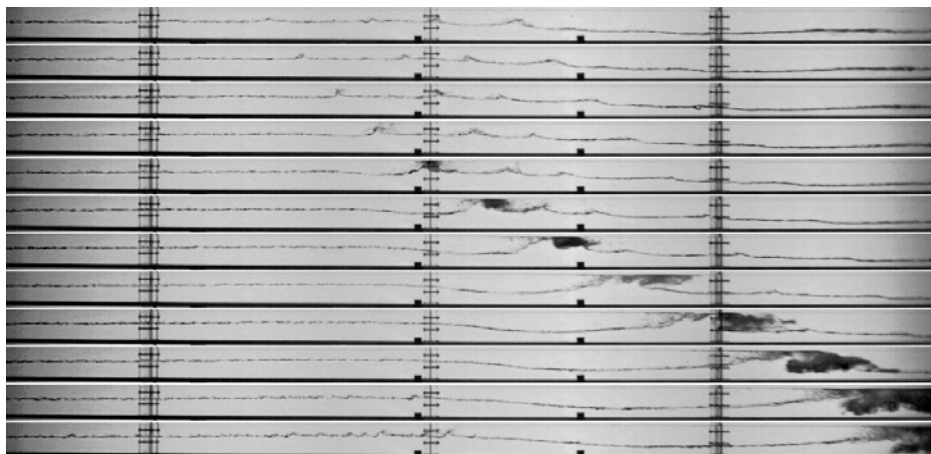


Fig. 6: Measured picture sequence at $J_L = 1.0$ m/s and $J_G = 5.0$ m/s with $\Delta t = 50$ ms (depicted part of the channel: 0 to 3.2 m after the inlet)

In both cases, a slug is generated. The sequences show that the qualitative behaviour of the creation and propagation of the slug is similar in the experiment and in the calculation. In the CFD calculation, the slug develops at approximately $t = 1.30$ s after the beginning of the simulation, induced by instabilities.

The single effects leading to slug flow that can be simulated are shown in details in Fig. 7. These phenomena are:

- Instabilities and small waves are randomly generated by the interfacial momentum transfer (Fig. 7-a). As a result bigger waves are generated.
- The waves can have different velocities and can merge (Fig. 7-b and c).
- Bigger waves roll over (Fig. 7-c) and can close the channel cross-section (Fig. 7-d).

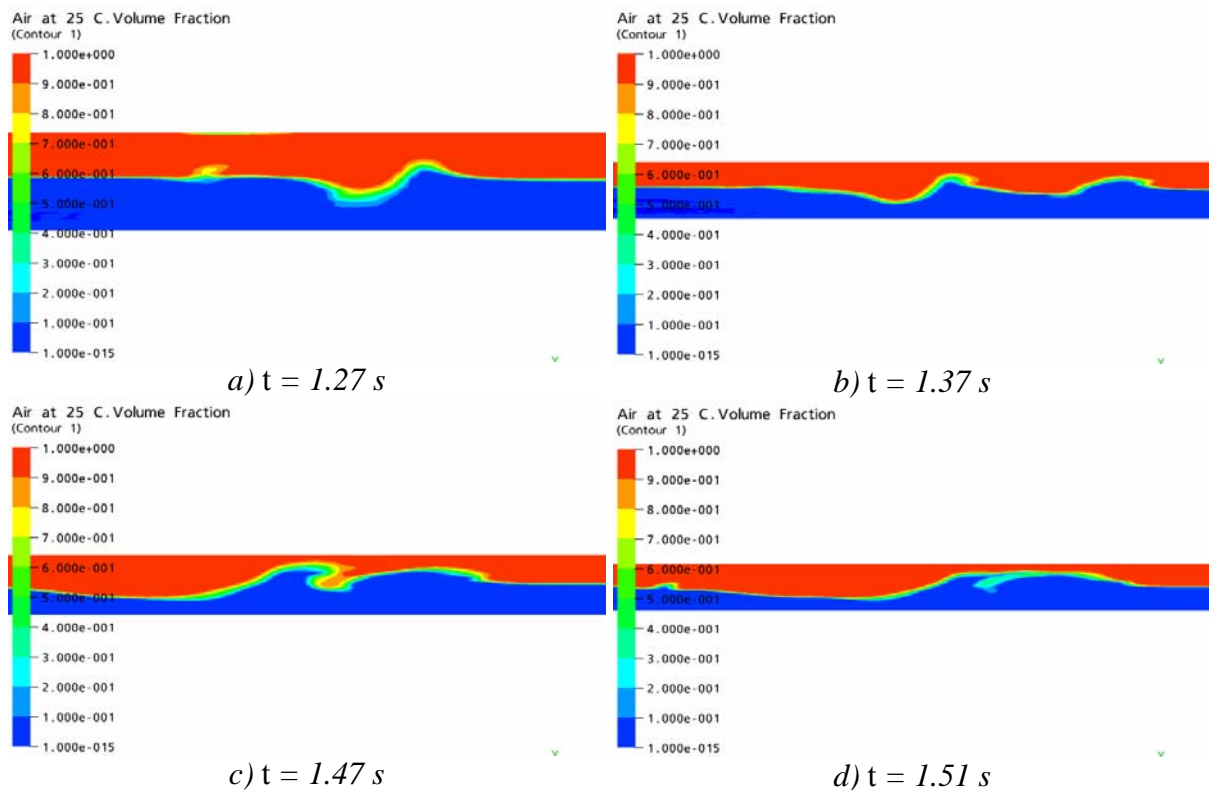


Fig. 7: Details of the slug generation calculated with ANSYS CFX at different simulation time

The needed entrance length for slug generation was defined as the length between the inlet and the location nearest the inlet where a wave closes nearly the entire cross-section. This was observed at about 1.5 m in the experiment and 2.5 m in the calculation.

In contrast to the measurement, the stratified flow after the slug calculated with ANSYS CFX is too smooth which defers the generation of the next slug. Since the slug cleared an important amount of water from the channel, the next slug appears after the channel is slowly filled up again by the transport of liquid from the inlet. This process takes approximately 1.5 s. In the experiment, small waves are generated immediately after the slug and create the next one within 0.3 to maximum 0.7 s. Sources of instabilities are not only the high air velocity but also the pressure surge created by the slugs, particularly when they leave the channel. This effect has not been properly simulated since just the half of the channel was modelled. Therefore, the slug frequency cannot be compared at this stage of the simulation.

5. Summary and conclusions

For the investigation of co-current two-phase flows, the horizontal air/water channel (HAWAC) was built at *Forschungszentrum Dresden-Rossendorf* (FZD). A special inlet device provides well defined as well as variable boundary conditions, which allow very good CFD-code validation possibilities. Optical measurements were performed with a high-speed video camera. The water level history can be extracted from the image sequences by an interface capture method.

A picture sequence recorded during slug flow was compared with the equivalent CFD simulation made with the code *ANSYS CFX*. The two-fluid model was applied with a special free surface treatment. Due to the interfacial momentum transfer, it was possible to generate slugs based on instabilities. The behaviour of slug generation and propagation at the experimental setup was qualitatively reproduced, while deviations in the slug frequency require further work. The creation of small instabilities due to pressure surge or increase of interfacial momentum transfer should be analysed in the future. Furthermore, pressure and velocity measurements should be performed in the HAWAC channel to allow quantitative comparisons.

Due to the success and promising future research activities, the HAWAC was chosen as an OECD Benchmark test facility and as a reference test facility for the German CFD network program.

References

- [1] ANSYS Inc., 2006, ANSYS CFX-10.0 User Manual
- [2] Yegorov, Y. 2004. Contact condensation in stratified steam-water flow, EVOL-ECORA – D 07.

Acknowledgements

This work is carried out in the frame of a current research project funded by the German Federal Ministry of Economics and Labour, project number 150 1265.

CFD SIMULATION OF THE TWO PHASE FLOW AROUND AN OBSTACLE APPLYING AN IMHOMOGENEOUS MULTIPLE BUBBLE SIZE CLASS APPROACH

Eckhard Krepper, Dirk Lucas, Horst-Michael Prasser¹, Matthias Beyer,
and Thomas Frank²

1. Introduction

In recent years, numerous experiments in straight vertical pipes were performed at the FZD TOPFLOW facility for the development of closure relations for CFD codes describing the forces acting on bubbles of different size. In the current TOPFLOW experiments, the large test section with a nominal diameter of DN200 was used to study the flow field around an asymmetric obstacle. This is an ideal test case for CFD code validation, since the obstacle creates a pronounced three-dimensional two-phase flow field. Curved stream lines, which form significant angles with the gravity vector, a recirculation zone in the wake and a flow separation at the edge of the obstacle are common in industrial components and installations.

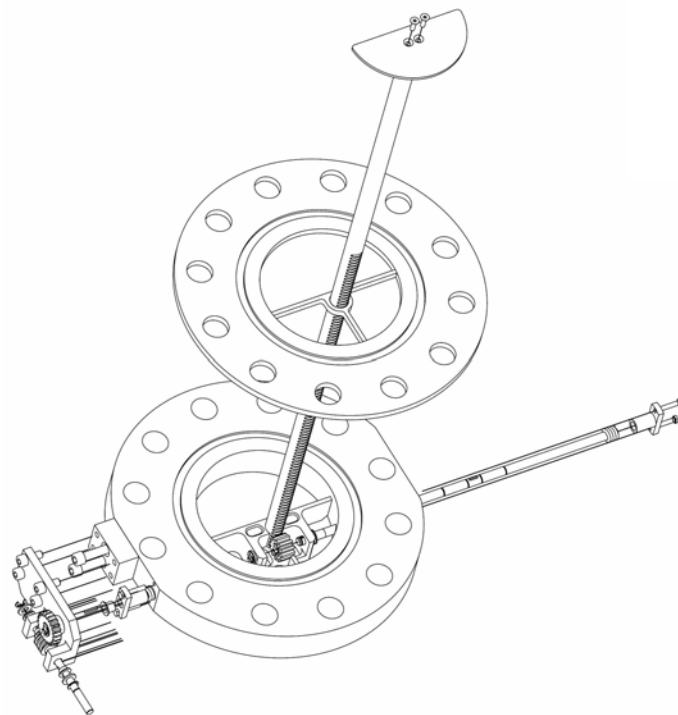


Fig. 1: Sketch of the movable obstacle with driving mechanism - a half-moon shaped horizontal plate mounted on top of a toothed rod

Experiments were performed with an air-water flow at ambient conditions as well as with a steam-water mixture at a saturation pressure of 6.5 MPa. The measurements were carried out in the vertical test section of TOPFLOW using a DN200 wire-mesh sensor. The wire-mesh sensors supply detailed data on the instantaneous flow structure with a high resolution in space and time. In particular, they allow visualizing the structure of the gas liquid interface.

¹ ETH Zürich, Department of Mechanical and Process Engineering

² ANSYS Germany, Staudenfeldweg 12, 83624 Otterfing

Pretest calculations using CFX-10 applying a monodispersed bubble size approach were performed for the conditions of test run 074 ($J_L = 1.017$ m/s, $J_G = 0.0368$ m/s) (see Frank, 2006, Prasser et al. 2005a, Prasser et al. 2005b). In the calculation, a fluid domain was modeled 1.5 m upstream and downstream the obstacle. Half of the tube including a symmetry xz-plane was simulated.

In recent years in close cooperation with ANSYS/CFX a population balance model was developed to simulate flow situations with higher gas volume fraction. Several dispersed gaseous phases are modeled having a distinct velocity field. Bubble fragmentation and coalescence are simulated by decades of gaseous sub-size mass fractions. Preliminary investigations have shown that it is necessary for an adequate resolution of the size spectrum. These sub-size mass fractions are assigned to few dispersed gaseous phases. This approach called “inhomogeneous multiple bubble size group (MUSIG) approach” enables the simulation of bubble size dependent bubble forces. In the present report this model approach is applied to air/water obstacle experiments run 096 ($J_L = 1.017$ m/s, $J_G = 0.0898$ m/s) and run 097 ($J_L = 1.611$ m/s, $J_G = 0.0898$ m/s).

2. The main observed phenomena

In the presented calculations for run 096 respective run 097 25 respective 20 sub-size gas fractions representing equidistant bubble sizes up to 25 mm respective 20 mm were simulated assigned to 2 dispersed gaseous phases. The first 6 fractions were assigned to the first and the remaining fractions to the second gaseous phase. The bubble size distribution measured at the largest upstream position was set as a boundary condition for the calculation.

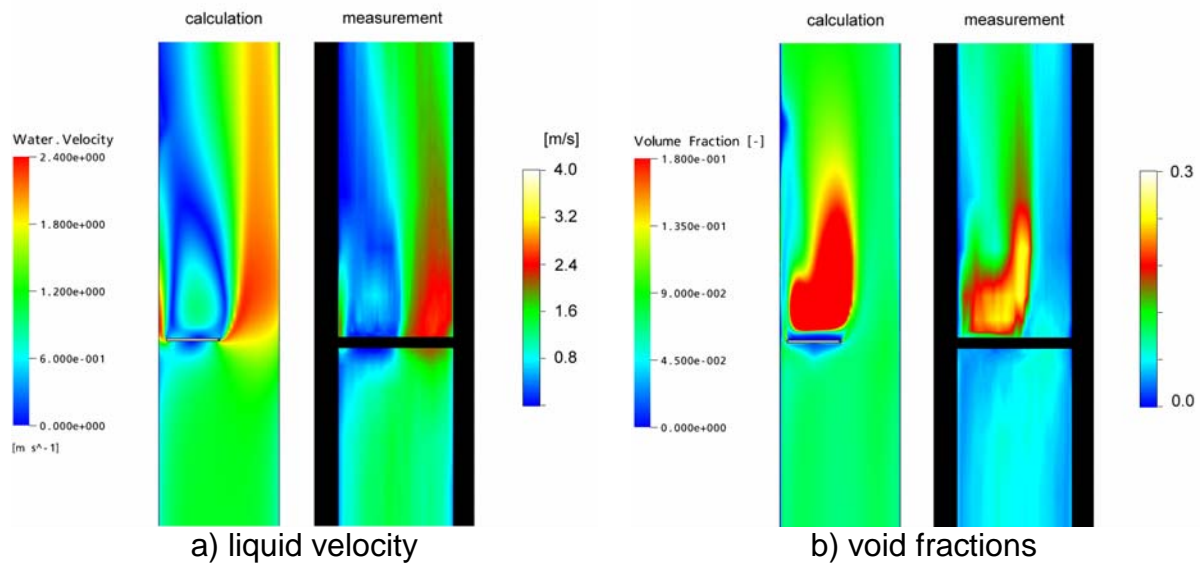


Fig. 2: Comparison of time averaged calculated(left) and measured(right) values up- and downstream of the obstacle in the air-water test run 096, $J_L = 1.017$ m/s, $J_G = 0.0898$ m/s

The ANSYS CFX simulation results have been compared to three-dimensional wire-mesh sensor data in Fig 2. The water velocity and the total gaseous void fraction are presented. Like for the pretest calculations also here for the test with higher gas fractions all qualitative details of the structure of the two-phase flow field around the obstacle could be reproduced. In this chapter the general phenomena are discussed first.

Shortly behind the obstacle a strong vortex of the liquid combined with the accumulation of gas is found. The measured and calculated shape and extension of the recirculation area agree very well. Upstream the obstacle a stagnation point with lower gas content is seen in experiment and calculation. Details, like the velocity and void fraction maxima above the gap between the circular edge of the obstacle and the inner wall of the pipe are also found in a good agreement between experiment and calculation. In the undisturbed cross sectional part of the tube a strong jet is established.

3. Phenomena in the wake of the obstacle

More detailed understanding of the flow situation can be gained, comparing the results of the inhomogeneous MUSIG model. According to the applied bubble fragmentation model of Luo and Svendsen (1996), bubble fragmentation can be expected in regions showing high turbulence eddy dissipation. Fig. 3 presents maximum values of the turbulence eddy dissipation at the edges of the obstacle.

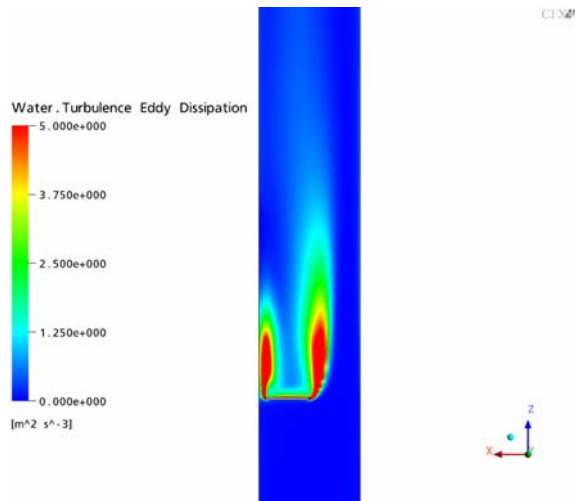


Fig. 3: Calculated turbulence eddy dissipation (run 096)

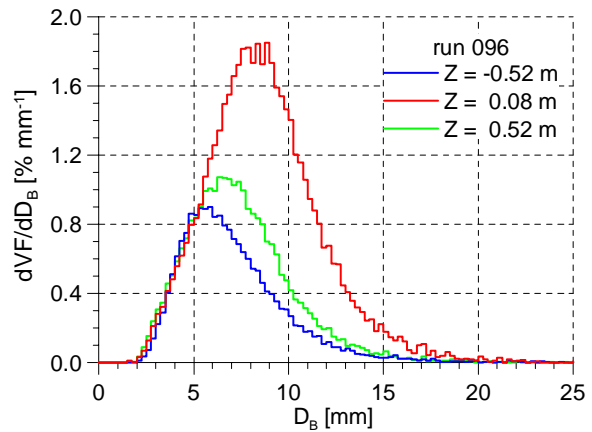


Fig. 4: Measured bubble size distribution for run 096

At the same time the applied bubble coalescence model of Prince and Blanch (1990) indicates strong importance of coalescence in regions of bubble accumulation i.e. in the wake behind the obstacle (see Fig. 2b). Both bubble coalescence (see gas accumulation shown in Fig. 2) and bubble breakup (see distribution of turbulence dissipation Fig. 3) partially compensating each other are expected shortly behind the obstacle.

Fig. 4 shows measured cross sectional averaged bubble size distributions upstream ($z = -0.52$ m), shortly behind ($z = 0.08$ m) and downstream the obstacle ($z = 0.52$ m). In the bubble accumulation zone at $z = 0.08$ m the cross sectional average shows a shift towards larger bubbles. The calculated bubble size distributions (see Fig. 5 for the run 096 and Fig. 6 for run 097) however show a shift of the mean bubble diameter towards smaller bubbles shortly behind the obstacle. In the calculations the bubble breakup is overestimated. This disagreement was found not solvable by simply changing of breakup or coalescence coefficients, which were set here $F_B = F_C = 0.05$. Similar deviations would arise at other locations of the flow domain.

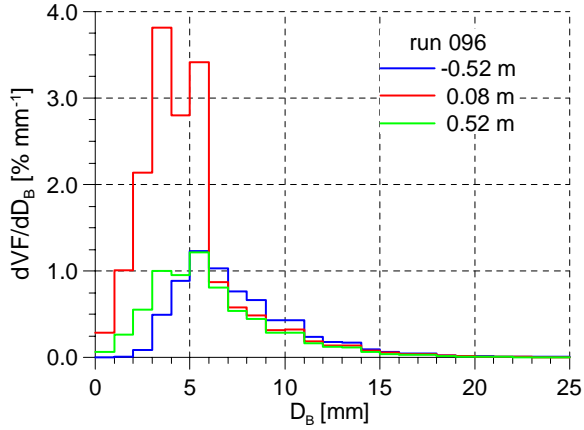


Fig. 5: Calculated bubble size distributions for run 096 ($J_L = 1.017$ m/s, $J_G = 0.0898$ m/s)

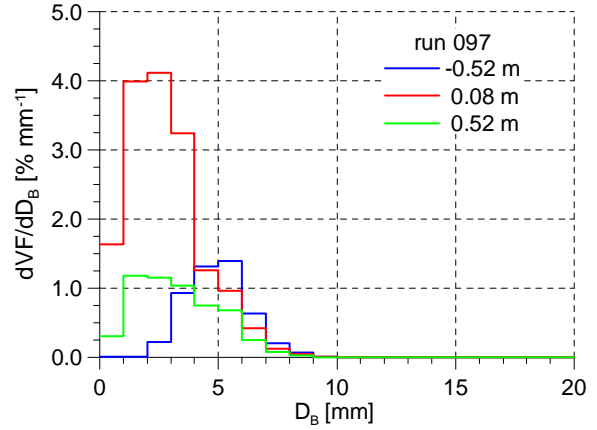


Fig. 6: Calculated bubble size distributions for run 097 ($J_L = 1.611$ m/s, $J_G = 0.0898$ m/s)

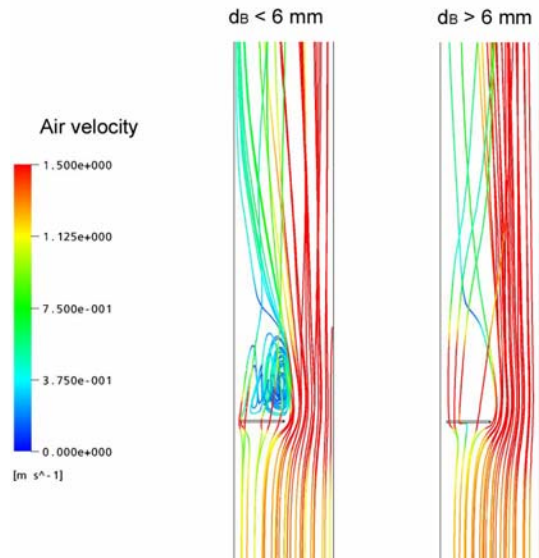


Fig. 7: Streamlines for small (left) and large (right) bubbles (run 096)

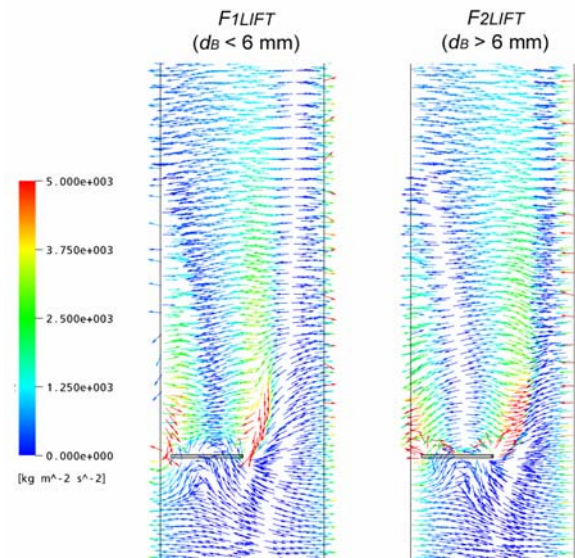


Fig. 8: Bubble lift force vectors for the different gas velocity groups (run 096)

On the one hand the liquid velocity flow field generates a lift force field which transports the small bubbles into the region behind the obstacle (see Fig. 7 for the bubble streamlines and Fig. 8 for the lift force arrows). On the other hand, the air accumulation in this region leads to bubble coalescence and the generation of large bubbles. This phenomenon is underestimated in the calculations. Fig. 9 shows very well that small bubbles are transported behind the obstacle. In the experiments larger bubbles are created by coalescence in this region. In the calculations however, bubble coalescence is exceeded in this region by bubble fragmentation. Caused by the lift force large bubbles are redirected into the downstream jet (see Fig. 9). The streamline representation (see Fig. 7) clearly shows this phenomenon for large bubbles already present in the upstream flow.

4. Phenomena in the jet

In the cross sectional area beside the obstacle a strong jet is established creating strong shear flow. The resulting phenomena are more pronounced with increasing water velocity. Therefore, run 097 is considered, where the liquid velocity was increased to $J_L = 1.611$ m/s. Fig. 10 presents measured and calculated cross sectional gas fraction distributions for this run.

In the most downstream cross section of the measurements an almost gas bubble free region is found. This effect is seen in almost all air/water measurements but not in the steam/water tests. The streamline representation of the calculations however (e.g. Fig. 7 for run 096), indicate large bubbles being directed into the jet caused by the lift force.

This discrepancy between experiment and calculation can possibly be explained by the strong water velocity gradient near the jet. This strong shear flow induces bubble fragmentation which is not yet considered in the model of Luo and Svendsen (1996). In the tests, the big bubbles migrate towards the jet, but are fragmented at the relatively sharp boarder of this jet. Only a small fraction of the small bubbles created by this breakup process can enter the jet by action of the turbulent dispersion force.

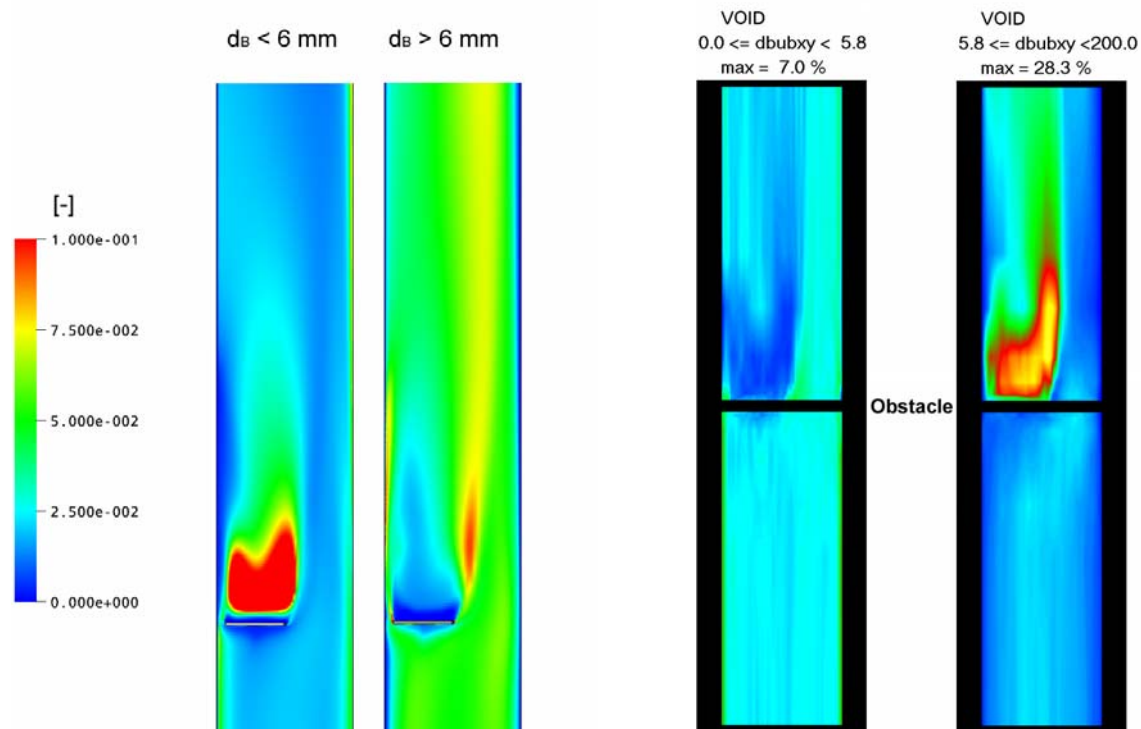


Fig. 9: Calculated (left) and measured (right) gas distributions up- and downstream of the obstacle resolved to bubble size classes (run 096 $J_L = 1.017$ m/s, $J_G = 0.0898$ m/s)

5. Summary

Applying the inhomogeneous MUSIG approach a more deep understanding of the flow structure is possible. The general structure of the flow around the obstacle could be well reproduced in the simulations. This test case demonstrates the complicated interplay between size dependent bubble migration and bubble coalescence and breakup effects for real flows. While the closure models on bubble forces, which are responsible for the simulation of bubble migration are in agreement with the experimental observations, clear deviations occur for bubble coalescence and fragmentation. The presently applied models describing bubble fragmentation and coalescence could be proved as weak points by Lucas and Krepper (2007) in numerous CFD analyses of vertical upward two phase pipe flow. Further work on this topic is under way.

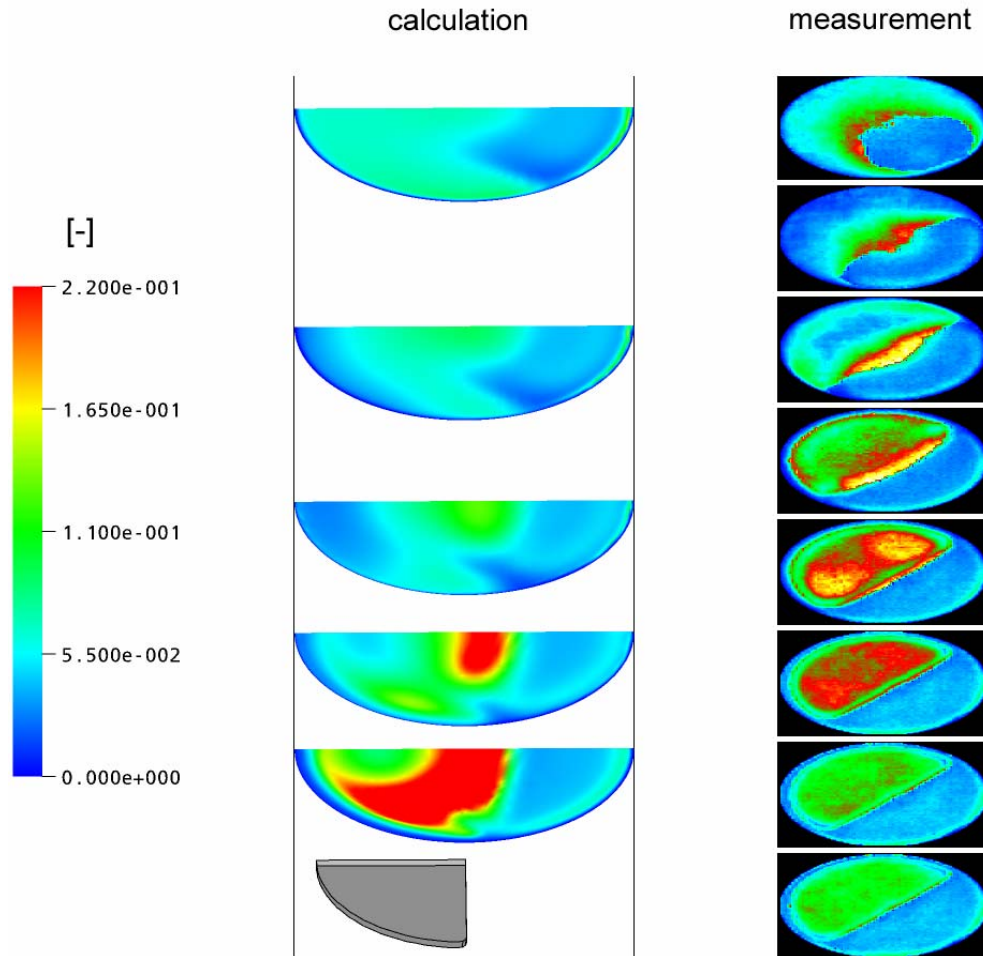


Fig. 10: Calculated (left) and measured (right) gas cross fractional distributions downstream the obstacle (run 097 $J_L = 1.611$ m/s, $J_G = 0.0898$ m/s)
 Calculations (obstacle shown), distances at $z = 0.08$ m, 0.16 m, 0.25 m, 0.37 m and 0.52 m
 Measurements (obstacle in the upper left area) distances at $z = 0.01$ m, 0.015 m, 0.02 m, 0.04 m, 0.08 m, 0.16 m, 0.25 m and 0.52 m

References

- [1] Frank, Th. (2006), Entwicklung von CFD Software zur Simulation mehrdimensionaler Strömungen im Reaktorkühlsystem, Abschlußbericht zum Vorhaben 150 1271, ANSYS/TR-06-01, 29.01.2006
- [2] Lucas, D., Krepper, E. (2007), CFD models for polydispersed bubbly flows, FZD-report (in print)
- [3] Luo, H. and Svendsen, H.F. (1996), Theoretical model for drop and bubble break-up in turbulent flows, *AICheJ*, 42, 5, pp. 1225-1233
- [4] Prasser, H.-M., Th. Frank, M. Beyer, H. Carl, S. Al-Issa, H. Pietruske, and P. Schütz (2005a), Gas-liquid flow around an obstacle in a vertical pipe - experiment and computational fluid dynamics simulation, Forschungszentrum Rossendorf Institute of Safety Research, Annual Report 2005.
- [5] Prasser, H.-M., Frank, T., Beyer, M., Carl, H., Pietruske, H., Schütz, P. (2005b), Gas-liquid flow around an obstacle in a vertical pipe experiments and CFD simulation, Annual Meeting on Nuclear Technology, Nuremberg

- [6] Prince, M.J. and Blanch, H.W. (1990), Bubble coalescence and break-up in air-sparged bubble columns, *AIChEJ*, 36, No 10, pp. 1485-1499

Acknowledgements

The work is carried out as a part of current research projects funded by the German Federal Ministry of Economics and Labour, project numbers 150 1265 and 150 1271. The authors express their gratitude to the technical TOPFLOW team.

CFX SIMULATIONS OF ROCOM SLUG MIXING EXPERIMENTS

Fabio Moretti¹, Daniele Melideo¹, Francesco D'Auria¹,
Thomas Höhne, and Sören Kliem

1. Introduction

In the safety analysis of nuclear reactors, a number of scenarios have to be addressed in which a safety-relevant role is played by the space and time distribution of primary coolant physical and/or thermodynamic properties, such as temperature, density, concentration of additives etc. [1]. For example, transients have to be analyzed which are featured by a perturbation of the coolant properties at the reactor core inlet, since such a perturbation can introduce a positive reactivity and determine a rapid power excursion, potentially leading to core damage. Those transients include the so-called boron dilution scenarios in Pressurized Water Reactors (PWR), leading to a reduction in the boron concentration at the core inlet, and Main Steam Line Break (MSLB) accidents in PWRs, leading to an overcooling in the loop, and thus to relatively cold water reaching the core inlet.

Another typical problem related to the distribution of coolant properties, is whether an Emergency Core Cooling (ECC) injection following a Small Break Loss-of-Coolant Accident (SB-LOCA) may lead or not to a Pressurized Thermal Shock (PTS) scenario, due to the relatively cold injected water being not sufficiently mixed with the water already present in the cold legs.

The ANSYS CFX-10.0 CFD software has been used for simulating a number of experiments conducted on the German ROCOM test facility at Forschungszentrum Dresden-Rossendorf (FZD). One experiment in particular is addressed here, which reproduced the injection of a de-borated water slug (simulated by a tracer) into the RPV of a PWR with all circulation pumps at steady-state operation.

The results of the simulations (in terms of tracer space and time distribution) were compared against the experimental data kindly made available by FZD to DIMNP (Department of Mechanics, Nuclear and Production Engineering, University of Pisa, Italy) within a Cooperation Agreement, in order to evaluate the capabilities of the code in predicting the flow phenomena (in particular the turbulent mixing) affecting the addressed scenarios.

2. The ROCOM Test Facility

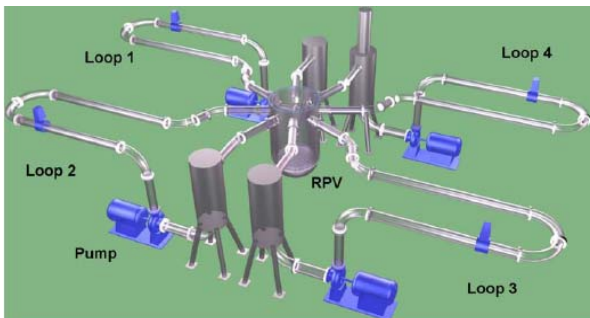


Fig. 1: Sketch of ROCOM facility layout

The ROCOM (Rossendorf Coolant Mixing Model) test facility is a 1/5 scaled model of the primary circuit of a Konvoi-type PWR reactor. It was built by FZD with the purpose of investigating the coolant mixing phenomena occurring in the reactor pressure vessel (RPV) of a PWR, and to provide experimental data for CFD code validation. A sketch of the facility layout is shown in Figure 1. Descriptions of the facility and of

¹ University of Pisa, Italy

its equipment can be found in [2], [3] and [4].

The local tracer concentration is derived from measurements of the electrical conductivity of the fluid (after obtaining proper calibration curves). The conductivity is measured by the so-called wire mesh sensors designed by the FZD experts.

When a ROCOM experiment is conducted to reproduce a boron dilution scenario, the injection of salted water is used to simulate the perturbed coolant (i.e. the coolant with low or no boron concentration), while the clear (i.e. non salted) water already present in the loops simulates the normally borated water in the real reactor. The measured values are normalized with respect to the values of conductivity that characterize the “clear water” and the “salted water”, by defining a scalar quantity named the mixing scalar (MS in the following) and defined by Equation (1).

$$\theta_{x,y,z,t} = \frac{\sigma_{x,y,z,t} - \sigma_0}{\sigma_1 - \sigma_0} \cong \frac{C_{x,y,z,t} - C_0}{C_1 - C_0} \quad (1)$$

where σ and C indicate the conductivity and the boron concentration respectively, while the sub-scripts 0 and 1 correspond to the unaffected water and the water subjected to the perturbation.

3. The Simulated Experiment

The simulated experiment is a steady-state test, and is identified as ROCOM_STAT_02. It was conducted with the four pumps running at 25 % of nominal speed (i.e. 46.25 m³/h volume flow rate per loop), and injecting the tracer for 35 s. Figure 2 shows the time history of the cross-section averaged MS as measured at inlet nozzle sensor, along with the maximum and the minimum values.

The tracer concentration is thus not perfectly uniform over the nozzle cross section (despite the use of the mixing device), and maximum deviations are in the range +/- 15 %.

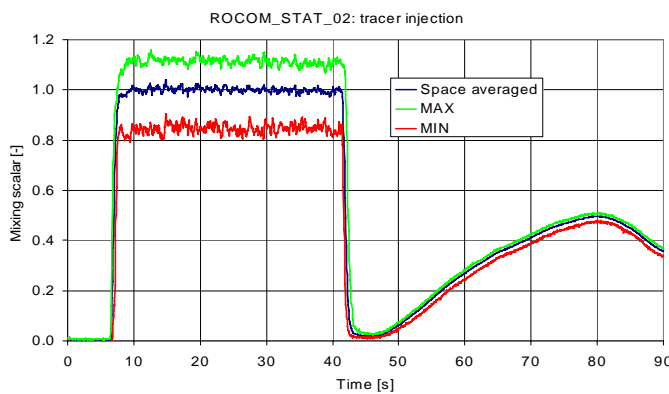


Fig. 2 ROCOM_STAT_02 experiment: time history of the inlet MS

The maximum reference conductivity value needed for the non-dimensionalisation (i.e. to calculate the MS) is derived from the space-averaged plateau-averaged value at inlet nozzle sensor (for the steady-state experiments), or from the maximum in time space-averaged value at inlet nozzle sensor (for the transient experiments). The available experimental data include the time-dependent MS at each measuring point of each sensor, with a time step of 0.05 s (i.e. 20 Hz frequency).

The Figure also shows a new increase in the measured MS after 45 s from the beginning of the experiment: this is because the injected tracer has gone through the whole circuit and enters the vessel for the second time.

Five realizations were performed for these experiments, and the time histories of the measured MS at each measuring position were averaged, so as to filter the effect of the turbulent fluctuations.

4. CFD simulations

The meshing tool used was ANSYS ICEM 10.0 [5]. Since the considered experiments and the related CFD calculations focus on the mixing phenomena occurring inside the reactor vessel, whereas no attention is paid to the flow phenomena in the other parts of the Reactor Coolant System (RCS) such as cold and hot legs, circulation pumps, etc.), the selected computational domain includes only the following parts of the ROCOM facility (Figure 3):

- downcomer (DC) (including 4 inlet nozzles)
- lower plenum (LP)
- core simulator (CS)
- upper plenum (UP)

The DC was modelled according to the real geometry of ROCOM without any simplification. In particular, the diameter variations both in the inlet nozzle and in the DC were taken into account, as well as the fillet radius in the connection between nozzle and DC, which was shown by preliminary CFD studies to sensibly affect the mass flow distribution in the DC. The LP sub-domain is defined by: the interface with DC part, the inner surface of the vessel bottom, the side and lower surfaces of the support plate, and the boundaries of the perforated drum. The drum was modelled along with its 410 holes (15 mm diameter), as shown in Figure 4.

The CS consists in 193 tubes connecting the LP to the UP. Its length has been extended downward so as to “replace” the complex geometry of the lower support plate with a simplified, tube-based geometry. This geometry simplification obviously affects the pressure losses that the flow encounters when crossing the plate. This was taken into account in the CFD simulations by defining additional pressure losses.

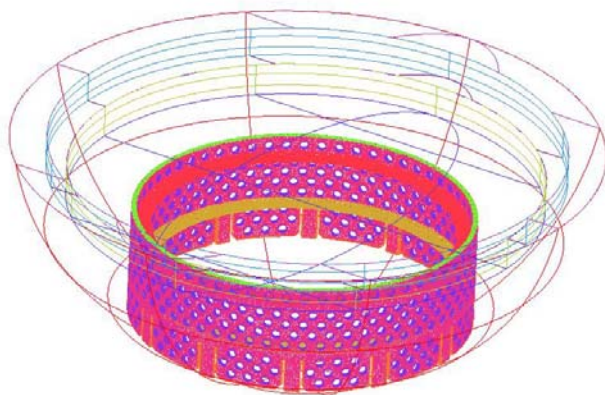


Fig. 4: LP solid model (perforated drum)

tetrahedra (Figure 6), because a hexa-meshing would be too difficult to achieve due to the geometric complexity. The LP of grid A07 has layers of prism elements to better comply with

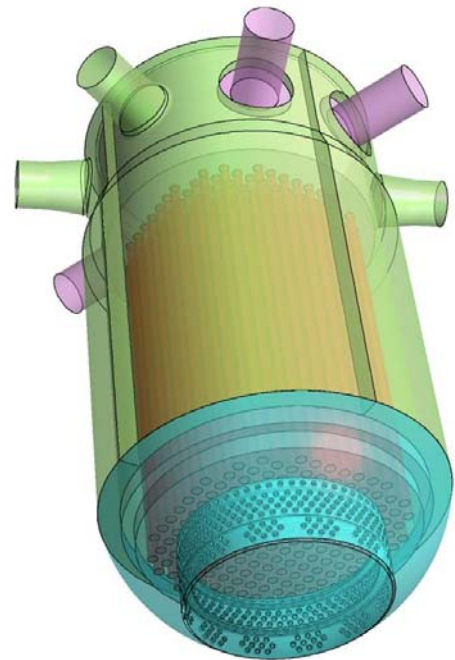


Fig. 3: ROCOM computational domain

The UP has a straightforward geometry, since it is simply made of five cylinders (the plenum itself and the four outlet nozzles) and does not have any internals.

Three of the several grids created were used for the simulations described in this paper. In all cases, around one half of the whole number of cells is present in the LP region, due to the presence of smaller scale geometric details. The DC grid was obtained using either hexa-meshing (A01, see Figure 5) or tetra-meshing (A04, A07).

In all cases the LP was meshed with

turbulent treatment at the walls. The CS region of grids A01 and A04 was obtained through axial extrusion of 2D meshes (triangles and quadrangles) of the tubes cross sections, thus generating prisms and hexahedra, and the UP was meshed with hexahedra. In grid A07 the CS is replaced by a “reduced core” meshed with prisms (extrusion of triangles), while a cylindrical outlet volume, meshed with tetrahedral, is present instead of the UP.

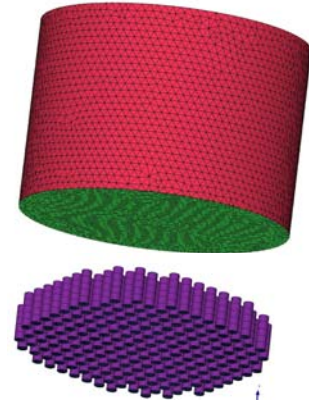
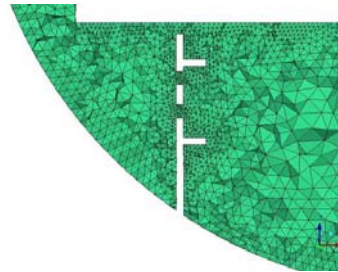
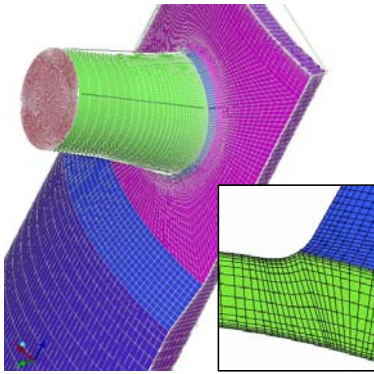


Fig. 5: DC mesh (A01 grid) Fig 6: LP mesh (A01, A04) Fig. 7: Reduced core (A07 grid)

The simulations were performed with the ANSYS CFX-10.0 package [6]. All the calculations performed share the following features (see also Table 1):

- Working fluid: incompressible water at 0.98 bar, 25°C
- Density: 997 kg/m³
- Dynamic viscosity: 8.899 x 10⁻⁴ kg m⁻¹ s⁻¹
- Constant inlet velocity
- Uniform inlet velocity profile (0.73 m/s, corresponding to 25 % of nominal volume flow rate)
- Pressure-controlled outlet boundary condition
- Uniform inlet turbulent intensity profile (either 5 % or 10 %)
- MS injected into loop #1 inlet nozzle (non-uniform extracted from sensor data)
- Upwind discretization scheme for advection terms
- k-ε or SST turbulence model

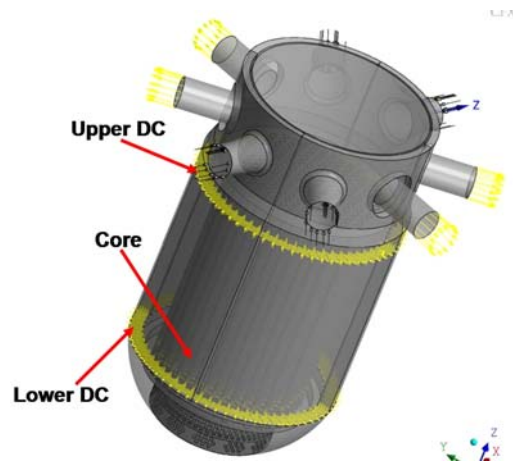


Fig. 8: Locations of monitor points

The purpose of the simulations was to calculate the local and instantaneous value of the MS, and then to compare it against the available experimental data. The following monitor points (also shown in Figure 8) were defined for the MS, according to the geometric location and configuration of the wire mesh sensors:

- 256 upper DC monitor points located in the upper part of the DC (4 radial and 64 azimuthal measuring positions)
- 256 lower DC monitor points located in the lower part of the DC (4 radial and 64 azimuthal measuring positions)

Table 1: Summary of CFX calculations for ROCOM_STAT_02 test

Run #	1	2	3	4	5
Run name	A01_Stat2_case1	A01_Stat2_case2	A01_Stat2_case3	A04_Stat2_case3	A07_Stat2_case1
Computational domain	whole RPV				with “reduced core”
Turbulence model	k-ε				SST
Restart from	-	A01_Stat2_case1	A01_Stat2_case2	A01_Stat2_case2 (with interpolation)	-
MS injection	Continuous				Slug
Inlet MS profile	Uniform	Non-uniform (with user function)			
Inlet turbulent intensity	5 %		10 %	5 %	
Equations solved	All	MS only	All		

5. Results

Since the addressed experiment involves symmetric and constant pumps operation, the resulting flow field in the RPV consists of four symmetric “flow sectors”, each one corresponding to one loop. The flow entering the RPV from the four inlet nozzles, first impinges against the barrel outer wall, so that complex local flow patterns develop in the inlet region. However the flow in the downcomer below the diffusion zone (diameter variation) is mainly directed downwards, as shown by the streamlines in Figure 9.

The downcomer flow is affected by turbulent mixing, which causes the MS field to diffuse in the transverse direction (i.e. azimuthally). This is shown by the experimental data represented in Figure 10 and Figure 11. In particular, the Figure 10 shows the comparison of MS azimuthal profile in the upper part of the downcomer: the agreement between the experiment and the calculations is good (max. 5 % difference of MS at local positions). The agreement between numerical predictions and experiment becomes poorer in the lower part of the downcomer, as evident from Figure 11. The MS field experiences a relatively strong diffusion in the azimuthal direction, which “smears” the profile, while the spatial gradients predicted by the simulations keep steeper. As a consequence, the predicted maximum values are higher than the experimental ones, and the MS perturbation does not affect the two adjacent sectors.

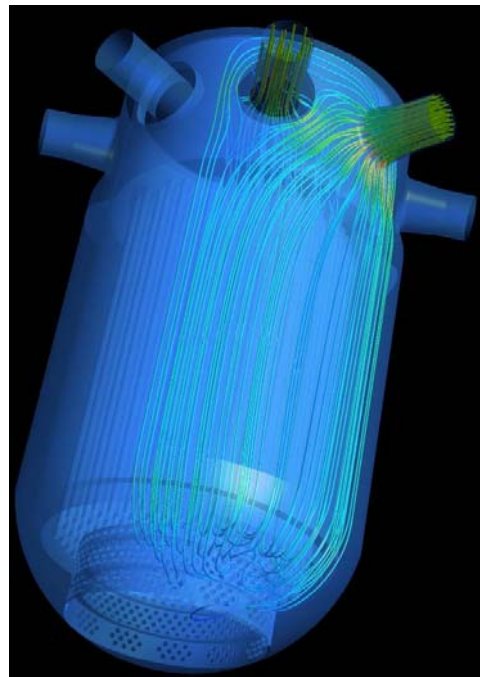


Fig. 9: CFD results: streamlines from loop #1

What stated above suggests that the code, despite the use of a first-order discretization scheme (i.e. “upwind”) for the advection terms, yet underestimates the turbulent diffusivity (in other words, the effectiveness of turbulent mixing). The best results are those yielded by calculation #4: this can be explained with the use of tetrahedral elements in the DC grid (instead of hexahedra), which introduce higher numerical diffusion and thus partly compensate for the above mentioned underestimation.

From these results about the mixing in the DC, one can expect that the predicted MS perturbation will affect a smaller number of fuel element positions than in the experiment, and that MS values in the most affected fuel element positions will be higher.

6. Summary and conclusions

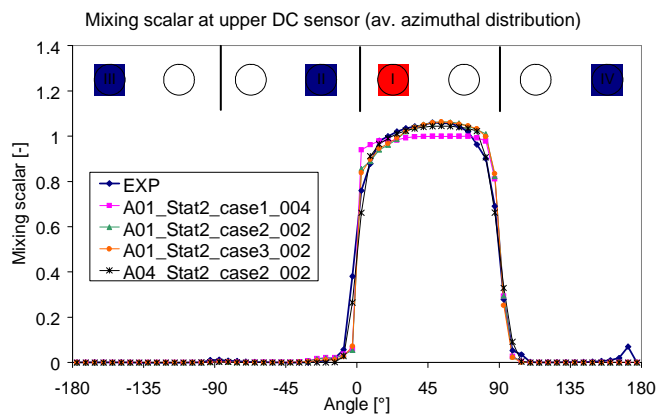


Fig. 10: Azimuthal profile of MS at the upper DC sensor

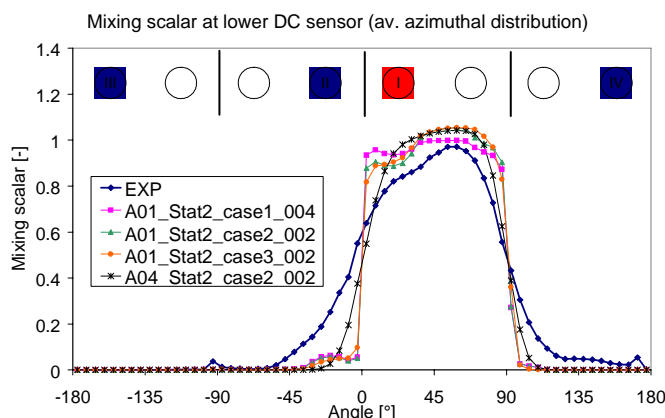


Fig. 11: Azimuthal profile of MS at the lower DC sensor

tends to predict steeper gradients of the concentration space profiles than in the experiment, that is the effectiveness of the turbulent mixing is generally under-predicted. This may be related to the limitations of 2-equation turbulence models in deal with the high anisotropy of the turbulent structures forming in the downcomer. This aspect was not further investigated.

Although higher accuracy in prediction of turbulent mixing would certainly be desirable for “best-estimate” purposes, the “conservativeness” of the results obtained should be put in evidence, since they predict a less mitigating effect played by the turbulence mixing in the assumed accidental scenarios.

References

- [1] Moretti, F., Del Nevo, A., D’Auria, F., 2006, Asymmetrical Boron Concentration / Temperature Events: Review of US Position and Approaches – Review of EU Framework Programmes Related to Computational Tools, DIMNP NT 575 (06), Pisa.

The CFD code CFX has been used, in the framework of CFD code validation activities ongoing at the University of Pisa, for the simulation of a slug-mixing experiment, conducted on the ROCOM test facility at Forschungszentrum Dresden-Rossendorf (FZD). Much effort was spent in obtaining several fine and high-quality computational grids, which could cope both with the relatively high geometric complexity of ROCOM vessel internals, and with computing power limitations as well. Several parallel simulations were set-up and run, based on different meshing solutions, numerical options and modelling assumptions. Then the numerical results, were compared against the experimental data, in terms of tracer concentration space and time profiles both in the downcomer and at the core inlet. The CFD simulations resulted to be able to correctly predict the formation of the perturbed region in the downcomer and in the lower plenum. Quantitatively, the code

- [2] Grunwald, G., Höhne, T., Kliem, S., Prasser, Richter, K.-H., H.-M., Rohde, U., Weiss, F.-P., 2002, Versuchsanlage ROCOM zur Untersuchung der Kühlmittelvermischung in Druckwasserreaktoren - Ergebnisse quasistationärer Vermischungsexperimente. FZR Report 348.
- [3] Höhne, T., Kliem, Prasser, H.-M., Rohde, U. , 2003, Experimental and numerical studies inside a reactor pressure vessel. 4th ASME/JSME Joint Fluids Engineering Conference, Hawaii, USA. CD-ROM.
- [4] Rohde, U. et al., 2004, Description of the slug mixing and buoyancy related experiments at the different test facilities, EU/FP5 FLOMIX-R Project, FLOMIX-R-D09, Germany.
- [5] ANSYS Inc., 2005a, ANSYS ICEM-CFD 10.0 User Manual, (embedded in the software package)
- [6] ANSYS Inc., 2005b, ANSYS CFX-10.0 User Manual, (embedded in the software package)

BUBBLE-DRIVEN LIQUID METAL FLOWS UNDER THE INFLUENCE OF A DC MAGNETIC FIELD

Chaojie Zhang, Sven Eckert, and Gunter Gerbeth

1. Introduction

Owing to buoyancy gas bubbles rise in a liquid metal bath and accelerate the initially quiescent liquid. In this manner a global recirculating motion of the melt is created. Such bubble plumes have found wide applications in both metallurgical and chemical engineering processes. The distribution of the gas phase and the flow field induced in the liquid phase are the key properties of interest. Magnetic fields can be used in practice to control both the flow pattern and the void distribution and, hence, the efficiency of the considered metallurgical process. Suitable combinations of external magnetic fields and gas bubble injections allow adjusting a favourable flow field with respect to optimization of the final product quality. The fluid dynamics of dispersed, compressible flows in general and the impact of an external magnetic field in particular are known to be outmost complex. A multitude of numerical and experimental investigations are already known concerning the fluid dynamics of bubble plumes. A comprehensive review about the flow in bubble columns has been given by Mudde [1,2]. Experimental investigations of bubble plumes have been done either in air-water systems (see, for instance, [3, 4]) or utilising appropriate metallic melts [5, 6].

In this paper we present measurements of the flow field for a bubble plume, which is affected by a horizontal DC magnetic field. The findings will be discussed in terms of the Hartmann number indicating the ratio between the electromagnetic and the viscous forces (with the material properties σ , ρ and ν denoting the electrical conductivity, the density and the kinematic viscosity, B is the magnetic field strength and R the radius of the fluid vessel)

$$Ha = BR \sqrt{\frac{\sigma}{\rho\nu}} \quad (1)$$

2. Experimental set-up

The experimental set-up for the measurements is shown in figure 1. A cylindrical container made from Perspex contains the eutectic alloy $\text{Ga}^{68}\text{In}^{20}\text{Sn}^{12}$ (melting point 10°C). The vessel with an inner diameter $2R$ of 90 mm was filled until a height H of 220 mm leading to an aspect ratio $2R/H$ of 0.41. Argon gas was injected through a single nozzle with an inner diameter of 1 mm located at the container bottom in the centre of the circular cross section. A mass flow controller (MKS 1359C) was utilised to adjust the gas flow rate in a range between 0.3 and 7 cm^3/s . Such low gas flow rates were selected to ensure the formation of a dispersed bubbly flow regime. This set-up was positioned inside a pair of water-cooled copper coils providing a horizontal, homogeneous magnetic field over the entire fluid volume. The maximum field strength of 0.28 T corresponds to a Hartmann number Ha of 484.

The DOP2000 velocimeter (Model 2032, Signal-Processing, Lausanne, Switzerland) alternatively equipped with a standard 4 MHz (TR0405LS) or 8 MHz transducer, respectively, was used for velocity measurements. The measuring principle of the Ultrasound Doppler Velocimetry (UDV) is based on the pulsed echo technique and described in detail by Takeda [7]. The ultrasonic transducer was installed outside on the cylinder wall either at the

bottom wall or the side wall for the measurement of the vertical and the radial velocity component, respectively. A reproducible positioning of the sensor was ensured using a mechanical traversing system. Velocity profiles were recorded with a sampling rate of 27.5 Hz. The size of the measuring volume is determined by several factors, such as the material properties of the liquid, the ultrasonic frequency, the burst length and the band width of the velocimeter. Taking into account the divergence of the beam with growing distance from the sensor, the lateral resolution typically varies between 3 and 8 mm along the measuring line, whereas an axial resolution of about 1.4 mm was achieved in the experiments considered here. The velocity resolution was about 1 mm/s.

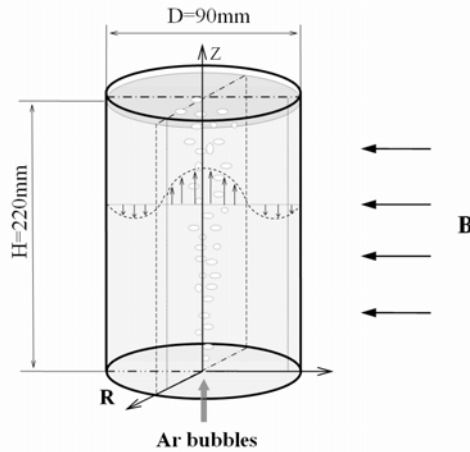


Fig. 1: Schematic drawing of the experimental configuration

The feasibility of velocity measurements by UDV in liquid metals has already been demonstrated by several authors [8-10]. Successful applications in two-phase flows have also been reported showing the capability to measure simultaneously the bubble and the liquid velocity [11, 12]. Multiple reflections of the ultrasonic beam between numerous gas bubbles occurring at higher gas flow rates cause artefacts in the signal. This fact usually complicates a precise discrimination between both phase velocities. Therefore, an iterative threshold method [13] was applied to obtain accurate values of the liquid velocity. This method was verified by accompanying LDV measurements in a transparent liquid.

3. Bubble plume in a DC magnetic field

The situation of a liquid metal bubble plume has been studied in detail by Zhang et al. [14]. A selection of results is presented here. Figure 2 displays time-averaged flow velocity patterns obtained at a relatively low gas flow rate of $0.33 \text{ cm}^3/\text{s}$ in two orthogonal half-planes (longitudinal sections) parallel and perpendicular to the field lines, further called as parallel and perpendicular plane, respectively. The flow field in each plane is visualised by the velocity vectors. The colour scale represents the amplitude of the vertical velocity component. The typical flow field for a bubble plume is shown in figure 2(a). In the central region of the fluid container the liquid metal is driven upwards by the rising gas bubbles. The corresponding downward motion appears in the regions close to the side walls. The application of a magnetic field changes the velocity field considerably which becomes anisotropic as illustrated in figure 2(b). Different flow patterns can be observed in both the parallel and perpendicular plane. The downward motion in the parallel plane is obstructed by the magnetic field, whereas an intensification of the circulation can be observed in the perpendicular plane. A distinct vortical flow structure appears at a Hartmann number of 273 (see figure 2(b)) which is damped in turn with further increase of the magnetic field strength

(figure 2(c)). Equivalent velocity measurements performed at higher gas flow rates revealed qualitatively analogue flow pattern. Generally, substantial modifications of the flow structure are noticed in case of an applied magnetic field. Considering the flow in the perpendicular plane, the recirculation is intensified in the lower region of the vessel. Moreover, the zones of recirculation are extended closer to the axis of the fluid container [14]. The fluid is set in an upwards motion in the overall plane parallel to the magnetic field. A similar phenomenon has already been discussed by Davidson [15]. An example of an axisymmetric jet imposed to an external magnetic field was shown to evolve in such a manner that the Joule dissipation will be minimized, which is achieved by a propagation of linear or angular momentum parallel to the magnetic field. The Joule dissipation is reduced if the cross section of the jet has been stretched along the field lines. This mechanism is responsible for the reorganization of the velocity field observed in our experiment.

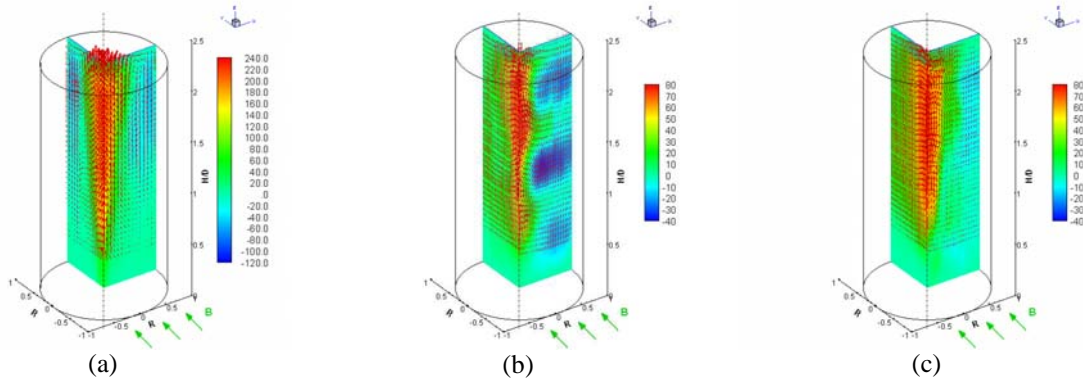


Fig. 2: Time averaged velocity structure at various Hartmann numbers: (a) $Ha = 0$, (b) $Ha = 273$, (c) $Ha = 484$

Velocity time series were recorded along a vertical line at a radial position of $r/R = 0.87$ at a gas flow rate of $0.83 \text{ cm}^3/\text{s}$. Figure 3 provides spatiotemporal plots of the vertical velocity component obtained for $Ha = 0$ and $Ha = 162$. In the case of an ordinary bubble plume (figure 3(a)) a continuously descending flow can be observed in a region from about 30–70 cm below the free surface. The imposition of the magnetic field results in distinct modifications of the flow structure. Drawing of the velocity in the perpendicular plane (figure 3(b)) reveals a zone of descending flow which is quasi-periodically moving downwards from the free surface. A similar flow pattern with an opposite sign of the velocity appears in the parallel plane (figure 3(c)). Cross correlation measurements (not shown here, see [14]) show that the cylinder half-volumes along the magnetic field direction are filled out with anisotropic, large-scale vortical flow structures oriented parallel to the magnetic field lines. The position of these vortices is changing in time. However, owing to the magnetic field direction and the geometrical confinement the motion is allowed only in vertical direction. Thus, a separated, reciprocal progression of vortices in both half-volumes is observed with a distinct periodicity. The corresponding, predominant frequencies occurring in the power spectra of the velocity time series increase with increasing gas flow rate.

Figure 4 presents the time-averaged velocity and the RMS values as a function of the Hartmann number obtained at the position $r/R = 0.87$ and $z/H = 0.5$ for a gas flow rate of $3.67 \text{ cm}^3/\text{s}$, respectively. While the absolute values of the time-averaged velocity grow almost continuously with increasing Ha , the RMS values show at first a considerable enhancement and then a decrease at higher field intensities. This is related to the occurrence of oscillating flow structures as shown in figure 3 which are especially pronounced at moderate Hartmann

numbers. The reduction of the RMS values at higher Ha particularly increases the magnitude of the mean velocity. This means that the kinetic energy contained in the oscillating, vortical structures is likely not dissipated by the Joule effect in its entirety, but rather transferred towards the mean flow to some extent.

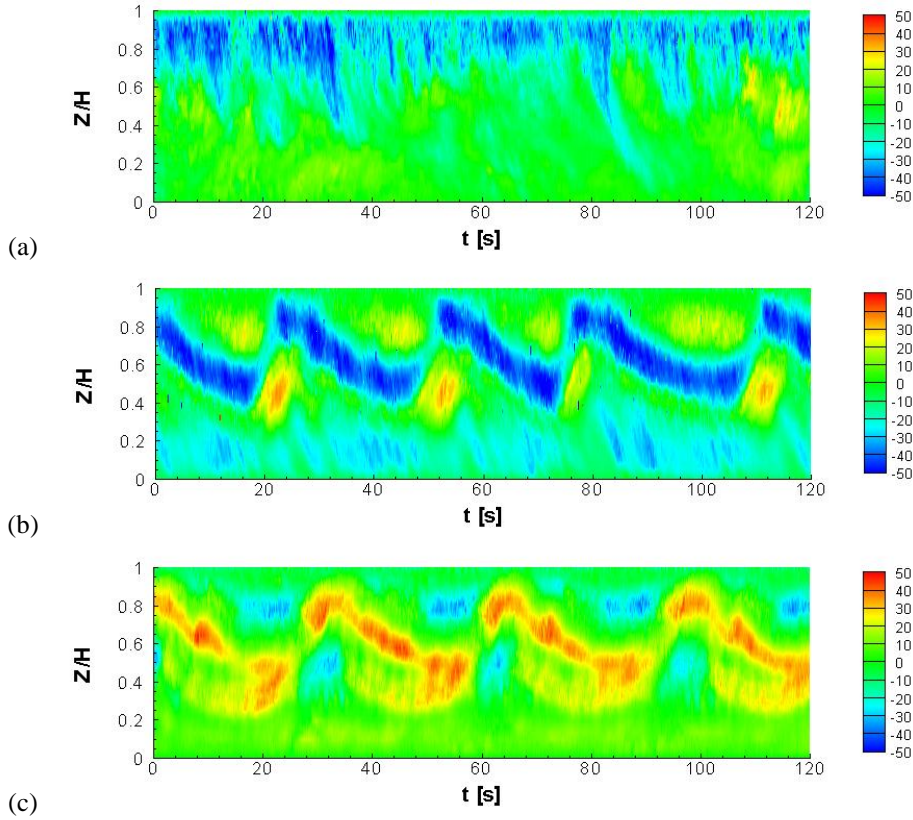


Fig. 3: Spatiotemporal distributions of the vertical velocity along a vertical line at a radial position $r/R = 0.87$ and a gas flow rate of $Q_g = 0.83 \text{ cm}^3/\text{s}$, (a) $Ha = 0$, (b) $Ha = 162$ perpendicular plane, (c) $Ha = 162$ parallel plane

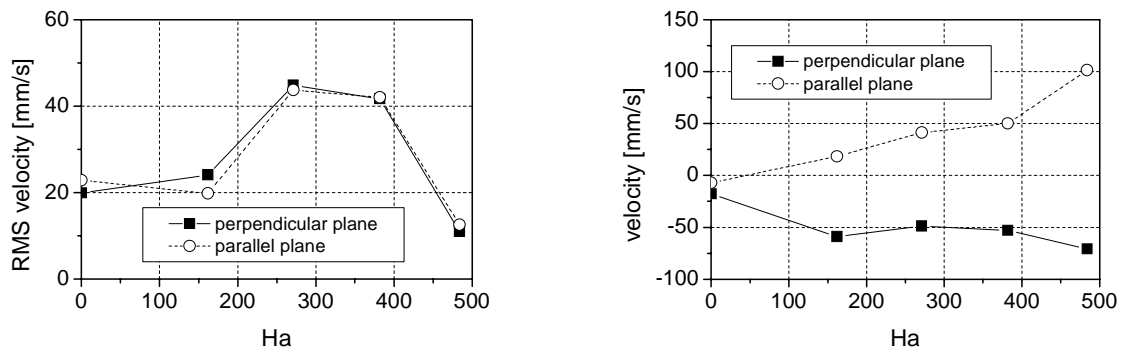


Fig. 4: RMS values and time-averaged velocities as a function of the Hartmann number ($Q_g = 3.67 \text{ cm}^3/\text{s}$)

4. Conclusions

Our velocity measurements demonstrated that the use of DC magnetic fields applied to a bubble plume in a liquid metal can lead to completely new flow structures in the liquid phase. This fact offers new perspectives regarding the control of the heat and mass transfer in liquid

metal bubble plumes. The feature, that a static magnetic field may give rise to non-steady, non-isotropic and large-scale flow structures is rather unknown until now and therefore not sufficiently considered for electromagnetic processing of materials. However, this effect could attain a key importance for the continuous casting, where the employment of a DC magnetic field as a electromagnetic brake is suggested to stabilise the flow. Here, a two-phase flow is present, because argon bubbles are injected to avoid clogging of the submerged entry nozzle. The potentially arising oscillations within a range of moderate magnetic fields need to be taken into account for future activities using an electromagnetic brake for flow control.

References

- [1] R.F. Mudde (2005), Gravity-driven bubbly flows, *Ann. Rev. Fluid Mech.*, 27, 393
- [2] D. Lucas, E. Krepper, H.-M. Prasser, A. Manera (2006), Investigations on the stability of the flow characteristics in a bubble column, *Chem. Eng. Techn.* 29, 1066
- [3] J. Rensen, V. Roig (2001), Experimental study of the unsteady structure of a confined bubble plume, *Int. J. Multiphase Flow*, 27, 1431
- [4] A.M. Leitch, W.D. Baines (1989), Liquid volume flux in a weak bubble plume, *J. Fluid Mech.*, 205, 77
- [5] M. Iguchi, Y. Demoto, N. Sugarwara, Z. Morita (1992), Bubble behaviour in Hg-air vertical bubbling jets in cylindrical vessels, *ISIJ Int.*, 32, 998
- [6] M. Iguchi, Y. Tsuji, T. Mizuno, T. Mashiko, M. Sano, H. Kawabata (1994), Continuous measurements of bubble characteristics in molten iron bath with Ar gas injection, *ISIJ Int.*, 34, 980
- [7] Y. Takeda (1991), Development of an ultrasound velocity profile monitor, *Nucl. Eng. Design* 126, 277
- [8] D. Brito, H.-C. Nataf, P. Cardin, J. Aubert, J.P. Masson (2001), Ultrasonic Doppler velocimetry in liquid gallium, *Exp. Fluids*, 31, 653
- [9] A. Cramer, C. Zhang, S. Eckert (2004), Local structures in liquid metals measured by ultrasonic Doppler velocimetry, *Flow Meas. Instrum.*, 15, 145
- [10] S. Eckert, G. Gerbeth (2002), Velocity measurements in liquid sodium by means of ultrasound Doppler velocimetry, *Exp. Fluids*, 32, 542
- [11] T. Wang, J. Wang, F. Ren, Y. Jin (2003), Application of ultrasound Doppler velocimetry in multiphase flows, *Chem. Eng. J.*, 92, 111
- [12] C. Zhang, S. Eckert, G. Gerbeth (2005), Experimental study of single bubble motion in a liquid metal column exposed to a DC magnetic field, *Int. J. Multiphase Flow*, 31, 824
- [13] C. Zhang, S. Eckert, G. Gerbeth (2004), Gas and liquid velocity measurements in bubble chain driven two-phase flow by means of UDV and LDA, *Proc. 5th Int. Conf. Multiphase Flow, Yokohama, ICMF04-260*
- [14] C. Zhang, S. Eckert, G. Gerbeth (2006), The flow structure of a bubble-driven liquid metal jet in a horizontal magnetic field, *J. Fluid Mech.*, 575, 57
- [15] P. Davidson (1995), Magnetic damping of jets and vortices, *J. Fluid Mech.*, 299, 153

Acknowledgement

This work was financially supported by Deutsche Forschungsgemeinschaft in form of the collaborative research centre SFB 609 "Electromagnetic Flow Control in Metallurgy, Crystal Growth and Electrochemistry".

OBSERVATION OF MAGNETOROTATIONAL INSTABILITY IN A LIQUID METAL TAYLOR-COUPETTE EXPERIMENT

Frank Stefani, Thomas Gundrum, Gunter Gerbeth, Rainer Hollerbach¹,
and Günther Rüdiger²

1. Introduction

Magnetic fields play a double role in the cosmos: First, planetary, stellar and galactic fields are produced by the homogeneous dynamo effect in moving electrically conducting fluids. Second, magnetic fields accelerate the formation of stars and black holes, by enabling outward transport of angular momentum in accretion disks by virtue of the so-called magnetorotational instability (MRI). This instability had been discovered as early as 1959, when Velikhov showed that a Taylor-Couette flow in its hydrodynamically stable regime (i.e. with outward increasing angular momentum) can be destabilized by an applied axial magnetic field [1]. But it was only in 1991, that the relevance of MRI for accretion disks in the vicinity of young stars and black holes was realized in a seminal paper by Balbus and Hawley [2].

The last decades have seen remarkable theoretical and computational progress in understanding the dynamo effect and the MRI. The dynamo effect has even been verified experimentally, in large-scale liquid sodium facilities in Riga and Karlsruhe, and is presently studied in laboratories around the world [3]. In contrast, obtaining the MRI experimentally has been less successful thus far [4]. Recently, an MRI-like instability has been observed on the back-ground of a turbulent spherical Couette flow [5], but the genuine idea that MRI would destabilize an otherwise stable flow was not realized in experiment up to present.

If only an axial magnetic field is externally applied, the azimuthal field that is necessary for the occurrence of the MRI must be produced by induction effects, which are proportional to the magnetic Reynolds number (R_m) of the flow. But why not substitute this induction process simply by externally applying an azimuthal magnetic field as well? This question was addressed by Hollerbach and Rüdiger [6], who showed that the MRI is then possible with far smaller Reynolds (Re) and Hartmann (Ha) numbers. In this paper, we report the first experimental verification of this idea, presenting evidence of the MRI in a liquid metal co-rotating Taylor-Couette cell with externally imposed axial and azimuthal (i.e., helical) magnetic fields. Further details can be found in [7,8].

2. The experimental facility

The basic part of our facility “PROMISE” (Potsdam Rossendorf Magnetic InStability Experiment) is a cylindrical containment vessel V made of copper (see Fig. 1). The use of copper was motivated by the finding that the instability usually occurs at lower Reynolds and Hartmann numbers for the case of ideally conducting boundaries than for non-conducting boundaries [6,9]. The inner wall of the vessel V is 10 mm thick, and extends in radius from 22 to 32 mm; the outer wall is 15 mm thick, extending from 80 to 95 mm. This vessel is filled with the eutectic alloy $Ga^{67}In^{20.5}Sn^{12.5}$, which has the advantage of being liquid at room temperatures.

¹ Department of Applied Mathematics, University of Leeds, United Kingdom

² Astrophysikalisches Institut Potsdam, Germany

The copper vessel V is fixed, via an aluminium spacer D , on a precision turntable T ; the outer wall of the vessel thus serves as the outer cylinder of the Taylor-Couette cell. The inner copper cylinder I of the Taylor-Couette flow is fixed to an upper turntable, and is immersed into the liquid metal from above. It has a thickness of 4 mm, extending in radius from 36 to 40 mm, thus leaving a gap of 4 mm between this immersed cylinder I and the inner wall of the containment vessel V . The actual Taylor-Couette cell then extends in radial direction over a cylindrical gap of width $d = r_{\text{out}} - r_{\text{in}} = 40$ mm, and in axial direction over the liquid metal height of $0 \text{ mm} < z < 410$ mm.

In the present configuration, the upper endplate is a Plexiglas lid P fixed to the frame F . In contrast, the bottom is simply part of the copper vessel, and hence rotates with the outer cylinder. There is thus a clear asymmetry in the endplates, with respect to both their rotation rates and electrical conductivities.

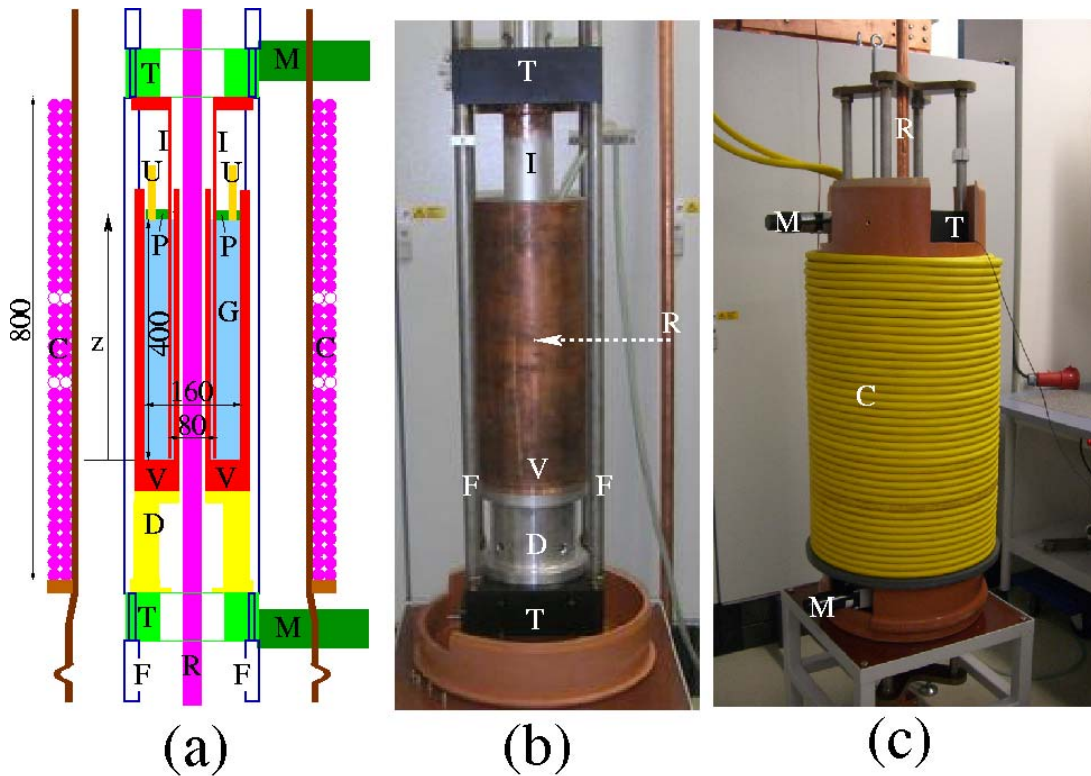


Fig. 1: The PROMISE experiment. (a) - Sketch. (b) - Photograph of the central part. (c) - Total view. V - Copper vessel, I - Inner cylinder, G - GaInSn, U - Two ultrasonic transducers, P - Plexiglas lid, T - High precision turntables, M - Motors, F - Frame, C - Coil, R - Copper rod. The dimensions are in mm.

It should be mentioned that the tolerance of the key components of the apparatus is not quite at the 10^{-2} mm level that can be achieved in ordinary, hydrodynamic Taylor-Couette experiments, e.g. [10]. One of the reasons is that it is necessary to intensively rub the fluid into the copper in order to ensure a well-defined electrical contact between the GaInSn and the walls. Due to the resulting abrasion, the accuracy of the copper cylinders is certainly not better than 10^{-1} mm. Note also that the typical Reynolds number $Re = 2 \cdot \pi \cdot f_{\text{in}} \cdot r_{\text{in}} \cdot d/v$ in the experiment is $O(10^3)$, which is considerably greater than the critical value $Re_c = 68$ for the transition to the Taylor vortex flow in the non-magnetic Taylor-Couette problem (for this radius ratio, with stationary outer cylinder).

Axial magnetic fields of order 10 mT are produced by a double-layer coil with 76 windings (C in Fig. 1). The omission of windings at two symmetric positions close to the middle, as seen in Fig. 1a, resulted from a coil optimization to maximize the homogeneity of the axial field throughout the volume occupied by the liquid. The coil is fed by currents up to approximately 200 A. Beyond this value the coil is significantly heating up. The azimuthal field, also of order 10 mT, is generated by a current through a water-cooled copper rod R of radius 15 mm. The power supply for this axial current delivers up to 8000 A.

In the present set-up, the measuring instrumentation consists exclusively of two ultrasonic transducers with a working frequency of 4 MHz; these are fixed into the Plexiglas lid, 15 mm away from the outer copper wall, flush mounted at the interface to the GaInSn. Using Ultrasound Doppler Velocimetry (UDV) [11], they provide full profiles of the axial velocity v_z along the beam-lines parallel to the axis of rotation. The spatial resolution in axial direction is 0.685 mm, the time resolution is 1.84 sec. It should be mentioned that the necessary velocity resolution in the order of 0.1 mm/s is at the margin of applicability of the UDV system. The width of the beam (over which v_z is averaged) is approximately 8 mm, according to the diameter of the ultrasonic transducers. The comparison of the two signals from two opposite sensors is important in order to clearly distinguish between the expected axisymmetric ($m = 0$) MRI mode [9] and certain $m = 1$ modes which also play a role in some parameter regions of the experiment.

3. Experiments and their main results

We have carried out a large number of experimental runs in order to cover a wide range of parameter dependencies. Typically, the duration of an experimental run was 1900 sec, after a waiting time of one hour. Such a long waiting time was chosen not only due to the hydrodynamic gap diffusion time $\tau_{\text{gap}} = d^2/\nu$, but also due to our numerical predictions of rather small growth rates of the MRI mode in helical fields.

In pre-experiments, both with a water-glycerol mixture and with GaInSn, we had clearly identified the expected Taylor vortex flow in the hydrodynamically unstable regime (e.g. with stationary outer cylinder). As a consequence of the reflection symmetry breaking under the influence of a helical magnetic field [12], the Taylor vortex flow is replaced by an oscillatory axi-symmetric vortex flow that propagates in a unique direction along the vertical axis [6]. This direction depends on the screw-sense of the magnetic field and the direction of the flow rotation (all results presented in the following are for an upward travelling wave). This travelling wave appears already with a stationary outer cylinder, i.e. at $\mu := f_{\text{out}}/f_{\text{in}} = 0$, although with a very low frequency. With increasing μ , the wave frequency increases and typically reaches a value of $0.2 \times f_{\text{in}}$ at the Rayleigh value $\mu_{\text{Ray}} = (r_{\text{in}}/r_{\text{out}})^2$ (we have $r_{\text{in}}/r_{\text{out}} = 0.5$ here, hence $\mu_{\text{Ray}} = 0.25$). The crucial point now is that under the influence of helical magnetic fields the critical Reynolds numbers remain relatively small increasingly far above the Rayleigh value which loses its character as a sharp boundary between unstable and stable flows. Typically, this shift to larger values of μ becomes larger for increasing values of the ratio of azimuthal field to axial field, $\beta := B_{\phi}(r = r_{\text{in}})/B_z$.

Another typical feature of the MRI is that, for fixed Re and fixed azimuthal field, it sets in at a certain critical value of the Hartmann number $Ha = B_z \cdot (r_{\text{in}} \cdot d \cdot \sigma \cdot \rho \cdot \nu)^{1/2}$, and disappears again at some higher value. This appearance and disappearance of a travelling mode is a suitable indicator for the existence of the proper MRI mode and its distinction from other

possible flow structures. In the following, we focus exclusively on experimental results which substantiate this behaviour.

All results presented in the following are for rotation rates of $f_{\text{in}} = 0.06$ Hz and $f_{\text{out}} = 0.0162$ Hz, i.e. for $\mu = 0.27$ which is above the Rayleigh value $\mu_{\text{Ray}} = 0.25$. Figure 2 documents a selection of four experimental runs for coil currents I_{coil} of 10, 50, 75 and 120 A. In each case, the axial current I_{rod} was fixed to 6000 A. The colour coding of the plots indicates the axial velocity component v_z measured along the ultrasound beam, from which we have subtracted the z -dependent time average in order to filter out the two Ekman vortices which appear already without any magnetic field. These vortices, characterized by inward radial flows close to the upper and lower endplates, show up in our UDV data in the form of positive and negative axial velocities, separated approximately at mid-height by a rather sharp boundary. This boundary most likely corresponds to a jet-like radial outflow in the centre of the cylinder, as discussed in [13].

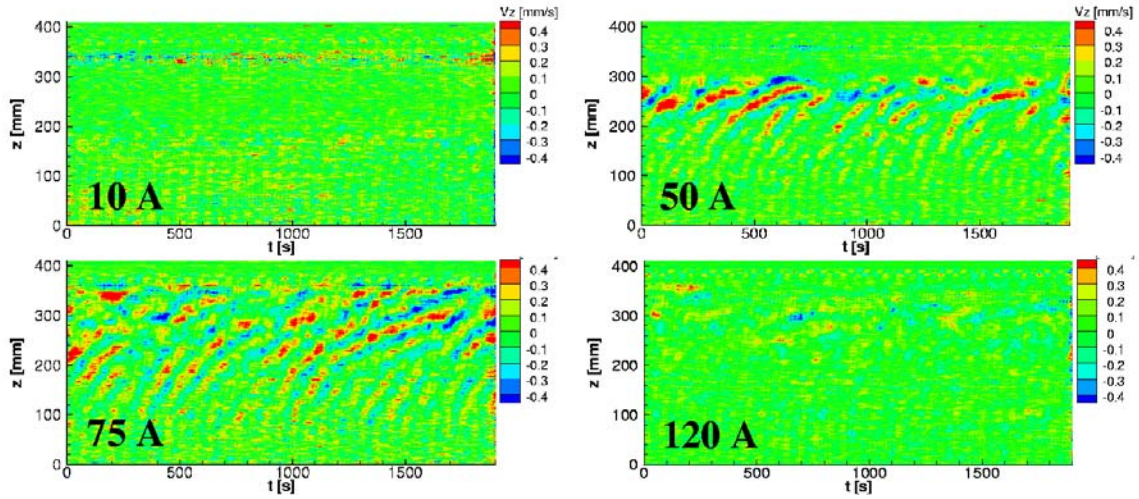


Fig. 2: Measured axial velocities in dependence on the vertical position and the time, for different coil currents. The appearance and disappearance of a travelling wave mode for increasing coil current (i.e., Hartmann number) is clearly visible.

For $I_{\text{coil}} = 50$ A we already observe a travelling wave-like structure which is, however, still restricted to the middle part of the cylinder. One might speculate that, due to the (jet-like) radial outward flow there, fluid with lower angular momentum is transported outward, which leads to a locally steeper decrease of v_ϕ than what would be expected from the rotation ratio μ of outer to inner cylinder [13]. At $z \sim 300$ mm, i.e. closely above the radial outflow region, the wave dies away.

For $I_{\text{coil}} = 75$ A this travelling wave fills the entire cylinder. Some refraction of the wave remains visible approximately at mid-height. Increasing I_{coil} even further though, at 120 A this wave ceases to exist, and we again have a rather featureless flow. This is shown more quantitatively in Fig. 3, where we exhibit the power spectral density (PSD) for the axial velocity for 5 selected values of I_{coil} . A feature common to all five curves is the appearance of the rotation rates of the inner and outer cylinders. This reflects certain geometric imperfections of the facility, probably in the form of cylinder eccentricities or metal oxides sticking to some parts of the walls. There is also a peak approximately at the mean of the inner and outer cylinder frequencies, which, on closer inspection of the two transducer

signals, turns out to be a non-axisymmetric $m = 1$ mode. Most interesting for us here, however, is the MRI mode at $f/f_{in} \sim 0.1-0.2$. These frequencies have been analysed in detail for all values of I_{coil} chosen in the experiment.

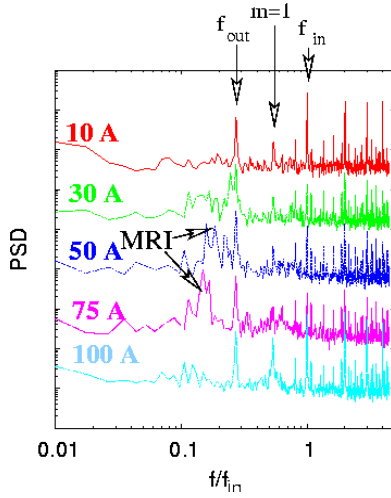


Fig. 3: Power spectra of the measured v_z fluctuations for 5 different coil currents.

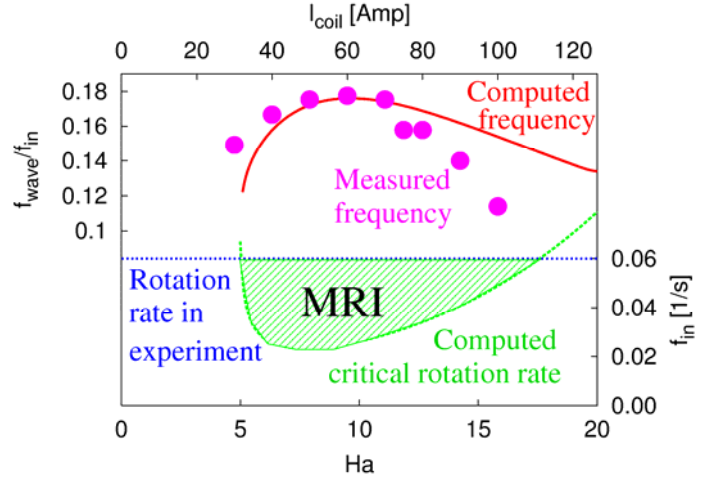


Fig. 4: Computed critical rotation rate for varying I_{coil} (and hence Ha), for fixed $I_{rod} = 6000$ A, and measured and computed frequency f_{wave} of the travelling MRI wave normalized to f_{in} .

We now interpret these experimental data in the context of numerical predictions, obtained and cross-checked by various independent codes [6, 9, 14] for the solution of the linear eigenvalue problem in unbounded cylinders with ideally conducting radial boundaries. First, the lower part of Fig. 4 shows the computed critical rotation rate of the inner cylinder, compared with the rotation rate of 0.06 Hz chosen in the experiment. According to this plot, MRI should be expected approximately between $30 \text{ A} < I_{coil} < 110 \text{ A}$, were the experimental rotation rate is above the critical one. Actually, MRI appears in this region, although it is hard to indicate precise boundaries. This is typical for an imperfect bifurcation in finite systems for which the instability sets in gradually instead of abruptly.

In the upper part of Fig. 4, we compare the measured frequencies of the travelling wave, normalized to the rotation rate of the inner cylinder, with the frequencies computed for the infinite cylinder. Evidently, the measured frequencies are in reasonable correspondence with the computed ones, and show a similar dependence on Ha , with a maximum close to $Ha = 10$.

4. Summary and outlook

We have obtained experimental evidence for the existence of the MRI in current-free helical magnetic fields, by showing its appearance in a certain interval of Hartmann numbers, in good agreement with numerical predictions. Certainly, much numerical work remains to be done, including the treatment of the non-linear regime, a more realistic handling of the magnetic radial boundary conditions, and a detailed investigation into the role of the magnetic axial boundary conditions. For later experiments, a symmetrization of the axial boundaries is envisioned. Connected with this, a suppression of the Ekman vortices by means of split rings (proposed in [13]), may also help to avoid artefacts in the mid-height of the cylinder.

References

- [1] E. P. Velikhov (1959), Stability of an ideally conducting liquid fluid between cylinders rotating in a magnetic field, *Sov. Phys. JETP* 36, 995
- [2] S. A Balbus and J. F. Hawley (1991), A powerful local shear instability in weakly magnetized disks. 1. Linear Analysis, *Astrophys. J.*, 376, 214
- [3] A. Gailitis, O. Lielausis, E. Platacis, G. Gerbeth and F. Stefani, (2002), Laboratory experiments on hydromagnetic dynamos, *Rev. Mod. Phys.*, 74, 973
- [4] R. Rosner, G. Rüdiger and A. Bonanno (Eds.) (2004), *MHD Couette flows: Experiments and Models*, AIP Conference Proceedings No. 733, AIP, New York
- [5] D. Sisan et al. (2004), Experimental observation and characterization of the magnetorotational instability, *Phys. Rev. Lett.* 93, Art. No. 114502
- [6] R. Hollerbach and G. Rüdiger (2005), New type of magnetorotational instability in cylindrical Taylor-Couette flow, *Phys. Rev. Lett.* 95, Art. No.124501
- [7] F. Stefani et al. (2006), Experimental evidence for magnetorotational instability in a Taylor-Couette flow under the influence of a helical magnetic field, *Phys. Rev. Lett.* 97, Art. No. 184502
- [8] G. Rüdiger, R. Hollerbach, F. Stefani, Th. Gundrum, G. Gerbeth and R. Rosner (2006), The travelling-wave MRI in cylindrical Taylor-Couette flow: Comparing wavelengths and speeds in theory and experiment, *Astrophys. J.* 649, L145
- [9] G. Rüdiger, R. Hollerbach, M. Schultz and D. A. Shalybkov (2005), The stability of MHD Taylor-Couette flow with current-free spiral magnetic fields between conducting cylinders, *Astron. Nachr.* 326, 409
- [10] F. Schultz-Grunow (1959), Zur Stabilität der Couette-Strömung, *Z. Angew. Math. Mech.* 39, 101
- [11] A. Cramer, C. Zhang and S. Eckert (2004), Local flow structures in liquid metals measured by ultrasonic Doppler velocimetry, *Flow Meas. Instrum* 15, 145
- [12] E. Knobloch (1996), Symmetry and instability in rotating hydrodynamic and magnetohydrodynamic flows, *Phys. Fluids* 8, 1446
- [13] A. Kageyama, H. Ji, J. Goodman, F. Chen and E. Shoshan (2004), Numerical and experimental investigation of circulation in short cylinders, *J. Phys. Soc. Jpn*, 73, 2424
- [14] F. Stefani and G. Gerbeth (2004), MRI in Taylor-Dean flows, in Ref. [4], 100

Acknowledgments

This work was supported by German Leibniz Gemeinschaft, within its SAW programme. We thank Heiko Kunath for technical assistance, and Markus Meyer for assistance taking some of the data. We are grateful to Janis Priede and Ilmars Grants for stimulating discussions.

HIGH RESOLUTION GAMMA RAY TOMOGRAPHY AND ITS APPLICATION TO THE MEASUREMENT OF PHASE FRACTIONS IN CHEMICAL REACTORS

Uwe Hampel, Andre Bieberle, Eckhard Schleicher, Günther Hessel,
and Cornelius Zippe

1. Introduction

The measurement of the hydrodynamics in chemical reactors is a challenging problem. Gamma ray tomography is one potential method that may be applied to measure the distribution of phases respectively the hold-up of liquid or gas in metallic vessels. It is, however, a rather slow measurement technique that provides time integral information on the phase distribution. There are some reports in literature describing the application of gamma ray densitometry or tomography to flow measurement problems [1] - [4]. Most of the introduced systems have a comparatively low spatial resolution due to the use of photomultiplier technology. Recently our group has developed a high resolution gamma ray tomography device with primary use in nuclear thermal hydraulics diagnostics such as void fraction measurement in fuel rod bundles. With this device, we are now able to scan objects at a spatial resolution close to that of X-ray systems but at much higher photon penetration capability. The present study on a stirred chemical reactor has been performed to prove the applicability of gamma ray CT and to generate data for CFD code validation.

2. The gamma ray CT system

The gamma ray tomography system (Fig. 1) essentially consists of five parts: the isotopic source, the detector arc, a signal processing unit, a rotational stage to manipulate the object of investigation and a measurement PC. The object is placed in the centre between source and detector. In our tomography system we currently use a Cs-137 source with 662 keV gamma photon energy, 165 GBq activity and 5.6 mm source spot size. The capsule resides within a shielding container and can be manually drawn into working position by means of a bowden cable. The detector arc is made of 320 single lutetium yttrium orthosilicate scintillation crystals coupled to avalanche photodiodes and associated detector electronics [5]. The crystals have an active area of 2 mm width, 8 mm height and 22 mm length. Stopping efficiency is roughly 75 % whereas energy resolution is about 25 %. The in-plane resolution of the gamma ray CT setup is 3.5 mm. The axial resolution is about 7 mm for the uncollimated system but may be increased by applying further spatial collimation to source and detector. Thus, in this study we have used additional tungsten collimators at source and detector to reduce the axial extension of the radiation fan to 2 mm. The detector is operated in pulse counting mode, that is,

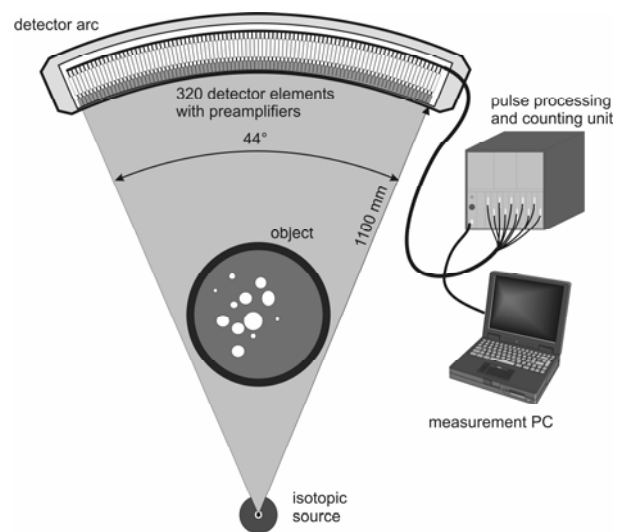


Fig. 1: Sketch of the gamma ray CT system.

each gamma photon that interacts in the scintillation crystal is electronically converted into a voltage pulse by the avalanche photodiode and a following preamplifier. Further electronic processing includes pulse shaping, pulse height discrimination with dual window comparator and pulse counting via a 24 bit counter stage with digitally multiplexed output. The counter data is transferred to the PC via USB 2.0 interface at user defined intervals. Further, the object can be appropriately moved in vertical direction and rotated as required by means of a translational-rotational stage.

3. Measurement on a stirred tank reactor

Gamma ray CT has been applied to the measurement of the fluid distribution in a stirred tank reactor at different stirrer speeds. The aim of this study was the provision of reference data for CFD simulations. Thus, special parameters of interest are the shape of the fluid-gas boundary around the stirrer shaft and the gas distribution in the impeller region. Experiments were carried out on a double wall cylindrical reactor Ecoclave 150 (Büchi AG, Switzerland) made of borosilicate glass with an inner diameter of 80 mm (Fig. 2). The fluid is stirred by a six blade mechanical stirrer mounted at the lower end of a hollow shaft. The shaft is motor driven with a controllable speed between 50 and 2000 rpm. Between the stirrer blades there are holes which allow gas flow from the upper gas volume into the fluid. With increasing stirrer speed the static pressure in the stirrer region drops accordingly, drawing gas from the upper gas compartment downwards through the hollow shaft. At a critical stirrer speed the fluid-gas interface reaches the holes and is there radially dispersed into the fluid by the mechanical forces of the stirrer. The gas flow rate is thus dependent on the angular stirrer speed. During the experiments the reactor was placed in the centre of the gamma ray CT setup and scanned in 150 successive axial slices of 2 mm separation. In each plane photon counting was done for 10 seconds giving an average number of approximately $2 \cdot 10^4$ counts in regions outside the stirrer shaft and $1.2 \cdot 10^4$ counts right behind the stirrer shaft. This gives a statistical noise/signal ratio of less than 1 % for a single gamma ray. Due to the rapidly rotating fluid distribution inside the reactor we make the assumption, that the fluid distribution is rotationally symmetric. Thus, we aim at the measurement of axially and radially resolved fluid respectively gas distributions instead of real 3D distributions. This is a consequence of the time integral gamma ray measurement. Hardware changes are currently being implemented with that system for a more advanced angle resolving measurement. However, for the comparison of measurement results with CFD predictions this poses no major problem since CFD data may accordingly be averaged along the angular direction.

4. Measurement and data processing

During a scan the signal processing unit constantly transfers count rate data from all detector elements to the measurement PC. The count rate is defined as the number of unscattered gamma photons that interact in a detector element per unit time interval. Let i denote the index of the detector element (the radial coordinate) and j the index of the plane (the axial coordinate), then the gamma ray extinction values are calculated according to

$$E(i, j) = -\log \frac{N(i, j) - N_d(i)}{N_0(i) - N_d(i)}, \quad (1)$$

where $N(i, j)$ denotes the count rate for a given measurement channel (plane and detector), N_d the dark count rate and N_0 the reference count rate.

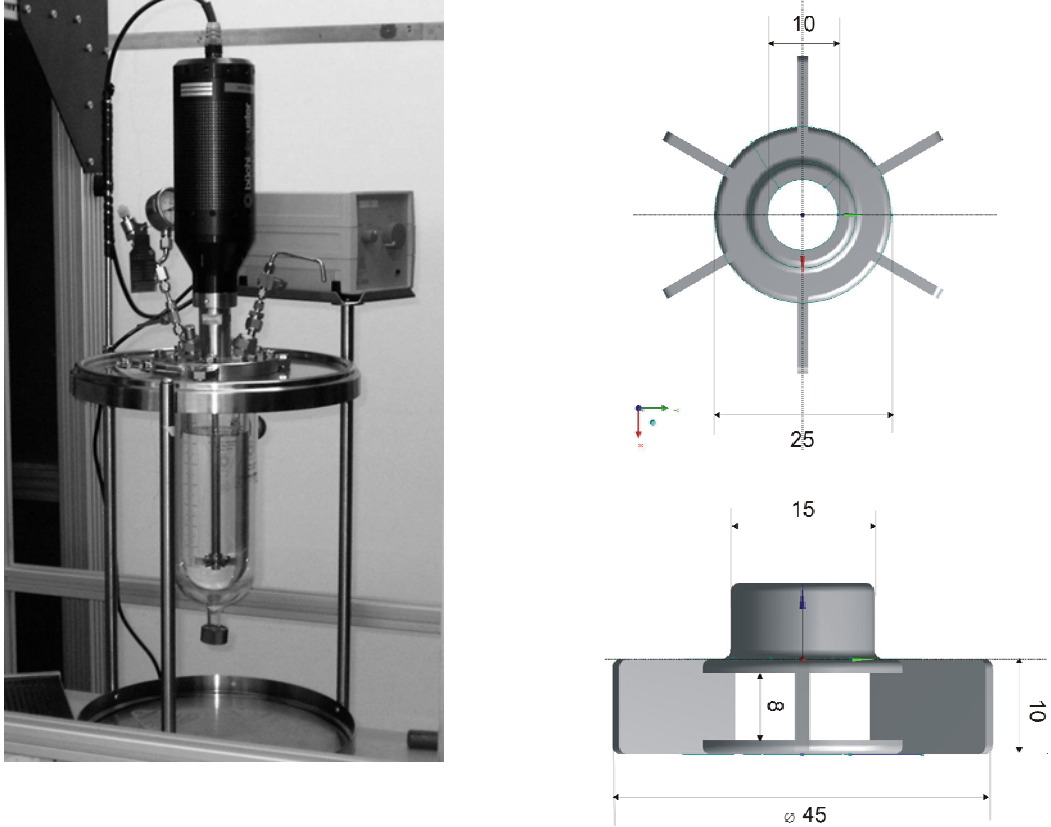


Fig. 2: Stirred tank reactor and stirrer geometry.

The dark count rate is recorded once with the isotopic source not being in operation. The reference count rate could in principle be measured at an empty vessel, which would then give the differential extinction from the fluid only. But in practice it is difficult to fill or empty the vessel between two measurements without causing some geometrical displacement of the components which would result in measurement errors. Thus, we used a free space reference, that is, the detector readings without any object in the fan. This data can be obtained from measurement planes below the bottom of the vessel.

Since the measurement data is still a line integral projection of the object we need to apply a tomographic inversion algorithm to reconstruct the fluid distribution in details. For this purpose we use the filtered backprojection technique [6]. First, we synthesise a backprojection image b_j by applying

$$b_{m,n}^j = \sum_{p=0}^{N_p-1} \sum_{i=0}^{N_D-1} a_{p,i,m,n} E_{i,j}, \quad (2)$$

where $a_{p,i,m,n}$ denote the pixel weights, i. e. the geometric share of pixel (m,n) to the finite width fan beam ray (p,i) . The backprojection operation is carried out for a sufficient number of identical projections which secures an artefact free image. This number is given by $N_p \geq 2\pi d/L_{pix}$ where d denotes the inner vessel diameter and L_{pix} the pixel edge length. After backprojection the two-dimensional image is restored applying a suitable inverse filter, where in our case we chose a Hamming modified ramp filter.

Having done this subsequently for all the 150 scanned slices we synthesise a volume image of the fluid distribution by a three-dimensional image assembly in the computer memory. The

results for the filled reactor with the stirrer at different speeds are shown in Fig. 3 for the central axial plane. The liquid-gas boundary is well restored at a high spatial accuracy. For the gas fraction measurement in the impeller region the integration time of 10 s turned out to be too low for sufficient measurement accuracy due to the low gas fraction values, which are typically below 10 %. Therefore we performed another set of measurements at 120 s integration time in a selected plane at the very axial centre position of the impeller structure. Fig. 4 shows the radial gas fraction values for different stirrer speeds which have been obtained with this procedure.

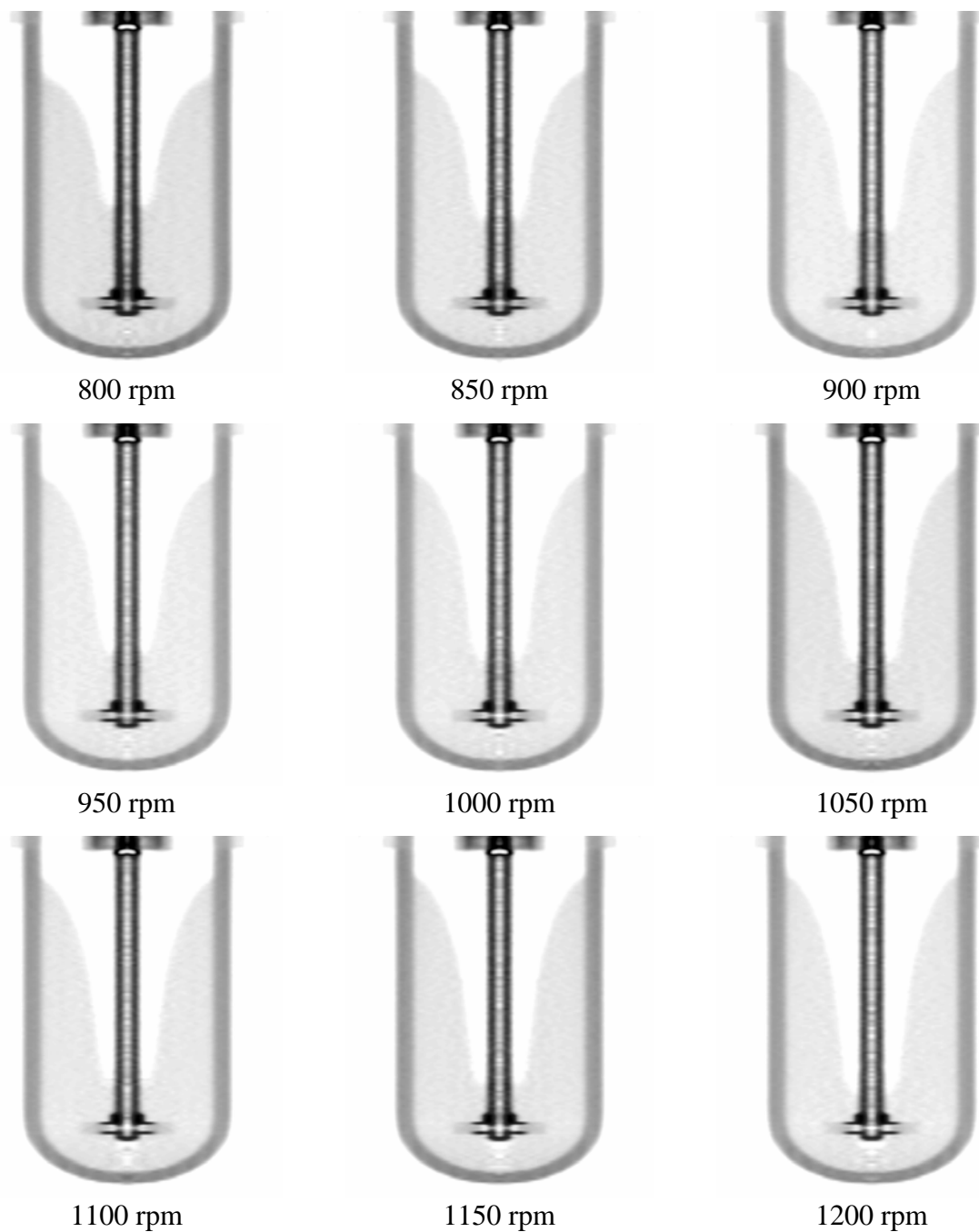


Fig. 3: Axial and radial fluid distribution in the stirred tank reactor measured with gamma ray CT.

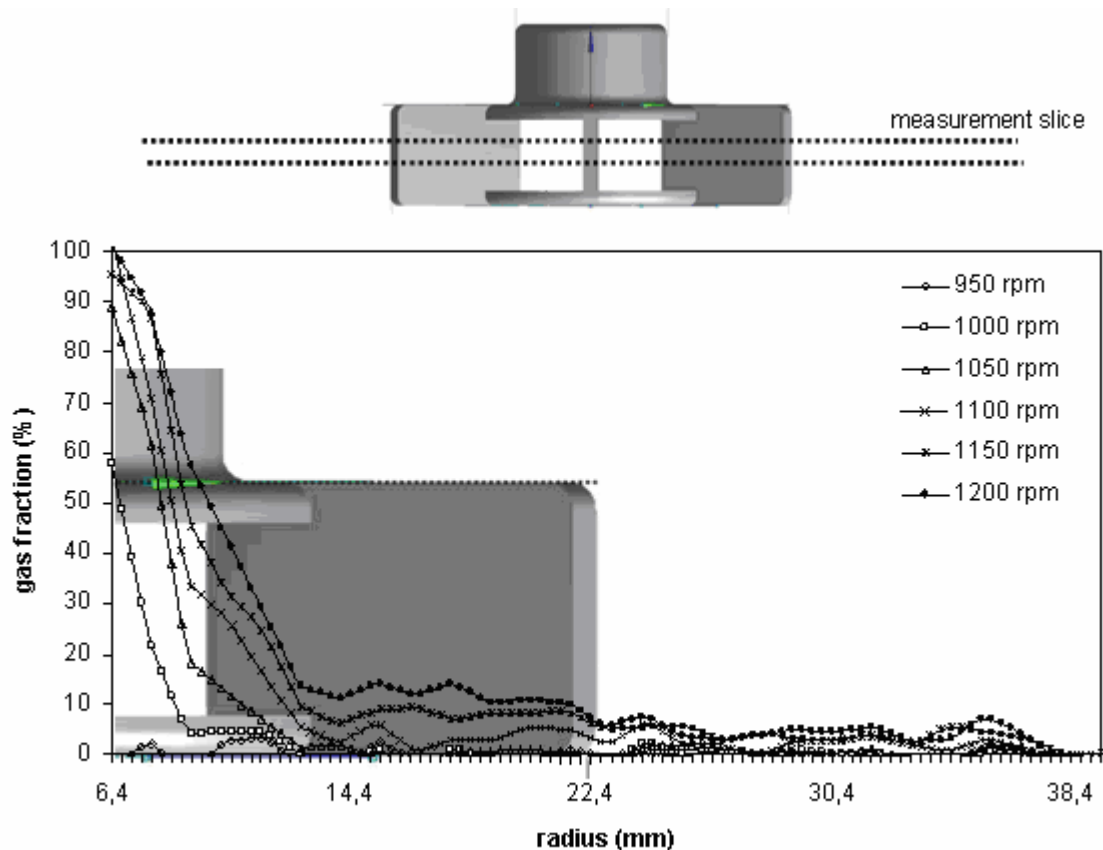


Fig. 4: Radial gas fraction profiles in the impeller region for different stirrer speeds. The stirrer geometry is shown in the background to indicate the extension of the main stirrer parts in radial direction.

5. Conclusions

Gamma ray tomography has been successfully applied to visualise and measure liquid and gas distributions in a stirred chemical reactor. The main advantage of the gamma ray technique is given by the high energy of the Cs-137 photons which allows penetration of steel vessel parts. Thus, opposed to an earlier experimental study on a stirred tank reactor performed with cone-beam X-ray tomography we now are able to resolve the gas phase in the region within the impeller blade at locations with high pressure gradients which are most critical for CFD code evaluation.

References

- [1] A. C. Devuono, P. A. Schlosser, F. A. Kulacki, P. Munshi, "Design of an isotopic CT scanner for two-phase flow measurements", IEEE T. Nucl. Sci., NS-27, 1980.
- [2] S. B. Kumar, D. Moslemian, M. P. Dudukovic, "A γ -ray tomographic scanner for imaging voidage distribution in two-phase flow systems", Flow Meas. Instrum., vol. 6, pp. 61-73, 1995.
- [3] K. A. Shollenberger, J. R. Torczynski, D. R. Adkins, T. J. O'Hern, N. B. Jackson, "Gamma-Densitometry Tomography of Gas Holdup Spatial Distribution in Industrial-Scale Bubble Columns", Chem. Eng. Sci., vol. 52, pp. 2037-2048, 1997.
- [4] U. P. Veera, "Gamma ray tomography design for the measurement of hold-up profiles in two-phase bubble columns", Chem. Eng. Journal 81, pp. 251-260, 2001.

- [5] A. Bieberle, U. Hampel, E. Schleicher, D. Hoppe, H.-M. Prasser, T. Sühnel, C. Zippe, “Design and performance of a high-resolution gamma tomography device”, Proceedings of the 4th World Congress on Industrial Process Tomography, Aizu, Japan, Sept. 2005, pp. 18-23, 2005.
- [6] A. C. Kak, M. Slaney, Principles of Computerized Tomographic Imaging. IEEE Press, New York, 1987.
- [7] S. Boden, U. Hampel, M. Bieberle, “Quantitative measurement of gas hold-up distribution in a stirred chemical reactor using X-ray cone-beam computed tomography”, Chem. Eng. J. (submitted), 2006.

ONLINE MONITORING OF GRIGNARD REACTIONS

Holger Kryk, Günther Hessel, and Wilfried Schmitt

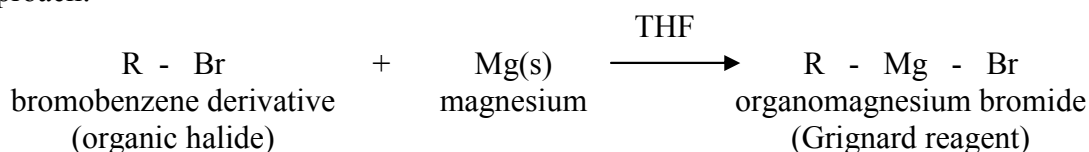
1. Introduction

Metal-organic compounds like Grignard reagents are of vital importance as an initial stage of numerous organic syntheses in the fine-chemical and pharmaceutical industries. Reactions between organic halides and solid magnesium in an ethereal solution comprise one of the most common methods to prepare Grignard reagents. Due to the spontaneous heat release during the delayed autocatalytic initiation of these strongly exothermic reactions and the high reactivity of the Grignard compounds, the formation reactions of Grignard reagents (herein after referred to as Grignard reactions) possess considerable hazard potentials [1]. Primary sources of hazards can be attributed to a long delayed reaction start due to traces of impurities after the accumulation of a high amount of the organic halide or to undesired exothermic consecutive reactions of the Grignard reagent with such impurities. Therefore, it is of vital importance to establish industrially applicable methods for an objective detection of the reaction start-up and accumulation of the organic halide during the process.

Industrial Grignard processes are normally carried out in stirred tank reactors, equipped with a reflux system at the boiling point of the reaction mixture to ensure removal of the spontaneous heat release. This process control complicates an objective detection of the reaction start-up and increases the risk of intrusions of impurities into the reactor. A few methods for online concentration measurements using FTIR and NIR spectroscopy have been developed [2, 3]. However, such methods and the appropriate devices require high investments and operating costs and, especially in case of quantitative measurements, huge calibration efforts. The process control of Grignard reactions in pressurized vessels without reflux system opens up new perspectives towards the estimation of concentration courses and safety relevant parameters using heat and mass balance-based online monitoring systems.

2. Laboratory investigations

The following reaction between bromobenzene derivative and magnesium in a THF solution was used as a model Grignard formation process to develop and test the online monitoring approach:



It is of vital importance for the application of heat balance-based monitoring systems to the reactive processes to know the exact reaction enthalpy. Since calorimetric measurements under reflux conditions produce higher errors than in closed systems, the reaction enthalpies were measured using the high pressure RC1e/HP60 calorimeter. Experiments, carried out in the isothermal operating mode, gave a reaction enthalpy of $\Delta H_r = -(307 \pm 5)$ kJ/mol independent of the reaction temperature in the 25 °C to 120 °C temperature range. The enthalpies were calculated for the main reaction stage to ensure maximum accuracy and reproducibility.

The Grignard reaction experiments have been carried out in a miniplant consisting of a 10 liters STR and a jacket cooling system to test the monitoring system. In accordance to indus-

trial applications, an isoperibolic process mode was used for the experiments. The organic halide concentrations were measured in-situ using the FTIR spectrometer ReactIR1000 for validation purposes. Two sets of experiments acted as test runs for the monitoring approach:

- a) common process mode:
separate start and main reaction stage by interruption of the dosage
- b) improved process mode:
non-stop semi-batch mode with continuous dosage to demonstrate the efficiency improvement capabilities of an online monitoring system

Typical profiles of process variables of the experiments according to set (a) and (b) are depicted in Fig. 1.

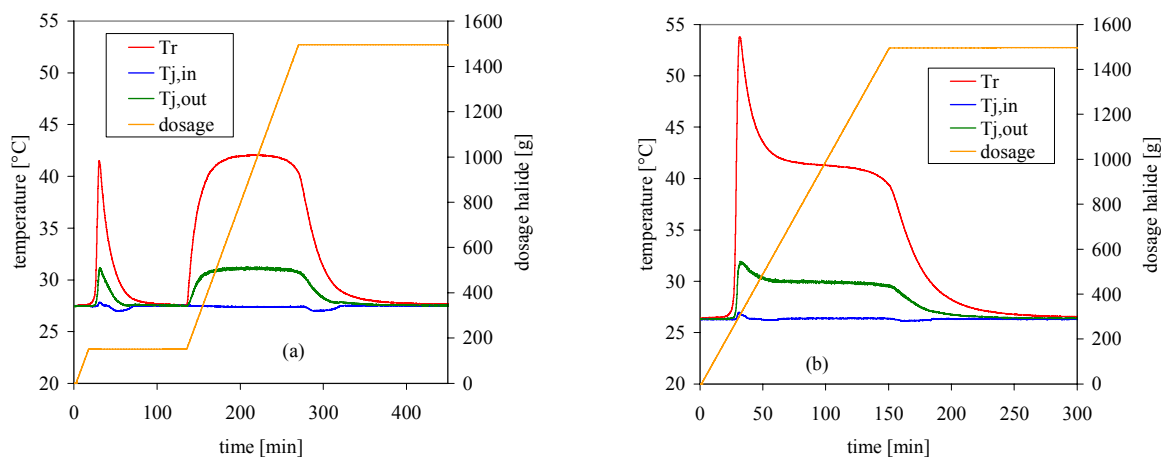


Fig. 1: Process variables of Grignard reactions (process mode (a) and (b))

Additional non-reactive experiments were carried out to estimate plant parameters like the heat capacities of the vessel and the cooling jacket as well as the heat loss coefficients of the apparatus.

3. Working principle of the monitoring system

The heat and mass balance model is part and parcel of the online calculation algorithm. By solving a set of dynamic heat / mass balances in real time, the concentrations of the reacting species can be monitored. On the basis of these results, the courses of safety relevant data like adiabatic temperature and pressure rises can be estimated. Fig. 2 illustrates the heat and mass flows in the stirred tank reactor during the Grignard reaction.

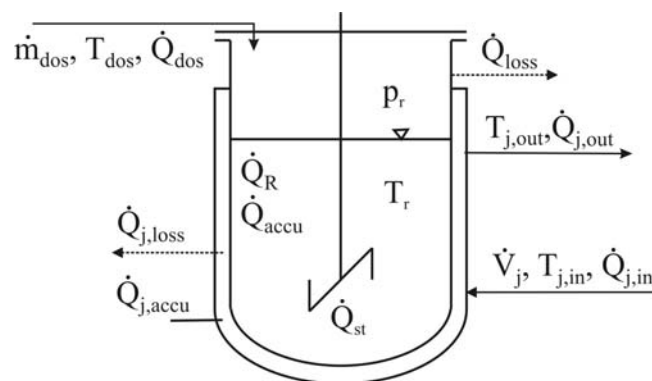


Fig. 2: Heat and mass flows during the Grignard reaction

The reactor heat balance is given by:

$$\dot{Q}_R = \Delta\dot{Q}_j + \dot{Q}_{accu} - \dot{Q}_{st} - \dot{Q}_{dos} + \dot{Q}_{j,accu} + \dot{Q}_{loss} + \dot{Q}_{j,loss} \quad (1)$$

The main portion of the heat release rate \dot{Q}_R , generated by the exothermic reaction, can be eliminated from the reactor content by the jacket cooling system. The resulting heat flux difference $\Delta\dot{Q}_j$ can be calculated as follows:

$$\Delta\dot{Q}_j = \dot{Q}_{j,out} - \dot{Q}_{j,in} = \rho_{j,in} \dot{V}_j (c_{p,j,out} T_{j,out} - c_{p,j,in} T_{j,in}) \quad (2)$$

Particularly during the initiation reaction, a good portion of the reaction heat is accumulated in the reaction mixture, the vessel and the cooling jacket. The resulting heat fluxes are considered by the \dot{Q}_{accu} and $\dot{Q}_{j,accu}$ terms respectively.

$$\dot{Q}_{accu} = (m_r c_{p,r} + C_{p,app}) \frac{dT_r}{dt} \quad (3) \quad \dot{Q}_{j,accu} = (V_j \rho_j c_{p,j} + C_{p,j,app}) \frac{dT_j}{dt} \quad (4)$$

The calculation of the heat flux caused by the dissipation energy of the stirrer \dot{Q}_{st} is based on common NEWTON number correlations [4]. Especially, if the reactor temperature T_r differs from the temperature of the dosed halide T_{dos} , the cooling or heating of the reactor mixture by the dosed liquid has to be considered. The corresponding heat flux \dot{Q}_{dos} is calculated as follows:

$$\dot{Q}_{dos} = \dot{m}_{dos} c_{p,dos} (T_{dos} - T_r) \quad (5)$$

The heat losses through the top of the reactor \dot{Q}_{loss} and the cooling jacket $\dot{Q}_{j,loss}$ can be considered by experimental assessment of the heat flux coefficients at the target plant. Probably, more appropriate approach in order to consider the difficult to model heat losses and heat bridges at industrial plants would be the addition of correction terms to the heat balance. These terms include adaptive parameters, which can be determined by a neural network adaptation algorithm described in detail in [5]. However, a set of process signals of at least one batch at normal operating conditions is necessary in order to adapt the monitoring system to the target plant.

Assuming an instantaneous reaction according to the dosage of the organic halide \dot{m}_{dos} (no accumulation of the halide), the heat release rate \dot{Q}_{inst} can be calculated on the basis of the reaction enthalpy ΔH_R according to the following equation:

$$\dot{Q}_{inst} = (-\Delta H_R) \frac{\dot{m}_{dos}}{M_{dos}} \quad (6)$$

In case of reactant accumulation in the reaction mixture, a difference of the instantaneous heat release rate \dot{Q}_{inst} and the heat flow \dot{Q}_R according to the heat balance occurs. The integral

value of this difference $\Delta Q_{R,accu}$ from the reaction start t_{start} to the actual time t is a measure of the accumulated amount of the dosed halide $n_{R,accu}$.

$$\Delta Q_{R,accu} = \int_{t_{start}}^t (\dot{Q}_{inst} - \dot{Q}_R) dt' \quad (7) \quad n_{R,accu} = \frac{\Delta Q_{R,accu}}{-\Delta H_R} \quad (8)$$

Since the pre-filled and dosed amounts of reactants and solvents are known, the concentration profiles of the organic halide and the Grignard reagent during the process can be computed simply by application of appropriate mass balances.

In addition to the online monitoring of substance amounts and concentrations, the heat and mass balance approach opens up new opportunities in safety oriented process control strategies as well as process automation using online computing of safety-relevant parameters. The approach provides an estimation of the hazard potential caused by the reactivity of the halide accumulated in the reaction mixture. Assuming an adiabatic behavior as a worst case, the maximum temperature profile $T_{ad,max}$ can be estimated according to the following equation:

$$T_{ad,max} = T_r + \frac{\Delta Q_{R,accu}}{m_r c_{p,r}} \quad (9)$$

The maximum reactor pressure profile $p_{ad,max}$ is primarily a result from the rise of the vapor pressure p_v of the reaction mixture and secondarily from the expansion of the gas phase above the liquid surface. To simplify the calculations, the gas phase can be assumed to have the properties of an ideal gas.

$$p_{ad,max} = [p_v(T_{ad,max}) - p_v(T_r)] + p_r \frac{T_{ad,max} + 273 K}{T_r + 273 K} \quad (10)$$

An objective evaluation of the process state is feasible at any time by comparing the time dependent courses of $T_{ad,max}$ and $p_{ad,max}$ with predefined by means of design parameters of the industrial plant and the initial response pressure of the safety valve respectively, thresholds.

4. Test results

After developing the approach by means of calorimetric experiments in the RC1 calorimeter, the monitoring system was tested at process conditions using results from two sets of experiments at 10 liters scale (see chapter 2).

As an example for the functionality of the method, selected results of Grignard reactions at common process mode (a) are displayed in Fig. 3 and Fig. 4. Fig. 3 shows the profiles of the heat release rate according to the heat balance \dot{Q}_R , the heat release rate of an assumed instantaneous reaction \dot{Q}_{inst} and the integral value of the difference $\Delta Q_{R,accu}$ as a measure for the accumulated halide. The resulting concentration courses of the organic halide and the Grignard reagent are diagrammed in Fig. 4. The molar concentrations are calculated with respect to the total reaction mixture without consideration of the solid magnesium in order to be able to compare the results with related online FTIR measurements. Especially for the concentration profile of the organic halide accumulated during the process, the results of the monitoring system exhibit a good agreement with the FTIR measurements.

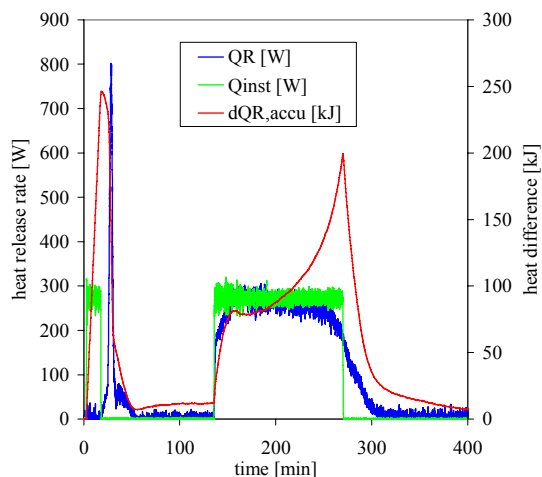


Fig. 3: Heat release rates during a Grignard reaction for the common process mode

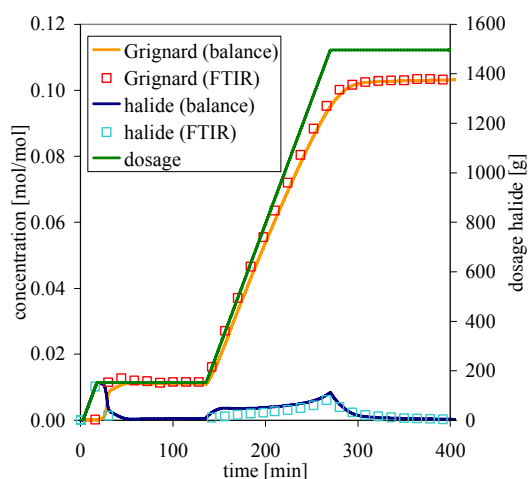


Fig. 4: Molar concentration profiles during a Grignard reaction for the common process mode

The highest amounts of organic halide occur after the dosage before the reaction starts and at the end of the main reaction stage. The accumulation rise at the end of the main reaction stage is caused by the decrease of the reaction rate due to the lack of magnesium.

Whenever a balance-based online monitoring method is used to trace the accumulation of the dosed organic halide, it is no longer necessary to interrupt the process after dosing the halide amount sufficient to start the reaction. Continuous dosage over the whole reaction period leads to an improvement of the space-time yield and opens up new opportunities regarding full automated process control strategies. To demonstrate the capabilities of the safety-oriented online monitoring, a set of experiments in non-stop semi-batch mode were carried out. Fig. 5 shows the concentration courses in comparison to FTIR measurements. Again, the results of the monitoring system are in good agreement with the related FTIR measurements.

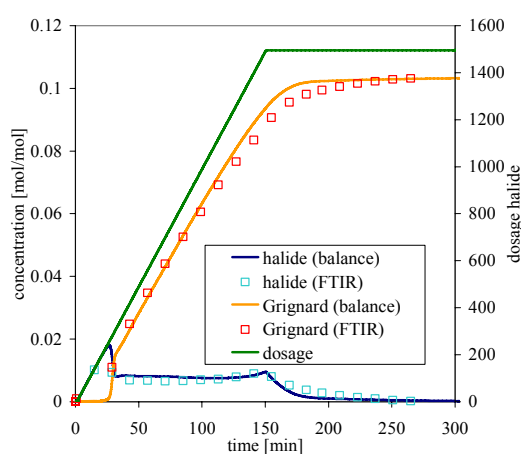


Fig. 5: Concentration profiles during a Grignard reaction for the improved process mode

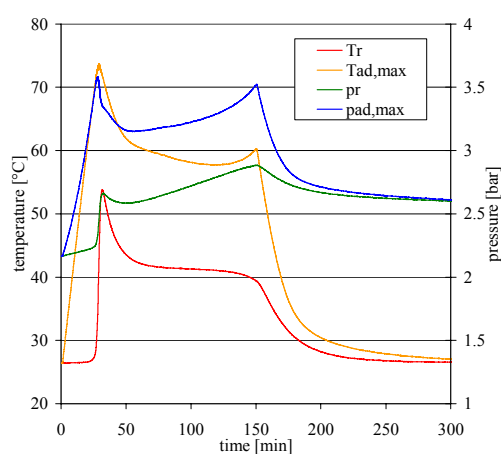


Fig. 6: Profiles of the safety-relevant parameters $T_{ad,max}$ and $p_{ad,max}$

By means of an online estimation of the safety-relevant parameters $T_{ad,max}$ and $p_{ad,max}$ according to Fig. 6, the hazard potential due to the reactivity of the accumulated halide can be evaluated at any time during the process. If one of the parameters exceeds the pre-defined thresh-

olds, the dosage of the organic halide can be interrupted by the process control system. Furthermore, the online data of $T_{ad,max}$ and $p_{ad,max}$ can be used as reference values for a full-automated dosage control of the halide.

5. Summary

The objective detection of the initiation reaction as well as of reactant accumulations during the process is of vital importance for the safety oriented process control of Grignard reactions. To establish industrially applicable methods for an objective online detection of the reaction start-up and for the accumulation of the organic halide during the process, miniplant studies of a special Grignard reaction using a 10 liters pressurized stirred tank reactor were carried out. Operating in closed systems opens up new opportunities with respect of the use of online monitoring systems. On the basis of the experimental results, a heat / mass balance-based online monitoring approach has been developed which is capable of providing the operator with additional information on the process state particularly for the accumulation of the organic halide. Additionally, the online estimation of the safety-relevant parameters, like adiabatic temperatures and pressures, enables application of advanced control strategies up to the point of a safety-oriented full automatic control of Grignard reactions. In the same time, such systems can contribute to improved process efficiency by increasing the space-time yield as well as to an improvement of the inherent process safety.

Nomenclature

Br	brome	C_p	heat capacity	accu	accumulated
FTIR	Fourier transform infrared	c_p	specific heat capacity	ad	adiabatic
Mg	magnesium	H	enthalpy	app	apparatus
NIR	near infrared	\dot{m}	mass flow	dos	dosage
R	organic residue	n	amount of substance	in	inlet
STR	stirred tank reactor	p	pressure	inst	instantaneous
s	solid state	Q	heat	j	cooling jacket
THF	tetrahydrofurane	\dot{Q}	heat flow	max	maximum
		T	temperature	out	outlet
		t	time	R	reaction
		V	volume	r	reactor
		\dot{V}	flow rate	start	reaction start

References

- [1] M.-H. Yue, J. J. Sharkey and J. C. Leung (1994), Relief vent sizing for a Grignard reaction, *J. Loss Prev. Process Ind.*, Vol. 7, No. 5, 413-418.
- [2] D. J. am Ende, P. J. Clifford, D. M. DeAntonis, C. SantaMaria and S. J. Brenek (1999), Preparation of Grignard reagents: FTIR and calorimetric investigation for safe scale-up, *Org. Process Res. Dev.*, Vol. 3, No. 5, 319-329
- [3] J. Wiss, M. Länzlinger and M. Wermuth (2005), Safety improvement of a Grignard reaction using online NIR monitoring, *Org. Process Res. Dev.*, Vol. 9, No. 3, 365-371
- [4] C. G. Koen (1977), presented at Mixing VII, in: D. S. Dickey, K. J. Bittorf, C. J. Ramsey and K. E. Johnson (2004), Understand flow patterns in glass-lined reactors, *Chem. Eng. Prog.*, Vol. 100, No. 11, 21-25
- [5] G. Hessel, H. Kryk, W. Schmitt, T. Seiler and F.-P. Weiss (2001), Monitoring system for batch reactors using adaptive heat balances, *Wissenschaftlich-Technische Berichte / Forschungszentrum Rossendorf, FZR-318*, 74-82

TREPANING PROCEDURE APPLIED AT THE RPV OF THE FORMER GREIFSWALD NUCLEAR POWER PLANT

Hans-Werner Viehrig, Udo Rindelhardt, and Werner Keller¹

1. Introduction

The integrity assessment procedure for the reactor pressure vessels (RPV) of nuclear power plants (NPP) is based upon fracture mechanics methodologies. The fracture toughness parameters of the RPV steels after long-term service irradiation are determined in surveillance programs using so-called surveillance specimens. Radiation loading, metallurgical and environmental histories, however, can differ between the surveillance specimens and the steel of the operated RPV. Therefore, the investigation of RPV steels from decommissioned NPPs offers the unique opportunity to evaluate the real fracture toughness values. A chance is given now through the investigation of material from the former Greifswald NPP (VVER-440/230; shutdown in 1990) to evaluate the material states of a standard RPV design (including annealed material states) and to assess the quality of prediction rules and assessment tools. The well documented different irradiation/annealing states of the four Greifswald RPVs are very useful for an integrated approach to study the embrittlement phenomena. This approach includes:

- Neutron and gamma fluence calculations,
- Niobium based experimental dosimetry and
- comprehensive material investigation program.

In autumn 2005 the first trepans (diameter 120 mm) were gained from unit 1 of the Greifswald NPP. The paper describes some details about the trepanning procedure.

2. Characteristics of the Greifswald NPP

Between 1973 and 1979, four units (unit power 440 MW_{el}) of the Russian Pressurized Water Reactor line VVER-440/230 were put into operation in Greifswald. Design, material production and operation conditions are identical or almost identical for more than 30 similar units in Russia and Eastern Europe.

Table 1: Radiation characteristics of the Greifswald reactor units 1 – 4

unit	cycles	effective days	annealed in	azimuthal maximum of $\phi_{E>1\text{MeV}}$ in units of 10^{19} n/cm^2			
				inner wall axial maximum	inner wall weld 4	outer wall axial maximum	outer wall weld 4
1	15	4215.0	1988	4.4	3.3	0.69	0.49
1*	2	627.4	-	0.40	0.29	0.058	0.042
2	14	4067.4	1990	5.3	4.1	0.83	0.60
3	12	3581.8	1990	4.4	3.4	0.68	0.50
4	11	3207.9	not	4.0	3.1	0.62	0.45

*after annealing

$\phi_{E>1\text{MeV}}$ - neutron fluence (E>1MeV)

¹ Studsvik IFM GmbH&Co.KG, Karlsruher Str. 20, 75179 Pforzheim

The neutron flux is very high (small water gap: 16 cm), the operation temperature is low (270 C) and the material is sensitive to neutron embrittlement (Cu content > 0.12 %, high P content in the weld). Therefore, the accepted embrittlement limits had already been reached after about 12 cycles, and the units had to be annealed around the most loaded core weld to continue their operation. In 1990, after the German reunification all units were shut down.

The operation time, radiation characteristics and annealing states of the four Greifswald units are given in Table 1.

3. The trepanning procedure

The trepanning process had to be integrated in the dismantling procedure of the Greifswald NPP. The originally planned procedure was based on a complete cutting of the RPV. In this case the trepans could easily be taken using the normal dismantling equipment. In 2004 the strategy was changed. Now, it is intended to store the complete RPV in an interim storage near the NPP. Therefore, a special trepanning machine had to be designed. The trepanning machine shown in Fig. 1 allows the following remote controlled actions:

- labeling the position and orientation of the trepan,
- drilling the trepan and ejection of the trepan into the RPV and
- closing the hole in the RPV with a lead plug.

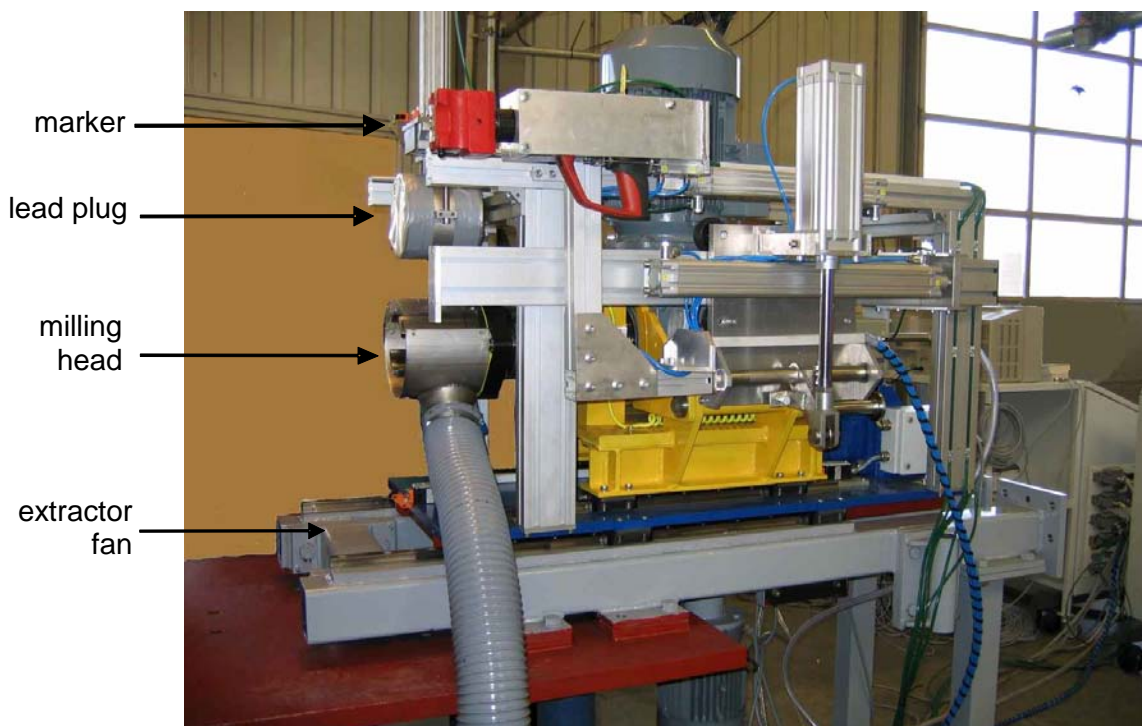


Fig. 1: Trepanning machine with the driving and positioning units and detail of the milling head

This trepanning machine was mounted outside of the RPV in the height of the coolant loops on the top of the annular water tank. This water tank has a shielding function and acts additionally as support construction of the RPV. To drill the trepans from the predefined positions, the whole RPV was lifted and rotated by crane. Before the drilling process was started, the selected position was marked and numbered. The trepan was drilled using an air

cooled hollow milling tool. The generated waste was collected by an extractor fan. The trepan was finally kicked into the RPV.



Fig. 2: Detail of the milling head

The drilled hole in the RPV was then closed by a lead plug. The plug was first cooled down by depressurization of CO₂-gas and pressed into the hole and fixed during the warming up phase. All the described actions are remote controlled.

The function of the drilling machine was tested in summer 2005. By thermographic measurement was proved, that the maximum temperature in the RPV material does not exceed 190°C direct in the drilling region and 80 °C within the body of the trepan, respectively. A negative influence on the material properties could so excluded. After transferring the machine to the NPP, a total of five trepans were gained from unit 1 end of 2005.

4. Location of the trepans in the RPV

Fig. 3 shows the location of the trepans taken from the RPV of Greifswald Unit 1. Trepans were taken from the welding seam SN0.1.4., and the base metal ring 0.3.1. Table 2 provides the location, the estimated neutron fluences ($E > 1$ MeV) of the trepans, and the maximum temperatures during the annealing procedure at the location of the trepans.

Table 2: RPV steels, irradiation and annealing conditions of the trepans sampled from Greifswald Unit 1

code	RPV material	location		condition	inner wall fluence in 10^{18} n/cm ²	annealing temperature in °C
		axial in mm	azimuthal in grd			
A1	weld metal SN0.1.4	-6850	330	IAI	29.4	475
A2	weld metal SN0.1.4	-6850	270	IAI	29.4	475
A3	weld metal SN0.1.4	-6850	90	IAI	29.4	475
B	base metal ring 0.3.1.	-6430	330	IAI	>29.4	475
C	base metal ring 0.3.1.	-4440	300	U	<0.07	<300

IAI irradiated, annealed, irradiated after annealing
 U unirradiated

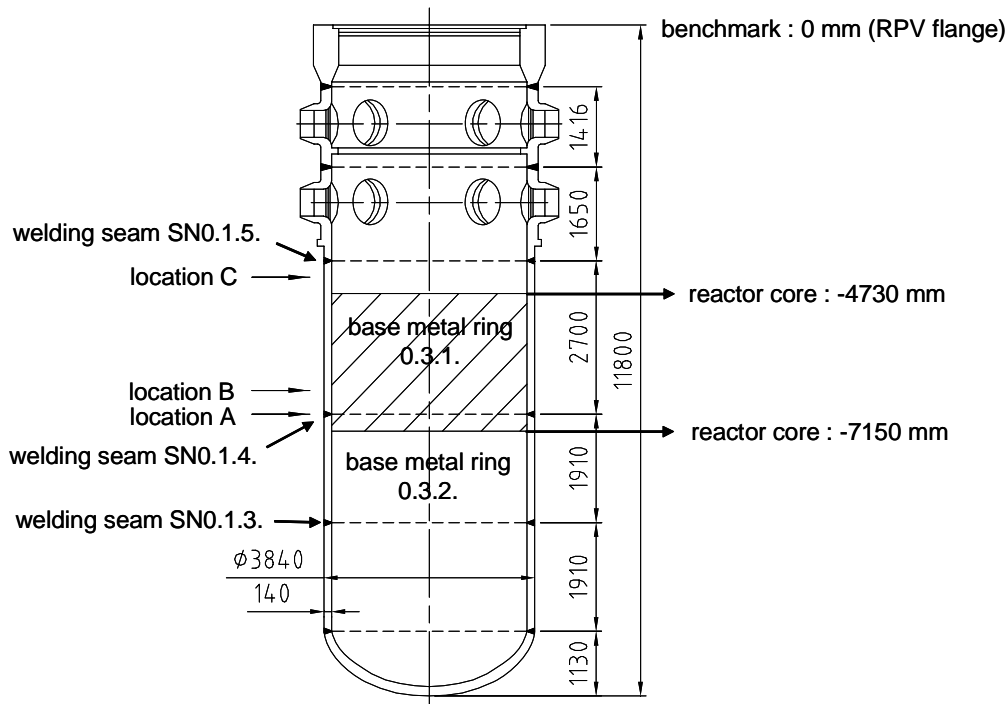


Fig. 3: RPV VVER 440 Greifswald Unit 1 and locations of the sampled trepans

The trepans were transported to the Hot Cell laboratory of the Institute for Safety Research for the planned investigations.

5. Running research program

A comprehensive research program was started in 2006 around the gained trepans. The aim of these investigations is to evaluate the material state of a standard RPV design and to assess the quality of prediction rules and of the state of the art assessment tools, as well as of the advanced RPV integrity assessment codes.

The program includes the following main parts:

- Calculation of the received neutron/gamma fluence in a fine grid. These calculations will be performed using the Monte Carlo code TRAMO [1].
- Verification of the calculated fluence with measured Niobium activities. Nb is a well suited monitor to measure the fast fluence of reactor pressure vessels [2]. The low Nb content in the material will be a special challenge, because Nb is only contained as trace metal in base as well as weld material.
- Investigation of microstructure [3] and chemical composition, i.e.:
 - chemistry profiles
 - metallographic characterization
 - SANS investigations
- Investigation of the mechanical properties [4] of the weld and the base metal, i.e.:
 - cleavage fracture toughness values and Master Curve based reference temperatures,
 - J- Δa curves and ductile initiation fracture toughness values,
 - full Charpy-V transition curves,
 - tensile properties,
 - hardness HV10 properties.

References

- [1] H.-U. Barz, J. Konheiser, Monte-Carlo Programm TRAMO - Möglichkeiten und Anleitung zur Nutzung, FZR Bericht-245, Rossendorf, Dezember 1998
- [2] L.B. Baers, E.K. Hasanen, Neutron Flux estimations Based on Nb Impurities in Reactor Pressure Vessel Steel, Reactor Dosimetry ASTM STP 1228, Harry Farrar IV, E. Parvin Lippincott, John G. Williams and David W. Vehar, Eds., American Society for Testing and Materials, Philadelphia, 1994.
- [3] A. Ulbricht (2006), Untersuchungen an neutronenbestrahlten Reaktordruckbehälterstählen mit Neutronen-Kleinwinkelstreuung, Dissertation, TU BA Freiberg, 23.März 2006, Wissenschaftlich-Technische Berichte, Forschungszentrum Rossendorf, FZR-453, April 2006, ISSN 1437-322X
- [4] Viehrig, H.-W.; Scibetta, M.; Wallin, K., Application of advanced Master Curve approaches on WWER-440 reactor pressure vessel steels International Journal Pressure Vessel and Piping 83(2006), pp. 584-592

SANS RESPONSE OF VVER440-TYPE WELD MATERIAL AFTER NEUTRON IRRADIATION, POST-IRRADIATION ANNEALING AND REIRRADIATION

Andreas Ulbricht and Frank Bergner

1. Introduction

Thermal annealing of embrittled reactor pressure vessel (RPV) steel and weld material is a well-known option for life time extension of light water reactors [1]. In fact, large-scale annealing of the core belt region for the purpose of life time extension was successfully applied in a number of cases including the first-generation VVER440-type RPVs [1]. In the last three decades major scientific efforts have been focussed on the optimization of the temperature-time regime for recovery of mechanical properties, the methodology for verification of the annealing effect (i.e. degree of reversal of irradiation hardening and embrittlement) using non-destructive techniques or small-specimen tests, and the phenomenological description of the reirradiation behaviour of RPV steels based on mechanical testing.

However, mechanistic understanding of the materials response to neutron irradiation, post-irradiation annealing and reirradiation is still far from being satisfactory or even complete. Indirect conclusions about the mechanisms underlying the annealing and reirradiation response of RPV steels and welds have been drawn via analysing results of mechanical testing and fractographic observations [2] of these materials. More direct evidence has been collected by means of quantitative TEM [2] and three-dimensional atom probe field ion microscopy (3DAP) [3]. In particular, it was shown that reirradiation-induced microstructural changes are different from the original irradiation response not only quantitatively but also in nature [3]. In the present paper results are reported of small-angle neutron scattering (SANS) experiments performed for a VVER440-type weld material including three reirradiated conditions and a reirradiated and annealed condition [4].

2. Experiments

The material investigated is VVER440-type weld material Sv10KhMFT of the composition given in Table 1 in a total of seven different irradiation conditions summarized in Table 2. Irradiations were carried out at surveillance positions of NPP Loviisa (Finland). The irradiation temperature was 270°C. Specimens were provided by VTT Espoo (Finland) as slices of dimensions of 10 mm by 10 mm and thickness of 0.8 mm. No additional surface preparation was needed for the SANS experiments.

The SANS measurements were carried out at the PAXE spectrometer of the Orphee research reactor at LLB Saclay and at the BENSC V4 spectrometer of HMI Berlin. A neutron wavelength of 0.5 nm ($\pm 10\%$) at half maximum was used. A beam diameter of 8 mm was realized by a Cd aperture fixed directly in front of the sample. The SANS intensity was measured with a 2-dimensional 64 cm x 64 cm BF₃-detector (LLB) or ³He-detector (HMI) at two different sample-detector distances of about 1 m and 4 m corresponding to a measuring range of the scattering vector of approximately 0.13 nm⁻¹ to 2.9 nm⁻¹. During the SANS measurements the samples were placed in a saturation magnetic field of 1.4 T perpendicular to the neutron beam direction. The scattering intensity was calibrated by direct measurement of the intensity of the incident beam. The calibration was checked by comparing the measuring results for a reference sample of known scattering cross section.

Table 1: Composition (wt.-%)

C	Mn	Si	Cr	Ni	Mo	V	S	P	Cu	Co
0.06	1.14	0.40	1.63	0.11	0.48	0.20	0.016	0.035	0.14	0.010

Table 2: Irradiation conditions

Designation	Details
U	unirradiated
I	irradiated ($\Phi = 2.5 \cdot 10^{19} \text{ cm}^{-2}$, $\varphi = 3.0 \cdot 10^{11} \text{ cm}^{-2} \text{ s}^{-1}$)
IA	annealed (475 °C / 100 h) after irradiation
IAI-1	reirradiated ($\Phi = 0.9 \cdot 10^{19} \text{ cm}^{-2}$, $\varphi = 3.0 \cdot 10^{11} \text{ cm}^{-2} \text{ s}^{-1}$)
IAI-2	reirradiated ($\Phi = 1.8 \cdot 10^{19} \text{ cm}^{-2}$, $\varphi = 3.0 \cdot 10^{11} \text{ cm}^{-2} \text{ s}^{-1}$)
IAI-3	reirradiated ($\Phi = 2.7 \cdot 10^{19} \text{ cm}^{-2}$, $\varphi = 3.0 \cdot 10^{11} \text{ cm}^{-2} \text{ s}^{-1}$)
IAI-3A	annealed (475 °C / 100 h) after reirradiation 3

Φ and φ denote neutron fluence and flux for neutron energies, $E > 1 \text{ MeV}$.

The SANS data were processed by software routines of LLB and BENSC. In particular, the angular dependence of the scattered neutron intensity was utilized to separate the magnetic contribution from the total scattered intensity.

3. Results

The measured scattering cross section is composed of coherent and incoherent contributions. The incoherent contribution was eliminated assuming the scattering intensity to follow Porod's law (i.e. to be proportional to Q^{-4}) for large values of the scattering vector, Q . After subtraction of the incoherent contribution, the coherent scattering cross section is determined as shown in Fig. 1 for the unirradiated (U), the irradiated (I), and the irradiated and annealed (IA) condition of the VVER440-type weld material. Irradiation clearly raises the nuclear and the magnetic contribution to the scattering cross section for $Q > 0.8 \text{ nm}^{-1}$ (see Fig. 1b,c) in an analogous manner. Annealing reduces the effect to the initial level and gives rise to a small increase of the magnetic contribution in the Q range from 0.5 to 0.8 nm^{-1} (see Fig. 1c).

Further analysis is based on the indirect transformation method and provides the size distribution or the number density distribution of scatterers without assuming a certain type of distribution. According to our standard analysis we have assumed that the system consists of isolated scattering particles in a homogeneous matrix (two-phase approach), the particles are spherical and non-magnetic and the particle size is spatially uncorrelated. Multiple scattering is minimized by choosing a sufficiently small sample thickness on the expense of scattering intensity and measuring time.

The assumption of non-magnetic scatterers may be invalid in the case of significant fractions of Fe or Ni in the clusters. The size distributions given in this paper were still valid on a relative scale in this case, but the calculated absolute values of the volume fractions and number densities of scatterers would have to be interpreted as lower bound values. The issue is discussed in [5] but not solved completely. However, if the cluster composition is given, the size distribution of clusters can be calculated from the nuclear scattering cross section without any assumption on the magnetic character of the clustered atoms.

The size distribution of clusters obtained on the assumption of non-magnetic scatterers is presented in Fig. 2. It exhibits the features characteristic of RPV steels: a broad distribution without a clear maximum in the size range up to 10 nm in the unirradiated condition and an

additional sharp peak near a radius of 1 nm in the irradiated condition. Annealing reduces the volume fraction in the peak position to the initial level. Simultaneously, a new smaller peak appears centred at about 3 nm of radius. These effects can be traced back to the scattering curves (see Fig. 1c).

The same procedure applied to the reirradiated samples yields the results depicted in Figs. 3 and 4. We have observed that: (1) There is a reirradiation-induced increase of the volume fraction of scatterers in the size range around 1 nm of radius as for the original irradiation. (2) The increase due to reirradiation is smaller than due to the original irradiation. (3) The increase saturates at a neutron fluence corresponding to condition IAI-2. (4) The volume fraction of scatterers formed in the size range around 3 nm as a result of annealing remains unchanged. (5) Annealing of the reirradiated material in turn results in a reduction of the volume fraction around 1 nm of radius and a slight increase of the volume fraction of scatterers in the size range around 3 nm.

The above observations suggest the distinction of two particle size ranges: The first one from 0.5 nm (lower detection limit of SANS for commercial Fe-based alloys) to about 2.5 nm essentially applies to the irradiation or reirradiation response. The second range from about 2.5 nm to 4.5 nm is important for the annealing response after irradiation or reirradiation.

The *A*-ratio is defined as ratio of the SANS cross sections perpendicular and parallel to the direction of the applied saturation magnetic field and can be expressed as the ratio of the total SANS cross section and the nuclear cross section. The *A*-ratio was estimated by integrating the respective size distributions over either size range (0.5 to 2.5 nm and 2.5 to 4.5 nm) separately. The estimated values of the *A*-ratio are compiled in Table 3. Of course, the *A*-ratio can only be calculated provided that a significant volume fraction of scatterers has formed.

Table 3: Values of the A-ratio for extra scattering over the given reference conditions

Condition	Reference	<i>A</i> -ratio (0.5-2.5 nm)	<i>A</i> -ratio (2.5-4.5 nm)
I	U	1.56	-
IA	U	-	>10
IAI-1	IA	1.74	-
IAI-2	IA	1.88	-
IAI-3	IA	2.09	-
IAI-3A	IA	-	>10

4. Discussion

The major observation of the present investigation consists in the formation of irradiation-induced clusters in the size range from 0.5 to 2.5 nm (radius), the disappearance of these clusters after annealing accompanied by the appearance of scatterers in the size range from 2.5 to 4.5 nm, and the appearance of reirradiation-induced clusters in the former size range.

A more detailed discussion of the present results depends on the knowledge about the composition of the scatterers. Unfortunately, the composition of the detected irradiation-induced clusters cannot be inferred from SANS measurements alone. However, any candidate composition can be checked for consistency by comparing calculated and measured values of the *A*-ratio [5]. Cluster compositions observed by means of 3D Atom Probe investigations (3DAP) for similar VVER440-type weld material (0.16 wt.-% Cu) irradiated under similar

conditions are reported in [3]. These clusters are characterized as coherent Cu-Si-Mn-Ni-P-enriched clusters of about 2 nm in diameter and of a number density of $5 \times 10^{23} \text{ m}^{-3}$ [3].

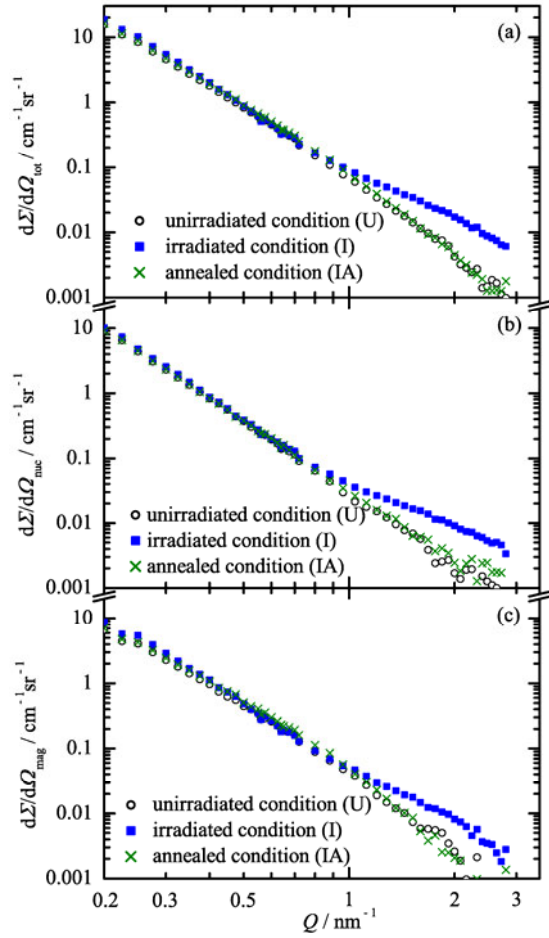


Fig. 1: Coherent neutron scattering cross section for unirradiated and irradiated conditions and after post-irradiation annealing; (a) total cross section, $d\Sigma/d\Omega_{tot}$, (b) nuclear cross section $d\Sigma/d\Omega_{nuc}$, (c) magnetic cross section $d\Sigma/d\Omega_{mag}$.

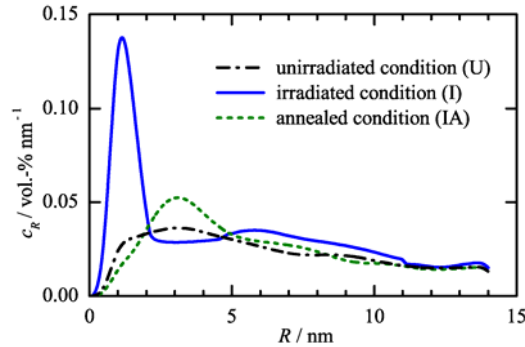


Fig. 2: Size distribution function, c_R , for unirradiated and irradiated conditions and after post-irradiation annealing calculated by Fourier transformation of curves from Fig. 1c assuming non-magnetic scatterers.

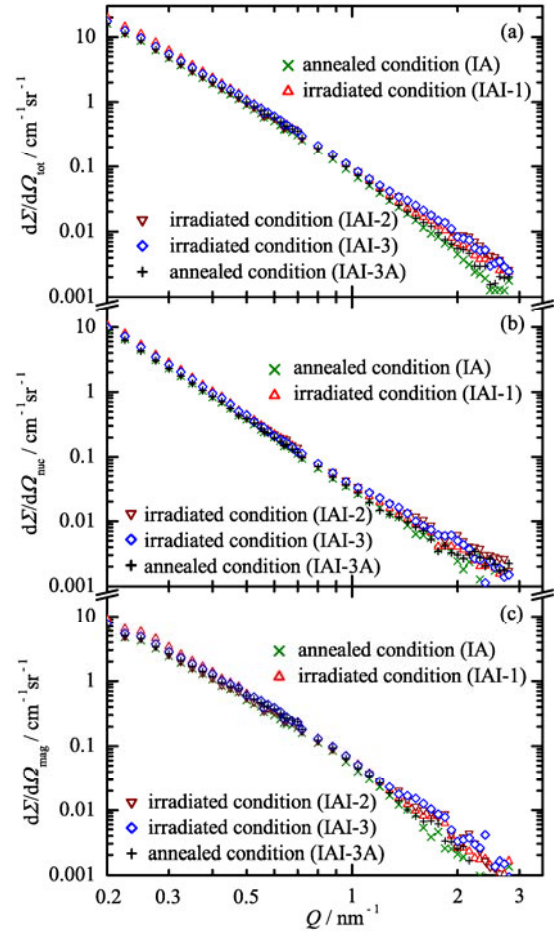


Fig. 3: Coherent neutron scattering cross section for annealed and reirradiated conditions and after post-irradiation annealing; (a) total cross section $d\Sigma/d\Omega_{tot}$, (b) nuclear cross section $d\Sigma/d\Omega_{nuc}$, (c) magnetic cross section $d\Sigma/d\Omega_{mag}$.

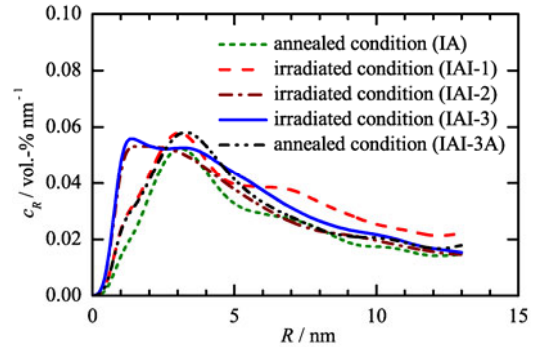


Fig. 4: Size distribution function, c_R , for annealed and reirradiated conditions and after post-irradiation annealing calculated by Fourier transformation of curves from Fig. 3c assuming non-magnetic scatterers.

In order to check for consistency of the typical compositions reported in [3] with the A -ratios obtained in the present case, a theoretical A -ratio was calculated according to eqs. (1)-(3).

$$A = 1 + \left(\frac{\sum_i n_i^{\text{Cluster}} b_{\text{mag},i}^{\text{Cluster}} - \sum_i n_i^{\text{Matrix}} b_{\text{mag},i}^{\text{Matrix}}}{\sum_i n_i^{\text{Cluster}} b_{\text{nuc},i}^{\text{Cluster}} - \sum_i n_i^{\text{Matrix}} b_{\text{nuc},i}^{\text{Matrix}}} \right)^2 \quad (1)$$

In equ. (1), b and n refer to scattering length and atomic fraction, respectively, subscripts nuc and mag refer to nuclear and magnetic scattering, respectively. Summation is performed over all types of atoms constituting cluster or matrix. If we restrict ourselves to the species the clusters are enriched with [3], ignore strain fields, assume the matrix to be pure Fe and assume the magnetic moments of Fe and Ni in the clusters to be the same as in the matrix, equ. (1) simplifies to

$$A = 1 + \left(\frac{6.0(n_{\text{Fe}} - 1) + 1.0n_{\text{Ni}}}{9.45(n_{\text{Fe}} - 1) + 10.3n_{\text{Ni}} + 7.72n_{\text{Cu}} - 3.75n_{\text{Mn}} + 4.15n_{\text{Si}} + 5.13n_{\text{P}}} \right)^2 \quad (2)$$

where the coefficients in the nominator are the values in units of fm (10^{-15} m) of the magnetic scattering length for Fe and Ni, the coefficients in the denominator are the values in units of fm of the nuclear scattering length for Fe, Ni, Cu, Mn, Si, and P. In the case of clusters containing a vacancy fraction, n_{vac} , the concentrations in equ. (2) have to be rescaled according to equ. (3):

$$n_{\text{Fe}} + n_{\text{Ni}} + n_{\text{Cu}} + n_{\text{Mn}} + n_{\text{Si}} + n_{\text{P}} = 1 - n_{\text{vac}} \quad (3)$$

The cluster compositions reported in [3] give A -ratios of 3.85 and 7.90 for typical clusters in the matrix and along dislocation lines, respectively, if vacancy-free clusters are assumed. Varying the levels of the cluster-constituting elements within the reported error range [3] gives rise to a maximum reduction of the calculated A -ratio down to about 3. We find the measured A -ratio of the irradiation-induced clusters (1.6 ± 0.1) to be significantly smaller than the calculated ones. This discrepancy can only be resolved assuming a vacancy fraction in the average clusters of at least 38% not detected by means of 3DAP.

Annealing is accompanied by the disappearance of the irradiation-induced volume fraction of clusters in the size range from 0.5 to 2.5 nm and the formation of a smaller fraction in the size range from 2.5 to 4.5 nm (Fig. 2). The high A -ratio ($A > 10$, Table 3) indicates that the scatterers observed after annealing are Cu-rich precipitates. This is in agreement with the conclusion inferred by Pareige et al. [3] from the reported 3DAP observations after reirradiation [3]. The Cu-rich precipitates are still coherent with the Fe matrix.

The basic observation from the SANS experiments for the reirradiated specimens (conditions IAI-1, IAI-2 and IAI-3) is that clusters are formed in the same size range and with a similar distribution as in the case of the original irradiation (condition I). These clusters are characterized by a slightly higher A -ratio than for the original irradiation and the A -ratio further increases with increasing neutron fluence (see Table 3). Furthermore, as the agreement of the volume fractions for conditions IAI-2 and IAI-3 (see Fig. 4) shows, the formation of reirradiation-induced clusters observed by SANS strongly decelerates or even saturates in the fluence range near or below the fluence corresponding to condition IAI-2. Provided the

magnetic character of the reirradiation-induced clusters and the clusters formed during the original irradiation is about the same, the maximum value of the volume fraction is only half as high as the volume fraction observed after the original irradiation. No significant reirradiation-induced changes in the size range larger than 2.5 nm are observed.

5. Conclusions

Irradiation-induced clusters in VVER440-type weld material are observed by SANS and contrasted with previous 3DAP measurements for similar weld material [3]. There is a discrepancy between the A -ratios measured by SANS and calculated on the basis of the reported composition. The conflict can be removed, if the average cluster is assumed to contain vacancies not detected by 3DAP.

Thermal annealing at 475 °C/100 h results in complete disappearance of irradiation-induced clusters in the size range from 0.5 to 2.5 nm accompanied by a reversal of the irradiation-induced hardness increase and in the formation of scatterers of radii between 2.5 and 4.5 nm. Because of their high A -ratio ($A > 10$) these scatterers are identified as Cu-rich precipitates.

As a result of reirradiation after annealing, clusters are formed in the same size range (0.5-2.5 nm) as for the original irradiation but their formation strongly decelerates or saturates at a smaller volume fraction. The new average cluster differs in composition from the original one.

References

- [1] T. Planman, R. Pelli, K. Törrönen (1995), Irradiation embrittlement mitigation, AMES Report No. 1, EUR 16072 EN, European Commission
- [2] B.A. Gurovich, E.A. Kuleshova, O.V. Lavrenchuk, K.E. Prikhodko, Ya.I. Shtrombakh (1999), The principal structural changes proceeding in Russian pressure vessel steels as a result of neutron irradiation, recovery annealing and re-irradiation, *J. Nucl. Mater.*, 264, 333
- [3] P. Pareige, B. Radiguet, R. Krummeich-Brangier, A. Barbu, O. Zabusov, M. Kozodaev (2005), Atomic level observation with three-dimensional atom probe of the solute behaviour in neutron-, ion- or electron-irradiated ferritic alloys, *Phil. Mag.* 85, 429
- [4] A. Ulbricht, F. Bergner, J. Böhmert, M. Valo, M.-H. Mathon, A. Heinemann (2007), SANS response of VVER440-type weld material after neutron irradiation, post-irradiation annealing and reirradiation, *Phil. Mag.* 87, 1855
- [5] R. G. Carter, N. Soneda, K. Dohi, J. M. Hyde, C. A. English, W. L. Server (2001), Microstructural characterization of irradiation-induced Cu-enriched clusters in reactor pressure vessel steels, *J. Nucl. Mater.* 298, 211

Acknowledgement

The material was provided by M. Valo (VTT Espoo, Finland). The assistance of M.-H. Mathon (LLB Saclay, France) and A. Heinemann (HMI Berlin) in the SANS experiments is gratefully acknowledged.

SIMULATION OF THE CORIUM-RPV-WALL INTERACTION FOR AN IN-VESSEL-RETENTION SCENARIO

Eberhard Altstadt and Hans-Georg Willschütz

1. Introduction

The improbable scenario of a severe accident with core meltdown and formation of a melt pool in the lower plenum of a Light Water Reactor (LWR) Pressure Vessel (RPV) can result in the failure of the RPV and the discharging of the melt to the containment. One accident management strategy could be to stabilize the in-vessel debris or melt pool configuration in the RPV as one major barrier against uncontrolled release of heat and radionuclides into the containment.

Based on the successful simulation and analysis work of the FOREVER-experiments [1] models have been developed to simulate the prototypical scenario of an In-Vessel-Retention in large PWRs [2]. From recently observed results of the METCOR-Experiments, it is known that the vessel wall ablation in case of melt-wall-contact can take place well below the steel melting point of $T = 1493 \text{ }^\circ\text{C}$. The finite element (FE) model developed at FZD was improved to consider the time dependent thermo chemical wall ablation process. Figure 1 shows the principal configuration of the considered scenario.

2. Modelling the thermo chemical interaction between melt and wall

Due to the high heat fluxes from the melt pool to the vessel wall it is obvious that a partial wall ablation will occur even if there is no dry out of the externally flooded vessel wall. Formerly an ablation of the internal wall elements was considered when the corresponding elements reached the melting point of steel. This approach is not conservative since the thermo chemical corrosion is neglected. In the frame of the METCOR-programme, performed at the Alexandrov-Research Institute (NITI) in Sosnovy Bor near St. Petersburg, the melt-metal-interaction is investigated in small scale experiments [3]. The results show, that the ablation of the steel starts clearly below its melting point due to the formation of eutectics. This process is dependent on the melt composition.

In the METCOR-tests, the corium is heated inductively, using the technology of the cold crucible. The melt is on top of a steel specimen, which is instrumented with thermo elements and ultrasonic sensors. Figure 2 shows the general setup of the experiments.

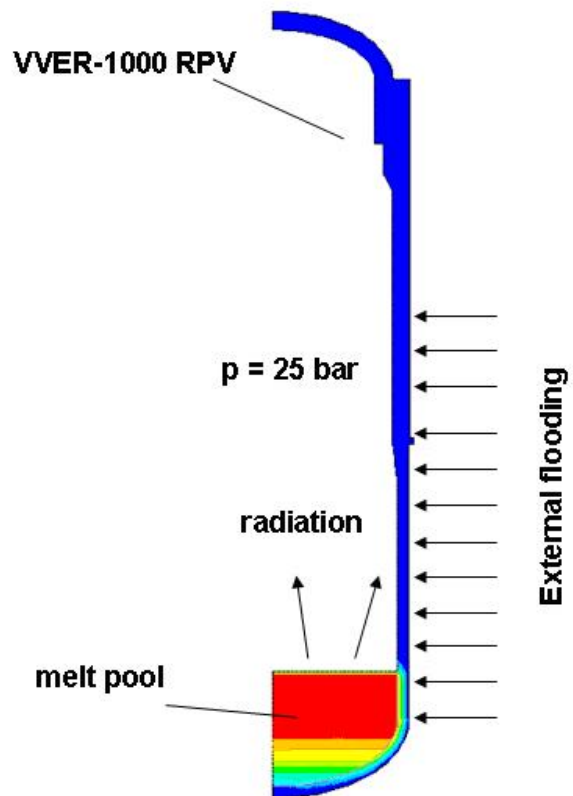


Fig. 1: Model overview for a VVER-1000 In-Vessel-Retention analysis.

Till now, the investigations were focussed on the RPV-steel 15 Kh2NMFAA (VVER-1000).

The progress of the ablation front is monitored by the thermocouples and ultrasonic sensors. The heat flux from the melt to the steel and respectively the interface temperature between corium crust and steel surface can be regulated by the cooling of the probe from the lower side or by adjusting the heat generation rate in the melt. A large number of tests were performed where the melt composition, the thermal conditions, and the atmosphere above the melt were varied.

For a suboxidized corium melt (oxidation 30 %) the following correlation for the ablation rate has been derived from the experimental results [3]:

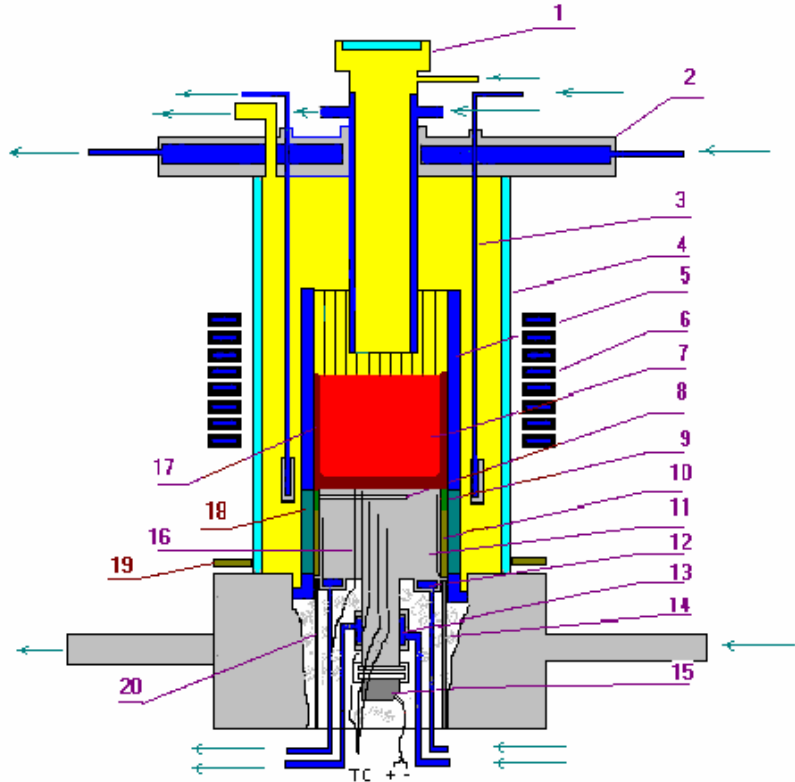


Fig. 2: Setup of the METCOR-Experiments: 1 – pyrometer shaft; 2 – cover; 3, 18, 19 – electromagnetic screens; 4 – quartz tube; 5 – crucible sections; 6 – inductor; 7 – melt; 8 – acoustic defect; 9 – fused ZrO_2 grains; 10 – ZrO_2 powder insulation; 11 – vessel steel specimen; 12 – top specimen calorimeter; 13 – bottom specimen calorimeter; 14 – kaolin wool insulation; 15 – ultrasonic sensor; 16 – thermocouples; 17 – crust; 20 – cylindrical support of the specimen: Source: S. Bechta (NITI).

$$\dot{h} = 0.46 \cdot 10^{-7} \frac{m}{s} \cdot \sqrt{\frac{T_{int} - T_B}{1K}} \quad (1)$$

Where \dot{h} is the ablation rate in meters per second, T_{int} the interface temperature and T_B the bounding temperature, where the ablation starts. The implementation within the FE-model is realised via the introduction of a corrosion damage variable D_{corr} for each element. The increment for the damage is calculated according to the following equation:

$$\Delta D_{corr}^{el} = \frac{\dot{h}(T_{int})}{h_{el}} \cdot \Delta t \quad (2)$$

$$D_{corr}^{el}(t) = D_{corr}^{el}(t - \Delta t) + \Delta D_{corr}^{el}$$

Here h_{el} is the element thickness perpendicular to the interface, \dot{h} represents the ablation rate (cf. eq. (1)). The interface temperature is calculated from those nodes which belong to the interface:

$$T_{int} = \frac{1}{N_i} \sum_{n=1}^{N_i} T_n \quad N_i = \{2, 3, 4\} \quad (3)$$

The number of interface nodes of a 4-node-element can range between 2 and 4. Figure 3 shows the approach in principle. If the corrosion damage of an element reaches the value 1 or

higher, the element status is changed from solid to liquid. This includes a material property change.

3. Investigation of a VVER-1000 Scenario

In [4] a possible – but nevertheless very unlikely – core melt down scenario is described for a VVER-1000. The scenario considers an uncontrolled Loss-of-Coolant Accident (break of surge line, diameter 346 mm). The time dependent decay heat, the melt composition, and the melt mass values are considered as calculated in [4] for the analysis discussed here. The main stages after the initiating event of the scenario are as follows:

- 2680 s: first relocation of molten fuel,
- 2710 s: filling of the stand pipes of the lower core support,
- 4210 s: melt through of the ground plate of the lower core support,
- 5730 s: melt relocation into the lower head.

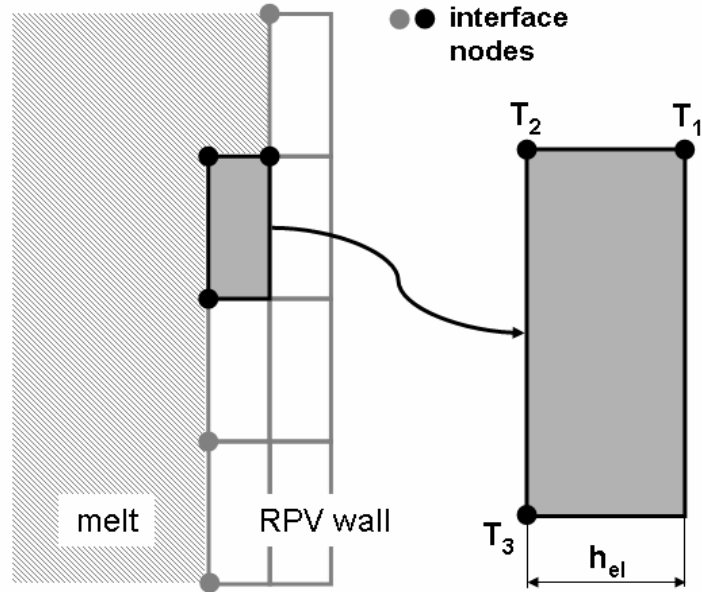


Fig. 3: Illustration of the calculation of the corrosion damage of elements at the interaction interface.

Table 1 summarizes the composition of the lower head melt pool. In the FZD-calculations, a homogeneous melt pool is assumed, i.e. no segregation of metallic and oxidic phases is modelled. The total melt mass of 165 t (20.7 m³) leads to a total melt height of 1.91 m under the geometrical conditions of the VVER-1000. The oxidation degree of the melt is C=0.357. The time dependent internal heat generation due to the decay is shown in Figure 4.

Table 1: Composition of the melt pool in the VVER-1000 scenario.

Component	Density [kg/m ³]	Mass %	Mass [t]	Volume [m ³]
Steel	7000	36.8	60.7	8.7
Zr	6000	8.6	14.2	2.4
ZrO ₂	5600	6.4	10.6	1.9
UO ₂	10300	48.2	79.7	7.7
<i>Total</i>	<i>7993</i>	<i>100</i>	<i>165.2</i>	<i>20.7</i>

At the beginning of the considered scenario, the total heat generation is some 193.5 MW which corresponds to 6.45 % of the nominal thermal power. Approximately 20 % of the power are not generated within the melt, because gaseous fission products and aerosols are rising up in the RPV. At the time of melt pool formation in the lower head (t_{sc}=5700 s) – which corresponds to the starting time for the IVR-simulation – the power released within the

pool amounts to some 30 MW, i.e. the heat generation density is 1.45 MW/m³. Table 2 shows the simulated material properties of the corium melt.

Table 2: Thermodynamic material properties of the homogeneous melt.

Liquidus temperature [K]	2 000
Heat of fusion [kJ/kg]	260
Density [kg/m ³]	8 000
Volumetric thermal expansion coefficient [1/K]	1.0 10 ⁻⁴
Heat conductivity [W/m K]	2.5
Specific heat capacity [J/kg K]	530
Dynamic viscosity [Pa s]	0.0045

A total external RPV flooding is assumed for the thermal simulation of the melt retention. Without flooding the vessel wall would fail within a short time, since the necessary temperature for a balanced heat release from the external surface via radiation is well above the melting point of the steel.

For the mechanical analysis an internal pressure of 25 bar is assumed. Two simulation cases of this scenario were performed:

Case A: No thermochemical interaction is considered, i.e., melting of the wall takes place only, if the melting point of the steel is exceeded.
Case B: The thermochemical interaction is considered according to eq. (2).

Figure 5 shows the ablation kinetics of

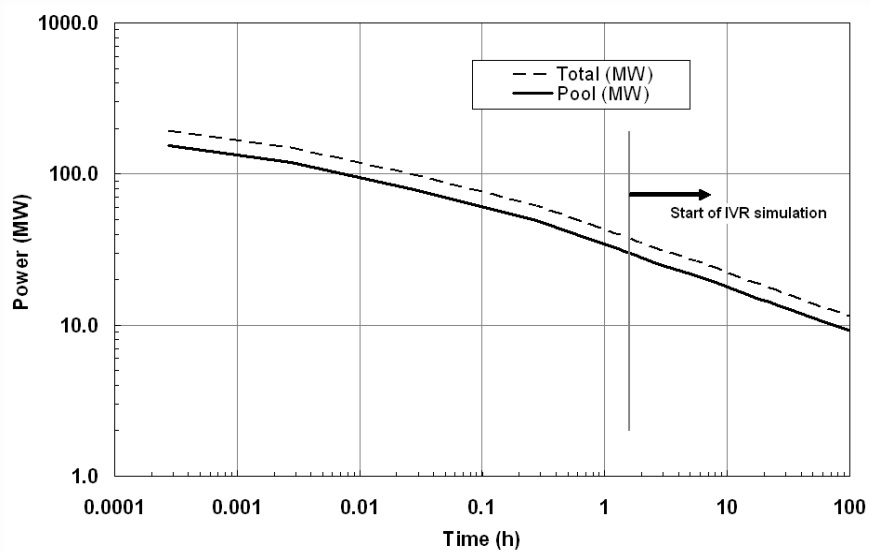


Fig. 4: Decay heat generation in the melt pool (VVER-1000).

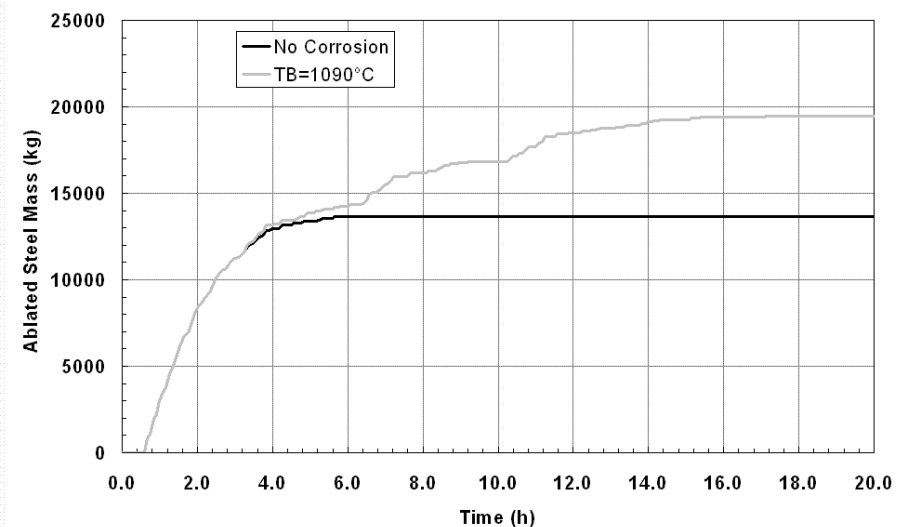


Fig. 5: Ablation kinetics (steel mass eroded from the RPV wall over time); grey with corrosion damage consideration, black without.

both calculations. At the beginning both curves are identical ($0 < t < 4$ h), this is the pure wall ablation regime due to transgression of the steel melting point. Later on the black curve (case A) becomes constant, i.e., the wall has reached that residual wall thickness, that allows the required heat flux at the given temperature difference. The temperature difference is defined by the melting point inside and the boiling surface superheat temperature outside. Contrary to this the grey curve for case B shows a further progress in the wall ablation, because the corrosion proceeds until the wall thickness is reduced to that value, that allows an internal temperature equal to the bounding temperature $T_B = 1090$ °C (compare to eq. (1)). At this point the corrosion is stopped.

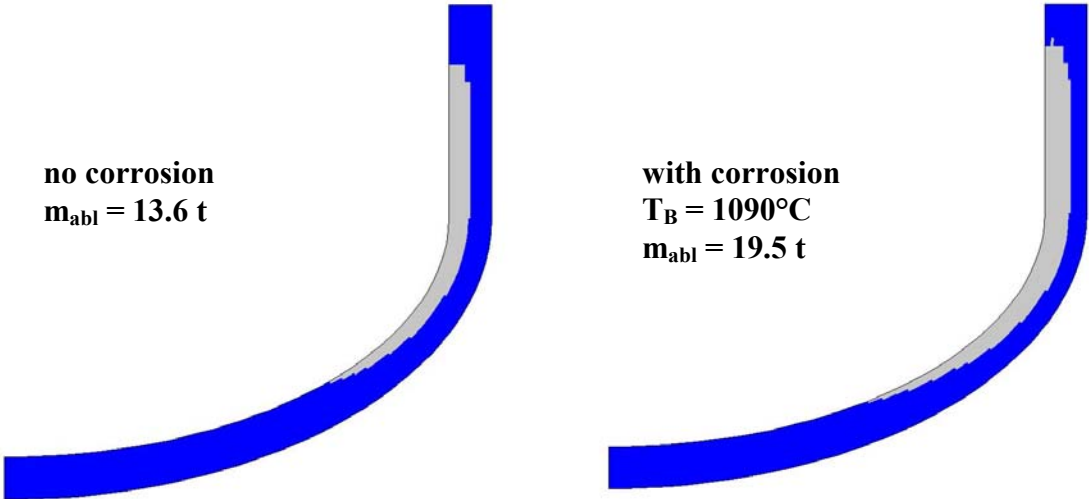


Fig. 6: Lower part of the RPV after 20 h, left: case A, right: case B; the ablated respectively corroded portion is represented in grey.

Figure 6 shows the eroded final RPV-wall shape for both calculations. With corrosion the amount of mass eroded from the wall is some 43 % higher. The residual wall thickness for case A has a minimum of ca. 100 mm, while case B gives only 75 mm.

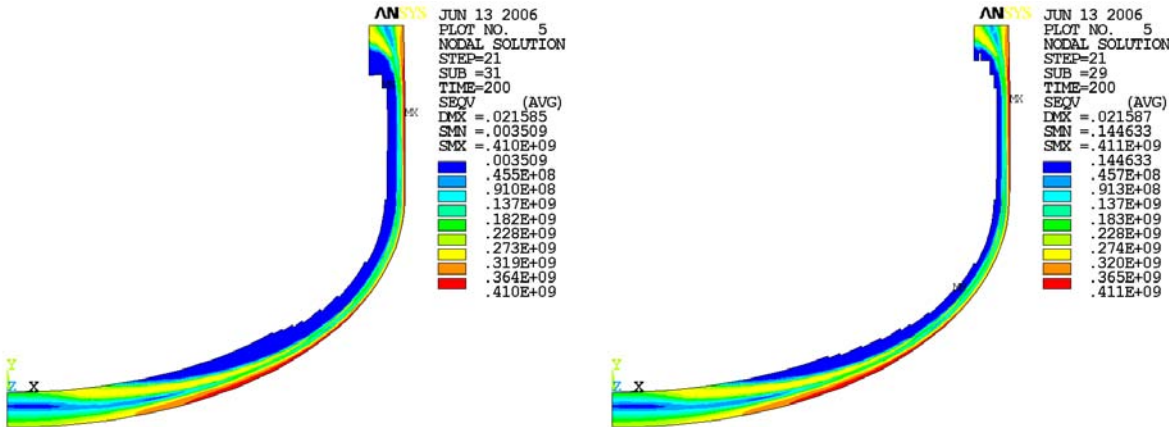


Fig. 7: Equivalent stress [Pa] in the lower part of the RPV, left case A, right case B.

The mechanical calculations have been performed considering the ablation processes. A viscoplastic material behaviour is modelled (cf. [5] for model description). Figure 7 shows the distribution of the equivalent stress in the lower part of the RPV within the final residual wall.

It can be seen that the maximum values are nearly identical despite the fact that the residual wall thickness is reduced by 25 %.

This is due to the strong temperature gradient over the vessel wall. The internal part is hot, i.e. close to the liquidus temperature of the steel for case A or close to the bounding temperature for case B. So especially in case A there is nearly no material strength to carry any relevant load at the wall inside. The load, consisting of dead weight and internal pressure, is carried almost exclusively by the external wall area, because this region is cooled by the external flooding and therefore shows a much higher strength.

4. Conclusions

An IVR scenario with external cooling of the RPV of a VVER-1000 was studied. The consideration of the thermo chemical interaction between the corium melt and the RPV wall leads to a considerable reduction of the residual wall thickness in comparison to the purely thermal driven ablation. However, this scarcely affects the strength of the remaining vessel wall, because the load is carried by the cold outer vessel parts. This statement is only valid if the external surface of the vessel is cooled by water at all times, so that the surface temperature is in the range of 110 °C. Thermo chemical processes are of bigger influence for scenarios with partial or delayed external flooding.

References

- [1] H.-G. Willschütz, E. Altstadt, F.-P. Weiss: Recursively Coupled FEM-Analysis Of Pressure Vessel Creep Failure Experiments. Jahrestagung Kerntechnik 2005, Proceedings on CD-ROM, pp. 202-208, Nürnberg, Germany, May 10-12, 2005.
- [2] H.-G. Willschütz, E. Altstadt, F.-P. Weiss: Application Of Recursively Coupled FE-Models To A PWR In-Vessel-Retention Analysis. Jahrestagung Kerntechnik 2006, Proceedings on CD-ROM, pp. 252-257, Aachen, Germany, May 16-18, 2006.
- [3] S. V. Bechta et al.; 2006. Experimental study of interactions between suboxidized corium and reactor vessel steel. Proceedings of the International Congress on Advances in Nuclear Power Plants (ICAPP) 2006, American Nuclear Society, KNS, SFEN, AESJ, SNE, 04.-08.06.2006, Reno, USA.
- [4] V. V. Bezlepkin et al.; 2003. Numerical investigation with RATEG/SVECHA/HEFEST Code on Possibility for long term In-Vessel Core melt retention. In: Voprosy atomnoj nauki i tehniki : Serija Fizika jadernych reaktorov: naucno-techniceskij sbornik / Rossijskij Naucnyj Centr Kurcatovskij Institut 4(2003) pp. 20-28 (in Russian).
- [5] E. Altstadt, H.-G. Willschütz: Beitrag zur Modellierung der Schmelzerückhaltung im RDB nach Verlagerung von Corium in das untere Plenum: Berechnung des Temperaturfeldes und der viskoplastischen Verformung der Behälterwand. Wissenschaftlich-Technische Berichte des Forschungszentrum Rossendorf; FZR-412, ISSN 1437-322X, Januar 2005.

Acknowledgement

The authors are grateful to Prof. Dr. S. V. Bechta, Alexandrov Research Institute of Technology (NITI), Sosnovy Bor, Russia, for the explanation of the METCOR-experiments the experimental results, and the derived correlations.

Summaries of research activities

Accident analysis of nuclear reactors

The research is aimed to improve the predictive capability of computer simulations of accident scenarios in nuclear reactors. This will be achieved by further developing the neutron kinetics methods and e.g. by coupling of the reactor dynamics core model DYN3D to thermo-hydraulics system codes and computational fluid dynamics (CFD) programmes. In particular, it is the objective to promote the basic understanding of coolant mixing phenomena relevant for boron dilution and pre-stressed thermal shock scenarios in Pressurized Water Reactors. Moreover, the field of applicability of the reactor dynamics simulations is going to be extended to innovative reactor concepts. Concerning severe accidents in Light Water Reactors, the aim is to better ascertain the capabilities of measures for in vessel retention of corium melt during severe LWR accidents.

*U. Grundmann,
S. Kliem,
Y. Kozmenkov,
S. Mittag,
U. Rohde,
F. Schäfer,
A. Gommlich,
G. Laczko*

Development, validation and application of the code complex DYN3D - ATHLET

The Rossendorf reactor dynamics code DYN3D is undergoing a continuous development with respect to the improvement of physical models and numerical methods. A multi-group approach was implemented for improved description of spectral effects, which are of increased importance in mixed-oxide (MOX) reactor core loadings. Moreover, a transport method was developed for DYN3D to overcome the limitations of the diffusion approximation. Within this approach, even a pin-wise calculation of the power distribution is offered. To validate the new version of DYN3D, an OECD benchmark on MOX cores was calculated.

The extended DYN3D version was integrated into the European code platform NURESIM. An interface to the platform was developed based on the NURESIM software environment SALOME. This makes it possible to link DYN3D to other components of the NURESIM platform. Moreover, a number of commercial licenses for DYN3D were provided to users in Germany and other European countries.

*Supported by
BMW, BMU, EC,
TÜV, Vattenfall
Europe Nuclear
Energy, VGB*

FZD was involved in analyses for regulatory procedures for NPP on request of the TÜV Hannover. Simulations of anticipated transients without scram (ATWS) for Pressurized and Boiling Water Reactors, including the corresponding methodical developments, were performed on demand of German utilities.

*T. Höhne,
S. Kliem,
U. Rohde,
T. Sühnel,
R. Vaibar*

Analysis of deboration transients

Based on experimental investigations of coolant mixing in PWR performed at the ROCOM test facility, various semi-analytical mixing models were developed and implemented into the coupled code system DYN3D/ATHLET. Using these tools, realistic boundary conditions concerning the core inlet distributions of coolant temperature and boron concentration can be provided for accident simulations. This leads to a reduction of conservatism and discloses reserves in operational limits of the power plants. Using the new tools, a number of boron dilution scenarios has been analysed. The results of the analyses are directly used in German nuclear safety assessment and regulatory procedures. The leading competence of FZD in boron dilution analyses is used in the framework of an EU TACIS project to support the Russian nuclear regulatory body.

*Supported by
BMW, EC and
VGB*

First experiments on the investigation of basic phenomena of buoyancy driven mixing of fluids with different density were performed at the new VEMIX test facility. Improved approaches for modelling buoyancy induced turbulence were implemented into the CFD code ANSYS-CFX. Validation of the new models is performed comparing CFD results with experimental data from the VEMIX facility.

*U. Grundmann,
J. Krepel,
U. Rohde*

Development of a DYN3D version for Molten Salt Reactors

Using a new version of the code DYN3D for dynamics studies of Molten Salt Reactors (MSR), which is one of the 'Generation IV' concepts, a series of reactivity initiated transients for that reactor type was analysed. The inherent safety features of the reactor concept could be demonstrated, provided that the core design ensures a negative reactivity feedback of the graphite temperature. This can be achieved by adding Erbium as a burnable absorber to the graphite. The subject was finalised with the defence of a superior PhD work.

*E. Krepper,
A. Grahn,
G. Cartland-Glover*

Simulation of sedimentation and re-suspension of insulating material in the reactor sump

Insulating material (mineral wool) may be released from pipes and components during loss-of-coolant accidents in NPP and will be transported with the coolant towards the reactor sump. There, it might lead to blockage of the sieves separating the suction chambers of the safety injection pumps from the sump and would impede late phase safety injection.

A follow-up research project has been started funded by BMWi aimed at the simulation of sedimentation and re-suspension of the mineral wool particles in the sump pool flow. The work is done in co-operation with the University of Applied Sciences Zittau/Görlitz, where the experiments are performed, while FZ Dresden-Rossendorf is responsible for the CFD modelling. Based on the results of the previous project, the new project is focussed on the modelling of the re-suspension of sedimented isolation material based on different CFD approaches (e.g. particle tracking, solidification models) as well as of an impinging water jet, which can re-mobilise sedimented material. A new physical model for the simulation of strainer clogging by agglomeration of mineral wool particles was implemented into the CFD code ANSYS-CFX.

*Supported by
BMW*

*H.-G. Willschütz,
E. Altstadt,
M. Abendroth*

In-vessel corium melt retention in LWRs

An empirical correlation of the Alexandrov Research Institute of Technology in Sosnovy Bor was applied, to consider the relationship between the corium oxidation degree, the interface temperature between melt and wall, and the resulting erosion rate of the RPV-steel. This correlation was extracted from the results of the METCOR-experiments. A successful running version of a corrosion damage model was implemented into the FE-model. Testing calculations were performed with the corrosion model for a VVER-1000 and for a German KONVOI. It could be shown that the consideration of the thermo-chemical corrosion leads to a significantly higher wall ablation. Nevertheless, under external flooding conditions a part of the RPV-wall still remains,

and the residual wall thickness is sufficient to carry the assumed mechanical loads. This is valid for VVER-1000 and for KONVOI reactors.

For the KONVOI the mechanical behaviour of the RPV after a thermal shock with a postulated crack (crack depth 1/10 of wall thickness) was modelled. The stress intensity was calculated with a local model via the J-integral. A homogeneous melt pool was assumed for this investigation. The 2D- and 3D-calculations show, that a further crack growth is unlikely under the assumed boundary conditions.

*supported by
BMW and EC*

Materials and components safety

The change in the toughness behaviour of reactor pressure vessel materials as a result of neutron and gamma irradiation is investigated. The consequences are evaluated with respect to the safety of light water reactors (LWRs). For this purpose, material and fracture mechanical parameters of irradiated specimens have to be measured under hot cell conditions. The interpretation of the experiments is supported by finite element calculations. The micro-structural reasons and mechanisms of the neutron embrittlement are studied by small angle neutron scattering experiments and by nano-scaled modelling.

*H.-W. Viehrig,
U. Rindelhardt,
E. Altstadt,
C. Zurbuchen,
J. Schuhknecht*

Investigation of reactor pressure vessel material of the dismantled Greifswald NPP

The investigation of the trepan (120 mm diameter, 140 mm length) taken from the RPV of unit 1 of the Greifswald NPP was started. One trepan from the core weld was cut into specimens using the discharging machine. The neutron fluence was calculated at 6 positions over the wall thickness. Fracture toughness and reference temperatures were determined according to the Master Curve concept. A supporting BMWi project could be launched in the frame of the Scientific Technical Cooperation with Russia. The Russian partners are Kurchatov-Institute Moscow, PROMETHEY St. Petersburg, and the Russian regulatory agency. Investigations on the unirradiated reference material from unit 8 were performed in cooperation with VTT Espoo, Finland, and SCK•CEN, Belgium.

*Supported by
BMWi*

*H.-W. Viehrig,
M. Abendroth,
M. Werner,
E. Altstadt,
C. Zurbuchen*

Application of the Master Curve concept to irradiated material

The BMWi project on the application of the master curve concept to highly irradiated RPV steels was successfully finished. The shift of the reference temperature T_0 with increasing neutron dose was investigated for three different RPV steels. T_0 was measured for the unirradiated and 3 different irradiated states. It was concluded that the master curve concept is well applicable to highly embrittled RPV steels. In the frame of the EU project PERFECT a data base (MySQL) for material data of RPVs was developed. The local approach model according to Beremin was applied to simulate the crack behaviour of irradiated VVER steels.

*Supported by EU,
BMWi and E.ON
Kernkraft*

*H.-W. Viehrig,
J. Schuhknecht,
M. Abendroth*

Small-Punch-Test (SPT) for the characterisation of irradiated reactor materials

In the frame of a common project with TU Bergakademie Freiberg, a special SPT gadgetry was designed and constructed for the hot cell laboratory. An adapted preparation technique was developed for irradiated SPT specimens. The SPT allows to measure fracture mechanical properties with small amounts of material.

*Supported by
BMWi*

*F. Bergner,
A. Ulbricht,
C. Heintze,
R. Kuchler*

Analysis of irradiation induced micro-structural changes

Small angle neutron scattering (SANS) experiments were performed at Hahn-Meitner-Institute (Berlin) with irradiated Fe based model alloys and with an irradiated, annealed and re-irradiated specimen of VVER weld material. Some remaining open questions regarding the influence of Ni could be answered. The results of the re-irradiated Greifswald weld specimen were compared with results for VVER-440 of different

origins. The results indicate that irradiation induced defects can be successfully annealed. After annealing the susceptibility to irradiation induced damage is significantly decreased.

A device for ultra micro hardness measurements and a connected atom force microscope (AFM) were put into operation. In the frame of a diploma thesis the depth sensing effect of the micro hardness was investigated using 3 different materials: RPV base material (bainitic steel), RPV cladding (austenitic steel) and the candidate material for fusion EUROFER 97 (martensitic steel). The micro hardness of the RPV steel and of EUROFER is dependent on the indentations depth. In contrast to that the austenitic cladding does not show the depth sensing effect.

Supported by EC

*F. Bergner,
U. Birkenheuer,
A. Gokhman,
R. Kuchler,
T. Schlemmer*

*Supported by EC,
BMW*

Modelling of irradiation induced embrittlement

Within a new BMWi project the development of a modular software package for evaluation of RPV steel embrittlement was started. Available stand alone routines were re-written in FORTRAN90 and tested with benchmark calculations. A detailed documentation of input parameters and of the implemented rate theory models was generated.

In the frame of EU-Project PERFECT, the French code RPV1 was applied to VVER-1000 steels.

Particle and radiation transport

The research project aims at the development, verification and application of computational methods for particle and radiation transport. At present, the focus is on neutron/gamma/electron transport with applications in reactor physics, shielding and radiation physical experiments.

The research project will be terminated at the end of 2007.

*J. Konheiser,
K. Noack,
G. Borodkin,
P. Borodkin*

Fluence and activity calculations for the pressure vessel of unit 1 of the decommissioned Greifswald NPP

In the framework of the German-Russian scientific-technical collaboration, neutron and gamma fluences were calculated along the depth of the vessel wall by means of the Monte Carlo code TRAMO and of the S_n -code DORT for trepans (120 mm diameter material probes) that were taken from the pressure vessel. The calculated values of the neutron fluences integrated over energies above 0.5 MeV were correlated with the material characteristics measured in the research project *Materials and Components Safety*. To verify the calculations, the specific activities of Nb-93m were calculated and measured at various points inside the trepan. The analysis of the results revealed an effect, which is not considered in the standard literature on reactor dosimetry, namely, that the Nb-93m activity can be produced through two channels: By neutron inelastic scattering at Nb-93 and by neutron capture at Mo-92. Both primary isotopes are contained in the bulk and weld material of the pressure vessel in such amounts that both channels yield activities of the same order. Consequently, an “experimental” value of the high-energetic neutron fluence can be derived only on the condition that the contribution by Mo-92 can be calculated with sufficient accuracy. For that, accurate neutron transport calculations covering the whole energy range were done and, subsequently, activity calculations for both channels were carried out, considering the built up and the decay of the Nb-93m activity over the reactor operation time and the cooling time of the vessel material. The present state of the analysis of calculated and measured activities is not yet satisfying: In some points the results agree within an acceptable deviation up to 30 %, but, for other points much greater discrepancies appear.

*Supported by
BMW*

*J. Konheiser,
K. Noack,
G. Borodkin,
S. Zaritsky*

Verification and application of TRAMO for fluence calculations in reactor dosimetry

In the framework of an STC-project with Russia, two topical issues of the Russian reactor safety research were studied. Both concern the safety of the pressure vessel of the Russian VVER-1000 type reactor. The first task consisted in examining the suitability of certain locations of a new system of surveillance specimens and the second task aimed at the calculation of the radiation load which accumulates in the support construction and in the weld No.5 of the RPV. The necessary neutron/gamma transport calculations were done by means of the Monte Carlo code TRAMO with the latest nuclear data libraries. The Russian partners used their codes and data libraries. Moreover, they made available the results of neutron activation measurements that were carried out in these reactor regions. In that way the codes and data

packages could be verified for both problems. The investigations were finished and led to the following important conclusions:

- Only a smaller part of the proposed locations for the Charpy-probes turned out to be suitable as surveillance specimens for the pressure vessel.
- In certain regions of the RDB-support construction and of the weld No.5 the accumulated fluence of high-energetic neutrons will exceed the limit that is defined in the Safety Regulations for the VVER-1000 reactor. The results demand both the re-evaluation of the mechanical loads, which could occur in these components during PTS-accidents (Pressurized Thermal Shock accidents) and the inclusion of these regions into the regular dosimetric monitoring.

*Supported by
BMW*

*K. Noack,
A. Rogov*

Burning of minor actinides in a sub-critical driven system

In the framework of a Co-ordinated Research Project of the IAEA the application of the gas dynamic trap (GDT) based fusion neutron source as driver of a sub-critical system for burning minor actinides was studied. The GDT neutron source was originally proposed by the Budker Institute Novosibirsk (Russia) as irradiation facility for fusion material research. The present study was focused on a project version the parameters of which were reduced for technical reasons and included the comparison with a spallation neutron source driven burner. The results of neutron transport calculations led to the following conclusions:

- The strength of the fusion neutron source is sufficiently high to drive a demonstration burner of minor actinides with a thermal power up to 150 MW.
- The comparison with a spallation neutron source driven burner reveals that the differences in the burning rates are negligibly small.
- The fusion neutron source suffers from the substantial disadvantage regarding the energetic efficiency, which turned out to be lower by almost one order of magnitude.
- The improvement of the energetic efficiency demands to considerably increase the electron temperature of the plasma, which just was artificially reduced in the recent project version.

*Supported by
BMBF*

D. Legrady

Monte Carlo simulations of the ELBE-n-TOF facility

Various simulations have been performed in the past for the neutronic design of the time-of-flight facility sometimes decoupling the electron-photon-neutron calculation. To incorporate the latest design changes, to verify the consistency and to further characterize the system full calculations have been performed with a new geometrical model with special attention to sources of uncertainty. Such approach has to overcome the slow convergence of Monte Carlo methods when calculating low transmission probabilities especially of those neutrons that undergo a scattering between radiator and measuring position thereby losing the correlation between time of flight and energy. Therefore the calculation scheme was optimized using the built-in options of the MCNP5 Monte Carlo code and additional computer programs have been written for data evaluation. As the result of the investigations it has been found that simplifications applied in past

calculations do not result in serious deviations compared to a full calculation regarding the neutron yield (being the most important neutronic quantity in the system), nor do design changes since the original calculational models. Compared to past calculations results show a 10-15 % deviation at the collimator inlet. This difference, however, is caused by neutrons which are unlikely to reach the measurement hall, therefore not bearing much significance.

Regarding the energy resolution of the facility, the electron transport modeling is of biggest importance whereby some information is lacking on the initial beam characteristics. The improved modeling shows considerably worse resolution characteristics in the interesting 0.5-5 MeV energy region at the collimator inlet. This discrepancy is again mostly due to neutrons not traveling in the direction of the measurement hall, though minor resolution decrease is noticeable at the measuring point.

Safety and efficiency of chemical processes

It is the objective of this research activity to increase the safety, efficiency and environmental sustainability of processes and plants in the field of chemical engineering. Therefore, experimental analyses of chemical engineering processes are carried out using advanced online measuring algorithms and sensors. The results provide the basis for the numerical process simulation at normal operating conditions as well as at safety relevant fault scenarios, i.e. local hot spots and exothermic runaways. Numerical simulations of reactive flows in multiphase/ multicomponent systems are handled using constantly developed CFD codes. Additionally, MHD-based techniques are used to optimise the energy efficiency as well as the space-time yield of electrochemical processes.

*G. Hessel,
H. V. Hristov,
H. Kryk,
W. Schmitt,
S. Boden,
U. Hampel,
D. Lucas,
E. Krepper,
H.-M. Prasser,
A. Manera*

CFD simulation of chemical engineering processes

The choice of optimal turbulence model is of vital importance for the hydrodynamic simulations of heterogeneous chemical engineering processes using CFD codes. Therefore, numerical studies of a gas-liquid two-phase flow were applied to a stirred tank reactor, agitated by a gas-inducing turbine. The suitability of different turbulence models, available in CFX-10, was tested. The k- ϵ turbulence model was found to be the most suitable one because of the numerical stability and the close correspondence to related X-ray tomography measurements.

The efficiency of bubble columns strongly depends on the flow structure. In previous research activities, criteria for the local stability of a bubbly flow dependent on the bubble size distribution were derived by means of a stability analysis. Now, the findings have been checked by CFD simulations using the CFX-10 software. Sources of local flow instabilities, which are characterised by a significant rise of the lateral velocity component, have been found in the regions predicted by the stability analysis. The flow behaviour is affected by interplay of local and global flow instabilities.

*G. Hessel,
H. Kryk,
W. Schmitt,
U. Hampel,
M. J. da Silva,
L. Liu,
C. Zippe*

Measurement of phase distributions and concentration profiles in chemical reactors

Transient mixing processes in stirred tank reactors were investigated using complex impedance needle probes and videometric measuring methods. Details of mixing processes can be captured due to the high measuring frequency of the needle probes. With the new in-house image processing software, it is possible to display the experimental results similar to CFD simulation results. Thus, the software outputs can be used straightforward for CFD validation purposes.

Within the scope of a third-party funded project, measurements of the hydrodynamics of fixed-bed column reactors were carried out using gamma ray radiography and tomography. The findings regarding residence time distributions of the liquid as well as local liquid and gas hold-up open up opportunities for reactor and process optimisation.

*G. Hessel,
H. Kryk,
W. Schmitt,
U. Hampel*

Desulphurisation of acid mining effluents

The crucial factors for the efficiency of systems for electrochemical treatment of acid mine effluents are the minimisation of the specific energy consumption as well as the optimisation of the space-time yield. Both parameters are strongly affected by the hydrodynamics inside the

electrolytic cell. Within the scope of a cooperative research project with VKTA, a pilot plant was designed for simultaneous measurements of chemical conversions and hydrodynamics in industrial electrolytic cells. Additionally, a novel technique for measurements of local residence time distributions in electrolytic cells was developed based on laser induced fluorescence. The investigations contribute to the optimisation of the cell design.

*Supported by
LMBV*

*G. Hessel,
H. Kryk,
W. Schmitt*

Strongly exothermic chemical reactions

Grignard reactions comprise considerable hazard potentials due to the specific process behaviour of the strongly exothermic formation reactions and the high reactivity of the Grignard compounds. To establish an industrially applicable method for an objective online detection of the reaction start-up and for the accumulation of reactants during the process, a heat/mass balance-based online monitoring approach was developed and tested by miniplant experiments. Additionally to the concentration profiles provided by the approach, the online estimation of safety-relevant parameters enables application of advanced control strategies up to the point of a safety-oriented fully-automatic control of Grignard reactions. In the same time, such systems can contribute to improve process efficiency by increasing the space-time yield.

*T. Weier,
C. Cierpka,
J. Hueller,
G. Gerbeth*

Application of MHD to optimise electrochemical processes

The experiments on copper electrolysis under magnetic field influence in cylindrical vessels, started in 2005, have been finished and completed with corresponding numerical investigations. Based on the excellent agreement of the experimental and numerical results, it could be proven that the magnetic field influence on the flow is solely due to the Lorentz forces. Other possible forces of magnetic nature did not play any role. These findings contribute to the current lively discussion on Kelvin forces in electrochemical systems.

Liquid metal magnetohydrodynamics

Magnetohydrodynamics investigates the interaction of electrically conducting liquids (liquid metals and semiconductors, electrolytes) with magnetic fields. In various applications, the use of magnetic fields provides a comfortable contact-less possibility to control the transport processes in such melts. On the other hand, problems as MHD turbulence, the homogeneous dynamo or the magnetorotational instability are the subject of intense basic research.

*A. Cramer,
S. Eckert,
V. Galindo,
I. Grants,
J. Pal,
J. Priede,
Ch. Zhang,
G. Gerbeth*

Basics of MHD flows and MULTIMAG

Buoyancy driven flows may disturb various technological processes, particularly in case of transition to turbulent flow. For the stabilization of buoyant convection, the optimal combination of rotating and steady magnetic fields has been determined and experimentally studied. In that way, the temperature fluctuations could be reduced by more than one order of magnitude. This reduction of fluctuations is even more expressed for larger fluid volumina, which makes this effect very attractive for applications in crystal growth technologies. In metallurgy, the efficient stirring of melts is of serious importance. For this purpose, flows in modulated rotating and superimposed rotating-travelling magnetic fields have been investigated at the MULTIMAG facility. It was shown that such kind of tailored magnetic field systems can provide an intense three-dimensional mixing of melts even for rather low field strength. The experimental results are based on ultrasonic measurements of the related velocity fields.

Supported by DFG

*Th. Gundrum,
F. Stefani,
G. Gerbeth*

Magneto-Rotational Instability (MRI)

The MRI is of significant relevance in astrophysics. The growth in stars or black holes in accretion disks can only be explained if the necessary transport of angular momentum can be understood. The latter, in turn, is only possible if the flow in the accretion disk is turbulent. However, from the basic fluiddynamic point of view this flow field must be laminar since the angular momentum increases with the radius according to the third Kepler rule. The theoretical idea to resolve this contradicting situation was that the transition to turbulence is triggered by some magnetic field. In frame of a project of the Leibniz Association (WGL) and in close cooperation with AIP Potsdam, a Taylor-Couette experiment has been set-up using the room-temperature melt GaInSn and corresponding external magnetic fields. At appropriate values of the applied magnetic fields, the basic laminar flow between the rotating cylinders became unstable in form of the theoretically predicted travelling waves. A good agreement with theory was found for the frequency of those travelling waves. In that way, the MRI effect was for the first time experimentally demonstrated in a laboratory experiment.

Supported by WGL

*S. Eckert,
Th. Gundrum,
G. Gerbeth*

Ultrasonic velocity measurements

Special wave-guides made of molybdenum foils were built and tested. They are supposed to work reliably in hot melts in the temperature range of 500 to 900 °C. Tests in a tin melt under industrial conditions showed that ultrasonic velocity measurements based on such wave-guides are indeed possible in a robust way.

*Supported by
industry*

*T. Weier,
Ch. Cierpka,
G. Mutschke,
V. Shatrov,
G. Gerbeth*

Boundary layer control in electrolytes

The influence of the electromagnetic excitation wave-form on separated flows has been systematically studied using the Particle-Image-Velocimetry (PIV). The phase-averaged evaluation of the PIV measurements allowed to correlate the measured velocity structures to the amplitude and frequency of the excitation. Experiments with variable wave forms of the electrode current confirmed that the unsteady excitation of the boundary layer is mainly determined by the amplitude of the Lorentz force rather than by its duration.

Supported by DFG

*S. Eckert,
B. Willers,
Dong Jie*

Magnetic control of solidification processes

In close cooperation with TU Dresden tailored magnetic field configurations have been identified which cause the columnar-equiaxed transition of the solidified microstructure. Related solidification experiments were performed using PbSn- as well as AlSi alloys. A periodic on-off of a rotating magnetic field turned out to be much more efficient for this kind of microstructure control compared to a permanently acting rotating magnetic field.

Supported by DFG

*S. Eckert,
S. Boden,
B. Willers*

X-ray laboratory

Based on the microfocus X-ray tube first results for the visualization of gas bubbles in metallic melts as well as for the phenomena in alloy solidification have been obtained. The resolution of a few micrometers allows to analyze the growth of single dendrites and dendrite arms, which gives access in next future to investigate in much more detail the influence of melt flows on the processes at the solidification front.

Supported by DFG

Thermal fluid dynamics of multiphase systems

The general aim of the work done in the field of thermal fluid-dynamics is the qualification of Computational Fluid Dynamics (CFD) codes for the simulation of complex two-phase flows with relevance for industrial applications. To achieve this goal, closure models are needed for the interaction between the phases, i.e. mass, momentum and heat transfer. For the special case of dispersed bubbly flow, all these transfers strongly depend on the local bubble size distribution. For this reason, the gas phase has to be split into a number of size groups in case of poly-dispersed flows. Transfers between these groups are amongst others determined by bubble coalescence and fragmentation. The theoretical work is based on sound experiments at the TOPFLOW test facility using advanced two-phase measuring instrumentation, which is developed in the framework of the present project.

*E. Krepper,
D. Lucas*

Qualification of CFD models

The experimental data basis for upwards flow in vertical pipes obtained at the TOPFLOW facility was used for the test and validation of the Inhomogeneous MUSIG (**MU**lti **B**ubble **S**ize **G**roup) model, which was developed during recent years and finally implemented into the CFD code CFX of ANSYS®. The simulations were done for air-water flows as well as for steam water flows under adiabatic conditions, i.e. with negligible phase transfer. For all the cases considered, two velocity groups for the gas phase were sufficient for a qualitative agreement with the experimental findings. The separation of small and large bubbles is well reflected by the simulations, what confirms the potential of the model. Problems arise from the models for bubble coalescence and breakup. After tuning the coefficients of the implemented models in fact good agreement was achieved, but no parameter set could be found which is applicable for a range of different flow parameters. Further investigations for the improvement of such models are required.

*Supported by
BMW*

*E. Krepper,
H.-M. Prasser,
S. Alissa*

Validation of CFD codes for complex geometries

The above mentioned Inhomogeneous MUSIG model was validated for a complex flow with pronounced 3D effects for the first time. The simulations base on experimental two-phase flow data from a vertical pipe in which one half of the pipe was blocked by a vertically moveable half-moon shaped obstacle. The 3D flow fields in the region influenced by the obstacle were measured. A new data evaluation method was developed, which allows calculating beside the void fraction distribution also the field of the liquid velocity. Even for such a flow, the calculated separation of small and large bubbles and the 3D void fraction and velocity field show a good agreement with the experimental data. However, the simulated bubble size distributions clearly differ from the experiment. This is caused by the weaknesses of the models for bubble coalescence and fragmentation.

*Supported by
BMW*

*Ch. Vallee,
T. Höhne*

Experiments and CFD-simulations for stratified flows

For the investigation of stratified two-phase flow, a new horizontal channel was built from acrylic glass with rectangular cross-section (30 mm * 100 mm). Water and air is injected into the 8 m long channel separately to obtain well defined boundary conditions at the inlet. Experiments were conducted for stratified co-current flow at different

combinations of volume flow rates and angles of the inclinable inlet blade, which determines the inlet velocities. A new flow map for horizontal rectangular channels was generated from these experiments. It slightly differs from flow maps, which can be found in literature for round channels. One test with slug flow was chosen as a basis for the validation of CFX. The transient water level was deduced from high speed camera observations by a special algorithm. In the simulation, the diffusion of turbulence was reduced close to the interface, where large velocity gradients exit, to improve the simulation of instabilities. The generation of waves and their evolution up to slug flow is qualitatively well reflected by the simulation.

*Supported by
BMW*

*E. Bodele,
D. Lucas,
E. Krepper*

CFD-Simulations on the bubble entrainment by a liquid jet

The bubble entrainment caused by an impinging liquid jet considerably influences the flow in the pool. For practical applications questions as the mixing between hot water in a pool with cold water from the jet (e.g. in case emergency core cooling injection into the cold leg of a Pressurized Water reactor) and re-suspension of particles in the pool have to be answered. In such a flow situation the gas phase simultaneously occurs as continuous phase (gas above the pool surface) and dispersed phase (entrained bubbles). Investigations were done on the influence of different model parameters and the consideration of bubble forces. Up to now no satisfactory simulation of the bubble entrainment from the continuous gas phase to below the pool surface exists.

Supported by EC

*U. Hampel,
E. Schleicher,
M. Bieberle,
F. Fischer*

Progress in ultra fast X-ray tomography

Within the project „Ultra fast X-ray tomography“ funded by the DFG we developed and manufactured a high resolution X-ray detector. This detector comprises 240 fast CZT detector elements which are read out by dedicated fast data acquisition electronics at 1 MHz sampling rate for each detector. With this detector we were able to perform first basic experiments where we achieved tomographic imaging at up to 20.000 frames per second on static phantoms.

For the TOPFLOW-II sub-project “Fast X-ray tomography of two-phase flows“ we developed an electron beam tomography device with electron beam generator (max. 150 kV tube voltage, max. 65 mA beam current) and xy-deflection unit (up to 10 kHz), the X-ray detector, target, target cooling circuit, control unit and data acquisition and imaging software. The device was subjected to first performance tests.

*Supported by DFG
and BMW*

*E. Schleicher,
M. Ritterath*

Measurement of gas fraction distributions in the ThAI facility with Becker Technologies

In continuation of a recent project we conducted two measurement campaigns at the ThAI facility of Becker Technologies GmbH in Eschborn (Germany). It is the aim of the project to investigate correlations between bubble size distributions and aerosol concentrations above the sump level of a reactor. With a set of newly developed double-tip conductivity needle probes we measured gas fraction as well as bubble size and velocity distributions in the sump of the ThAI vessel.

*Supported by
Becker
Technologies
GmbH, BMW*

*E. Schleicher,
F. Schäfer*

Validation of Russian thermal hydraulic code KORSAR

In 2006, the WTZ sub-project “Validation of the Russian thermal hydraulic code KORSAR” was successfully accomplished. For that we developed, manufactured and delivered a 16 channel conductivity needle probe system with 40 single needle probes of different lengths and installed the system at EREC in Elektrogorsk (Russia). Meanwhile we dispose of measurement results from two different experiments for natural circulation in a PSB-VVER test loop for further processing.

*Supported by
BMW*

*U. Hampel,
M. da Silva,
D. Hoppe,
A. Fleischer*

High resolution measurement of flow patterns in a hydrodynamic coupling

Within the frame of an industrial project at Voith Turbo GmbH in Crailsheim we performed, for the first time, measurements of flow patterns within a rotating hydrodynamic coupling. For that we applied two novel measurement techniques which were developed at the Institute of Safety Research. High resolution gamma ray tomography has been used to measure three dimensional phase distributions within the coupling chambers at approximately 3 mm spatial resolution. Additionally, we developed and applied a new surface conductivity sensor that is able to measure two-dimensional surface flow patterns at the suction respectively pressure side of a chamber wall with 10.000 frames per second. With this sensor it is even possible to obtain velocity fields by measuring wave phenomena of the liquid film. The acquired data is highly important for future improvements of the coupling design as well as for CFD code development and validation.

*Supported by Voith
Turbo GmbH*

*U. Hampel,
A. Bieberle,
D. Hopp,e
E. Schleicher,
C. Zippe*

Gamma ray tomography for void fraction measurements in fuel rod assemblies

A second campaign was performed for the measurement of void fraction distributions in BWR fuel rod assemblies with gamma ray tomography at the KATHY test loop of AREVA GmbH in Karlstein (Germany). Within the frame of this project we currently work on the improvement of quantification algorithms and the temperature stability of the radiation detector.

*Supported by
AREVA*

M. da Silva

Development of capacitance wire mesh sensors

For the first time, we developed and tested a new capacitance wire mesh sensor for measurements of highly transient two-phase flows involving non-conducting fluids, such as oil. The prototype sensor comprises two wire planes of 16 wires each with 3 mm wire distance and 0.12 mm wire diameter. Currently, we achieve a frame rate of 700 frames per second with this prototype. Faster sensor electronics for frame rates of 10.000 per second is currently being developed. The sensor is able to discriminate differences in the relative dielectric constant of $\Delta\epsilon_r$ up to 1. The sensor has been tested with air-gas two-phase flows.

*E. Schleicher,
H. Fatterschneider,
W. Zimmermann*

New design and manufacturing technologies for low-pressure wire mesh sensors

For manufacturing of low-pressure wire mesh sensors up to 20 bar we developed a new manufacturing technology that greatly improves

simplicity of design and operational reliability. The technology has been patented.

*U. Hampel,
E. Schleicher*

Optical tomograph

We developed a new optical tomograph for fast studies of transient liquid and droplet flows with low gas respectively liquid content in pipes or similar vessels. The tomograph comprises 256 light emitters and 32 fibre optic light detectors and achieves currently up to 5.000 frames per second.

TOPFLOW thermal hydraulic test facility

The acronym TOPFLOW stands for Transient Two Phase Flow Test Facility. This multipurpose thermal hydraulic facility is mainly used for the investigation of generic and applied steady state and transient two phase flow phenomena in either steam-water or air-water-mixtures. TOPFLOW has a maximum heating power of 4 MW and allows operation at pressures up to 7 MPa and temperature up to 285 °C in pipes and vessel geometries of industrial relevance. It has become the major experimental facility of the German CFD (Computational Fluid Dynamic) Research Alliance. Recently, a contract has been signed with Commissariat à l’Energie Atomique (CEA) France, Electricité de France (EDF), AREVA NP France, Institut de Radioprotection et de Sûreté Nucléaire (IRSN) France, and Paul Scherrer Institute (PSI) Switzerland for experiments at TOPFLOW aiming at the investigation of pressurised thermal shock related phenomena (PTS). For the future it is planned to acquire EU and further industry funding and to obtain the status of an OECD large scale test facility. To support the theoretical model development and the CFD code validation, a series of experiments has been conducted at TOPFLOW at different test rigs in 2006.

*M. Beyer,
H. Carl,
K. Lindner,
H. Pietruske,
P. Schütz,
S. Weichelt*

Experiments in the vertical test section DN200 for the evolution of the dynamics of the gas-liquid interface

In the frame of a co-operation with the University of Nottingham saturated steam-water experiments at 4.6 MPa and 259 °C were carried out in the vertical test section DN200. Measured void fractions and bubble size distributions were used for a comparison with available experimental data for nitrogen-naphtha flows. The results enable an analysis of the influence of the physical parameters of the different liquids and gases on the evolution of the flow structures.

*S. Al-Issa,
M. Beyer,
H. Carl,
H. Rußig,
P. Schütz,
M. Tamme*

Two-phase flow experiments in complex geometries

Further experiments with the moveable, half-moon-shaped obstacle in the vertical test section DN200 were carried out. As a result three-dimensional void fraction distributions together with local bubble size distributions and the liquid velocity field in the up- and down-stream regions of the obstacle were obtained. Further, lateral gas bubble migration within the measuring plane was investigated. With these experiments, we provided for the first time reliable and comprehensive experimental data for a steam-liquid two-phase flow at high pressures and temperatures in a complex geometry. Currently, the data is used to check the general applicability of the Multi Bubble Size Group model (MUSIG) for bubbly two-phase flows.

*Supported by
BMW*

*M. Beyer,
H. Carl,
K. Linder,
H. Pietruske,
H. Rußig,
P. Schütz,
M. Tamme,
Ch. Vallee,
S. Weichelt*

Stratified two-phase flows in the hot leg of a pressurized water reactor during loss of coolant accidents

During a commissioning test of the new test channel on May 12th, 2006, a fire occurred inside the pressure tank, which was caused by a self-inflammation of a new material for the thermal isolation (Polysiloxan). The pressure and temperature increase connected with the fire caused local damages at pressure tank and at the infrastructure of the hot leg model. Because of these problems it was not possible to carry out the planned hot leg experiments in 2006. In the meantime the damages are fully repaired, so that the further use of the tank is possible. In the future, only oxidized isolation materials will be used and in some

Supported by

BMWi

experiments the pressure tank atmosphere will be inerted by nitrogen.

*U. Hampel,
M. Beyer,
H. Carl,
H. Pietruske,
E. Schleicher,
P. Schütz,
T. Sühnel,
M. Tschofen,
Ch. Vallee,*

*Supported by CEA
(France), EDF,
AREVA NP
(France), IRSN
(France), and PSI
(Switzerland).*

TOPFLOW- pressurised thermal shock phenomena (PTS)

In January 2006, we started the TOPFLOW-PTS project which aims at the investigation of thermal hydraulic phenomena for an emergency cooling scenario at a French pressurized water reactor of CPY type. The project is commissioned and run by a consortium of international industry and scientific partners, including CEA, EDF, AREVA NP, IRSN (France), and PSI (Switzerland). Experiments will be conducted in the TOPFLOW pressure vessel on a 1:2.5 scaled model of a reactor cold leg section, comprising main coolant pump, ECC injection line and downcomer. During the last year we designed the test rig in full detail, devised the required TOPFLOW facility extensions, such as media supply and cooling system, designed special instrumentation such as thermocouple lances, different wire mesh sensors, thermo needle probes and optical and IR observation technique together with specialised data acquisition units. As a consequence of the fire damage in May 2006 the project was delayed by about 6 months.

Publications

Publications in journals

Abendroth, M.; Kuna, M.

Identification of ductile damage and fracture parameters from the small punch test using neural networks

Engineering Fracture Mechanics Vol. 73(2006)Issue 6, 710-725

DOI: 10.1016/j.engfracmech.2005.10.007

Albrecht, T.; Grundmann, R.; Mutschke, G.; Gerbeth, G.

On the stability of the boundary layer subject to a wall-parallel Lorentz force

Physics of Fluids 18(2006), 098103

Bieberle, A.; Hampel, U.; Kronenberg, J.

Void fraction distribution measurement in fuel element bundles with a new high-resolution gamma tomograph

atw - International Journal for Nuclear Power 51(2006)8/9, 539-540

Bieberle, M.; Hampel, U.

Evaluation of a limited angle scanned electron beam X-ray CT approach for two-phase pipe flows

Measurement Science and Technology 17(2006), 2057-2065

Biswas, K.; Hermann, R.; Das, J.; Priede, J.; Gerbeth, G.

Tailoring the microstructure and mechanical properties of Ti-Al alloy using a novel electromagnetic stirring process

Scripta Materialia Vol. 55(2006)I2, 1143-1146

Biswas, K.; Hermann, R.; Filip, O.; Acker, J.; Gerbeth, G.; Priede, J.

Influence of melt convection on microstructure evolution of Nd-Fe-B alloys using a forced crucible rotation technique

Physica Status Solidi (C) Vol. 3(2006), 3277-3280

Boehmer, B.; Konheiser, J.; Noack, K.; Rogov, A.; Stephan, I.; Hansen, W.; Hinke, D.; Unholzer, S.; Grantz, M.; Mehner, H.-C.

Measurements and Monte Carlo calculations of gamma and neutron flux spectra inside and behind iron/steel/water configurations

Journal of ASTM International 3(2006)8

Bojarevics, A.; Cramer, A.; Gelfgat, Yu.; Gerbeth, G.

Experiments on the magnetic damping of an inductively stirred liquid metal flow

Experiments in Fluids Vol. 40(2006)No.2, 257-266

Borodkin, G.; Khrennikov, N.; Böhmer, B.; Noack, K.; Konheiser, J.

Deterministic and Monte Carlo neutron transport calculation for Greifswald-1 and comparison with ex-vessel measurement data

Journal of ASTM International 3(2006)4

Bousbia Salah, A.; Kliem, S.; Rohde, U.; D'Auria, F.; Petruzzi, A.
Uncertainty and sensitivity analyses of the Kozloduy pump trip test using coupled thermal-hydraulic 3D kinetics code
Nuclear Engineering and Design 236(2006), 1240-1255
ISSN: 0029-5493
DOI: 10.1016/j.nucengdes.2005.11.05

Cramer, A.; Varshney, K.; Gundrum, Th.; Gerbeth, G.
Experimental study on the sensitivity and accuracy of electric potential local flow measurements
Flow Measurement and Instrumentation 17(2006), 1-11

Eckert, S.; Cramer, A.; Gerbeth, G.
Velocity measurement techniques for liquid metal flows
Magnetohydrodynamics: evolution of ideas and trends (2006)

Eckert, S.; Willers, B.; Michel, U.
Gerichtete Erstarrung von Pb-Sn-Legierungen unter Einwirkung eines rotierenden Magnetfeldes
International Foundry Research Vol. 58(2006)2, 38-46

Gailitis, A.; Lielausis, O.; Gerbeth, G.; Stefani, F.
Dynamo experiments
Magnetohydrodynamics: evolution of ideas and trends (2006)

Grahn, A.
Two-dimensional numerical simulations of Marangoni-Bénard instabilities during liquid-liquid mass transfer in a vertical gap
Chemical Engineering Science 61(2006)11, 3586-3592
DOI: doi:10.1016/j.ces.2006.01.006

Grahn, A.; Krepper, E.; Alt, S.; Kästner, W.
Modelling of differential pressure buildup during flow through beds of fibrous materials
Chemical Engineering & Technology 29(2006)8, 997-1000
DOI: 10.1002/ceat.200600084

Grants, I.; Pedchenko, A.; Gerbeth, G.
Experimental study of the suppression of Rayleigh--Benard instability in a cylinder by combined rotating and static magnetic fields
Physics of Fluids 18, 124104(2006)

Grauf, E.; Stoll, U.; Teschendorff, V.; Weiß, F.-P.
Aktuelle Themen der Reaktorsicherheitsforschung in Deutschland - KTG-Fachtagung 2006
atw - International Journal for Nuclear Power (2006)6, 405-409

Gundrum, Th.; Gerbeth, G.; Stefani, F.; Xu, M.
Experimental aspects of contactless inductive flow tomography
Magnetohydrodynamics 42(2006)2/3, 153-160
ISSN: 0024-998X

Günther, U.; Kirillov, O.

Krein space related perturbation theory for MHD α^2 -dynamos and resonant unfolding of diabolical points

Journal of Physics A 39(2006)32, 10057-10076

ISSN: 0305-4470, 1361-6447

DOI: 10.1088/0305-4470/39/32/S08

Höhne, T.; Kliem, S.; Bieder, U.

Modeling of a buoyancy-driven flow experiment at the ROCOM test facility using the CFD-codes CFX-5 and TRIO_U

Nuclear Engineering and Design Volume 236(2006)Issue 12, 1309-1325

DOI: 10.1016/j.nucengdes.2005.12.005

Hoppe, D.; Zaruba, A.; Prasser, H.-M.

Modellierung von Luftblasen als Rotationsellipsoide anhand paarweiser ebener Projektionen

Technisches Messen 2(2006), 103-108

Hristov, H. V.; Boden, S.; Hampel, U.; Kryk, H.; Schmitt, W.; Hessel, G.

Experimental and numerical assessment of the phase distribution in a stirred tank reactor agitated by a gas-inducing turbine

Chemie Ingenieur Technik, 78(2006)9, 1274

Hüttenbrink, K.-B.; Wrede, H.; Lagemann, S.; Schleicher, E.; Hummel, T.

Lokalisierte, endonasale Messung der mukoziliären Transportgeschwindigkeit als neues Verfahren für die nasale Diagnostik

Laryngo-Rhino-Otologie 85(2006), 25-31

DOI 10.1055/S-2005-870274

Kenjeres, S.; Hanjalic, K.; Renaudier, S.; Stefani, F.; Gerbeth, G.; Gailitis, A.

Coupled fluid-flow and magnetic-field simulation of the Riga dynamo experiment

Physics of Plasmas 13(2006), 122308

DOI: 10.1063/1.2404930

Kirillov, O.; Günther, U.

On Krein space related perturbation theory for MHD α^2 -dynamos

Proceedings in Applied Mathematics and Mechanics 6(2006), 637-638

ISSN: 1617-7061

DOI: 10.1002/pamm.200610299

Kliem, S.; Kozmenkov, Y.; Höhne, T.; Rohde, U.

Analyses of the V1000CT-1 benchmark with the DYN3D/ATHLET and DYN3D/RELAP coupled code systems including a coolant mixing model validated against CFD calculations

Progress in Nuclear Energy 48(2006), 830-848

DOI: 10.1016/j.pnucene.2006.06.008

Krause-Rehberg, R.; Sachert, S.; Brauer, G.; Rogov, A.; Noack, K.
EPOS - An intense positron beam project at the ELBE radiation source in Rossendorf
Applied Surface Science 252(2006)9, 3106-3110
ISSN: 0169-4332
DOI: 10.1016/j.apsusc.2005.08.109

Lantzsch, R.; Galindo, V.; Grants, I.; Pätzold, O.; Gerbeth, G.; Stelter, M.; Cröll, A.
Fluid flow analysis and vertical gradient freeze crystal growth in a traveling magnetic field
Magnetohydrodynamics 42(2006)No. 4, 445-449

Lucas, D.; Krepper, E.; Prasser, H.-M.; Manera, A.
Investigations on the stability of the flow characteristics in a bubble column
Chemical Engineering & Technology 29(2006)9, 1066-1072

Manera, A.; Prasser, H.-M.; Lucas, D.; van der Hagen, T. H. J. J.
Three-dimensional flow pattern visualization and bubble size distributions in stationary and transient upward flashing flow
International Journal of Multiphase Flow 32 (2006), 996-1016

Müller, G.; Uhlemann, M.; Ulbricht, A.; Böhmert, J.
Influence of hydrogen on the toughness of irradiated reactor pressure vessel steels
Journal of Nuclear Materials (2006)359, 114-121
DOI: <http://dx.doi.org/10.1016/j.jnucmat.2006.08.004>

Mutschke, G.; Gerbeth, G.; Albrecht, T.; Grundmann, R.
Separation Control at Hydrofoils using Lorentz forces
European Journal of Mechanics B/Fluids 25(2006)2, 137-152

Petkov, P. T.; Mittag, S.
VVER-1000 radial reflector modeling by diffusion codes
Progress in Nuclear Energy 48(2006), 764-772

Prasser, H.-M.; Beyer, M.; Carl, H.; Manera, A.; Pietruske, H.; Schütz, P.; Weiss, F.-P.
The multipurpose thermalhydraulic test facility TOPFLOW: an overview on experimental capabilities, instrumentation and results
Kerntechnik 71(2006)4, 163-173

Priede, J.; Gerbeth, G.
Boundary-integral method for calculating poloidal axisymmetric AC magnetic fields
IEEE Transactions on Magnetics 42(2006)2, 301-308

Priede, J.; Gerbeth, G.
Stability analysis of an electromagnetically levitated sphere
Journal of Applied Physics 100(2006), 054911

Rohde, U.; Höhne, T.; Kliem, S.
Using CFD to simulate turbulent mixing in nuclear reactor pressure vessels
ANSYS Solutions 7(2006)2, 27-28

Rüdiger, G.; Hollerbach, R.; Stefani, F.; Gundrum, T.; Gerbeth, G.; Rosner, R.
The traveling wave MRI in cylindrical Taylor-Couette flow: comparing wavelengths and speeds in theory and experiment
The Astrophysical Journal Letters 649(2006)2, L145-L147
DOI: 10.1086/508422

Schäfer, F.; Manera, A.
Investigation of flashing-induced instabilities at CIRCUS test facility with the code ATHLET
International Journal of Nuclear Energy Science and Technology 2(2006)3, 209-218
ISSN: 1741-6361

Shatrov, V.; Gerbeth, G.
On magnetohydrodynamic drag reduction and its efficiency
Magnetohydrodynamics 42(2006)2/3, 181-186

Sorriso-Valvo, L.; Carbone, V.; Stefani, F.; Nigro, G.
A statistical analysis of polarity reversals of the geomagnetic field
EOS, Transactions of the American Geophysical Union, 87(2006)52, GP21B-1308
ISSN: 0096-3941

Stefani, F.; Gerbeth, G.; Günther, U.
A paradigmatic model of Earth's magnetic field reversals
Magnetohydrodynamics 42(2006)2/3, 123-130
ISSN: 0024-998X

Stefani, F.; Gerbeth, G.; Günther, U.
Reversals in a nutshell
Geophysical Research Abstracts 8(2006), 03265
ISSN: 1029-7006

Stefani, F.; Gerbeth, G.; Günther, U.; Gundrum, T.; Xu, M.
Inverse problems in magnetohydrodynamics: theoretical and experimental aspects
Inverse Problems in Science and Engineering 14(2006)4, 411-422
DOI: 10.1080/17415970600573791

Stefani, F.; Gerbeth, G.; Günther, U.; Xu, M.
Why dynamos are prone to reversals
Earth and Planetary Science Letters 243(2006)3-4, 828-840
ISSN: 0012-821X
DOI: doi:10.1016/j.epsl.2006.01.030

Stefani, F.; Gundrum, T.; Gerbeth, G.; Rüdiger, G.; Schultz, M.; Szklarski, J.; Hollerbach, R.
Experimental Evidence for Magnetorotational Instability in a Taylor-Couette Flow under the Influence of a Helical Magnetic Field
Physical Review Letters 97(2006) 184502
DOI: 10.1103/PhysRevLett.97.184502

Stefani, F.; Xu, M.; Gerbeth, G.; Ravelet, F.; Chiffaudel, A.; Daviaud, F.; Leorat, J.
Ambivalent effects of added layers on steady kinematic dynamos in cylindrical geometry: application to the VKS experiment

European Journal of Mechanics / B: Fluids 25(2006), 894-908

DOI: 10.1016/j.euromechflu.2006.02.002

Stiller, J.; Frana, K.; Cramer, A.

Transitional and weakly turbulent flow in a rotating magnetic field

Physics of Fluids 18(2006) 074105

Ulbricht, A.; Bergner, F.; Dewhurst, C. D.; Heinemann, A.

Small-angle neutron scattering study of post-irradiation annealed neutron irradiated pressure vessel steels

Journal of Nuclear Materials 353(2006), 27-34

Vallee, C.; Höhne, T.; Prasser, H.-M.; Sühnel, T.

Experimental investigation and CFD simulation of horizontal air/water slug flow

Kerntechnik 71(2006)3, 95-103

ISSN: 0932-3902

Viehrig, H.-W.; Scibetta, M.; Wallin, K.

Application of advanced Master Curve approaches on WWER-440 reactor pressure vessel steels

International Journal Pressure Vessel and Piping 83(2006) IPVP2676

DOI: 10.1016/j.ijpvp.2006.04.005

Weier, T.; Cierpka, C.; Hüller, J.; Gerbeth, G.

Velocity measurements and concentration field visualizations in copper electrolysis under the influence of Lorentz forces and buoyancy

Magnetohydrodynamics 42(2006)4, 379-387

ISSN: 0024-998X

Weier, T.; Shatrov, V.; Gerbeth, G.

Flow control and propulsion in weak conductors

Magnetohydrodynamics: evolution of ideas and trends (2006)

Willschütz, H.-G.

Eine Frage der Kühlbarkeit

Brennstoff, Wärme, Kraft: BWK 58(2006)12, 27-30

Willschütz, H.-G.; Altstadt, E.; Sehgal, B. R.; Weiss, F.-P.

Recursively coupled thermal and mechanical FEM-analysis of lower plenum creep failure experiments

Annals of Nuclear Energy 33(2006)2, 126-148

DOI: 10.1016/j.anucene.2005.08.006

Conference contributions and other oral presentations

Al Issa, S.; Prasser, H.-M.; Beyer, M.

Experimental data on a three dimensional flow field around an obstacle in a vertical pipe

Multiphase Flows: Simulation, Experiment and Application, FZR & ANSYS, 26.-29.06.2006, Dresden, Deutschland

Albrecht, T.; Grundmann, R.; Mutschke, G.; Gerbeth, G.

Electromagnetic control of a transitional boundary layer

Fifth International Conference on Computational Fluid Dynamics in the Process Industries, CSIRO, Melbourne, Australia, 13.-15.12.2006, Melbourne, Australia

Albrecht, T.; Mutschke, G.; Grundmann, R.

On the stability of boundary layer flows controlled by Lorentz forces

7th World Congress on Computational Mechanics, UCLA and Northwestern University, 16.-22.07.2006, Los Angeles, California, USA

Alt, S.; Hampel, R.; Kästner, W.; Grahn, A.; Krepper, E.

Experimental investigations for head loss build up at clogged strainers after LOCA

Annual Meeting on Nuclear Technology 2006, May 16-18, Aachen, Deutschland,

Altstadt, E.

Materialaspekte bei der Untersuchung von Störfallszenarien in Kernkraftwerken

Ringvorlesung des Materialforschungsverbundes Dresden für das Studium generale der TU Dresden, Technische Universität Dresden, 29.11.2006, Dresden, Deutschland

Altstadt, E.

Materialforschung für sichere Kernkraftwerke

Ringvorlesung des Materialforschungsverbundes Dresden für das Studium generale der TU Dresden, Technische Universität Dresden, 25.01.2006, Dresden, Deutschland

Altstadt, E.; Willschütz, H.-G.

FZR activities on in-vessel melt retention

2nd meeting of the ISTC-project "Reactor Core Melt", IBRAE Moscow, 05.07.2006, Moscow, Russia

Altstadt, E.; Willschütz, H.-G.

Modellierung der Wechselwirkung zwischen Corium und RDB-Stahl im Rahmen von Schmelzerückhaltungsszenarien

MPA Seminar, MPA Stuttgart, 05.-06.10.2006, Stuttgart, Deutschland

Anikeev, A. V.; Bagryansky, P. A.; Deichuli, P. P.; Ivanov, A. A.; Kireenko, A. V.; Lizunov, A. A.; Murakhtin, S. V.; Prikhodko, V. V.; Solomakhin, A. L.; Sorokhin, A. V.; Stupishin, N. V.; Collatz, S.; Noack, K.

The synthesized hot ion plasmoid experiment at GDT

6th International Conference on Open Magnetic Systems for Plasma Confinement, University of Tsukuba, Plasma Research Center, 17.-21.07.2006, Tsukuba, Japan

Bauer, T.; Schubert, M.; Hampel, U.; Lange, R.

Zweiphasige Strömung in Kapillaren und strukturierten Packungen

Multiphase Flows: Simulation, Experiment and Application, FZR & ANSYS, 26.-29.06.2006, Dresden, Deutschland

Bergner, F.

Application of rate theory modelling to neutron-irradiated low-Cu and Cu-enriched Fe-based model alloys

International School on Experimental Quantification of Irradiation Damage (ISQUID), SCK-CEN Mol, 25.-29.09.2006, Rochehaut sur Semois, Belgien

Bergner, F.; Ulbricht, A.

Application of the virtual test reactor RPV-1 to VVER-1000 RPV steels

The 5th Perfect Users Group Meeting, JRC Petten, 22.-23.11.2006, Bergen, Niederlande

Bergner, F.; Ulbricht, A.

RPV-1 models sensitivity for VVER 1000 materials parameters

3rd Plenary Meeting of the Perfect Physics Subproject, SCK.CEN, 08.-10.11.2006, Mol, Belgien

Bergner, F.; Ulbricht, A.

SANS investigation of neutron-irradiated pressure vessel steels and model alloys

13th Meeting of the International Group on Radiation Damage Mechanisms in Pressure Vessel Steels (IGRDM 13), IGRDM, 16.-20.10.2006, Tsukuba, Japan

Bieberle, A.; Hampel, U.; Kronenberg, J.

Void fraction distribution measurement in fuel element bundles with a new high-resolution gamma tomograph

Annual Meeting on Nuclear Technology 2006, May 16-18, Aachen, Deutschland

Bieberle, A.; Kronenberg, J.; Hampel, U.

Dampfgehaltsmessung in Brennelementbündeln mittels hochauflösender Gammatomographie

Kompetenzzentrum Ost für Kerntechnik - Doktorandenseminar, 15.12.06, Rossendorf, Deutschland

Bieberle, A.; Schleicher, E.; Hoppe, D.; Kronenberg, J.; Hampel, U.

Measurement of void fraction distributions in full scale fuel element bundles using gamma ray tomography

4th International Symposium on Process Tomography, 14.-15.09.06, Warschau, Polen

Biswas, K.; Hermann, R.; Acker, J.; Gerbeth, G.; Priede, J.; Shatrov, V.

Effect of melt convection on microstructure evolution of Nd-Fe-B alloys using a forced crucible rotation technique

DPG-Jahrestagung, 27.-31.03.2006, Dresden, Germany

Cierpka, C.; Weier, T.; Gerbeth, G.

Electromagnetic control of separated flows using periodic excitation with different wave forms

Conference on Active Flow Control 2006, Berlin University of Technology, 27.-29.09.2006, Berlin, Deutschland

Cramer, A.; Priede, J.; Galindo, V.; Andersen, O.; Kostmann, C.

Container-less melt extraction of metallic fibres

The 5th International Symposium on Electromagnetic Processing of Materials (EPM2006), Tohoku University, 23.-27.10.2006, Sendai, Japan

Da Silva, M. J.; Brückner, F.; Schleicher, E.; Hampel, U.

High-speed complex admittance/permittivity needle probe for investigation of multiphase flows

IEEE Instrumentation and Measurement Technology Conference, IEEE Instrumentation and Measurement Society, 24.-27.04.2006, Sorrento, Italy

Da Silva, M. J.; Schleicher, E.; Hampel, U.

Electrical impedance sensors for multiphase flow measurement

Multiphase Flows: Simulation, Experiment and Application, FZR & ANSYS, 26.-29.06.2006, Dresden, Deutschland

Frank, T.; Lucas, D.; Prasser, H.-M.; Krepper, E.; Shi, J.-M.

Entwicklung und Validierung von CFD-Modellen für Zweiphasenströmungen

Aktuelle Themen der Reaktorsicherheitsforschung in Deutschland, KTG-Fachtagung, Forschungszentrum Rossendorf e.V., 03.-04.04.2006, Dresden, Deutschland

Frank, T.; Zwart, P.; Krepper, E.; Prasser, H.-M.; Lucas, D.

Validation of CFD models for mono- and polydisperse air-water two-phase flows in pipes

OECD/NEA International Workshop on The Benchmarking of CFD Codes for Application to Nuclear Reactor Safety (CFD4NRS), 05.-09.09.2006, Garching, Deutschland

32

Gailitis, A.; Lielausis, O.; Platacis, E.; Gerbeth, G.; Stefani, F.

Magnetic turbulence in the Riga dynamo experiment

Workshop: Modelling MHD Turbulence: Application to Planetary and Stellar Dynamos, National Center for Atmospheric Research (NCAR), 27.-30.06.2006, Boulder, USA

Galindo, V.; Eckert, S.; Gerbeth, G.; Willers, B.

Computational studies on the design of an electromagnetic pump for the process of aluminum investment casting

7th World Congress on Computational Mechanics, UCLA and Northwestern University, 16.-22.07.2006, Los Angeles, California, USA

Galindo, V.; Grants, I.; Lantsch, R.; Pätzold, O.; Gerbeth, G.

Numerical and experimental modeling of the melt flow in a traveling magnetic field for Vertical Gradient Freeze crystal growth

5th Int. Workshop on Modelling in Crystal Growth, 10.-13.09.2006, Bamberg, Germany

Gerbeth, G.

Applied MHD at Forschungszentrum Rossendorf – a review of R&D activities on tailored magnetic fields and liquid metal measuring techniques

Research Institute of Industrial Science & Technology, 29.03.2006, Pohang, Korea

Gerbeth, G.

MHD turbulence in electromagnetic processing of materials

Graduate School and Workshop on Instabilities and Turbulence in MHD Flows, 26.-30.06.2006, University of Warwick, United Kingdom

Gerbeth, G.; Eckert, S.; Galindo, V.; Willers, B.; Hewelt, U.; Katz, H.-W.; Ziemann, M.

Use of magnetic fields in aluminum investment casting

The 5th International Symposium on Electromagnetic Processing of Materials (EPM2006), Tohoku University, 23.-27.10.2006, Sendai, Japan

Gerbeth, G.; Shatrov, V.

On the efficiency of MHD drag reduction

7th World Congress on Computational Mechanics, UCLA and Northwestern University, 17.-22.07.2006, Los Angeles, USA

Gleisberg, B.; Rindelhardt, U.; Konheiser, J.

Radiochemische Analysen von ^{93m}Nb in Druckkesselstahl und Vergleiche mit Fluenzberechnungen

Radiochemische Analytik bei Betrieb und Rückbau kerntechnischer Anlagen, der Deklaration von Abfällen und im Strahlenschutz, VKTA Dresden, 19.-20.06.2006, Dresden, Deutschland

Gokhman, A.; Bergner, F.; Ulbricht, A.

Kinetics of precipitation in neutron irradiated steel

Mathematical problems to describe the phase transformation of the 1-st kind, 02.-08.07.2006, Bugas, Ukraine

Gokhman, A.; Bergner, F.; Ulbricht, A.

The problem to account for processes on different time scales in the investigation of neutron embrittlement

4-th Russian Symposium "PHYSICS PROBLEMS OF ULTRASHORT PHENOMENA IN STRONGLY NON-EQUILIBRIUM MEDIA", 22.07.-01.08.2006, New Athos, Russia

Gommlich, A.

Integration of DYN3D into the SALOME platform

First NURESIM Seminar, Paris, November 7-8, 2006, CEA France, 07.-08.11.2006, Paris, Frankreich

Grahn, A.; Krepper, E.; Alt, S.; Kästner, W.

1D-modelling of differential pressure build-up at clogged containment sump strainers after LOCA

Annual Meeting on Nuclear Technology 2006, May 16-18, Aachen, Deutschland

Grants, I.; Pedchenko, A.; Gerbeth, G.

Experimental study of the suppression of Rayleigh--Benard instability in a cylinder by combined rotating and static magnetic fields

2nd International Symposium "Instabilities and Bifurcations in Fluid Dynamics", 15.-18.08.2006, Copenhagen, Denmark

Grundmann, U.

Calculations of a steady state of the OECD/NRC PWR MOX/UO₂ transient benchmark with DYN3D

Annual Meeting on Nuclear Technology 2006, May 16-18, Aachen, Deutschland

Grundmann, U.

Multigroup kinetic methods RTD in DYN3D

First NURESIM Seminar, Paris, November 7-8, 2006, CEA France, 07.-08.11.2006, Paris, Frankreich

Gundrum, T.; Gerbeth, G.; Stefani, F.; Rüdiger, G.; Hollerbach, R.

Observation of magnetorotational instability in a liquid metal Taylor-Couette experiment

9th MHD Days 2006, Max-Planck-Institut für Astronomie, Heidelberg, 04.-05.12.2006, Heidelberg, Deutschland

Günther, U.

Stability aspects of higher dimensional gravitational models with nonlinear scalar curvature coupling R^4

Eleventh Marcel Grossmann Meeting on recent developments in theoretical and experimental general relativity, gravitation and relativistic field theories., Freie Universität Berlin, 23.-29.07.2006, Berlin, Deutschland

Günther, U.; Kirillov, O.

New results on the spectrum of the MHD α^2 -dynamo and on Jordan algebra related canonical structures of PT-symmetric matrices

5th International Workshop on pseudo-Hermitian Hamiltonians in Quantum Physics, Departments of Physics and Mathematics of Bologna University, 03.-08.07.2006, Bologna, Italy

Günther, U.; Kirillov, O.; Stefani, F.

Three models of Krein-space related physics: PT-symmetric Quantum Mechanics, Squire equation and the MHD α^2 -dynamo

The Seventeenth International Workshop on Operator Theory and Applications (IWOTA 2006), Research Institute of Mathematics, Seoul National University, 31.07.-03.08.2006, Seoul, South Korea

Günther, U.; Stefani, F.; Znojil, M.

A toy model of PT-symmetric Quantum Mechanics, the Squire equation and UV-IR-duality

6th Workshop "Operator Theory in Krein Spaces and Operator Polynomials", Institut für Mathematik, Technische Universität Berlin, 14.-17.12.2006, Berlin, Deutschland

Hampel, U.

Advanced measurement techniques for multiphase flows

CFD OIL 2006, Petrobras Brasil, 15.-18.08.2006, Rio de Janeiro, Brasil

Hampel, U.

Gamma and X-ray tomography

Annual Meeting of the Virtual Center of Process Tomography, VCIPT, 05.04.2006, Huddersfield, UK

Hampel, U.

High resolution gamma ray tomography for two-phase flow studies

Multiphase Flows: Simulation, Experiment and Application, FZR & ANSYS, 26.-29.06.2006, Dresden, Deutschland

Hampel, U.

Review on gamma and X-ray tomography in process engineering - major groups and technical drivers -

Annual Meeting of the Virtual Center of Process Tomography, VCIPT, 05.04.2006, Huddersfield, UK

Hampel, U.

Ultraschnelle Elektronenstrahl-Röntgentomographie

Ehrenkolloquium des FEP Dresden für Herrn Dr. Panzer, FEP Dresden, 01.06.2006, Dresden, BRD

Hampel, U.; Bieberle, A.; Schleicher, E.; Hessel, G.; Zippe, C.; Friedrich, H.-J.

High resolution gamma ray tomography and its application to the measurement of phase fractions in chemical reactors

The 5th International Symposium on Measurement Techniques for Multiphase Flows, 10.-13.12.2006, Macao, China

Hampel, U.; Bieberle, A.; Schleicher, E.; Kronenberg, J.

High-resolution gamma ray detector for process tomography

IEEE Sensors 2006, IEEE, 22.-26.10.2006, Daegu, Korea

Hampel, U.; Bieberle, M.; Fischer, F.; Schleicher, E.; Mattausch, G.; Flaske, H.; Bartel, R.; Do Couto Aktay, K. S.; Koch, D.; Menz, H.-J.; Mayer, H.-G.

Recent developments in ultra fast X-ray computed tomography

PROCTOM 2006 4th International Symposium on Process Tomography in Poland, 14.-15.09.2006, Warszawa, Poland

Hampel, U.; Schleicher, E.; Da Silva, M. J.; Li, A.; Thiele, S.; Wollrab, E.

Optical tomograph for the investigation of single and two phase pipe flows

PROCTOM 2006 4th International Symposium on Process Tomography in Poland, 14.-15.09.2006, Warszawa, Poland

Hampel, U.; Speck, M.; Prasser, H. M.; Fischer, F.; Mattausch, G.; Flaske, H.; Bartel, R.; Koch, D.; Menz, H.-J.; Mayer, H.-G.

Development of a scanned electron beam X-ray tomography system for high-speed imaging of technical multiphase flows

E-BEAM 2006, International Conference on High-Power Electron Beam Technology, 15.-17.10.2006, Reno, Nevada, USA

Höhne, T.

CFD für Sicherheitsventile und andere Anwendungen

GVC-Arbeitsausschuß "Sicherheitsgerechtes Auslegen von Chemieapparaten" 61. Sitzung, DECHEMA, 08.-09.03.2006, FZR Dresden, Deutschland

Höhne, T.

CFD-Analysen der Kühlmittelvermischung in Druckwasserreaktoren

DECHEMA/GVC-Arbeitsausschuß "Sicherheitsgerechtes Auslegen von Chemieapparaten", Ciba Spezialitätenchemie, 22.11.2006, Lampertheim, Deutschland

Höhne, T.

CFD-simulation of OECD V1000CT2 with advanced turbulence models

Annual meeting of Working Group C and G of AER, 22.-23.05.2006, Balatonfüred, Ungarn

Höhne, T.

CFD-simulation of thermalhydraulic benchmark V1000CT2 - analysis with advanced turbulence models

V1000CT4 Workshop, OECD/NEA, 24.-29.04.2006, Pisa, Italien

Höhne, T.; Friedel, L.

Nachrechnung der Leistungsparameter eines Vollhub-Feder –Sicherheitsventils mit ANSYS CFX

24th CADFEM & ANSYS Germany Users Meeting, 26.10.2006, Stuttgart/Fellbach, Deutschland

Höhne, T.; Kliem, S.

Coolant mixing studies of natural circulation flows at the ROCOM test facility using ANSYS CFX

*OECD/NEA International Workshop on The Benchmarking of CFD Codes for Application to Nuclear Reactor Safety (CFD4NRS), 05.-09.09.2006, Garching, Deutschland
NEA-CD 6298, Paper 23*

Höhne, T.; Kliem, S.; Rohde, U.; Weiß, F.-P.

CFD-Analysen zur Kühlmittelvermischung in DWR

Fachtagung "Aktuelle Themen der Reaktorsicherheitsforschung", KTG, 03.-04.04.2006, Dresden, Deutschland

Höhne, T.; Kliem, S.; Rohde, U.; Weiss, F.-P.

Buoyancy driven coolant mixing studies of natural circulation flows at the ROCOM test facility using ANSYS CFX

14th International Conference on Nuclear Energy (ICONE-14), May 17-22, 2006, Miami, USA

Höhne, T.; Kliem, S.; Weiss, F.-P.
Buoyancy driven mixing studies of natural circulation flows at the ROCOM facility using ANSYS CFX
Annual Meeting on Nuclear Technology 2006, May 16-18, Aachen, Deutschland

Höhne, T.; Vallee, C.
Experiments and ANSYS CFX simulations of horizontal air-water channel flow phenomena
Multiphase Flows: Simulation, Experiment and Application, FZR & ANSYS, 26.-29.06.2006, Dresden, Deutschland

Hristov, H. V.; Boden, S.; Hampel, U.; Kryk, H.; Schmitt, W.; Hessel, G.
CFD simulations and X-ray measurements of the local gas hold-up in a stirred tank reactor agitated by a gas-inducing turbine
Multiphase Flows: Simulation, Experiment and Application, FZR & ANSYS, 26.-29.06.2006, Dresden, Deutschland

Hristov, H. V.; Boden, S.; Hampel, U.; Kryk, H.; Schmitt, W.; Hessel, G.
Experimental and CFD analysis of a stirred tank reaction mechanically agitated by gas-inducing turbine
17th International Congress of Chemical and Process Engineering, CHISA, 27.-31.08.2006, Praha, Czech Republic

Hristov, H. V.; Boden, S.; Hampel, U.; Kryk, H.; Schmitt, W.; Hessel, G.
Phase distribution in a stirred tank reactor mechanically agitated by gas-inducing turbine
VDI-GVC-Fachausschusssitzung "Mehrphasenströmungen" und "Computational Fluid Dynamics", 02./03. März 2006, Überlingen bei Friedrichshafen, 01.-03.03.2006, Überlingen, Deutschland

Kirillov, O.; Günther, U.
Krein space related perturbation theory for MHD α^2 -dynamos
77th Annual Meeting of the Gesellschaft für Angewandte Mathematik und Mechanik e.V. (GAMM), Technische Universität Berlin, 27.-31.03.2006, Berlin, Germany

Kirillov, O.; Günther, U.
Krein space related perturbation theory for MHD α^2 -dynamos and resonant unfolding of diabolical points
International Congress of Mathematicians, International Mathematical Union, 22.-30.08.2006, Madrid, Spain

Kirillov, O.; Günther, U.
Resonance effects in α^2 -dynamos
9th MHD Days 2006, Max-Planck-Institut für Astronomie, Heidelberg, 04.-05.12.2006, Heidelberg, Deutschland

Kirillov, O.; Günther, U.

Some aspects of a Krein space related perturbation theory for MHD α^2 -dynamos and the resonant unfolding of diabolical points

International Summer School and Workshop "Operator algebras, operator theory and applications" (WOAT 2006), Satellite conference to the International Congress of Mathematicians, Madrid 2006, Instituto Superior Tecnico, Universidade Tecnica de Lisboa, 01.-05.09.2006, Lisboa (Lissabon), Portugal

Kliem, S.; Prasser, H.-M.; Sühnel, T.

High-resolution measurements of the coolant mixing in the downcomer of the ROCOM test facility

Annual Meeting on Nuclear Technology 2006, May 16-18, Aachen, Deutschland

Kliem, S.; Prasser, H.-M.; Sühnel, T.; Weiss, F.-P.; Hansen, A.

Experimental investigation of coolant mixing in the RPV of PWR in the late phase of a SBLOCA event

14th International Conference on Nuclear Energy (ICONE-14), May 17-22, 2006, Miami, USA

Kliem, S.; Rohde, U.

State of the art regarding the safety analysis of boron dilution events in Germany

XVI. AER-Symposium on VVER Physics and Reactor Safety, VUJE Trnava, 25.-29.09.2006, Bratislava, Slovakische Republik

Kliem, S.; Sühnel, T.; Prasser, H.-M.; Weiß, F.-P.

Experimente an der Versuchsanlage ROCOM zur Kühlmittelvermischung bei Wiederanlauf der Naturzirkulation

Fachtagung "Aktuelle Themen der Reaktorsicherheitsforschung", KTG, 03.-04.04.2006, Dresden, Deutschland

Kliem, S.; Sühnel, T.; Rohde, U.; Höhne, T.; Prasser, H.-M.; Weiss, F.-P.

Experiments at the mixing test facility ROCOM for benchmarking of CFD-codes

OECD/NEA International Workshop on The Benchmarking of CFD Codes for Application to Nuclear Reactor Safety (CFD4NRS), 05.-09.09.2006, Garching, Deutschland

Koncar, B.; Krepper, E.

CFD Simulation of forced convective boiling in heated channels

OECD/NEA International Workshop on The Benchmarking of CFD Codes for Application to Nuclear Reactor Safety (CFD4NRS), 05.-09.09.2006, Garching, Deutschland

Kozmenkov, Y.; Grundmann, U.; Kliem, S.; Rohde, U.; Bousbia Salah, A.

DYN3D/RELAP5 and RELAP5/PARCS calculations of the Kozloduy-6 pump trip test

Annual Meeting on Nuclear Technology 2006, May 16-18, Aachen, Deutschland

Krepel, J.; Rohde, U.; Grundmann, U.

Dynamics of molten salt reactors

International Congress on Advances in Nuclear Power Plants - ICAPP 2006, 04.-08.06.2006, Reno, Nevada, USA

Krepper, E.; Egorov, Y.; Koncar, B.

Towards CFD modelling of critical heat flux in fuel rod bundles

International Congress on Advances in Nuclear Power Plants - ICAPP 2006, 04.-08.06.2006, Reno, Nevada, USA

Krepper, E.; Grahn, A.; Kästner, W.

CFD-Simulation von Mineralwollpartikeln in der Sumpfstromung

Fachtagung "Aktuelle Themen der Reaktorsicherheitsforschung", KTG, 03.-04.04.2006, Dresden, Deutschland

Kryk, H.; Hessel, G.; Beyer, M.; Carl, H.; Hampel, U.; Strobel, H.

Ereignis an der Versuchsanlage TOPFLOW-HeiBstrang des Forschungszentrums Dresden - Rossendorf

DECHEMA/GVC-Arbeitsausschuss "Sicherheitsgerechtes Auslegen von Chemieanlagen", 22.-23.11.2006, Lampertheim, Deutschland

Lantzsch, R.; Galindo, V.; Pätzold, O.; Gerbeth, G.; Stelter, M.

Flow experiments and VGF growth with a travelling magnetic field

DGKK-Arbeitskreis, 22.03.2006, Erlangen, Germany

Lenz, M.; Shirai, K.; Büttner, L.; Csarske, J.; Eckert, S.; Gerbeth, G.

Untersuchung elektromagnetischer Strömungsbeeinflussung in elektrisch leitfähigen Fluiden mit Hilfe von 2d2k/1d3k-Ultraschall-Doppler-Array-Techniken

14. Fachtagung "Lasermethoden in der Strömungsmesstechnik", GALA2006, Deutsche Gesellschaft für Laser -Anemometrie GALA e.V.in Zusammenarbeit mit der PTB, 05.-07.09.06, Braunschweig, Deutschland

Lucas, D.

NURESIM-Thermohydraulic Subproject, Work Package Pressurized Thermal Shock (PTS)

NURESIM Seminar, CEA, 07.-08.11.2006, Paris, France

Lucas, D.; Prasser, H.-M.

Steam bubble condensation in sub-cooled vertical pipe flow

44rd European Two-Phase Flow Group Meeting, 07.-09.06.2006, Lausanne, Schweiz

Lucas, D.; Prasser, H.-M.; Manera, A.

Linear stability analysis for the effect of the lift force in a bubble column

7th German/Japanese Symposium on Bubble Columns, GVC, 20.-23.05.2006, Goslar, Deutschland

Lycklama à. Nijeholt, Jan-Aiso; Höhne, T.

On the application of CFD modeling for the prediction of the degree of mixing in a PWR during a boron dilution transient

International Congress on Advances in Nuclear Power Plants - ICAPP 2006, 04.-08.06.2006, Reno, Nevada, USA

Mutschke, G.; Weier, T.; Gerbeth, G.; Albrecht, T.; Grundmann, R.

Electromagnetic control of separation at hydrofoils

7th World Congress on Computational Mechanics., UCLA and Northwestern University, 16.-22.07.2006, Los Angeles, California, USA

Noack, K.

The use of the GDT based neutron source as driver in a sub-critical burner of minor actinides

Institutskolloquium des Budker Instituts Novosibirsk, Budker Institut Novosibirsk, 26.09.2006, Novosibirsk, Russland

Noack, K.; Rogov, A.; Ivanov, A. A.; Kruglyakov, E. P.

The GDT as neutron source in a sub-critical system for transmutation?

Open Magnetic Systems for Plasma Confinement, University of Tsukuba, Plasma Research Center, 17.-21.07.2006, Tsukuba, Japan

Pal, J.; Eckert, S.; Zhang, C.; Gerbeth, G.

Velocity measurements in metallic melts driven by AC magnetic fields in a square vessel

The 5th International Symposium on Electromagnetic Processing of Materials (EPM2006), Tohoku University, 23.-27.10.2006, Sendai, Japan

Petkov, P. T.; Mittag, S.

Evaluation of homogenisation error in two-group nodal diffusion calculation for VVER-1000 core

Annual Meeting on Nuclear Technology 2006, May 16-18, Aachen, Deutschland

Prasser, H.-M.; Frank, T.; Beyer, M.; Carl, H.; Pietruske, H.; Schütz, P.

Gas-liquid flow around an obstacle in a vertical pipe - experiments and cfd simulation

Annual Meeting on Nuclear Technology 2006, May 16-18, Aachen, Deutschland

Priede, J.; Buchenau, D.; Gerbeth, G.

Contactless electromagnetic induction flowmeter based on phase shift measurements

The 5th International Symposium on Electromagnetic Processing of Materials (EPM2006), Tohoku University, 23.-27.10.2006, Sendai, Japan

Priede, J.; Grants, I.; Gerbeth, G.

Paradox of inductionless magnetorotational instability

2nd Int. Symposium "Instabilities and Bifurcations in Fluid Dynamics", 15.-18.08.2006, Copenhagen, Denmark

Rindelhardt, U.; Konheiser, J.; Viehrig, H.-W.; Gleisberg, B.

Pressure vessel investigations of the former Greifswald NPP: Fluence calculations and Nb based fluence measurements

14th International Conference on Nuclear Energy (ICONE-14), May 17-22, 2006, Miami, USA

- Rindelhardt, U.; Konheiser, J.; Viehrig, H.-W.; Gleisberg, B.
Retrospective dosimetry of Greifswald VVER 440 RPV: Fluence calculations and Nb based fluence measurements
9th International Conference on "MATERIAL ISSUES IN DESIGN, MANUFACTURING AND OPERATION OF NUCLEAR POWER PLANTS EQUIPMENT", CRISM Prometey, 05.-09.06.2006, St. Petersburg, Russland
- Rohde, U.; Grundmann, U.; Kozmenkov, Y.; Pivovarov, V.; Matveev, Yu.
Core design and transient analyses for weapons plutonium burning in VVER-1000 type reactors
KTG-Fachtagung "Stand der Entwicklung für LWR-Brennelemente und Auslegungsmethoden", KTG, 2.-3.3. 2006, Rossendorf
- Rohde, U.; Petkov, P.; Hadek, J.; Kereszturi, A.; Hegyi, G.; Kolev, N.
Benchmarking of reactor physics codes for VVER
1st NURESIM Seminar, CEA, Frankreich, 07.-08.11.2006, Paris, Frankreich
- Schleicher, E.; Hampel, U.; Da Silva, M. J.; Zschau, J.; Fatterschneider, H.; Zimmermann, W.
Development of an optical wire-mesh tomograph for the study of multi-phase flows.
OPTO 2006, 31.05.2006, Nürnberg, Deutschland
- Shatrov, V.; Gerbeth, G.
How to increase the MHD drag reduction efficiency for turbulent flows
Whither Turbulence Prediction and Control, 26.-29.03.2006, Seoul, Korea
- Sorriso-Valvo, L.; Carbone, V.; Stefani, F.; Nigro, G.
A statistical analysis of polarity reversals of the geomagnetic field
AGU 2006 Fall Meeting, American Geophysical Union, 11.-15.12.2006, San Francisco, USA
- Stefani, F.; Gerbeth, G.; Gailitis, A.
The geomagnetic dynamo - laboratory experiments
International Final Colloquium of the German Science Foundation Priority Programme 1097 "Geomagnetic Field Variations: Space-Time Structure, Processes, and Effects on System Earth", Deutsche Forschungsgemeinschaft, 04.-05.10.2006, Braunschweig, Deutschland
- Stefani, F.; Gerbeth, G.; Günther, U.; Xu, M.; Sorriso-Valvo, L.
Reversals made simple: some new results
9th MHD Days 2006, Max-Planck-Institut für Astronomie, Heidelberg, 04.-05.12.2006, Heidelberg, Deutschland
- Stefani, F.; Gundrum, T.; Gerbeth, G.; Xu, M.
Perspectives of contactless inductive flow tomography
The 5th International Symposium on Electromagnetic Processing of Materials (EPM2006), Tohoku University, 23.-27.10.2006, Sendai, Japan
- Stefani, F.; Günther, U.; Gerbeth, G.
Reversals in nature and the nature of reversals
AIMS' Sixth International Conference on Dynamical Systems, Differential Equations and Applications, American Institute of Mathematical Sciences, 25.-28.06.2006, Poitiers, France

Ulbricht, A.

Application of small-angle neutron scattering (SANS) to irradiated pressure vessel steels and iron based model alloys

International School on Experimental Quantification of Irradiation Damage (ISQUID), SCK-CEN Mol, 25.-29.09.2006, Rochehaut sur Semois, Belgien

Vallee, C.

Experimente zur CFD-Validierung für horizontale Zweiphasen-Strömungen

Seminar des Lehrstuhl für Thermodynamik, Lehrstuhl für Thermodynamik, Technische Universität München, 09.01.2006, Garching, München, Deutschland

Vallee, C.; Höhne, T.; Prasser, H.-M.; Sühnel, T.

Experimental investigation and CFD simulation of horizontal stratified two-phase flow phenomena

OECD/NEA International Workshop on The Benchmarking of CFD Codes for Application to Nuclear Reactor Safety (CFD4NRS), 05.-09.09.2006, Garching, Deutschland

Viehrig, H.-W.; Murasov, M.

Bruchmechanische Charakterisierung von WWER-440 Reaktordruckbehälterstählen des Blockes 8 KKW Greifswald

32. MPA-Seminar "Werkstoff- & Bauteilverhalten in der Energie- & Anlagentechnik" 5. und 6. Oktober 2006, Stuttgart, Universität MPA Stuttgart, 05.-06.10.2006, Stuttgart, Deutschland

Viehrig, H.-W.; Murasov, M.

Master Curve testing on WWER-440 reactor pressure vessel steels

ASME Pressure Vessels and Piping Conference/ICPVT-11, 23.-27.07.2006, Vancouver, British Columbia, Canada,

Weier, T.; Cierpka, C.; Gerbeth, G.

Effects of excitation wave form on an electromagnetically forced separated flow

European Drag Reduction and Flow Control Meeting, ERCOFTAC, 10.-14.04.2006, Ischia, Italien

Weiß, F.-P.; Willschütz, H.-G.

Wie sicher sind Kernkraftwerke? - Stand der Sicherheitsforschung

Ganztagskolloquium am 28. September 2006 "50 Jahre Forschung für die friedliche Nutzung der Kernenergie", Dresdner Seniorenakademie Wissenschaft und Kunst und Leibniz-Sozietät Berlin, 28.09.2006, Dresden, Deutschland

Willers, B.; Eckert, S.; Nikrityuk, Petr A.; Eckert, K.

Modification of temperature and solute distribution during directional solidification caused by electromagnetically-driven convection

MCWASP Conference, Modeling of Casting, Welding and Advanced Solidification Processes XI, TMS, ESA, 28.05.-02.06.2006, Opio, France

Willers, B.; Nikrityuk, Petr A.; Eckert, S.; Eckert, K.

The influence of electromagnetically-driven convection on temperature field and solute distribution during directional solidification

5th International Symposium on Electromagnetic Processing of Materials, 23.-27.10.2006, Sendai, Japan

Willschuetz, H.-G.

Enhancement of the simulation of scaled vessel failure experiments by a recursive coupling of the thermal and mechanical FEM-models

International Youth Nuclear Congress, Stockholm and Olkiluoto, IYNC2004 International Youth Executive Committee, 18.-23.06.2006, Stockholm and Olkiluoto, Sverige and Suomi

Willschuetz, H.-G.; Altstadt, E.

Consideration of steel corrosion rates from the MASCA / METCOR-tests to the RPV strength under IVR conditions

Seminar at the Division of Nuclear Power Safety, Division of Nuclear Power Safety, Royal Institute of Technology (KTH), Stockholm, 26.06.2006, Stockholm, Sverige

Willschuetz, H.-G.; Altstadt, E.; Weiss, F.-P.

Application of recursively coupled FE-models to a PWR In-Vessel-Retention analysis

Annual Meeting on Nuclear Technology 2006, May 16-18, Aachen, Deutschland

Willschütz, H.-G.

Der Reaktordruckbehälter in der Spätphase eines Kernschmelzunfalls - eine thermomechanische Modellierung

Jahresabschlussveranstaltung 2006 der Sektion Sachsen der Kerntechnischen Gesellschaft, Kerntechnischen Gesellschaft, Sektion Sachsen, 12.12.2006, Dresden, Deutschland

Willschütz, H.-G.; Altstadt, E.; Weiß, F.-P.

Wechselwirkung zwischen Corium und Reaktordruckbehälter - Experimente, Versagensmodus, Versagenszeitpunkt

Workshop: Corium - Eigenschaften, Wechselwirkungen und Beherrschungskonzepte, Gesellschaft für Anlagen- und Reaktorsicherheit (GRS) mbH, Köln, 09.-10.02.2006, Köln, Deutschland

Zhang, C.; Eckert, S.; Gerbeth, G.

Determination of the flow structure in bubble-driven liquid metal flows using ultrasound Doppler method

5th International Symposium on Ultrasound Doppler Methods (ISUD), 12.-14.09.2006, Zürich, Schweiz

Zhang, C.; Eckert, S.; Gerbeth, G.

Effect of an external magnetic field on the flow in a liquid metal bubble plume

17th International Congress of Chemical and Process Engineering, CHISA, 27.-31.08.2006, Praha, Czech Republic

Zhang, C.; Eckert, S.; Gerbeth, G.

Flow control in bubble-driven liquid metal flows by means of external magnetic fields

The 5th International Symposium on Electromagnetic Processing of Materials (EPM2006), Tohoku University, 23.-27.10.2006, Sendai, Japan

Contributions to proceedings and other collected editions

Al Issa, S.; Prasser, H.-M.; Beyer, M.

Experimental data on a three dimensional flow field around an obstacle in a vertical pipe

Multiphase Flows: Simulation, Experiment and Application, FZR & ANSYS, 26.-29.06.2006, Dresden, Deutschland

CD - Multiphase Flow Workshop, paper II-05

Alt, S.; Hampel, R.; Kästner, W.; Grahn, A.; Krepper, E.

Experimental investigations for head loss build up at clogged strainers after LOCA

Annual Meeting on Nuclear Technology 2006, May 16-18, Aachen, Deutschland,

Proceedings p. 147

Altstadt, E.; Willschütz, H.-G.

Modellierung der Wechselwirkung zwischen Corium und RDB-Stahl im Rahmen von Schmelzerückhaltungsszenarien

MPA Seminar, MPA Stuttgart, 05.-06.10.2006, Stuttgart, Deutschland

Proceedings on CD-ROM, Paper 16.1

Bauer, T.; Schubert, M.; Hampel, U.; Lange, R.

Zweiphasige Strömung in Kapillaren und strukturierten Packungen

Multiphase Flows: Simulation, Experiment and Application, FZR & ANSYS, 26.-29.06.2006, Dresden, Deutschland

CD - Multiphase Flow Workshop, III-6

Bechta, S. V.; Khabensky, V. B.; Granovsky, V. S.; Krushinov, E. V.; Vitol, S. A.; Gusarov, V. V.; Almiyashev, V. I.; Lopukh, D. B.; Tromm, W.; Bottomley, D.; Fischer, M.; Piluso, P.; Miassoedov, A.; Altstadt, E.; Willschütz, H.-G.; Fichot, F.

Experimental study of interactions between suboxidized corium and reactor vessel steel

International Congress on Advances in Nuclear Power Plants - ICAPP 2006, 04.-

08.06.2006, Reno, Nevada, USA

Proceedings on CD-ROM, Paper 6054, p. 1355 – 1362

Bergner, F.; Ulbricht, A.

SANS investigation of neutron-irradiated pressure vessel steels and model alloys

13th Meeting of the International Group on Radiation Damage Mechanisms in Pressure Vessel Steels (IGRDM 13), IGRDM, 16.-20.10.2006, Tsukuba, Japan

Proceedings of IGRDM 13 (on CD), Paper P016, pp. 1-15

Bergner, F.

Application of rate theory modelling to neutron-irradiated low-Cu and Cu-enriched Fe-based model alloys

International School on Experimental Quantification of Irradiation Damage (ISQUID), SCK-CEN Mol (Belgien), 25.-29.09.2006, Rochehaut sur Semois, Belgien

Proceedings of ISQUID (on CD), Mol: SCK-CEN, 1-47

Beyer, H. G.; Drews, A.; Rindelhardt, U.

Irradiance maps applied for the performance assessment of PV-Systems- a case study for the German federal state of Saxony

21th European Photovoltaic Solar Energy Conference and Exhibition, EU DG JRC, 04.-08.09.2006, Dresden, Deutschland
ISBN 3-936338-20-5, p. 2756

Bieberle, A.; Hampel, U.; Kronenberg, J.

Void fraction distribution measurement in fuel element bundles with a new high-resolution gamma tomograph

Annual Meeting on Nuclear Technology 2006, May 16-18, Aachen, Deutschland, Proceedings p. 14-23

Bieberle, A.; Schleicher, E.; Hoppe, D.; Kronenberg, J.; Hampel, U.

Measurement of void fraction distributions in full scale fuel element bundles using gamma ray tomography

4th International Symposium on Process Tomography, 14.-15.09.06, Warschau, Polen, 95-97 Proceedings pp. 95-97, 2006.

Boden, S.; Bieberle, M.; Hampel, U.

Measurement of porosity in polyolefin particles using X-ray microtomography

4th International Symposium on Process Tomography in Poland, 14.-15.09.2006, Warsaw, Poland

4th International Symposium on Process Tomography in Poland, Proceedings, 83-60660-01-8, 102-105

Cramer, A.; Priede, J.; Galindo, V.; Andersen, O.; Kostmann, C.

Container-less melt extraction of metallic fibres

EPM 2006, Tohoku University, 23.-27.10.2006, Sendai, Japan

The 5th International Symposium on Electromagnetic Processing of Materials (EPM2006), Tokyo: The Iron and Steel Institute of Japan, 4-93 980-55-0 C3057, 335-340

Da Silva, M. J.; Brückner, F.; Schleicher, E.; Hampel, U.

High-speed complex admittance/permittivity needle probe for investigation of multiphase flows

IEEE Instrumentation and Measurement Technology Conference, IEEE Instrumentation and Measurement Society, 24.-27.04.2006, Sorrento, Italy

Proceedings of the 23rd IEEE Instrumentation and Measurement Technology Conference: IEEE, 0-7803-9360-0, 1937-1941

Da Silva, M. J.; Schleicher, E.; Hampel, U.

Electrical impedance sensors for multiphase flow measurement

Multiphase Flows: Simulation, Experiment and Application, FZR & ANSYS, 26.-29.06.2006, Dresden, Deutschland

CD - Multiphase Flow Workshop, II-19

Drews, A.; Heinemann, D.; Rindelhardt, U.

Solarstrahlungskarten und Erträge von PV-Anlagen: Ergebnisvergleich in Sachsen

21. Symposium Photovoltaische Solarenergie, DGS, OTTI, 08.-10.03.2006, Staffelstein, Deutschland

Tagungsband S. 450

Frank, T.; Lucas, D.; Prasser, H.-M.; Krepper, E.; Shi, J.-M.

Entwicklung und Validierung von CFD-Modellen für Zweiphasenströmungen

Fachtagung "Aktuelle Themen der Reaktorsicherheitsforschung", KTG, 03.-04.04.2006, Dresden, Deutschland

Tagungsband Beitrag III-16

Frank, T.; Zwart, P.; Krepper, E.; Prasser, H.-M.; Lucas, D.

Validation of CFD models for mono- and polydisperse air-water two-phase flows in pipes

OECD/NEA International Workshop on The Benchmarking of CFD Codes for Application to Nuclear Reactor Safety (CFD4NRS), 05.-09.09.2006, Garching, Deutschland

NEA-CD 6298, Paper 32

Frielinghaus, H.; Ulbricht, A.; Bergner, F.

Characterization of deformed and undeformed Al-alloys

in: T. Brückel, D. Richter, R. Zorn: Neutron Scattering at FRJ-2, Experimental Reports 2005/6, Jülich: Forschungszentrum Jülich GmbH, 2006, 457-458

Gerbeth, G.; Eckert, S.; Galindo, V.; Willers, B.; Hewelt, U.; Katz, H.-W.; Ziemann, M.

Use of magnetic fields in aluminum investment casting

EPM 2006, Tohoku University, 23.-27.10.2006, Sendai, Japan

The 5th International Symposium on Electromagnetic Processing of Materials (EPM 2006), Tokyo: The Iron and Steel Institute of Japan, 4-930980-55-0 C3057, 323-328

Gokhman, A. R.; Bergner, F.; Ulbricht, A.

Iron matrix effects on cluster evolution in neutron irradiated reactor steels

in: Schmelzer, J. W. P., Roepke, G., Priezhev, V.B.: Nucleation Theory and Applications, Dubna, Russia: Joint Institute for Nuclear Research Publ., 2006, 408-419

Grahn, A.; Krepper, E.; Alt, S.; Kästner, W.

1D-modelling of differential pressure buildup at clogged containment sump strainers after LOCA

Annual Meeting on Nuclear Technology 2006, May 16-18, Aachen, Deutschland,

Proceedings p. 154

Grundmann, U.

Calculations of a steady state of the OECD/NRC PWR MOX/UO₂ transient benchmark with DYN3D

Annual Meeting on Nuclear Technology 2006, May 16-18, Aachen, Deutschland,

Proceedings p. 27

Günther, U.; Vargas Moniz, P.; Zhuk, A.

A brane model, its AdS-dS states and their agitated extra dimensions

The tenth Marcel Grossmann meeting on recent developments in theoretical and experimental general relativity, gravitation and relativistic field theories., Brazilian Center for Research in Physics (CBPF), 20.-26.07.2003, Rio de Janeiro, Brazil

Proceedings of the MG10 Meeting held at Brazilian Center for Research in Physics (CBPF), Singapore, New York, Boston: World Scientific Publishing Co., 981-256-667-8, 1715-1717

Günther, U.; Zhuk, A.

Remarks on dimensional reduction of multidimensional cosmological models

The tenth Marcel Grossmann meeting on recent developments in theoretical and experimental general relativity, gravitation and relativistic field theories., Brazilian Center for Research in Physics (CBPF), 20.-26.07.2003, Rio de Janeiro, Brazil

Proceedings of the MG10 Meeting held at Brazilian Center for Research in Physics (CBPF), Singapore, New York, Boston: World Scientific Publishing Co., 981-256-667-8, 877-889

Hampel, U.

Advanced measurement techniques for multiphase flows

CFD OIL 2006, Petrobras Brasil, 15.-18.08.2006, Rio de Janeiro, Brasil

Electronic Proceedings, Paper No. 3, 2006

Hampel, U.

High resolution gamma ray tomography for two-phase flow studies

Multiphase Flows: Simulation, Experiment and Application, FZR & ANSYS, 26.-29.06.2006, Dresden, Deutschland

CD - Multiphase Flow Workshop, II-18

Hampel, U.; Bieberle, A.; Schleicher, E.; Hessel, G.; Zippe, C.; Friedrich, H.-J.

High resolution gamma ray tomography and its application to the measurement of phase fractions in chemical reactors

The 5th International Symposium on Measurement Techniques for Multiphase Flows, 10.-13.12.2006, Macao, China

Multiphase Flow: The Ultimate Measurement Challenge, 942-948

Hampel, U.; Bieberle, A.; Schleicher, E.; Kronenberg, J.

High-resolution gamma ray detector for process tomography

IEEE Sensors 2006, IEEE, 22.-26.10.2006, Daegu, Korea

Proceedings of IEEE Sensors 2006, Paper No. 1159, pp. 510-513, 2006.

Hampel, U.; Bieberle, M.; Fischer, F.; Schleicher, E.; Mattausch, G.; Flaske, H.; Bartel, R.; Do Couto Aktay, K. S.; Koch, D.; Menz, H.-J.; Mayer, H.-G.

Recent developments in ultra fast X-ray computed tomography

PROCTOM2006 4th International Symposium on Process Tomography in Poland, 14.-15.09.2006, Warszawa, Poland, 83-60660-01-8, 173-175

Hampel, U.; Schleicher, E.; Da Silva, M. J.; Li, A.; Thiele, S.; Wollrab, E.

Optical tomograph for the investigation of single and two phase pipe flows

PROCTOM2006 4th International Symposium on Process Tomography in Poland, 14.-15.09.2006, Warszawa, Poland, 83-60660-01-8, 134-137

Hampel, U.; Speck, M.; Prasser, H. M.; Fischer, F.; Mattausch, G.; Flaske, H.; Bartel, R.; Koch, D.; Menz, H.-J.; Mayer, H.-G.

Development of a scanned electron beam X-ray tomography system for high-speed imaging of technical multiphase flows

EBEAM 2006: International Conference on High Powder Electron Beam Technology, 15.-17.10.2006, Reno, USA

Electronic Proceedings, Paper No. 25, 2006

Höhne, T.

CFD-simulation of thermalhydraulic benchmark V1000CT2 - analysis with advanced turbulence models

V1000CT4 Workshop, OECD/NEA, 24.-29.04.2006, Pisa, Italien

Proceedings CD-ROM, p. 16

Höhne, T.; Kliem, S.

Coolant mixing studies of natural circulation flows at the ROCOM test facility using ANSYS CFX

International Workshop on The Benchmarking of CFD Codes for Application to Nuclear Reactor Safety (CFD4NRS), 05.-09.09.2006, Garching, Deutschland

NEA-CD 6298, Paper 23

Höhne, T.; Kliem, S.; Rohde, U.; Weiß, F.-P.

CFD-Analysen zur Kühlmittelvermischung in DWR

Fachtagung "Aktuelle Themen der Reaktorsicherheitsforschung", KTG, 03.-04.04.2006, Dresden, Deutschland

FZR-455, 1437-322X, III-14

Höhne, T.; Kliem, S.; Rohde, U.; Weiss, F.-P.

Buoyancy driven coolant mixing studies of natural circulation flows at the ROCOM test facility using ANSYS CFX

14th International Conference on Nuclear Energy (ICONE-14), May 17-22, 2006, Miami, USA

Proceedings ISBN 0-7918-3783-1, ICONE 14-89120

Höhne, T.; Kliem, S.; Weiss, F.-P.

Buoyancy driven mixing studies of natural circulation flows at the ROCOM facility using ANSYS CFX

Annual Meeting on Nuclear Technology 2006, May 16-18, Aachen, Deutschland,

Proceedings p. 85

Höhne, T.; Vallee, C.

Experiments and ANSYS CFX simulations of horizontal air-water channel flow phenomena

Multiphase Flows: Simulation, Experiment and Application, FZR & ANSYS, 26.-29.06.2006, Dresden, Deutschland

CD - Multiphase Flow Workshop, III-5

Hoppe, D.; Hampel, U.; Kronenberg, J.

Algorithmic treatment of structure deviations in gamma ray tomography data sets

4th International Symposium on Process Tomography, University of Technology, 14.-15.09.2006, Warsaw, Poland, 83-60660-01-8, 163-164

Kliem, S.; Prasser, H.-M.; Sühnel, T.

High-resolution measurements of the coolant mixing in the downcomer of the ROCOM test facility

Annual Meeting on Nuclear Technology 2006, May 16-18, Aachen, Deutschland, Proceedings p. 78-84

Kliem, S.; Prasser, H.-M.; Sühnel, T.; Weiss, F.-P.; Hansen, A.

Experimental investigation of coolant mixing in the RPV of PWR in the late phase of a SBLOCA event

14th International Conference on Nuclear Energy (ICONE-14), May 17-22, 2006, Miami, USA

Proceedings ISBN 0-7918-3783-1, ICONE14- 89472

Kliem, S.; Rohde, U.

State of the art regarding the safety analysis of boron dilution events in Germany

XVI. AER-Symposium on VVER Physics and Reactor Safety, VUJE Trnava, 25.-29.09.2006, Bratislava, Slovakische Republik

Proceedings of the XVI. AER-Symposium on VVER Physics and Reactor Safety, Budapest: AEKI Budapest, 9789633726334, 411-422

Kliem, S.; Sühnel, T.; Prasser, H.-M.; Weiß, F.-P.

Experimente an der Versuchsanlage ROCOM zur Kühlmittelvermischung bei Wiederanlauf der Naturzirkulation

Fachtagung "Aktuelle Themen der Reaktorsicherheitsforschung", KTG, 03.-04.04.2006, Dresden, Deutschland

FZR-455, ISSN 1437-322X, I-6

Kliem, S.; Sühnel, T.; Rohde, U.; Höhne, T.; Prasser, H.-M.; Weiss, F.-P.

Experiments at the mixing test facility ROCOM for benchmarking of CFD-codes

OECD/NEA International Workshop on The Benchmarking of CFD Codes for Application to Nuclear Reactor Safety (CFD4NRS), 05.-09.09.2006, Garching, Deutschland

NEA-CD 6298, Paper 17

Klug, J.; Altstadt, E.; Beckert, C.; Beyer, R.; Freiesleben, H.; Galindo, V.; Greschner, M.; Grosse, E.; Junghans, A. R.; Légrády, D.; Naumann, B.; Noack, K.; Schilling, K. D.; Schlenk, R.; Schneider, S.; Seidel, K.; Wagner, A.; Weiss, F.-P.

Development of a neutron time-of-flight source at the ELBE accelerator

International Workshop on Fast Neutron Detectors and Applications, University of Cape Town, 03.-06.04.2006, Cape Town, South Africa

Proceedings of Science, PoS(FNDA2006) 015, Italien

Klug, J.; Altstadt, E.; Beckert, C.; Beyer, R.; Freiesleben, H.; Greschner, M.; Grosse, E.; Junghans, A. R.; Naumann, B.; Noack, K.; Schneider, S.; Seidel, K.; Wagner, A.; Weiss, F.-P.
Development of a neutron time-of-flight source at the ELBE accelerator
New Trends in Nuclear Physics Applications and Technology, European Physical Society, 22.06.2006, Pavia, Italien
Journal of Physics: Conference Series, 296

Koncar, B.; Krepper, E.
CFD Simulation of forced convective boiling in heated channels
OECD/NEA International Workshop on The Benchmarking of CFD Codes for Application to Nuclear Reactor Safety (CFD4NRS), 05.-09.09.2006, Garching, Deutschland
NEA-CD 6298, Paper 37

Kozmenkov, Y.; Grundmann, U.; Kliem, S.; Rohde, U.; Bousbia Salah, A.
DYN3D/RELAP5 and RELAP5/PARCS calculations of the Kozloduy-6 pump trip test
Annual Meeting on Nuclear Technology 2006, May 16-18, Aachen, Deutschland, Proceedings p. 54-59

Krepel, J.; Rohde, U.; Grundmann, U.
Dynamics of molten salt reactors
International Congress on Advances in Nuclear Power Plants - ICAPP 2006, 04.-08.06.2006, Reno, Nevada, USA
Proceedings CD, p. 714

Krepper, E.; Egorov, Y.; Koncar, B.
Towards CFD modelling of critical heat flux in fuel rod bundles
International Congress on Advances in Nuclear Power Plants - ICAPP 2006, 04.-08.06.2006, Reno, Nevada, USA
Proceedings CD, p. 1672

Krepper, E.; Grahn, A.; Kästner, W.
CFD-Simulation von Mineralwollpartikeln in der Sumpfstromung
Fachtagung "Aktuelle Themen der Reaktorsicherheitsforschung", KTG, 03.-04.04.2006, Dresden, Deutschland
FZR-455, ISSN 1437-322X, III-15

Kryk, H.; Hessel, G.; Schmitt, W.; Tefera, N.
Safety aspects of the process control of Grignard reactions
ISCRE 19, 19th International Symposium on Chemical Reaction Engineering, DECHEMA e.V., 03.-06.09.2006, Potsdam, Deutschland
Book of Abstracts, 362-363

Lenz, M.; Shirai, K.; Büttner, L.; Csarske, J.; Eckert, S.; Gerbeth, G.
Untersuchung elektromagnetischer Strömungsbeeinflussung in elektrisch leitfähigen Fluiden mit Hilfe von 2d2k/1d3k-Ultraschall-Doppler-Array-Techniken
GALA-Fachtagung: Lasermethoden in der Strömungsmesstechnik, Deutsche Gesellschaft für Laser Anemometrie GALA e.V., 05.-07.09.06, Braunschweig, Deutschland
Lasermethoden in der Strömungsmesstechnik, 3-98056 13-3-X, 5.1-5.9

Lucas, D.; Prasser, H.-M.; Manera, A.

Linear stability analysis for the effect of the lift force in a bubble column

7th German/Japanese Symposium on Bubble Columns, GVC, 20.-23.05.2006, Goslar, Deutschland, Proceedings, pp. 223-228

Lycklama à. Nijeholt, Jan-Aiso; Höhne, T.

On the application of CFD modeling for the prediction of the degree of mixing in a PWR during a boron dilution transient

*International Congress on Advances in Nuclear Power Plants - ICAPP 2006, 04.-08.06.2006, Reno, Nevada, USA
Proceedings CD, p. 1646*

Noack, K.; Rogov, A.; Shabalin, E.

Verification of geometrical perturbation calculations for the pulsed fast reactor IBR-2

Monte Carlo 2005 Topical Meeting, 17.-21.04.2005, Chattanooga, Tennessee, USA, 0 89448 695 0

Pal, J.; Eckert, S.; Zhang, C.; Gerbeth, G.

Velocity measurements in metallic melts driven by AC magnetic fields in a square vessel

5th Int. Conference on Electromagnetic Processing of Materials, 23.-27.10.2006, Sendai, Japan

*The 5th International Symposium on Electromagnetic Processing of Materials (EPM2006):
The Iron and Steel Institute of Japan (ISIJ), 4-930980-55-0 C3057, 725-730*

Petkov, P. T.; Mittag, S.

Evaluation of homogenisation error in two-group nodal diffusion calculation for VVER-1000 core

*Annual Meeting on Nuclear Technology 2006, May 16-18, Aachen, Deutschland,
Proceedings: CD, No. 107, p. 46-49*

Priede, J.; Buchenau, D.; Gerbeth, G.

Contactless electromagnetic induction flowmeter based on phase shift measurements

*EPM 2006, Tohoku University, 23.-27.10.2006, Sendai, Japan
The 5th International Symposium on Electromagnetic Processing of Materials (EPM2006),
Tokyo: The Iron and Steel Institute of Japan, 4-930980-55-0 C3057, 735-740*

Rindelhardt, U.; Bodach, M.; Gasch, S.; Hiller, W.; Mehlich, H.

A simple approach to estimate the Performance Ratio of distributed PV plants

*21st European Photovoltaic Solar Energy Conference and Exhibition, EU DG JRC, 04.-08.09.2006, Dresden, Deutschland
ISBN 3-936338-20-5, p.2723*

Rindelhardt, U.; Konheiser, J.; Viehrig, H.-W.; Gleisberg, B.

Pressure vessel investigations of the former Greifswald NPP: Fluence calculations and Nb based fluence measurements

*14th International Conference on Nuclear Energy (ICONE-14), May 17-22, 2006, Miami, USA
Proceedings ISBN 0-7918-3783-1, ICONE-14-89578*

Rindelhardt, U.; Konheiser, J.; Viehrig, H.-W.; Gleisberg, B.
Retrospective dosimetry of Greifswald VVER 440 RPV: Fluence calculations and Nb based fluence measurements

MATERIAL ISSUES IN DESIGN, MANUFACTURING AND OPERATION OF NUCLEAR POWER PLANTS EQUIPMENT, CRISM Prometey, IAEA, EU-JRC, 06.-09.06.2006, St. Petersburg, Russland

Proceedings of the 9th International Conference, p. 241-247

Rindelhardt, U.; Schlegel, H.-J.

Photovoltaic plants in Saxony: Development, status and perspectives

21th European Photovoltaic Solar Energy Conference and Exhibition, EU DG JRC, 04.-08.09.2006, Dresden, Deutschland

ISBN 3-936338-20-5, p.2719

Rindelhardt, U.; Schröder, A.

Betriebserfahrungen mit der ersten sächsischen Photovoltaik-Megawattanlage in Meerane

21. Symposium Photovoltaische Solarenergie, DGS, OTTI, 08.-10.03.2006, Staffelstein, Deutschland

Tagungsband "Photovoltaische Solarenergie", Regensburg: OTTI, 275-279

Rohde, U.; Grundmann, U.; Kozmenkov, Y.; Pivovarov, V.; Matveev, Yu.

Core design and transient analyses for weapons plutonium burning in VVER-1000 type reactors

KTG-Fachtagung "Stand der Entwicklung für LWR-Brennelemente und Auslegungsmethoden", KTG, 2.-3.3. 2006, Rossendorf

Proceedings CD-ROM, p.265

Schleicher, E.; Da Silva, M. J.; Hampel, U.

Enhanced local void and temperature measurements for high-transient two-phase flows

IEEE Instrumentation and Measurement Technology Conference, IEEE Instrumentation and Measurement Society, 24.-27.04.2006, Sorrento, Italy,

Proceedings of the 23rd IEEE Instrumentation and Measurement Technology Conference, 2006. IMTC 06, Piscataway, NJ 08855-1331 USA: IEEE, 0-7803-9360-0, pp. 596-599.

Schleicher, E.; Hampel, U.; Da Silva, M. J.; Zschau, J.; Fatterschneider, H.; Zimmermann, W.

Development of an optical wire-mesh tomograph for the study of multi-phase flows.

OPTO 2006, AMA Service GmbH, 30.05.-01.06.2006, Nürnberg, Deutschland

Sensor+Test 2006, Proceedings, Wunstorf: AMA Service GmbH, 3-9810993-0-3, 115-119

Shatrov, V.; Gerbeth, G.

How to increase the MHD drag reduction efficiency for turbulent flows

Whither Turbulence Prediction and Control, 26.-29.03.2006, Seoul, Korea

Proceedings of the Whither Turbulence Prediction and Control (WTPC) Conference, pp. 80-81

Stefani, F.; Gerbeth, G.; Gailitis, A.

The geomagnetic dynamo - laboratory experiments

International Final Colloquium of the German Science Foundation Priority Programme 1097 "Geomagnetic Field Variations: Space-Time Structure, Processes, and Effects on System Earth", Deutsche Forschungsgemeinschaft, 04.-05.10.2006, Braunschweig, Deutschland Terra Nostra, Heft 2006/3, Berlin: Selbstverlag der Alfred-Wegener-Stiftung, 0946-8978, 83-93

Stefani, F.; Gundrum, T.; Gerbeth, G.; Xu, M.

Perspectives of contactless inductive flow tomography

*EPM 2006, Tohoku University, 23.-27.10.2006, Sendai, Japan
The 5th International Symposium on Electromagnetic Processing of Materials (EPM2006), Tokyo: The Iron and Steel Institute of Japan, 4-930980-55-0 C3057, 745-750*

Ulbricht, A.

Application of small-angle neutron scattering (SANS) to irradiated pressure vessel steels and iron based model alloys

*International School on Experimental Quantification of Irradiation Damage (ISQUID), SCK-CEN Mol (Belgien), 25.-29.09.2006, Rochehaut sur Semois, Belgien
Proceedings of ISQUID (on CD), Mol: SCK-CEN, 1-22*

Ulbricht, A.; Bergner, F.; Pranzas, K. P.

SANS investigation of neutron-irradiated RPV steels with special emphasis on Ni effect

in: A. Schreyer, J. Vollbrandt, R. Willumeit: GeNF - Experimental Reports 2005, GKSS 2006/4, Geesthacht: GKSS Forschungszentrum Geesthacht GmbH, 2006, 107-108

Ulbricht, A.; Boehmert, J.; Viehrig, H.-W.

Microstructural and Mechanical Characterization of the Radiation Effects in Model Reactor Pressure Vessel Steels

*Effects of Radiation on Materials, ASTM, 08.-10.06.2004, Boston, USA
ASTM STP 1475, West Conshohocken, PA: ASTM International, 978-0-8031-3401-0, 151-164*

Vallee, C.; Höhne, T.; Prasser, H.-M.; Sühnel, T.

Experimental investigation and CFD simulation of horizontal stratified two-phase flow phenomena

*CFD4NRS - Benchmarking of CFD Codes for Application to Nuclear Reactor Safety, OECD/NEA International & International Atomic Energy Agency (IAEA), 05.-07.09.2006, Garching, München, Germany
NEA-CD 6298, Paper 31*

Weier, T.; Cierpka, C.; Gerbeth, G.

Effects of excitation wave form on an electromagnetically forced separated flow

European Drag Reduction and Flow Control Meeting, University of Rome "La Sapienza", 10.-13.04.2006, Ischia, Italy, Proceedings, p. 62-63

Willers, B.; Eckert, S.; Nikrityuk, Petr A.; Eckert, K.

Modification of temperature and solute distribution during directional solidification caused by electromagnetically-driven convection

MCWASP Conference, Modeling of Casting, Welding and Advanced Solidification Processes XI, ESA, TMS, 28.05.-02.06.06, Opio, France, Proceedings, 978-0-87339-629-5, 333-340

Willers, B.; Nikrityuk, Petr A.; Eckert, S.; Eckert, K.

The influence of electromagnetically-driven convection on temperature field and solute distribution during directional solidification

5th Int. Conference on Electromagnetic Processing of Materials, 23.-27.10.2006, Sendai, Japan

The 5th International Symposium on Electromagnetic Processing of Materials (EPM2006): The Iron and Steel Institute of Japan (ISIJ), 4-930980-55-0 C3057, 407-412

Willschuetz, H.-G.

Enhancement of the simulation of scaled vessel failure experiments by a recursive coupling of the thermal and mechanical FEM-models

International Youth Nuclear Congress, Stockholm and Olkiluoto, June 18–23, 2006, IYNC2004 International Youth Executive Committee, 18.-23.06.2006, Stockholm and Olkiluoto, Sverige and Suomi

Proceedings of the 2006 International Youth Nuclear Congress, CD-ROM, Paper 275

Willschuetz, H.-G.; Altstadt, E.; Weiss, F.-P.

Application of recursively coupled FE-models to a PWR In-Vessel-Retention analysis

Annual Meeting on Nuclear Technology 2006, May 16-18, Aachen, Deutschland, Proceedings. p. 229

Willschütz, H.-G.; Altstadt, E.; Weiß, F.-P.

Wechselwirkung zwischen Corium und Reaktordruckbehälter - Experimente, Versagensmodus, Versagenszeitpunkt

Workshop: Corium - Eigenschaften, Wechselwirkungen und Beherrschungskonzepte, Gesellschaft für Anlagen- und Reaktorsicherheit (GRS) mbH, 09.-10.02.2006, Köln, Deutschland

Proceedings on CD-ROM, Paper P03

Xu, M.; Stefani, F.; Gerbeth, G.

The integral equation approach to kinematic dynamo theory and its application to dynamo experiments in cylindrical geometry

ECCOMAS CFD 2006, European Conference on Computational Fluid Dynamics, TU Delft, ECCOMAS, 05.-08.09.2006, Egmond aan Zee, The Netherlands

Proceedings ECCOMAS CFD 2006, Eds. P. Wesseling, E. Oñate, J. Périaux, Delft: TU Delft, 90-9020970-0, paper 497

Zhang, C.; Eckert, S.; Gerbeth, G.

Determination of the flow structure in bubble-driven liquid metal flows using ultrasound Doppler method

ISUD5, 12.-14.09.2006, Zürich, Schweiz

Proceedings of the 5th International Symposium on Ultrasonic Doppler Methods for Fluid Mechanics: ETH Zürich, 51-54

Zhang, C.; Eckert, S.; Gerbeth, G.

Effect of an external magnetic field on the flow in a liquid metal bubble plume

17th International Congress of Chemical and Process Engineering, CHISA 2006, 27.-31.08.2006, Praha, Czech Republic, Proceedings CD-ROM, E3.9

Zhang, C.; Eckert, S.; Gerbeth, G.

Flow control in bubble-driven liquid metal flows by means of external magnetic fields

5th Int. Conference on Electromagnetic Processing of Materials, 23.-27.10.2006, Sendai, Japan

*The 5th International Symposium on Electromagnetic Processing of Materials (EPM2006):
The Iron and Steel Institute of Japan (ISIJ), 4-930980-55-0 C3057, 242-247*

FZR reports and other reports

Altstadt, E.; Böhmert, J.; Ulbricht, A.; Borodin, Vladimir A.; Ganchenkova, M.; Voskoboinikov, R.

Mikrostrukturelle Mechanismen der Strahlenversprödung

Wissenschaftlich-Technische Berichte / Forschungszentrum Rossendorf; FZR-452 Mai 2006
117 Seiten

Beckert, C.; Rohde, U. [Projektleiter]

Entwicklung eines 3D Neutronentransportcodes auf der Basis der Ray-Tracing-Methode und Untersuchungen zur Aufbereitung effektiver Gruppenquerschnitte für heterogene LWR-Zellen

Wissenschaftlich-Technische Berichte / Forschungszentrum Rossendorf; FZR-446 Januar 2006
144 Seiten

Beyer, M.; Carl, H.

Ursachenermittlung und Beseitigung der Folgen des Brandes am Heißstrangmodell der TOPFLOW-Anlage

Forschungszentrum Rossendorf 2006; FZD\FWS\2006\02
8 Seiten

Gerbeth, G.; Buchenau, D.; Eckert, S.; Galindo, V.; Willers, B.; Witke, W.

Kontrolle von Aluminium-Feinguss mittels Einsatz einer elektromagnetischen Induktionspumpe

Forschungszentrum Rossendorf 2006
Abschlussbericht zum BMBF-Projekt 01 RW 0304, Dezember 2006

Gregor, S.; Prasser, H.-M.; Beyer, M.

Thermohydraulische Modellierung der Kondensation von Dampf in einer unterkühlten Flüssigkeitsströmung

Wissenschaftlich-Technische Berichte / Forschungszentrum Rossendorf; FZR-440 Juli 2006
138 Seiten

Günther, U.; Stefani, F.; Gerbeth, G.

Untersuchung von Spektraleigenschaften kugelsymmetrischer α^2 -dynamos mit Techniken der Funktionalanalysis und Operatortheorie

Forschungszentrum Rossendorf 2006
Abschlussbericht zum DFG-Projekt Ge 682/12-2, Mai 2006

Hampel, U.; Bieberle, A.; Hessel, G.; Zimmermann, W.; Zippe, C.

Untersuchungen zum Flüssigkeits-Holdup und zur Flüssigkeitsverweilzeit in Schüttungen mittels Röntgenradiographie und Gammatomographie

Wissenschaftlich-Technische Berichte / Forschungszentrum Rossendorf; FZR-456 August 2006
28 Seiten

Kliem, S.

Realistische Simulation von Reaktivitätsstörfällen mit gekoppelten neutronenkinetisch-thermohydraulischen Systemcodes

Forschungszentrum Rossendorf 2006; FZD\FWS\2006\01

76 Seiten

Kliem, S.; Laczkó, G.; Mittag, S.

Berechnungen zur kritischen Leistung eines Siedewasserreaktors im kalten Zustand mit dem Programm DYN3D

Forschungszentrum Rossendorf 2006; FZD\FWS\2006\04

25 Seiten

Kliem, S.; Sühnel, T.

Experimente an der Versuchsanlage ROCOM zur Bestimmung der minimalen Borkonzentration bei postulierten Störfällen mit kleinem Leck im heißen Strang

Forschungszentrum Rossendorf 2006; FZD\FWS\2006\03

75 Seiten

Krepper, E.; Grahn, A.

Untersuchung des Verhaltens von freigesetztem Isolationsmaterial in einer Kühlmittelströmung (Kühlmittelströmung mit Feststoffpartikeln) - Modellentwicklung

Wissenschaftlich-Technische Berichte / Forschungszentrum Rossendorf; FZR-458 September 2006

58 Seiten

Lucas, D.

Synthesis report on work package 2.1: Pressurized Thermal Shock (PTS)

Forschungszentrum Rossendorf 2006; FZD\FWS\2006\06

19 Seiten

Ulbricht, A.

Untersuchungen an neutronenbestrahlten Reaktordruckbehälterstählen mit Neutronen-Kleinwinkelstreuung

Wissenschaftlich-Technische Berichte / Forschungszentrum Rossendorf; FZR-453 April 2006

105 Seiten

Ulbricht, A.; Bergner, F.; Cizek, J.; Melikhova, O.; Prochazka, I.; Kuriplach, J.

Complete characterization of selected model alloys and VVER1000 steels by SANS, TEM and PAS

Forschungszentrum Rossendorf 2006; FZD\FWS\2006\05

14 Seiten

Weier, T.

Elektromagnetische Strömungskontrolle mit wandparallelen Lorentzkräften in schwach leitfähigen Fluiden

Wissenschaftlich-Technische Berichte / Forschungszentrum Rossendorf; FZR-454 Mai 2006

252 Seiten

Weiß, F.-P. (Editor)

Aktuelle Themen der Reaktorsicherheitsforschung in Deutschland

Wissenschaftlich-Technische Berichte / Forschungszentrum Rossendorf; FZR-455 Juni 2006
300 Seiten

Weiß, F.-P. (Editor)

Stand der Entwicklung für LWR Brennelemente und Auslegungsmethoden

Forschungszentrum Rossendorf 2006; FZD/FWS/2006/07
350 Seiten

Weiss, F.-P.; Rindelhardt, U. (Editors)

Annual Report 2005 - Institute of Safety Research

Wissenschaftlich-Technische Berichte / Forschungszentrum Rossendorf; FZR-457 November 2006
170 Seiten

Willschütz, H.-G.

Thermomechanische Modellierung eines Reaktordruckbehälters in der Spätphase eines Kernschmelzunfalls

Wissenschaftlich-Technische Berichte / Forschungszentrum Rossendorf; FZR-447 Januar 2006
0192 Seiten

Granted Patents

Hampel, U. Schleicher, E.:

Faseroptischer Sensor zur Bestimmung von Stoff- und Phasenverteilungen.

DE 10 2004 037 883 B4

Priede, J.; Gerbeth, G.; Hermann, R. Filip, O.:

Verfahren und Vorrichtung zur schmelzmetallurgischen Herstellung von Magnetlegierungen auf Nd-Fe-B-Basis.

DE 103 31 152 B4

Prasser, H.-M.; Pietruske, H. Sühnel, T.:

Gittersensor.

DE 10 2005 019 739 B

Willschütz, H.-G.

Steuereinrichtung für den Kühlkreislauf von Kernreaktoren.

EP 1410402 B1 - Nationalisiert nach DE, CH, FI, FR, SE

Gerbeth, G.; Eckert, S. Stafani, F.; Cramer, A.:

Verfahren und Anordnung zur kontaktlosen Bestimmung von räumlichen Geschwindigkeitsverteilungen in elektrisch leitenden Flüssigkeiten.

EP 1285277 B1

Prasser, H.M.; Zschau, J.:

Arrangement for the Determination by Measurement of a Projection of the Radiation Absorption Capacity of a periodically-variable Measured Object.

US 7,085,344 B2

PhD and diploma theses

PhD theses

Tom Weier

Elektromagnetische Strömungskontrolle mit wandparallelen Lorentzkräften in schwach leitfähigen Fluiden
TU Dresden

Andreas Ulbricht

Untersuchungen an neutronenbestrahlten Reaktordruckbehälterstählen mit Neutronen-Kleinwinkelstreuung
Bergakademie Freiberg

Jiri Krepel

Dynamics of Molten Salt Reactors
TU Prag

Diploma theses

Bin Cai

Entwicklung eines schnellen Datenerfassungsmoduls für einen räumlich hochauflösenden Gammatomographen
TU Dresden

Aiping Li

Experimentelle Untersuchungen zur optischen Tomographie von Zweiphasenströmungen
TU Dresden

Ling Liu

Anwendung von Bildverarbeitungsmethoden zur Analyse von Vermischungsvorgängen in einem Chemiereaktor
TU Dresden

Martin Tschofen

Technologische Weiterentwicklung von Nadelsonden zur Messung von lokalen Gasgehalten in Zweiphasenströmungen bei hohen Temperaturen und Drücken
FH Jena

Eginard Wollrab

Entwicklung eines Kapazitäts-Gittersensors für die Untersuchung von Mehrphasenströmungen
HTW Dresden

Cornelia Heintze

Anforderungsprofil und Eigenschaftsspektrum ausgewählter Stähle für Kernenergieanlagen
TU Dresden

Awards 2006

André Bieberle

Kompetenzpreis der KTG 2006

Voidmessung am Test – Brennstabündel KATHY

Date: 18 May 2006

G. Gerbeth, Th. Gundrum, F. Stefani

Forschungspreis 2006 des FZD

Experimenteller Nachweis der Magneto-Rotationsinstabilität

Date of award: 07 February 2007

H. G. Beyer, A. Drews, U. Rindelhardt

Poster Award of the 21st European Photovoltaic Solar Energy Conference and Exhibition (Dresden, 4-8 September 2006) in the area "PV systems in grid connected applications"

Irradiance maps applied for the performance assessment of PV systems: A case study for the German federal state Saxony

Date of award: 08 September 2006

Jiri Krepel

Anerkennungspreis 2006 des FZD für Doktorandenarbeit

Dynamics of Molten Salt Reactors

Date of award: 07 February 2007

and for the same work:

2nd Price of CEZ Group (Prague) in Competition of Diploma and Doctor Thesis

Guests

Klukins, Alexandrs Dr.

25.01.2006 – 05.02.2006

Institute of Physics Riga/Lettland

Denisov, Sergey Dr.

09.02.2006 - 29.03.2006

Academy of Science Perm/Russland

Khripchenko, Stanislav Dr.

09.03.2006 – 29.03.2006

Academy of Science Perm/Russland

Osmera, Bohumil Dr.

06.03.2006 – 17.03.2006

UJV Rez/Tschechien

Cvachovec, Frantisek Prof.

06.03.2006 – 17.03.2006

UJV Rez/Tschechien

Rogov, Anatoly Dr.

01.03.2006 – 30.04.2006

01.11.2006 – 31.12.2006

Joint Institute for Nuclear Research Dubna/Russland

Kozmenkov, Yaroslav

01.03.2006 – 15.09.2006

Institute for Physics and Power Engineering Obninsk/Russland

Kaji, Ryuhai

18.03.2006 – 13.05.2006

University of Nottingham/England

Omebere-Iyari, Nkem Karl

18.03.2006 – 13.05.2006

University of Nottingham/England

Strmensky, Ctibor

12.03.2006 – 25.03.2006

VUJE Trnava/Slowakei

Priede, Janis Dr.

18.04.2006 – 05.05.2006

Institute of Physics Riga/Lettland

29.11.2006 – 01.12.2006

University of Coventry/England

Gashenko, Ilja

11.05.2006 – 30.06.2006

FSUE EREC Elektrogorsk/Russland

Borodkin, Gennadi

01.05.2006 – 30.06.2006

05.11.2006 – 29.12.2006

GOSATOMNADZOR Moscow/Russland

Khrennikov, Nikolai Dr.

02.05.2006 – 07.05.2006

GOSATOMNADZOR Moscow/Russland

Danitseva, Irina

02.05.2006 – 07.05.2006

GOSATOMNADZOR Moscow/Russland

Samsonov, Boris Prof.

24.04.2006 – 05.06.2006

22.10.2006 – 02.11.2006

Universität Tomsk/Russland

Erkaev, Nikolai Prof.

27.04.2006 – 29.04.2006

TU Braunschweig

Chernobaeva, Anna Dr.

10.05.2006 – 14.05.2006

Kurchatov Institut Moskau/Russland

Erak, Dimitry Dr.

10.05.2006 – 14.05.2006

Kurchatov Institut Moskau/Russland

Krasikov, Evgeny Dr.

10.05.2006 – 14.05.2006

Kurchatov Institut Moskau/Russland

Znojil, Miloslav Prof.

17.05.2006 – 19.05.2006

06.09.2006 – 10.11.2006

UJV Rez/Tschechien

Chrapciak, Vladimir Dr.

22.05.2006 – 02.06.2006

VUJE Trnava/Slowakei

Boushbia Salah, Anis Dr.

06.06.2006 – 31.08.2006

30.10.2006 – 31.12.2006

Universität Pisa/Italien

Dong, Jie Dr.

05.07.2006 – 31.08.2006

01.09.2006 – 31.12.2006

Jiao Tong Universität/China

Zhang, Xiugang

14.07.2006 – 13.10.2006

Jiao Tong Universität/China

Gokhman, Alexander Prof.

01.08.2006 – 30.09.2006

01.10.2006 – 31.10.2006

Universität Odessa/Ukraine

Bagryansky, Petr Dr.

19.08.2006 – 26.08.2006

Budker-Institut Novosibirsk/Russland

Plevachuk, Yuri Dr.

21.08.2006 – 24.08.2006

Staatliche Universität Lviv/Ukraine

Ivanov, Alexandre Prof.

02.09.2006 – 10.09.2006

Budker-Institut Novosiborsk/Russland

Petkov, Petko Dr.

24.09.2006 – 22.12.2006

Bulgarische Akademie der Wissenschaften/Bulgarien

Borodkin, Pavel

05.11.2006 – 29.12.2006

GOSATOMNADZOR Moscow/Russland

Tsildulko, Yuri Dr.

02.12.2006 – 22.12.2006

Budker-Institut Novosibirsk/Russland

Meetings and Workshops

KTG-Fachtagung „Stand der Entwicklung für LWR Brennelemente und Auslegungsmethoden“

KTG Fachgruppen „Brennelemente und Kernbauteile“ und „Reaktorphysik und Berechnungsmethoden“

Rosendorf, 02.-03.03.2006

61. Sitzung DECHEMA/GVC-Arbeitsausschuss

„Sicherheitsgerechtes Auslegen von Chemieapparaten“

Rosendorf, 08.-09.03.2006

KTG-Fachtagung „Aktuelle Themen der Reaktorsicherheitsforschung in Deutschland“

KTG-Fachgruppen “Sicherheit kerntechnischer Anlagen”, “Thermo- und Fluidodynamik” und “Betrieb von kerntechnischen Anlagen”

Rosendorf, 03.-04.04.2006

EUROTRANS-Meeting (EU-Projekt), Domain DEMETRA

Rosendorf, 21.-22.6.2006

Multiphase Flow Simulation, Experiment and Application Conference and Short course

Rosendorf, 26.-29.06.2006

Organizer: FZR and ANSYS Germany

Klausurtagung SFB 609: Elektromagnetische Strömungsbeeinflussung in Metallurgie, Kristallzüchtung und Elektrochemie

Rosendorf, 20.-21.07.2006

Workshop CFD-Verbund

Rosendorf, 11.09.2006

PERFECT-Meeting (EU-Projekt), Subproject Physics

Rosendorf, 02.-03.11.2006

IAEA-Meeting

Master Curve Approach to Monitor Fracture Toughness of Reactor Pressure Vessels in Nuclear Power Plant

Rosendorf, 06.-10.11.2006

Seminars of the Institute

D. Buchenau

Entwicklung von kontaktlosen, elektromagnetischen Durchflussmessern mit hoher zeitlicher und räumlicher Auflösung zur Strömungskontrolle in der Metallurgie
12.01.2006

Dr. D. Hennig (Berlin)

Prinzipien der SWR Stabilitätsanalyse
27.01.2006

Dr. E. Krepper

Auf dem Weg zur Vorhersage der Siedekrise in Brennstabbündeln mittels CFD
09.02.2006

H. Pietruske, Prof. H.-M. Prasser

Hochdruckgittersensor – Stand der Technik, Probleme, Ausblick
23.02.2006

S. Kliem

Analyse der Borverdünnungsszenarien in einem DWR mit dem gekoppelten Programmkomplex DYN3D/ATHLET
06.04.2006

Dr. H. Ait Abderrahim (SCK-CEN Mol/Belgien)

Status and Perspectives of X-ADS
20.04.2006

Prof. Dr. N.V. Erkaev (Russian Academy of Sciences Krasnoyarsk/Russia)

Magnetohydrodynamic modelling of solar wind interaction with planets
27.04.2006

C. Cierpka

Zeitaufgelöste Messungen der elektromagnetisch beeinflussten Plattenumströmung
04.05.2006

Prof. R. Pippan (Montanuniversität Leoben/Österreich)

Mechanische Untersuchungen im Mikrometer- und Submikrometerbereich
01.06.2006

Prof. Nam Dinh (KTH Stockholm)

Avenues and Challenges in Severe Accident Risk Management in a BWR Plant
27.06.2006

J. Krepel

DYN3D-MSR: Dynamik und Sicherheit der Salzschnmelzenreaktoren
31.08.2006

Dr. F. Stefani

Erste Ergebnisse des PROMISE-Experiments zum Nachweis der Magnetrotationsinstabilität
14.09.2006

Prof. Mohamed Gad-el-Hak (Virginia Commonwealth University/USA)

The Art and Science of Large-Scale Disasters
25.09.2006

Dr. T. Höhne, Ch. Vallee

Experimente und CFD-Simulation horizontaler Kanalströmungen
19.10.2006

Dr. E. Altstadt, Dr. H.-G. Willschütz

Schmelzerückhaltung im RDB eines WWER-1000 mit Berücksichtigung der Wechselwirkung
zwischen Corium und RDB-Stahl
26.10.2006

Dr. G. Scheuerer (ANSYS)

Möglichkeiten, Grenzen und Perspektiven von CFD-Methoden in Anwendungen für die
Reaktorsicherheitsforschung
02.11.2006

Dr. R. Koch

Praxis der Zell- und Abbrandrechnungen von Druckwasserreaktoren und Vergleich der
Ergebnisse deutscher Arbeitsgruppen
09.11.2006

Dr. B. Merk

Consequences of Different Fuel Cycle Options on the Produced Actinide Masses in the
German Reactor Park
14.12.2006

Lecture courses

Frank-Peter Weiß

Zuverlässigkeit und Sicherheit technischer Systeme
TU Dresden, Fakultät Maschinenwesen
SS 2006 und WS 2006

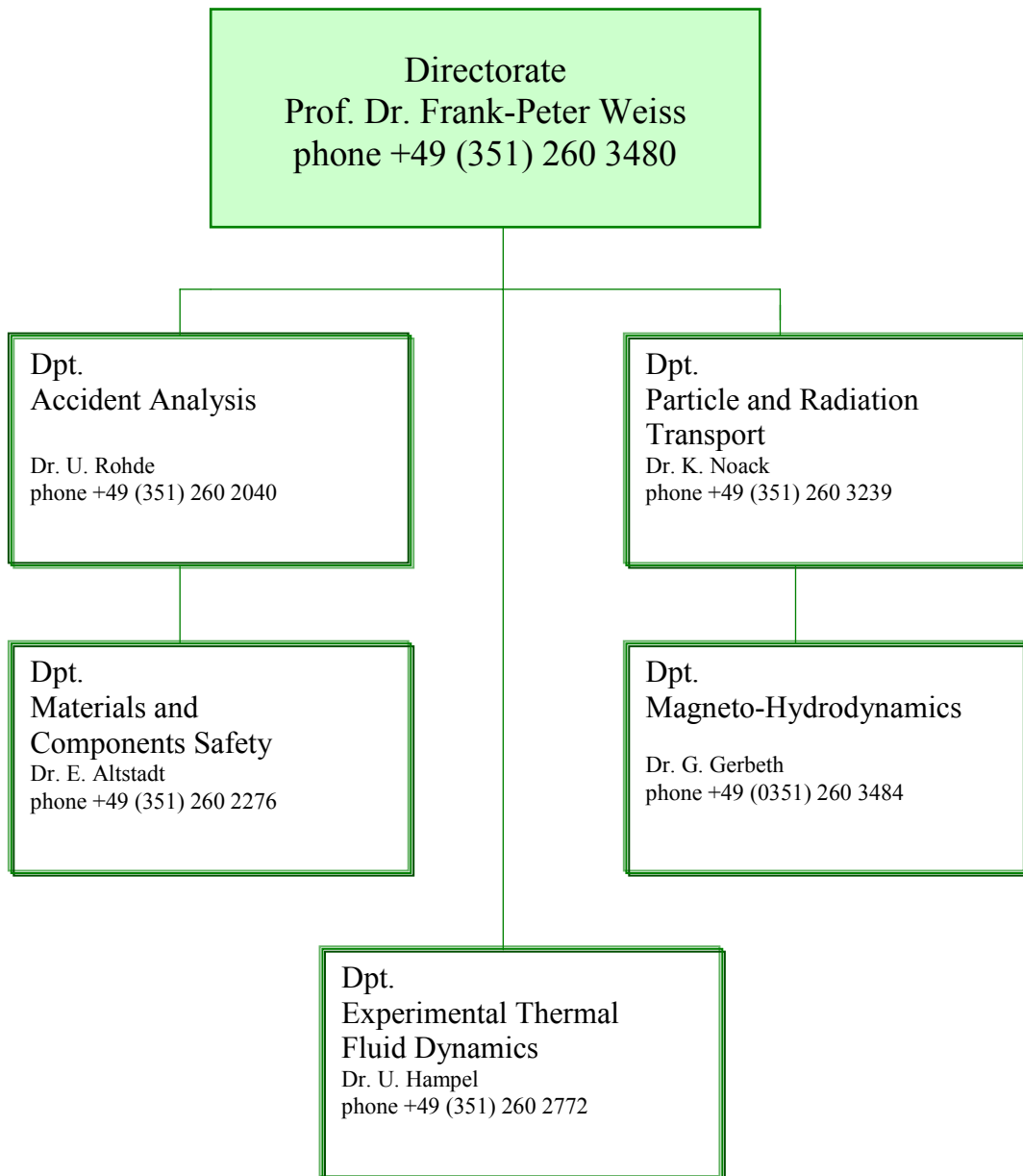
Udo Rindelhardt

Erneuerbare Energien I und II
Universität Chemnitz, Fakultät Elektrotechnik/Informationstechnik
SS 2006 und WS 2006

Uwe Hampel

Computertomographie in der Medizin und Prozessdiagnostik
TU Dresden, Fakultät Elektro- und Informationstechnik
SS 2006

Departments of the Institute



contact:

Forschungszentrum Dresden-Rossendorf e.V.
Institute of Safety Research
P.O. Box 51 01 19
D-01314 Dresden
Germany
phone +49 (351) 260 3480
fax +49 (351) 260 3448
e-mail f.p.weiss@fzd.de
internet <http://www.fzd.de/FWS>

Personnel 2006

Director: Prof. Dr. F.-P. Weiß

Scientific Staff

Abendroth, Martin Dr.
Altstadt, Eberhard Dr.
Beckert, Carsten
Bergner, Frank Dr.
Beyer, Matthias
Birkenheuer, Uwe Dr.
Bodele, Emmanuel Dr.
Carl, Helmar Dr.
Cartland-Glover, Gregory Dr.
Chatrov, Viktor Dr.
Cramer, Andreas Dr.
Eckert, Sven Dr.
Galindo, Vladimir Dr.
Gerbeth, Gunter Dr.
Grahn, Alexander Dr.
Grants, Ilmars Dr.
Grundmann, Ulrich Dr.
Gundrum, Thomas
Günther, Uwe Dr.
Hampel, Uwe Dr.
Hoppe, Dietrich Dr.
Höhne, Thomas Dr.
Hristov, Hristo Vesselin Dr.
Kliem, Sören
Klukins, Alexandrs Dr.
Koch, Reinhard Dr.
Krepel, Jiri
Krepper, Eckhard Dr.
Kryk, Holger Dr.
Küchler, Roland Dr.
Legrady, David Dr.
Lucas, Dirk Dr.
Manera, Annalisa Dr.
Merk, Bruno Dr.
Mittag, Siegfried Dr.
Mutschke, Gerd

Noack, Klaus Dr.
Pal, Josef Dr.
Prasser, Horst-M. Prof. Dr.
Rindelhardt, Udo Prof. Dr.
Rohde, Ulrich Dr.
Schäfer, Frank Dr.
Schleicher, Eckhard
Schmitt, Wilfried Dr.
Stefani, Frank Dr.
Ulbricht, Andreas Dr.
Viehrig, Hans-Werner Dr.
Weier, Tom Dr.
Werner, Matthias Dr.
Willers, Bernd
Willschütz, Hans-Georg Dr.
Xu, Mingtian Dr.
Zippe, Cornelius Dr.
Zurbuchen, Conrad

PhD Students

Al Issa, Suleiman
Bieberle, André
Bieberle, Martina
Bilodid, Yuri
Boden, Stephan
Buchenau, Dominique
Cierpka, Christian
Fischer, Frank
Laczko, Gabor
Miao, Xincheng
Schlemmer, Tobias
Silva da, Marco
Timmel, Klaus
Vallee, Christophe
Zhang, Chaojie
Zaruba, Aliaksandr

Technical Staff

Behrens, Sieglinde
Berger, Torsten
Bombis, Doris
Borchardt, Steffen
Erlebach, Stephan
Fleischer, Andreas
Forker, Klaus
Futterschneider, Hein
Gommlich, André
Hessel, Günther
Konheiser, Jörg
Kunadt, Heiko
Lindner, Klaus
Losinski, Claudia
Müller, Gudrun Dr.
Nowak, Bernd
Pietzsch, Jens
Pietruske, Heiko
Richter, Annett
Richter, Henry
Richter, Joachim
Richter, Petra
Roßner, Michaela
Rott, Sonja
Rußig, Heiko
Schleißiger, Heike
Schneider, Gisela
Schütz, Peter
Schuhknecht, Jan
Skorupa, Ulrich
Sühnel, Tobias
Tamme, Marko
Tschofen, Martin
Webersinke, Wolfgang
Weichelt, Steffen
Weiß, Rainer
Wollrab, Eginhard
Zimmermann, Wilfried